Numerical Modelling of the Influence of Lower Boundary Roughness on Turbulent Sedimentary Flows

Armin Arfaie

The University of Leeds

School of Chemical and Process Engineering

December 2015

Submitted in accordance with the requirements for the degree of

Doctor of Philosophy

The candidate confirms that the work submitted is his own, except where work which has formed part of jointly authored publications has been included. The contribution of the candidate and the other authors to his work has been explicitly indicated below. The candidate confirms that appropriate credit has been given within the thesis where reference has been made to the work of others. The work appears in the jointly authored publication appears in chaptrs 5, 6 and 7 of this thesis and the details of the works are as follows:

A. Arfaie, A.D. Burns, R. Dorrell, J.T. Eggenhuisen, D.B. Ingham, W.D. McCaffrey (2013)'Turbidity current interactions with rugose substrates', *30th International Association of Sedimentologists Meeting*, Manchester,UK.

A. Arfaie, A.D. Burns, R. Dorrell, J.T. Eggenhuisen, D.B. Ingham, W.D. McCaffrey (2013)'Optimised turbulence enhancement during shear flow over a rib roughened boundary: implications for turbidity currents run-out length', *52th BSRG Annual General Meeting*, Hull, UK.

A. Arfaie, A.D. Burns, R. Dorrell, J.T. Eggenhuisen, D.B. Ingham, W.D. McCaffrey (2014)'Turbidity Current Flows over Rough Substrates', Annual Convention & Exhibition, *The American Association of Petroleum Geologists (AAPG), Houston Texas, USA.*

A. Arfaie, A.D. Burns, R. Dorrell, J.T. Eggenhuisen, D.B. Ingham, W.D. McCaffrey (2014). Optimised turbulence enhancement during shear ow over a rib roughened boundary, *International Communications in Heat and Mass transfer*.

Dorrell, R., Arfaie, A.D. Burns, A., Eggenhuisen, J., Ingham, D. & McCaffrey, W. 2014. Turbulent Mixing and Flow Resistance over Dunes and Scours. *AGU Fall Meeting Abstracts, 1, 3535.*

All the work within the publication is directly attributable to the lead author and the contributions of the other authors was aiding in the interpretation of the results and the actual writing of the paper.

 Armin Arfaie

Acknowledgments

Abstract

Numerical computations have been performed to evaluate the influence of bedform roughness on turbulent transport of sediments in geophysical flows. Special attention is paid to turbidity currents, which are responsible for the transport of sedimentary rocks far into the deep ocean. It has been suggested that enhanced turbulence mixing in flows over rugose topography contributes to the unexpectedly large runout lengths of naturally occurring turbidity currents. One of the objectives of this study is to provide evidence for against this conjecture.

We perform computations over a wide range of periodic arrays of rectangular roughness elements, We find that a strong peak in turbulent mixing occurs when the width-to-height ratio equals a critical value of seven. We also find that a strong peak in resistance to flow occurs at the same critical value. These are competing effects, with the former acting to promote, and the latter acting to diminish runout length. So we are not able to conclude definitively that the enhancement of mixing is responsible for long runout lengths.

We continue by considering flows over periodic arrays of shapes which are representative of bedforms that occur in the natural environment. We again find a strong correlation between the optimisation of both turbulence mixing and resistance to the flow. We are unable to distinguish bedform shapes that promote long runout length relative to the flat bed case. However, we are able to distinguish those bedform shapes that have large resistance to flow and large turbulence mixing compared to those that have low resistance and low turbulent mixing, with the latter case occurring for widely spaced asymmetric dunes with a long low angled slope facing the flow.

Finally, we develop a model for flow and sediment transport which takes into account erosion and deposition from the bottom boundary. We first apply this model to flow over fixed dune shapes, in order to assess the influence of bedform shape on flow capacity, stratification, and the energy budget. An important result of this study is that flow capacity is optimised for the class of bedform shapes that promote low flow resistance and low turbulent mixing.

We conclude by applying the model to the two-way coupled flow of a mobile dune, starting from an initially symmetric inherited dune morphology. We find that, for sufficiently large grain sizes, the dune evolves into a sequence of asymmetric dunes, rather than to a flat bed, and that the long-time evolution tends to be towards those

dune shapes that promote large relative flow capacity. However, the model has a discrepancy in that it is unable to prevent the dune shape exceeding the maximum angle of repose. Hence, further work is required before these results can be regarded as reliable.

Conferences and Publications

A. Arfaie, A.D. Burns, R. Dorrell, J.T. Eggenhuisen, D.B. Ingham, W.D. McCaffrey (2013)'Turbidity current interactions with rugose substrates', *30th International Association of Sedimentologists Meeting*, Manchester,UK.

A. Arfaie, A.D. Burns, R. Dorrell, J.T. Eggenhuisen, D.B. Ingham, W.D. McCaffrey (2013)'Optimised turbulence enhancement during shear flow over a rib roughened boundary: implications for turbidity currents run-out length', *52th BSRG Annual General Meeting*, Hull, UK.

A. Arfaie, A.D. Burns, R. Dorrell, J.T. Eggenhuisen, D.B. Ingham, W.D. McCaffrey (2014)'Turbidity Current Flows over Rough Substrates', Annual Convention & Exhibition, *The American Association of Petroleum Geologists (AAPG), Houston Texas, USA.*

A. Arfaie, A.D. Burns, R. Dorrell, J.T. Eggenhuisen, D.B. Ingham, W.D. McCaffrey (2014). Optimised turbulence enhancement during shear ow over a rib roughened boundary, *International Communications in Heat and Mass transfer*.

Dorrell, R., Arfaie, A.D. Burns, A., Eggenhuisen, J., Ingham, D. & McCaffrey, W. 2014. Turbulent Mixing and Flow Resistance over Dunes and Scours. *AGU Fall Meeting Abstracts, 1, 3535.*

Table of Contents

List of Figures

List of Tables

Nomenclature

$\partial p/\partial x$	mean pressure gradient
$\overline{u_i' u_j'}$	Reynolds stress
P_0	reference pressure point

Greek

α	turbulence model empirical constant
α_{Ave}	total particle volume fraction
α_d	sediment volume fraction
ρ	density
ρ_s	sediment density
β	turbulence model empirical constant
β_0	turbulence model empirical constant
ΔB	velocity shift due to bed roughness
δt	time-step
δ	node displacement
κ	von Karman constant
λ	wavelength
μ	molecular or dynamic viscosity
μ_t	effective molecular viscosity
μ^+	non-dimensionalised eddy viscosity
ε	turbulence eddy diffusivity
ϵ_T	total energy of the system
τ	total wall shear stress
τ_f	wall shear stress due to pressure
τ_s	wall shear stress due to friction
τ_{cr}	critical wall shear stress
Θ_d	kinetic energy of the dispersed phase
Θ_c	kinetic energy of the continous phase
θ	Shields parameter
θ_{cr}	critical Shields parameter
θ_β	local shield parameter
Φ_d	volume-weighted average sediment mass conentration
ϕ	sediment diameter
ϕ_m	maximum packing concentration
ϕ_v	volumetric sediment concentration

ϕ_c	reference concentration
Δ_s	bedform height
γ_s	sediment gravity
Γ_{disp}	mesh stiffness
η	net deposition erosion rate
Π_d	potential energy of the dispersed phase
Π_c	potential energy of the continuous phase
ω	turbulent eddy frequency

Roman (upper-case)

F_1F_2	Blending function
Fr	Froude number
H	Height of the channel
Re	Reynolds number
Re_τ	shear Reynolds number
R_i	Richardson number
R_{id}	densimetric Richardson number
S	bedform shape
S_ϕ	source term
S_c	Schmidt number
D_s	skin friction
D_f	form drag
D_*	dimensionless grain size
D_v	volumetric sediment settling rate
D_m	deposition rate mass flux
A_w	wetted area
A_p	projected area
C	time-averaged mean particle concentration
C_a	near-bed concentration
C_t	temporal flow capacity
C_0	initial flow capacity
L	flow length scale
L_x	the horizontal length of the computational domain
L_y	the vertical length of the computational domain
M_s	momentum of the stratified fluid
M_u	momentum of the unstratified fluid
M_u	momentum of the unstratified fluid

N_x	number of nodes in the x-direction
N_y	number of nodes in the y-direction
J_s	mass flux of the stratified fluid
J_u	mass flux of the unstratified fluid
N	number of phases
E_v	volumetric erosion rate
E_m	erosion rate mass flux
V	overall volume of the computational domain
H	half channel height

Roman (lower-case)

$\acute{u}$	fluctuating velocity in x-direction
$\bar{u}$	average velocity in x-direction
C_ρ	roughness constant
h	characteristic height
h_f	height of gravity current front
k	turbulence kinetic energy
h_s^+	roughness Reynolds number
h_s	equivalent roughness height
m	mass
g	gravity
n	number of observations
P	pressure
t	time
u_*	shear velocity
u_p	sediment slip velocity in x-direction
u	velocity component in x-direction
υ	velocity component in y-direction
ω	velocity component in z-direction
x, y, z	cartesian coordinate variables
x_0	initial front position
y^+	dimensionless wall unit
y_t	truncated region in y-direction
y_l	the origin of the logarithmic profile
v_p	sediment slip velocity in y-direction
w	width
c	length of the crest
f	Darcy friction factor

u_f	flow velocity over the flat plate
$u_s^i a$	slip velocity
u_{Da}^i	drift velocity
s	the ratio of sediment density to fluid density
n_x	normal component in x-direction
n_y	normal component in y-direction
z_a	reference height
d_{50}	median grain diameter
w_s	sediment settling velocity

Vectors

$\overrightarrow{F_v}$	viscous force
$\overrightarrow{F_p}$	pressure force
ij	coordinate direction
p	point of centroid
rms	root mean square

Superscripts

u	denoting velocity component in x-direction
v	denoting velocity component in y-direction
ω	denoting velocity component in z-direction

Subscripts

0	initial value
f	front
ij	coordinate direction
p	point of centroid
rms	root mean square
c	continuous phase
d	dispersed phase
s	stratified
u	unstratified

Symbol

Δ	incerement
∇	vector differential operator
$\forall$	for all

Acronyms

CFD	Computational Fluid Dynamics
DNS	Direct Numerical Simulation
LES	Large Eddy Simulation
RANS	Reynolds-Averaged Navier-Stokes
LDA	Laser Doppler Anemometry
PIV	Particle Image Velocimetry
RNG	Renormalization group ($K - \varepsilon$ turbulent model)
SST	Shear stress (turbulence model)
RSM	Reynolds stress model

Chapter 1
Introduction

1.1 Thesis rationale

Close observation of geophysical flows commonly observed in rivers and oceans shows that gravity currents play a pivotal role, and encompass many different flow types. These may include debris flows, granular flows, and turbidity currents (see figure 1.1). Other examples of this occurrence in nature include snow avalanches and pyroclastic flows. Such flows are of great importance to the geophysics research community, as they are the agents of sediment transport and deposition in nature. The intermittent nature of large scale turbulence in boundary layers, with the consequent variations in stress and pressure on the bed of deep-oceans and fluvial waters, is responsible for the process of sediment being carried into suspension (Heathershaw and Thorne, 1985). Geophysical flows are generally regarded as stratified due to variation in density (e.g. gravity currents) or concentration of suspended particles (e.g. turbidity currents) (Li et al., 2015). For example gravity currents have a vertical concentration gradient including a denser upper homogenous region which is a well-mixed and a lower, less dense, heterogeneous region which is poorly mixed. As material gets transported across the Earth's surface morphological and geophysical features on the planet's surface are shaped by means of depositions which later formed into sedimentary rocks. The process of major deep-sea sediment transportation is illustrated in figure 1.2.

A gravity current is a wedge of fluid which intrudes horizontally into an ambient body of fluid of a different density. A well-known example of this is the discontinuation of oceanic saline water by a fresh riverine flow forming a salt wedge (Schijf and Schönfled, 1953). A density difference may also be manifested from the particle suspension in the fluid forming the current. Turbidity currents, which are derived from the word "turbid" (which means "muddy") represent an important class of such particle driven flows (Meiburg and Kneller, 2010). They are generally turbulent flows containing dilute particle suspensions. They occur in lakes as well as deep-sea, where they are steered by the difference in density between water containing clay/sand or mixture of both, and clear ambient water. In the deep sea environment, the sedimentary rocks that they deposit are called turbidites. Turbidity currents represent a key mechanism in the transportation of sediments from the continental

shelves to the deeper parts of sea and oceans. Finally, their interaction with the seafloor by means of erosion and deposition is accountable for the configuration of large-scale features including submarine sediment waves, dunes and canyons (Bonnecaze et al., 1993). Gravity currents can form in a wide variety of settings which presents many interesting research challenges (Meiburg et al., 2015).
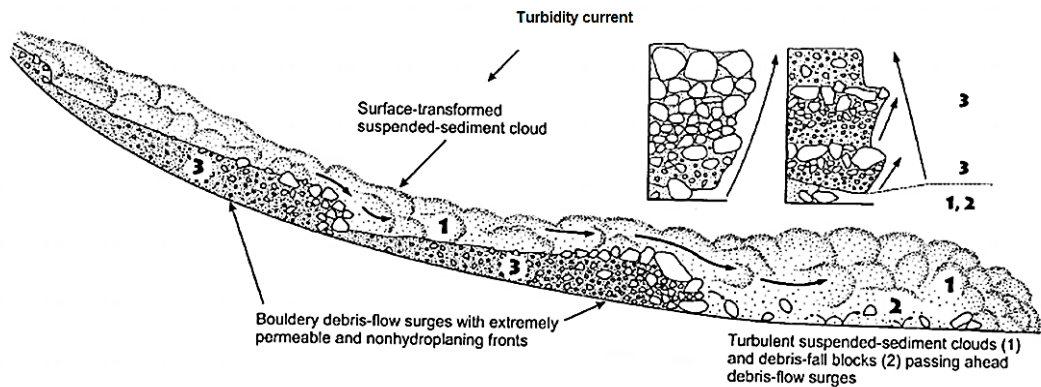
Figure 1. 1: The following illustration from Hiscott (1994) shows the process of debris flow, turbidity current and traction driven by a sediment gravity flow.
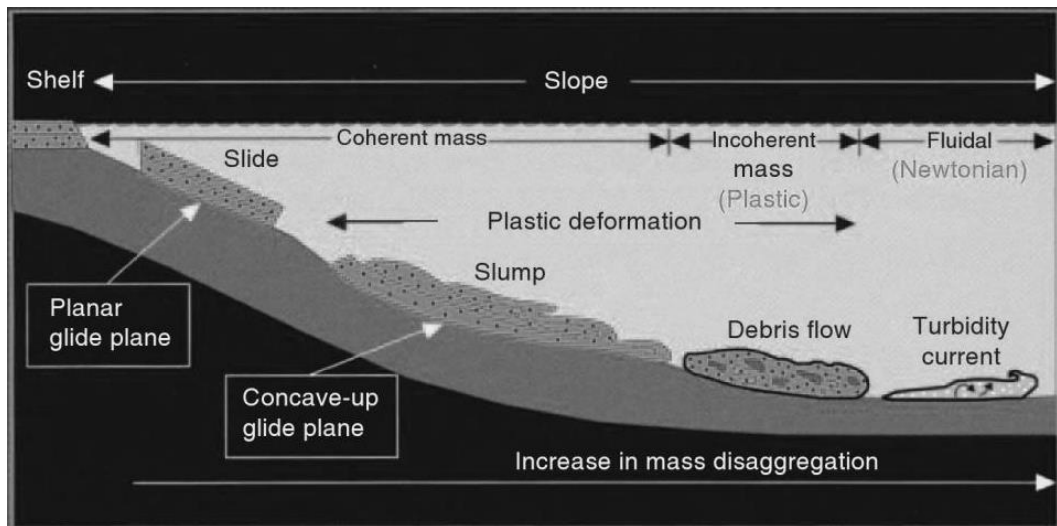
Figure 1. 2: Schematic diagram given by Steele et al. (2009), illustrating the major deep-sea sediment transport processes. The four most common gravity-driven downward routes that transport sediments into deep marine environments are shows in this diagram.
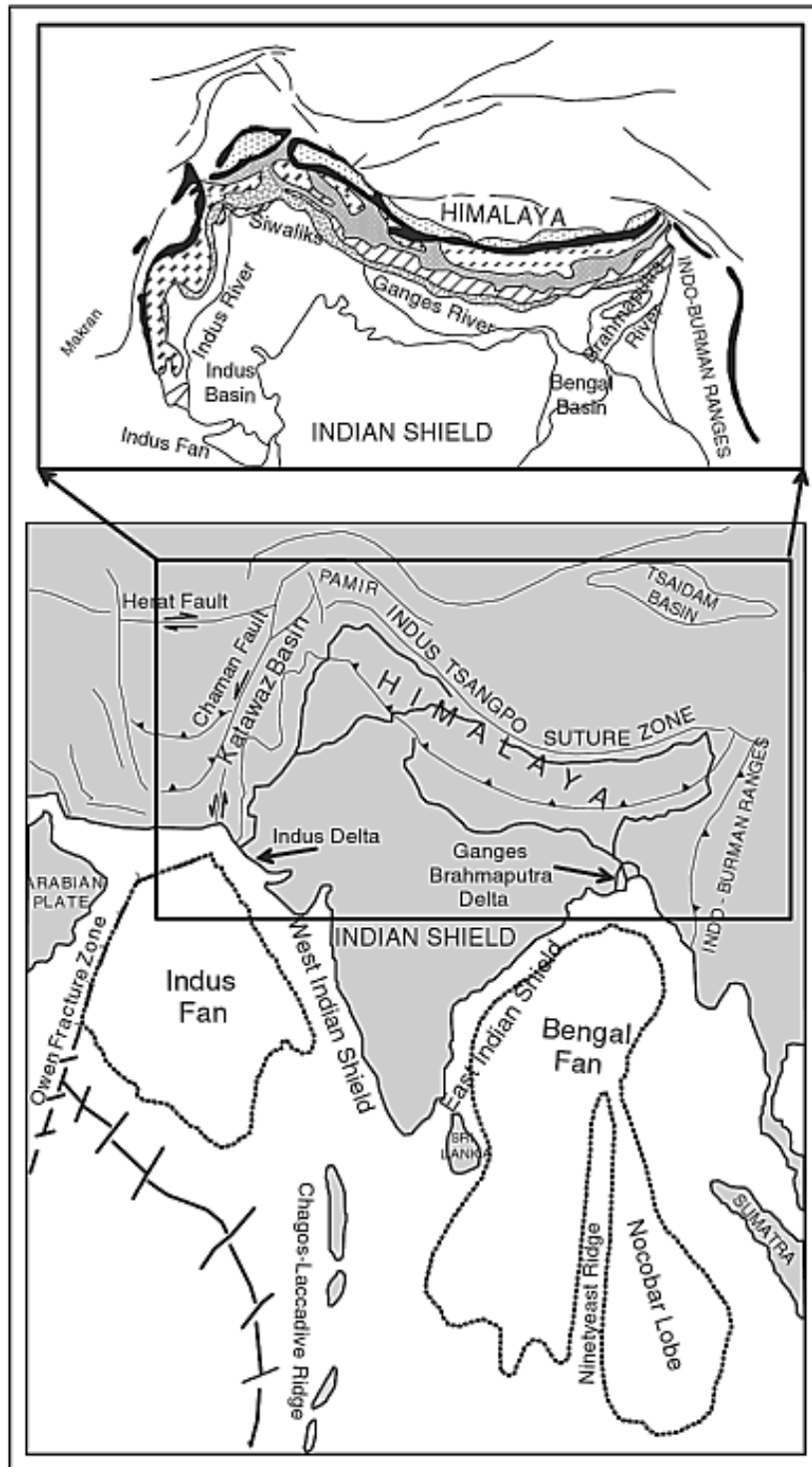
Figure 1. 3: a) Modern submarine fan model of Normark (1970). (b) Ancient submarine fan model of Mutti and Ricci Lucchi (1978).

a Modern fan model
Normark (1970)

b Ancient fan model
Mutti and Ricci Lucchi (1972)
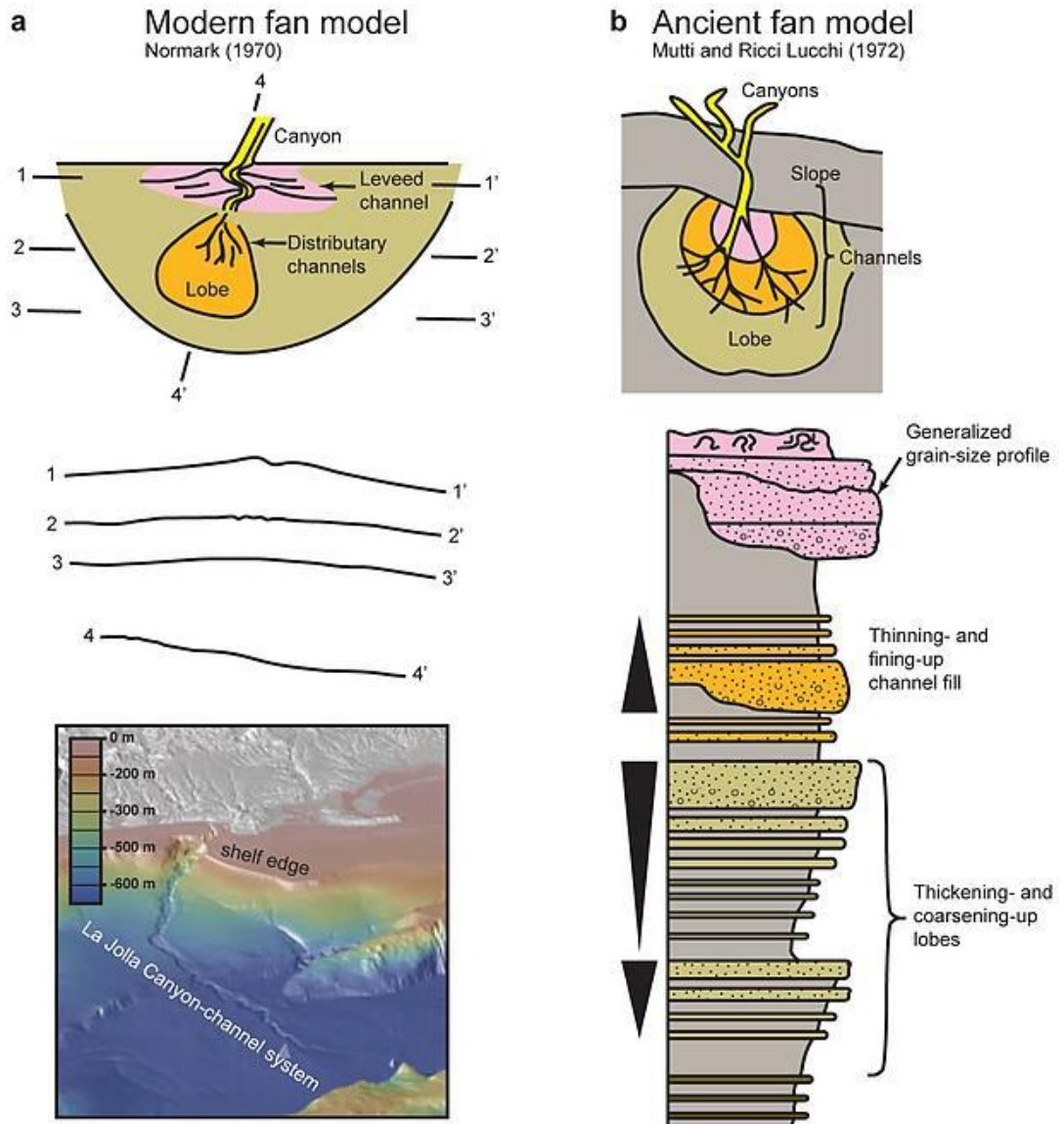
Figure 1. 4: This shows the tectonic map of south Asia and the surrounding oceanic regions encompassing the Persian Gulf and the Bay of Bengal (Bastia and Radhakrishna, 2012).

Over very long geological time scales, the deposits carried via turbidity currents can reach very large scales, e.g., approaching 10^6 km^3(figure 1.3). A good example of this can be seen by the map of surrounding oceanic regions encompassing Persian Gulf and more profoundly, the Bengal and Indus Fan as shown in figure 1.4.

In addition, the study of such flows has important commercial applications in fields as diverse as effluent dispersal, removal of dredging waste, mine tailing and oil transportation. Under certain ambient settings, the presence of organic matter found within the sediments has the tendency to form hydrocarbons, so that the sedimentary rock from the deposits of turbidity currents may take on a vital role as hydrocarbon reservoirs (Weimer et al., 2007). The occurrence of turbidites with their deposits and the formation of naturally occurring hydrocarbons that are trapped by the overlying rock is of great interest and is explained in detail in Meiburg and Kneller (2010). Thus an in depth investigation of the academic field of turbidity current mechanics can aid in locating the areas that may host oil and gas reservoirs. Hence, understanding the dynamics of turbidity currents is of huge industrial interest.

From an engineering standpoint, hazards accompanying turbidity currents are of great importance for risk analysts who deal with the maintenance and installation of submarine oil pipelines and offshore engineering structures such as underwater well heads. This is of significant importance since nowadays sustainable human life depends on oil and gas. This has led the industries to reach deeper into the ocean by means of constructing tall offshore engineering structures. The construction of such infrastructure under the sea-floor results in the exposure of the pipelines and pumps surfaces on and above the sea floor. Thus, the possibility of re-occurrence of gravity currents in such locations poses a significant geo-hazard risk (Gonzalez-Juez et al., 2010), with potentially serious consequence both economically, and to the natural environment. The spreading of the oil over the surface of the ocean is an environmental process with a very high risk factor, both economically and environmentally in which gravity currents play a critical role. Therefore understanding the mechanism of flow in turbulent gravity currents is certainly beneficial both industrially and environmentally.

By way of another example, the Storegga region area located off the western Norwegian coast has been recognised as a site of several giant slides invoked by gravity currents. It involved a volume of some 3000 km^3 which reached a run-out distance of $450\ km$ for the flow of debris and $800\ km$ for the association of turbidity currents (Yamada et al., 2012). (Studies of this system were required because the

Ormen Lange gas field is located approximately $15\,\mathrm{km}$ seaward from the present day headwall which raised a lot of concerns about the hazards to which the planned petroleum production installation would have uncovered (Issler et al., 2003).

Similarly, controlling the particulate gravity currents is advantageous to many species and their natural environment. For instance, controlling haboobs or dust storms are examples of this type of gravity currents which usually form in deserts or over the mountain ranges. The micro-particles that exist in these situations are most aggravating to the lungs and other respiratory diseases. Following this further, it is vital to understand what other factors affect the characteristics of the flow in gravity currents.

Understanding the role of turbulence is crucial to understanding the behaviour of gravity currents and other geophysical flows. For example, the role of turbulence in keeping particles in suspension is critical to the long run-out length observed in turbidity currents (Dade and Huppert, 1995b, Parker et al., 1987, Talling et al., 2015). Rouse (1937) showed that the balance between downward mass flux of particle due to particles settling with the upward mass flux of particles due to turbulence dispersion determines the vertical profile of particles concentration in fully developed channel flow. Turbulence dispersion is commonly modelled using the notion of eddy viscosity, which controls the amount of mixing due to turbulence in turbulent flows. In turn, the eddy viscosity is large in regions where turbulence kinetic energy is large. So, it is important to understand the mechanisms behind turbulence production and dissipation.

Turbulence is mainly generated in regions of large shear (Wilcox, 1998), namely, in internal shear layers, and in wall boundary layers. Turbulence structure in wall boundary layers is influenced a great deal by the roughness of the wall boundary. In geophysical flows, bottom boundary roughness manifests itself in two ways – e.g. on small scales due to sand grain roughness, and on large scales due to sedimentary structures such as scours and dunes. Eggenhuisen and McCaffrey (2012) observed that there exists field evidence supporting the hypothesis that boundary roughness promotes longer run out lengths of turbidity currents. They also performed an experiment over a single roughness element to support this hypothesis. One of the main aims of this thesis is to explore this conjecture further through the use of numerical simulations.

In addition to the role played by bed roughness on turbulence structure, another important aspect is the influence that it has on resistive drag. McLean and Smith (1986) emphasise the importance of splitting drag into its two main components – form drag caused by large pressure differences across boundary roughness structures, and skin friction due to tangential viscous forces. Form drag is largely responsible for increasing resistive drag to the flow, whilst skin friction is largely responsible for erosion of the surface, releasing particles into the main flow.

Karcz and Kersey (1980) investigated erosion and development of bed structure under pulsating shallow water flow over inclined slope at $\text{Re} \approx 10^3$ and for Froude number $(\text{Fr}) \approx 3.0$. They showed that once perturbations of finite amplitude are obtained, the larger stresses at the crests (relative to those near the troughs) causes crests to propagate much faster than the troughs, thus resulting in the development of asymmetrical wave forms. In a sense, when the asymmetry is strong enough, separation tends to occur, which in turn, manifests a momentum deficit downstream of the wave crest similar to that found in the wake of a circular cylinder. When reattachment point is reached, the velocity at the near-bottom region, including stress becomes zero. Downstream from this point, beneath the momentum deficit or the wake region, an internal boundary layer must develop as shown in figure 1.5.
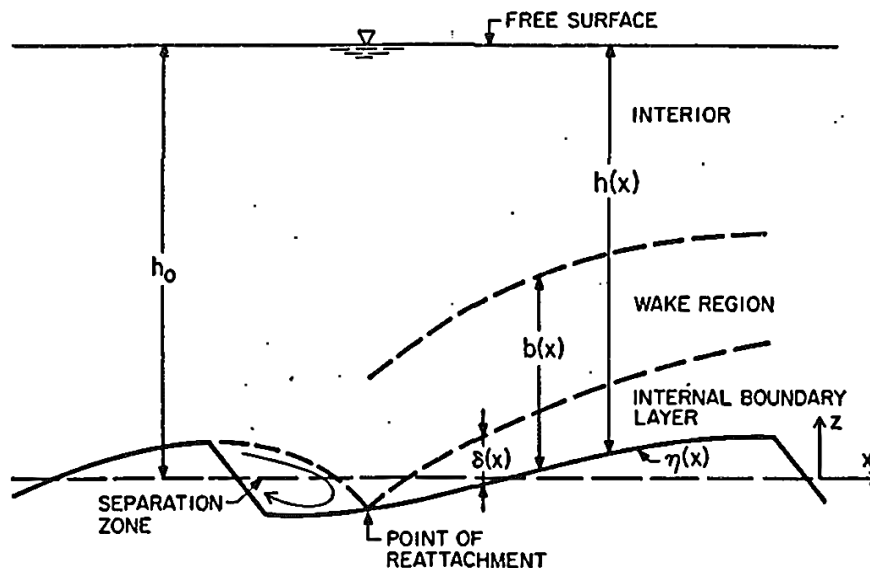
Figure 1. 5: Definition sketch from the work of McLean and Smith (1986), which illustrates that beneath the momentum deficit or the wake region, an internal boundary layer must develop.

There are two competing processes that are critical for determining the boundary shear stress. These are the effect of an outward acceleration from a diffusive velocity defect and the thickening of a boundary triggered from deceleration effect (McLean and Smith, 1986).

The amount of form drag and skin friction depends strongly on the shape of boundary bedforms, e.g. rectangular scours, symmetric dunes, and asymmetric dunes and anti-dunes. The work of this thesis starts with examining the structure of turbulent flows over rectangular roughness elements, and then goes on to study flows over more general roughness element shapes. The results have implications for flows in both the deep marine environment and in rivers (Baas et al., 2015, Best, 2005).

In addition, most of the man-made surfaces in engineering industry are rarely smooth and the flows over these surfaces are turbulent in character. Imperfection in manufacturing, icing of the air-foils, blades with surface roughness, ship-hulls with sea weed or shells and pressure drip in pipe due to the casting are common examples (Knopp et al., 2009, Aupoix, 2007). Therefore, a quantitative investigation of the effects of surface roughness on fluid flow makes an important contribution to research in both environmental and engineering fluid mechanics.

Moreover, it is of great interest to accurately predict these phenomena. Hence experimental and numerical methodologies should be applied. Unlike numerical methods, the experiments do not provide a detailed description of the flow field and can often be costly (Aupoix, 2007). Hence with a validated numerical model, it is possible to investigate additional relevant parameters.

1.2 Aims of thesis

In the past few decades, there has been extensive literature on the physical processes involved in the flow of gravity and turbidity currents. Despite this, there are still many questions to be answered concerning the structure of turbulence on the bed and other regions of the gravity current flows.

One of the main goals of this thesis is to provide evidence for or against the conjecture of Eggenhuisen and McCaffrey (2011) that rough boundaries promote longer run out lengths of turbidity currents, due to effect of enhanced turbulence mixing keeping particles in suspension for longer times. This is achieved by using a suitably validated computational fluid dynamics (CFD) model to compute flows over

a wide range of rough elements, starting with idealised rectangular elements, and generalising to roughness elements which approximate the shapes of natural bedforms.

In additional to studying the effects on turbulence mixing, we also study the effects of different roughness elements on form drag and skin friction, paying particular attention to their influence on flow resistance, and the ability of the flow to erode sediment from the bottom boundary into the main flow. This leads us to consider the competing effects of drag and turbulence mixing on the energy budget within the flow. Resistive drag tends to decrease kinetic energy, and hence reduce the run out length of gravity currents, whilst turbulence mixing tends to increase the potential energy of the flow, and hence increase run out lengths.

Finally, we consider the effects of erosion and deposition on the stability and evolution of inherited bedforms.

1.3 Thesis-outline

The outline of the thesis is as follows.

Chapter 2 focuses on the classification of different types of gravity currents. It contains the previous experimental methodology and measurement techniques related to particulate gravity currents. It also concludes the use of numerical methods to model the particulate gravity currents.

Chapter 3 starts with background on the single-phase fluid flow over surface roughness. The classification of surface roughness is discussed. The governing equations for turbulent rough wall channel flow are then presented. A literature review of previous work relating to particulate flow over surface roughness is also included in this chapter.

Chapter 4 concentrates on the numerical modelling aspects. For this chapter, a full explanation of a variety of turbulence models is given which can be implemented to mainly investigate shear flow.

Chapter 5 conducts a numerical studies using CFD to study the effect of lower boundary roughness on turbulent flow in a two-dimensional channel. Measurements of eddy viscosity and friction factor have been made over a range of aspect ratio to

establish the optimum spacing to produce maximum turbulence enhancement, mixing and resistance to flow.

Chapter 6 presents numerical modelling data on saline water flow over various surface roughness shape found in geophysical channels. This chapter studies how resistance and mixing vary with a range of aspect ratio keeping the distance between bedforms fixed at the same height-to-distance ratio as was found to optimise turbulence during flow over rectangular ribs in Chapter 5. This is studied to understand the factors controlling turbidity current run-out.

Chapter 7 studies details of sediment transport over idealised surface roughness shape found in in deep-sea and shallow water environments. A hydro-morphodynamic model is adapted to investigate the interaction of main body of the turbidity currents with macro-roughness. This was to investigate the link between sediment vertical mixing, flow drag and flow capacity over a range of idealized bedforms.

Chapter 8 presents detailed results and discussion on the evolution of low-angle symmetric dunes from a fixed starting point, and the long term stability of dunes.

Finally, overall conclusions and the scope for further work are discussed in Chapter 9.

Chapter 2
Gravity Currents: A Critical Review

2.1 Background

Gravity currents can occur naturally in the environment or be made artificially in experiments. They are often referred to as "density currents" or "buoyancy currents". This phenomenon occurs when a fluid from one domain enters a fluid in another domain which has a different density. The differential in density, temperature or concentration between the two fluids results in a reciprocal motion of a fluid which has a lower density. This can be observed in nature, where a cold dense air enters the atmosphere which result in sever squalls related to thunder storms (Simpson, 1999). What is of importance here is the understanding of the height, speed and the properties of this type of flow, which assists in preventing aviation related accidents. Typically gravity currents can be initiated from the movement and transport of the particles usually on the ground. Simpson (1987) describes it as a self-stoking process on a slope in which these small dense particles change the global density of their surrounding fluid.

As mentioned earlier the mobilization of airborne material due to density current dust storm, for example which often results in severe pollution, often hoover particles from dried cavities that are in the nearby deserts or cities. Such density current can be developed from convection in tropic or by orographic storm activities (Solomos et al., 2012). The scale of developed dust storm occurring in a form of density current is large and can transport air pollutant material over a wide regions. The developed dust fronts such as haboob have generally a life time of several hours and can travel horizontally to several hundred kilometres. The carried particles by density current can cause heart disease, lung cancer and asthma. According to the World's Health Organisation reported annually about two million people die worldwide as a result of direct or indirect contact with these air pollutants and the problem is worsened by particle driven atmospheric flows mainly in regions located near desert areas such as African and middle eastern countries.

2.2 Classification of gravity currents

Categorization of gravity currents may be done from the source of density difference between the two fluids. Therefore, it is on the basis of their source of density difference that they can be divided into three identifiable categories, namely homogeneous, non-homogeneous and particulate. In homogeneous gravity currents the temperature and concentration variations of dissolved chemical species results in a density difference. In contrast, in non-homogeneous gravity currents, the source of the difference in density is presented as a distinct break in the physical continuity between the two phases of the same immiscible fluid.

Particulate gravity currents are a general term given to any suspension flow in which the density difference occurs as a result of the suspension of the particles inside the flow with their ambient fluid. Examples of particulate gravity currents are debris flows, granular flow, and snow avalanches as well as pyroclastic flows and turbidity currents are also prime examples (McCaffrey et al., 2001). The term "particulate" is referred to solid or liquid particles suspended in the atmosphere, such as pollutants. These particles are dispersed in a continuous fluid, such as typically air or water. There is no distinct definition for these particles, other than they may break up, coalesce or change shape. In the particulate gravity currents, the concentration of particles is in general non-uniform; hence they result in a large scale fluid motion.

As already established, turbidity currents are sediment-laden underflows which are classified under the category of particulate gravity currents (McCaffrey et al., 2001). Turbidity current is classified as non-conservative gravity current as these class of flows are able to entrain and deposit sediments with the bed and hence the excess density is not constantly kept over the bulk . The driving force in such currents are by the excess in density of fine sediments which are kept in suspension by fluid turbulence produced by the mean flow. In other words, the gravity pulls the suspended sediments and the suspended sediment pull the ambient fluid with it. This driving force can be modified through deposition and resuspension of the suspended particles causing the current to attain a high flow velocity (Garcia, 1992, Cantero, 2008). Such strong flows can modify the sculpture of the submarine canyons, scouring sea floor generating various macro-scale surface roughness such as sediment waves, dunes, anti-dunes and gullies.

2.3 Structure of gravity currents

Understanding the fundamental structure of gravity currents is an important aspect in evaluating their behaviour. In breaking this down to simpler terms, gravity currents are typically composed of a head, a body and a tail structure. The head is located downstream of the current and has the highest point of the current. The body is a transition between a high to a low momentum in the current and it is located in between the head and the tail in the middle stream. As the downstream velocity of the current increases the thin, dense layer of the body mixes with the ambient fluid in the upper region. The tail is in the shallower stream up to a point where both fluids reach a stationary point as illustrated in figure 2.1. The shape of the gravity current is dependent on the Reynolds number of the current flow up to a critical value of Reynolds number. The morphology of the gravity currents alter with the increasing Reynolds number up to $\mathrm{Re} \lesssim 10^3$ (Simpson and Britter, 1979, Keulegan, 1957). Gravity currents propagating at high Reynolds number commonly have similar characteristics, and this is known as the similarity of gravity currents (Hoyes, 2008). This was initially proven by Schmidt (1911) whose work suggested that there is only a small change in the profile of a gravity current for $\mathrm{Re} \geq 10^3$.

It should be noted that the formation of Kelvin-Helmholtz instabilities can partly have an influence on the similarities of the gravity current above the mentioned specific Reynolds number. These types of instabilities are similar to the Kelvin Helmholtz instabilities observed in shear layers where two fluids of different densities are moving relative to each other (Thorpe, 1973). Similarly, Thorpe (1973) suggested that these instabilities occur in shear layers are found in situations where the height at which the two fluids interact is small enough and/or the velocity difference is large. Relatively, the Richardson number can be used to explain the relation between the fluids as the ratio of the potential to kinetic energy which is defined as follows:

$$\mathrm{R_i} = \frac{\tilde{h}_d \tilde{g}'}{\tilde{u}_d^2} \tag{2.1}$$

Where $\tilde{h}_d$ is the distance in y-direction between the gravity current and the ambient fluid in the shear layer, $\tilde{u}_d$ is the difference in velocity between the two light and heavy fluid, $\tilde{g}'$ is the reduced gravity and is given by,

$$\tilde{g}' = \frac{g(\rho_g - \rho_w)}{\rho_w} = \frac{g\Delta\rho}{\rho_w}, \qquad \rho_g > \rho_w \tag{2.2}$$

Where respectively ρ_g and ρ_w are the density of gravity current and ambient fluid.
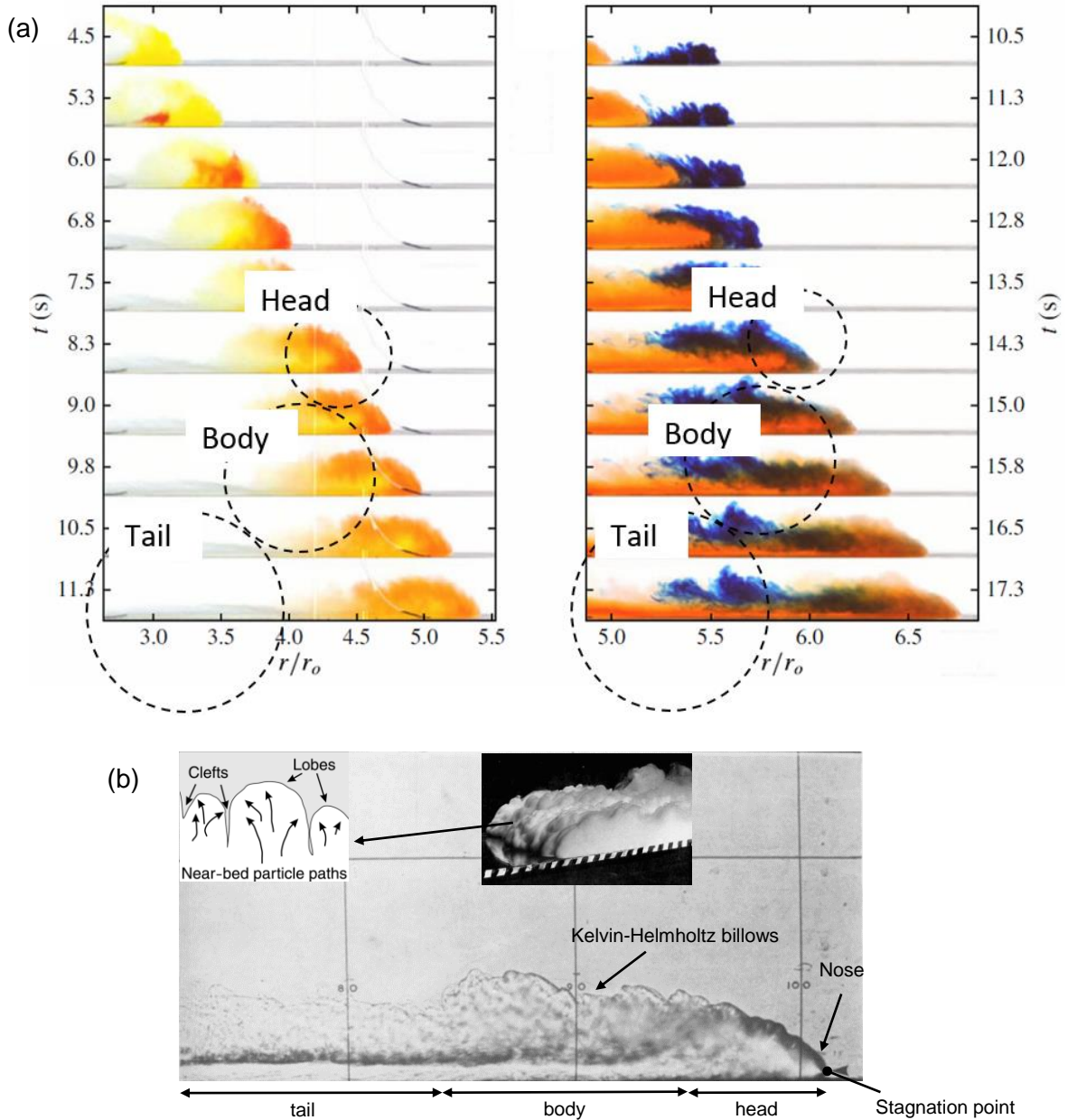
Figure 2. 1: (a) The sequential formation of two gravity currents at successive intervals. The graph on the left-hand side displays the transport of a red-dye pulse, injected just behind the front (or head) of the flow. The graph on the right-hand side shows the ejection of a dyed blue ambient fluid ahead of the front of the red current. Here, the tail, body and head of the gravity currents have been shown via dashed circular lines (Samasiri and Woods, 2015) (b) Images of gravity current passing along a flat surface highlighting the lobes, clefts, head, body and tail of the current (Simpson, 1969, Simpson and Britter, 1979, Kneller and Buckee, 2000).

The gravitational and shear instabilities that occur between the current and the fluid results in a mixing of the two (Simpson and Britter, 1979). Instabilities occur commonly in billows (Kelvin-Helmholtz instabilities) and in a complex shift pattern of lobes and clefts. Initially, Prandtl (1952) noted billows as recirculating fluids caused by the breaking waves. This was then further established by Benjamin (1968).

Billows occur in the upper regions of gravity currents along the density interface as vortices. The density interface over the head of the gravity current lead to a low Richardson number. Consequently, strong Kelvin-Helmholtz instabilities are instantly generated over the head of the gravity current. This phenomenon can be replicated in the laboratory (e.g. saline water) and can be observed in the natural environment (e.g. atmosphere). For example, Parsons and Garcıa (1998) observed that the structure of billows slightly vary with changing Reynolds number; while Benjamin (1968) used the flow force theory to prove the retention of the billows in two-dimensional gravity currents, which was additionally validated by Simpson and Britter (1979). Further observations by Rebesco et al. (2014) show that in certain situations a ring vortex is generated above the front; this ring vortex can dominate the propagation of the front and change the velocity profile within the head of the gravity current.

One main difference which can be observed in the 3D cases, and is absent in the 2D cases, is the mechanism for the dissipation of the billows (Hacker et al., 1996, Cantero et al., 2003). Figure 2.1 (b) shows as the vortical structures of the current break down the formation of the lobes and clefts takes place at the front region of the intruding gravity current. The initial mechanism that results in generation of the lobes and clefts are the buoyancy-induced instabilities (Härtel et al., 2000). Batt (2008) indicated that the formation of lobes and clefts is due to the instabilities at the bottom boundary of the front. These are found as an interaction of a more dense fluid, which dominates over the less dense fluid. Some literature has suggested that lobe and cleft instabilities accelerate the breakdown of the Kelvin-Helmholtz instabilities. In the natural environment, turbulence is three-dimensional and hence Kelvin-Helhmholtz instabilities can break down.

Simpson (1999) suppressed the lobe and cleft instabilities to allow the Kelvin-Helmholtz instabilities to develop into coherent two-dimensional billows. The buoyancy force applied by the less dense fluid makes it difficult for the current to continue and thus it results in an effective mixing of the head at the top. Then it would

appear that this results in the formation of the foremost point of the gravity current above the bed and lower than the head.

In gravity currents the stagnation point lies in the foremost point of a front part of the current where the velocity of the ambient fluid and the current are equal (Benjamin, 1968, Simpson et al., 1977, Simpson and Britter, 1979). Härtel et al. (2000) identified the location of the stagnation point with respect to and the nose of the gravity current. They noted that the stagnation point is behind and slightly lower than the nose of the gravity current. They concluded that the energy conserving instability which occurs downstream of the head is proportional to the amount of fluid entrained and hence indicated that there must be other factors resulting in the formation of the lobes and clefts.

The local instability occurring near the leading edge of the gravity current can often result in the formation of the lobe and cleft instabilities (Härtel et al., 2000). Härtel et al. (2000) initially formed the basis of a linear stability analysis based on the new location of the stagnation point which was then investigated experimentally by Neufeld (2002). He found that the wave number initially became higher than that predicted by the linear stability analysis and then transforms into the shifting pattern of lobes and clefts at lower wave numbers. The interfacial gravity currents occurring between two fluids comprise of the lobe and cleft type instability at the front of the stream. This is visualised by the high resolution eddy simulation, and is of particular interest since it could be used to suggest that the linear-stability analysis of Härtel et al. (2000) does not predict such instabilities in the case of interfacial gravity currents (Hoyes, 2008).

Simpson (1972) suggested that the mixing that takes place beneath the nose of the gravity currents has an important contribution in the meteorological research on cold outflows into the atmosphere and in the retention of the slumping flows, as in turbidity currents. For a constantly fed flow (flow with an external energy input), regardless of the presented surface stress, the ambient fluid mixes with the fluid current outside the flow. This can often be observed as a thick layer of a density interface between the two fluids. Conversely, if the flow is constant (constant flux and fixed volume), the mixing does not take place throughout the slumping stage of the lock release (Hallworth et al., 1996).

Most previous numerical, analytical and experimental work use either lock-exchange or lock-release to generate gravity currents. In these boundary conditions the fluids

of various density are initially divided by a vertical barrier known as lock-gate. The lock-release experimental set-up is performed with a rectangular channel where two fluids of different density are positioned at rest and separated from each other in two locations of the same channel. For this configuration, the two fluids have a bottom wall, top free surface, side-wall and end-wall as their boundaries. The depth of the denser fluid logically will not be greater than the height of the ambient. However, it would appear that when both of the fluid heights are at the same level for a test investigation, then the configuration is referred to as full-depth. In cases where the depth of denser intrusive fluid is less than the ambient, then the configuration is referred to as being partial-depth.

Furthermore, as the lock is released, the fluids flow relative to each other and subsequently will develop two gravity currents. Eventually, the denser fluid due to its heavier mass will flow near the bottom wall, while the less density fluid (lighter fluid) flows along the free surface at the top. The initial density and volume of each fluid can vary with respect to each other as two initial conditions. Similarly, other properties of the ambient and current fluid can vary to match the natural flow in the environment.

In natural flows that are most frequently encountered, the volume of denser fluid is significantly smaller than the ambient fluid. The lock-release method allows the intrusive fluid to have a significantly lower volume which is initially at rest to the ambient fluid; this situation occurs most frequently in natural flows. Lock-release configurations can be used for investigating oceanic thermohaline circulations and atmospheric fronts, where large volumes of fluids interact with each other. The other method that has also been routinely used to develop gravity currents is formerly known as the lock-exchange. The lock-exchange set ups have similar configurations to the lock-release set-up. The only difference between these two methods is that in the lock-exchange there is no initial confining boundary for light and heavy fluids. In other words, in the lock-exchange configuration both fluids are infinite in the x −direction.

Previous studies by Hacker et al. (1996) and Hallworth et al. (1996) would suggest that for lock release of a fixed volume of fluid, the mixing and the interior structure of the gravity currents depend on the aspect ratio of the fluid to be released. The aspect ratio is defined as the height to the length of the fluid in the initial release state. In contrast, for larger aspect ratio than 1, the volume of the mixed fluid is reduced from the head and it is overrun by the lower denser fluid. This will continue until there is no unmixed fluid left. When the aspect ratio is unity, intense mixing occurs with

Kelvin-Helmholtz billows, and therefore between the main vortex and the head a region of stratification is generated. This process continues until the vortex loses energy, which by then behaves in a similar manner to the larger aspect ratios. Furthermore, for smaller aspect ratios, the billows directly mix in the mixed fluid region. The rate of propagation and the velocity of the gravity current changes for different aspect ratios as it is being diluted.

However, there is still doubt to which location is best suited for the height of the current to be measured. On the other hand, in order to determine the Froude number, the height of the current must be known. This is of importance, since the height of the current varies in regions throughout the current. Therefore, measuring the height at non-hydrostatic locations should be avoided.

Reynolds number is another parameter which is dependent on the height of the current. The height which is used to measure the current is one half of the maximum height of the energy conserving current. In the experimental methodology, the height of the current is partly controllable by adjusting the aspect ratio of the flow.

Benjamin (1968) found that for an energy conserving flow with no energy losses, instantly the flow become steady and the receding stream must occupy one half the height of the channel. If it occupies less than one half the height, then the flow becomes susceptible to energy losses. Conversely if the flow occupies more than one half the height then energy losses can be triggered by external energy sources. The other parameter which was investigated by Benjamin (1968) is the ratio of the theoretical maximum current height to ambient height. They found that for a fixed volume release then this value is 0.347. This was later confirmed by Klemp et al. (1994) and Simpson and Britter (1979) with a maximum value of 0.33. Moreover, Shin et al. (2004) suggested that this value can also be obtained for lock-exchange flows.

Simpson (1972) introduced a correlation for the nose to head height ($\tilde{h}_n/\tilde{h}_f$) ratio for a range of Reynolds number $300 \lesssim Re \lesssim 1000$ in order to investigate the instability at the front which was defined as follows:

$$\frac{\tilde{h}_n}{\tilde{h}_f} = 0.61 Re^{-0.23 \pm 0.1}$$

(2.2)

Over the wide range in which gravity currents exist within the natural environment, the rate of propagation takes place at a high Reynolds number. It is of interest to

resolve the viscous layer for the slow moving gravity currents at low Reynolds number, for example for the purpose of investigating the entrainment of particulate in the bed. In the case of gravity currents, the Reynolds number is defined as follows:

$$\text{Re} = \frac{\tilde{u}_f \tilde{h}_f \tilde{\rho}}{\tilde{\mu}}$$

(2.3)

where $\tilde{u}_f$ is the velocity of the gravity current front, $\tilde{\mu}$ is the dynamic viscosity of the ambient fluid, $\tilde{\rho}$ is the density of the ambient fluid and $\tilde{h}_f$ is the front height of the gravity currents which was previously shown in figure 2.1. The Froude number in the case of gravity current can be defined as follows:

$$\text{Fr} = \tilde{u}_f / \sqrt{\tilde{g}' \tilde{h}_f}$$

(2.4)

The structure of the gravity current is also influenced by the Froude number. The Froude number varies up to $\text{Re} \lesssim 10^3$ and then the gradient of this variation becomes less and less as the Reynolds number passes above the value of 1000 (Simpson and Britter, 1979, Hoyes, 2008, Parsons and Garcıa, 1998, Abraham and Vreugdenhil, 1971). Eventually, at a very low Reynolds number the head disappears and becomes indistinguishable to an observer.

2.4 Experimental methodology

In order to fully appreciate the mechanism of naturally occurring gravity currents, it is necessary to analyse them through quantitative and qualitative measurements. However, the location and unpredictability of such phenomena presents a challenging task for scientists to measure these in the natural environment. In 1990, the eruption of Mount Unzen in Japan developed a pyroclastic flow which became active after 200 years. Also in 1991, a spontaneous ash-laden gravity current occurred in Mount Pinatubo and this reduced the visibility to near zero, making scientific measurements extremely difficult to obtain. Clearly, scientific measurement in such toxic and hard-to-reach environments is very difficult. Thus, it has been suggested that small scale laboratory experiments present a viable alternative. Quite simply, the experiments can be replicated as many times as required for the purpose of calibrating numerical and theoretical models,

Gravity currents were first experimentally investigated by Marsigli in 1681. He placed salt water on one side of a barrier and fresh water on the other side of the barrier.

Then he released the salt water from the bottom and fresh water from the top to develop two gravity currents respectively. This experiment was performed to study the exchange flow through the Bosphorus (Soffientino and Pilson, 2005). The other early recorded experimental investigation were from (Schmidt,1911).

The rate of propagation of gravity currents makes an important contribution to the understanding of gravity currents. For this reason, this parameter is most frequently measured in many gravity currents related experiments (Huppert and Simpson, 1980, Rottman and Simpson, 1983). This is extended to measuring the rate of propagation of particulate gravity currents; this can be found in the work of Bonnecaze et al. (1996). Such studies revealed the fact that the rate of propagation decreases as the particulate driven gravity current loses mass by depositing sediments. The other parameter which influences the rate of propagation of gravity currents by reducing the speed of the stream is the surface friction. The most common experimental methodology which is used to analyse the rate at which gravity currents propagate is the lock-release set up (Rottman and Simpson, 1983, Huppert and Simpson, 1980).

As the experimental results of Huppert and Simpson (1980) suggested, the life of gravity current follow three stages. The first stage is the slumping phase in which the denser fluid is damped by intruding into the ambient fluid. The duration of this stage depends on the depth ratio of the current propagating in to the ambient fluid. The second stage is the inertial phase wherein the buoyance forces of the denser fluid is balanced with the inertial forces. In the third stage the buoyance forces become balanced with the viscous forces. Further in their experiments confirmed that inertial phase become absent as the viscous effect overcome inertial effects.

Further, Rottman and Simpson (1983) experimented various phases of the gravity using a lock-release configuration where a homogenous fluid (salt) in finite volume was released into lower density fluid (fresh water). They also noted as the viscous effects disappear the current goes through two clear phases. In the initial adjustment phase, they observed that the gravity current front moves approximately at a constant speed. Subsequently, the flow encounters a long reflected wave along the fluid interface moving backwards towards the symmetry plane. This is exemplified in figure 2.2.
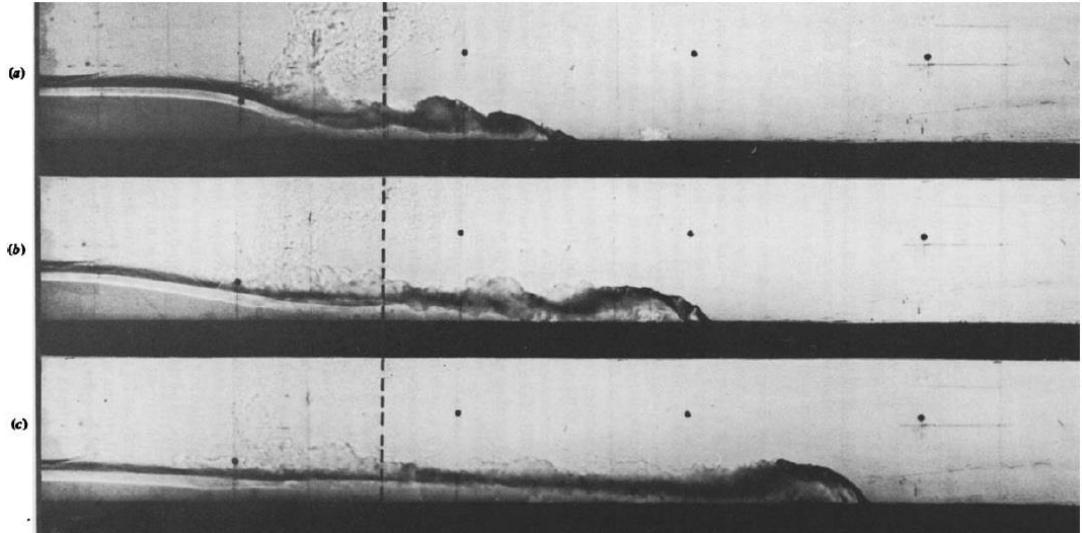
Figure 2. 2: Shadowgraph of the lock-release experiment performed by Rottman and Simpson (1983) showing the salt water collapsing into the ambient fresh water at times=2.2, 3.8 and 6 s after the release, respectively, in (a), (b) and (c).

In the self-similar phase (Second phase) as also predicted by the solutions of shallow-water equations, the front speed of the current decreases as $t^{-\frac{1}{3}}$ where t is equal to the initial time of the release. As the viscous forces begin to take effect, the buoyancy-inertia balance is no longer maintained, and the current enters the buoyancy-viscous regime. At this stage the speed of the front further decreases as $t^{-4/5}$. As the viscous effects contribution dominates over the inertial effects in the current, the moving length of the current can be defined as (Didden and Maxworthy, 1982, Huppert, 1982):

$$x_* = \left(\frac{x_0^5 h_0^5 \tilde{g}'}{\nu^2}\right)^{\frac{1}{7}} \tag{2.5}$$

Britter and Simpson (1978) formulated the relevant velocity scale of the gravity current using a modified lock-exchange methodology as follows:

$$U_\infty = \sqrt{\tilde{g}' h_b} \tag{2.6}$$

Where h_b is the height of the body of the gravity current.
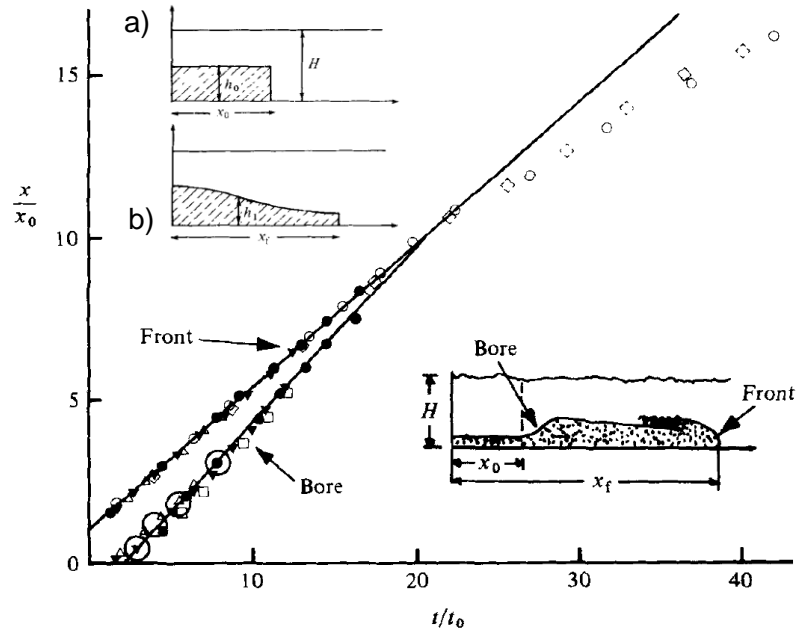
Figure 2. 3: The front and bore positions of gravity current against time modified from Rottman and Simpson (1983). Schematic of gravity current with a constant volume (a) at initial state and (b) after opening the lock-gate.

It would appear that measuring the speed of the front is one of the key objectives in analysing the mechanisms of the gravity currents. The flow in a gravity current is transient and depends on a balance of the forces at the position and time of the current (Huppert and Simpson, 1980, Didden and Maxworthy, 1982, Marino et al., 2005, Cantero et al., 2007). Hallworth et al. (1996) derived an expression from the result of the experiment conducted by Rottman and Simpson (1983) for a distance (x_s) that a gravity current travels before it starts to slow down and the initial distance (x_0) as follows:

$$\frac{x_s}{x_0} = 3 + 7.4\frac{h_0}{H} \tag{2.7}$$

The transition from the first phase to the second phase is abrupt and occur as the disturbances reflected by the symmetry plane propagates with a speed greater than the gravity front speed. This reflected wave is known as the *bore* which depends on the ratio of the initial dense fluid height to the ambient fluid height ratio h_0/H (see fig. 2.3). The ratio h_0/H must be greater than 0.5 for the bore to form.

Klemp et al. (1994) used shallow water equations to study the evolution of steady gravity current at initial state that bore forms for $h_0/H_0 > 0.5$ as the amount of disturbances increase. Further, D'Alessio et al. (1997) employed three-layer shallow water equation that applied a weak stratification in the analytical work which

suggested that the bore forms when $h_0/H = 0.5$. Shin et al. (2004) used a different theoretical approach for the existence of a bore, $h_0/H \gtrsim 2/3$ which was in agreement with the experimental result from Rottman and Simpson (1983).

The gravity currents propagating at low Re current set by changing the density of the intrusive fluid have been found to advance through a shorter inertia-buoyancy regime and in some cases the regime appear absent in the current (Huppert and Simpson, 1980, Marino et al., 2005, Cantero et al., 2007, Amy et al., 2005). Moreover, the transition from the slumping phase to the viscous phase has been found to be dependent on the initial Reynolds number of the flow and the initial aspect ratio of the current release. The slumping to the viscous phase transition is found to be shorter for gravity current at lower Reynolds number with shorter presence of the inertial phase (Cantero et al., 2007). In contrast, for high Reynolds number currents the slumping phase) is maintained for longer periods of time with longer presence of the inertial phase.

As mentioned in earlier, much of the experimental and theoretical work that has been investigated for gravity current are bounded by rectangular channels. Only a limited amount of work undertaken in this field has been for complex geometries. For example, Keevil et al. (2006) investigated flow of saline gravity current through a submerged and subaerial (under the air) channel. An ultrasonic Doppler velocity profiling was used to compare velocity profiles and secondary flows between a submarine and fluvial channels. The results from their experiments showed that the migration and evolution of the fluvial and submarine channels were different as these were evolved under a different fluid dynamics conditions.

Fortunately, in recent years the impact of modern techniques upon solving turbulent flow structures and velocity profile quantification for the advancement in the exploration of the flow processes in a variety of channels where gravity currents occur has been promising. For example, the latest flow measurements used include Laser Doppler Velocity Profiling (LDVP), Acoustic Doppler Velocity Profiling (ADVP) and Particle Imaging Velocimetry (PIV) (Peters and Venart, 1999, Buckee et al., 2009, Kneller et al., 1999, Zhu et al., 2006). Some other new techniques for the purpose of morphology measurements include acoustic or laser bed profilers and photogrammetry. However, there are still inconsistencies relating to the fluid dynamics of gravity currents in channel beds is still under research. In addition, the fluid dynamics of gravity currents in channel bends is still under research. Corney et al. (2006) obtained the first velocity data in curved bends using UDVP techniques

where he found that the helical gravity current flow behaves oppositely to the analogous free surface flows.

Moreover, physical modelling of particulate turbidity currents appear to be a challenging task, in particular in replicating particle-driven flows and modelling their boundaries as in realistic natural flows. Additionally the degree of inclination of the axial slope of the bed to employ a more realistic bed-shear conditions is still subject to much debate(Giorgio Serchi, 2010). Overall, the new technologies can be an excellent apparatus for the visualisation of the whole flow field in complex fluid flows. However, such quality and high resolution models are hugely costly. For this reason, numerical modelling of the flow fields provides a useful complementary and relatively inexpensive method of research.

2.5 Analytical and numerical methodologies

Imran et al. (2004) performed depth-resolved numerical simulations in three-dimension using a $k - \varepsilon$ model in FLUENT to investigate flow characteristics of density current through confined (bounded on both sides) and unconfined (no lateral boundaries with upper and lower boundaries only) submarine channels. In the case of the unconfined channel the density currents spilled in the lateral direction as the thickness of the current exceeded the channel height. This limited the propagation of the current in the vertical direction as the because of the spilling flow in the overbank region of the channel. In contrast for the confined channel no flow spillage was found as the current does not reach the height level of the side surfaces of the channel. Relatively, more entrainment of the flow was found in the vertical direction. In their second paper, Kassem and Imran (2004) conducted numerical experiments using the same model for density current flow in a confined and unconfined sinuous submarine channels. Numerical results showed that similar to pressure-driven channel flows, the primary flow structure of the density current does not change significantly. The $k - \varepsilon$ model captured the secondary flow circulation close to channel bed and weak recirculation on the upper region of the density current similar to unconfined straight channel. More recently, Giorgio Serchi et al. (2011) employed a $k - \varepsilon$ model with an enhanced wall treatment in FLUENT to investigation secondary and reversed secondary circulation in unconfined submerged channels for density current. Various axial slope angles of the bends were tested. A river-reversed secondary circulation was found for high axial slope angle and river-like circulation behaviour was found flow low axial angle of the bend. Similar behaviour of the

unconfined submarine channel was found to that of Kassem and Imran (2004). Yam et al. (2011) tested the accuracy of the algebraic slip model (Manninen et al., 1996) for investigating lock-release mono-disperse and bi-disperse sediment driven flow over a flat bed. The model showed a valid results for the structure of the flow but over-predicted the deposition rate for fine particles. In order to resolve this, they added the so called Simonin model (Simonin and Viollet, 1990) which is a turbulence dispersion model. This reduced the deposition rate, however lead to excessive dispersion forces. They proposed that this discrepancy can be resolved by using an appropriate turbulence dispersion model.

Further, research also shows that the physical experimental investigations are restricted to the level of the measurement and the design. In contrast, in theoretical and numerical models there are no measurement limitations but more flexibility. Nowadays, advanced numerical models provide the possibility of obtaining even higher resolution data than from the physical experiments.

One of the initial gravity current related investigations can be found in studies undertaken by Von Karman (1940). He obtained an analytical solution for the angle between the nose and the bed of the gravity current in case of an inviscid flow. Subsequently, Benjamin (1968) proposed a more accurate derivation of the equation of motion, which investigated a relation between the propagation speed and a depth of the gravity current. A depth-averaged, Boussinesq, four-equation turbulent model was developed by Parker et al. (1986) which was later employable in many applications. This model predicts the current height, front speed and position of the current at a specific height.

In addition, shallow-water theory has proved useful in many related problems that deal with particle-driven gravity current flows (Gonzalez-Juez and Meiburg, 2009, Sparks et al., 1993, Grundy and Rottman, 1985). Shallow water theory use depth integrated Navier-Stokes equations and assumes that in the shallow water the characteristics of the vertical scale is smaller than horizontal scale of fluid motion in the direction of the flow. Ideally it would be a model with two-layers and a free surface which neglects the hydrostatic constraints required for a front condition. The models are two-dimensional and consider gravity current advancement on the bed which is a rigid horizontal surface under the assumptions that firstly, there is no viscous effects and secondly no mixing occurs in the flow. Shallow water models have been successfully applied to homogeneous and particulate gravity currents in 2D, 3D and axisymmetric configuration both with or without the inclination of the bed (Klemp et

al., 1994, Rottman and Simpson, 1983, Bonnecaze et al., 1993, Bonnecaze et al., 1995, Bonnecaze and Lister, 1999, Groenenberg, 2007). The problem is, of course, these models do not provide insight into the internal structure of a gravity current. Therefore the density stratification and velocity effects are not resolved. Instead a more comprehensive numerical method should be employed to evaluate the whole flow field inside the domain. This was initially used when scientific computing was introduced; thereby providing a detailed and complex nature of turbidity currents, a way of resolving nonlinear and transient flows with better accuracy.

There were also other early models, the so called box models, which provided solutions for the propagation of a variety of gravity currents. As illustrated by Hoult (1972), the models were developed to solve problems concerning oil spillage. Later, these models were modified by Huppert and Simpson (1980) which and applied to homogeneous gravity current problems. Correspondingly, the propagation of a gravity current is modelled as a series of collapsing boxes which were independent of the Navier-Stokes equations. Therefore, it is important to note that the box models only provide information about the dynamics of the gravity current and do not model any flow fields (Hoyes, 2008). Furthermore, the box models have been modified further to suit particulate gravity current problems (Hogg et al., 2000, Dade and Huppert, 1995a, Gladstone and Woods, 2000).

The Reynolds-Averaged Navier-Stokes (RANS) models are examples of models which employ a greater description of the entire flow field. Daly and Pracht (1968) were the first to resolve lock-release turbidity currents using Computational Fluid Dynamics (CFD) methods. Not long after, Harlow and Welch (1965) and Daly and Pracht (1968) recorded the first numerical modelling result for a dam break to obtain the air-water interface with an early version of the moving free-surface numerical model. Therefore, there appears to be suggestions that in order to solve the nonlinear and non-conservative nature of such flows, a significant computational power is required. Recently with the aid of high performance computers, advanced simulations can be performed to evaluate the mechanisms of such complex flows in the lock-release configuration form. DNS (Direct Numerical Simulation) and LES (Large Eddy Simulation) are examples of such numerical models which evaluate the vortex structure of the current without taking the Reynolds averaging approximation into account. In the DNS, the whole range of temporal and spatial scales are fully resolved. In the calculations of the DNS, the full Navier Stokes equations are solved. Thus, both two-dimensional and three-dimensional DNS are computationally expensive and the resolving flow field is restricted to flow with low Reynolds number.

However the DNS calculations are valid for significantly higher values of the Reynolds number. Nevertheless, the vortex break down can only occur in 3D and hence the Kelvin-Helmholtz billows do not decay as in the form that they occur in the natural environment (Krogstad et al., 1992). In recent decades, the most accurate results have been obtained by 3D DNS which is requires a large amount of computational power and it is only feasible at low Reynolds numbers typical of lab-scale experiments (Meiburg et al., 2015). This method solves the full Navier-Stokes equations and gives the complex details of the turbulent fluctuations. The different classes of turbulence models are discussed in more detail in Chapter 4.

Härtel et al. (2000) performed a DNS simulation in two-dimension on compositional gravity currents at low Reynolds number. A vorticity-stream function formulation was employed which was adapted in conjunction with a mixed spectral finite difference discretisation. They further went on to three dimensional simulation which relied on primitive variables along with a mixed spatial discretisation which was based on spectral element collocation technique in the vertical direction. This was further enhanced with a Fourier expansion in the stream and spanwise direction in which the temporal discretisation was semi-implicit.

To summarise, Navier-Stokes models give a further insight into the fluid dynamics of gravity currents by resolving the flow field processes and are applicable to more complex three-dimensional geometrical boundaries. In other cases, similarity solutions have been employed to predict the propagation of gravity currents by a 2D and axisymmetric flow where the empirical constants for different flow regimes have to be specified (Huppert, 1982). Indeed, there has been wide ranging research in proposing analytical models. However, the problem with this approach is that, they only provide solutions to extremely simplified problems, and yet, there is no valid steady-state analytical solution for large time scale (Plapp and Mitchell, 1960, Stacey and Bowen, 1988a, Kneller and Buckee, 2000). As a result, considerable effort is being put into the numerical modelling for 2D and 3D gravity currents problems. The use of commercial software, such as ANSYS FLUENT and CFX has been effective in providing detailed visualisation of the related gravity current flows without the need to perform numerous experimental trials.

Chapter 3
Roughness effects on sedimentary flows

3.1 Introduction

In many studies, bed roughness is described as arrays of elements which disturb the incoming flow. A single element cannot be regarded as bed roughness, it is usually a series of elements which makes the bed roughness so that the flow boundary layer is similar to the flow over a flat-bed that is not completely developed with the next impact with the adjacent element (Batt, 2008). A single obstacle is normally considered as a localised porous barrier, or a patch of large-scale roughness, where as a result the flow becomes partially arrested. The bed roughness is sometimes used as a protective measure to prevent forms of gravity currents, such as avalanches in regions located at the foot of steep slopes. This can be replicated in the laboratory as an experiment, or it can be modelled numerically, as large scale roughness elements or isolated obstacles (Tokyay and Constantinescu, 2015, Tokyay et al., 2011b). An example of gravity current propagating over rough boundary is dust storm (Haboob) over a city with heterogeneous or uniform building height. Typically, a weak hydraulic jump is induced as the current flows over a roughness element which allows the rest of the slow moving flow over the barrier. The denser part of the current flow behaves differently to the mixing layer above it when encountering bed roughness. The head of the current may get arrested between bed roughness elements. If the height of the obstacle is greater than the incoming flow height then the hydraulic jump can be generated near the crest of the obstacles. In this case the advancement of the current upstream is strongly disturbed and the propagation rate of the current can be strongly reduced. Alternatively, under certain conditions the gravity current breaks down into a number of gravity currents in a condition known as flow coupling (Tokyay et al., 2011b).

3.2 Literature review

The study of turbulent flow over surface roughness is important in a variety of engineering and environmental applications. Surface roughness is used as a tool to enhance heat transfer in turbines (Lawson et al., 2011), heat exchangers (Webb and Eckert, 1972), micro-scale electric mechanical systems (Sun and Faghri, 2003), high heat flux heat transfer devices employed in nuclear fusion (Milnes et al., 2012),

chemical reactors, refrigeration systems and air conditioners (Liu and Sakr, 2013), etc. Examples of rough-wall flows include particle transport in pipes and channels with rough walls, supersonic flows inside cavities for aerospace applications, wind flow over urban-like surfaces and turbidity currents over rough substrates (Lawson et al., 2011, Young and Van Vliet, 1988, Millward-Hopkins et al., 2011, Eggenhuisen and McCaffrey, 2012, Castro et al., 2013).

A thin water layer formed close to the river and sea bed is called the benthic boundary layer (McCave, 2012). The thickness of this layer depends on the wall shear stress and the flow velocity. In an analogous manner to a rough-wall channel flow, very similar roughness properties are present in benthic boundary layers of gravel-bed river flows. This has received much attention in the past decade since macro-roughness has a strong influence on ecological processes within an ocean bed or river environment at multitude of scales and hierarchies. Relevant examples include: transport, fate and mixing of extremely diversified river substances such as dissolved or particulate nutrients and contaminants, natural sediments and benthic living organisms. A more comprehensive insight into the hydrodynamic mechanisms and properties above and across the flow at the gravel-bed interface are necessary as to gain a better understating of these coupled flow properties.

More natural elements in macro scale dimensions have been used in urban-like surfaces (Millward-Hopkins et al., 2011). Heterogeneous and homogeneous building heights are presented in the urban surfaces. The study of these types of roughness elements has application in dispersion modelling, wind loading calculations and estimating the wind energy source at urban locations. In this case, the velocity profile is expressed as a logarithmic function with a depth which is dependent on the shear velocity and the geometrical structure of the roughness at the bed. Thus it is important to predict the spatially averaged logarithmic wind profiles accurately.

The surface area density and building height variability are the two most important geometrical characteristics where the aerodynamic roughness length and the zero-plane displacement depend on them. A quasi-empirical modelling approach is used to measure the surface roughness and zero-plane displacement. The expression to estimate the wind speed u at a height z meters above the ground is given by (Thom, 1971, Jackson, 1981):

$$u_z = \frac{u_\tau}{\kappa}\left[\ln\left(\frac{z-d}{z_0}\right) + \psi\left(z, z_0, L\right)\right]$$

(3.1)
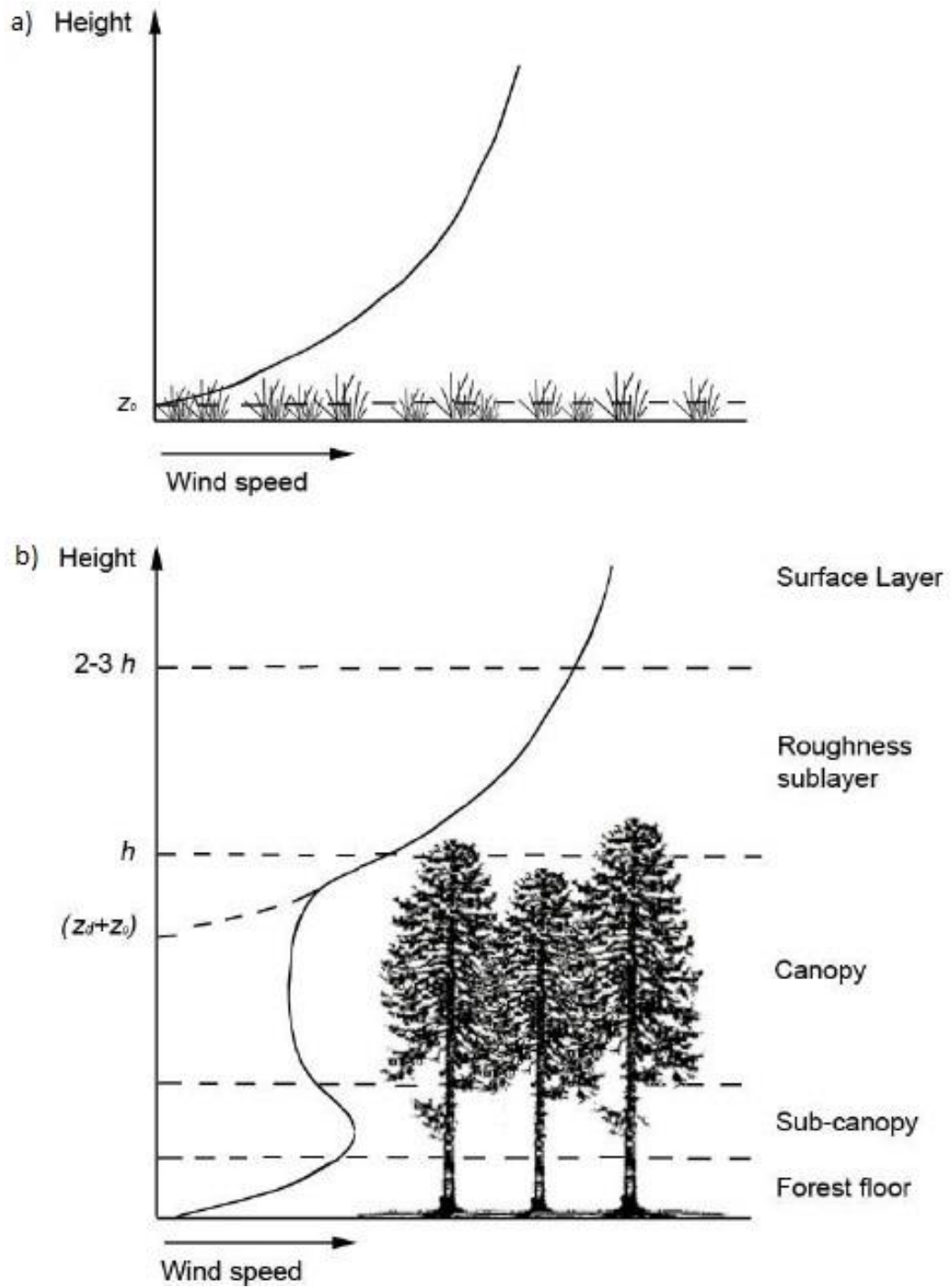
Figure 3.1: (a) Schematics of the wind profile for low vegetation, and (b) for forest regions (Junge and Westerhellweg, 2011, Gardiner, 2004).

where u_τ is friction or shear velocity, κ is Von Karman's constant (~ 0.41), d is the zero-plane displacement, z_0 is the roughness length, ψ is the stability term and L is the Monin-Obukhob stability parameter. As can be seen in figure 3.1, the wind speed increases with height above the ground. One can note how the expression equation (3.1) depends on the roughness length z_0

and z_d (where $z_0 = z_d - d$) which is the lower bound of the layer where the logarithmic law is still valid.
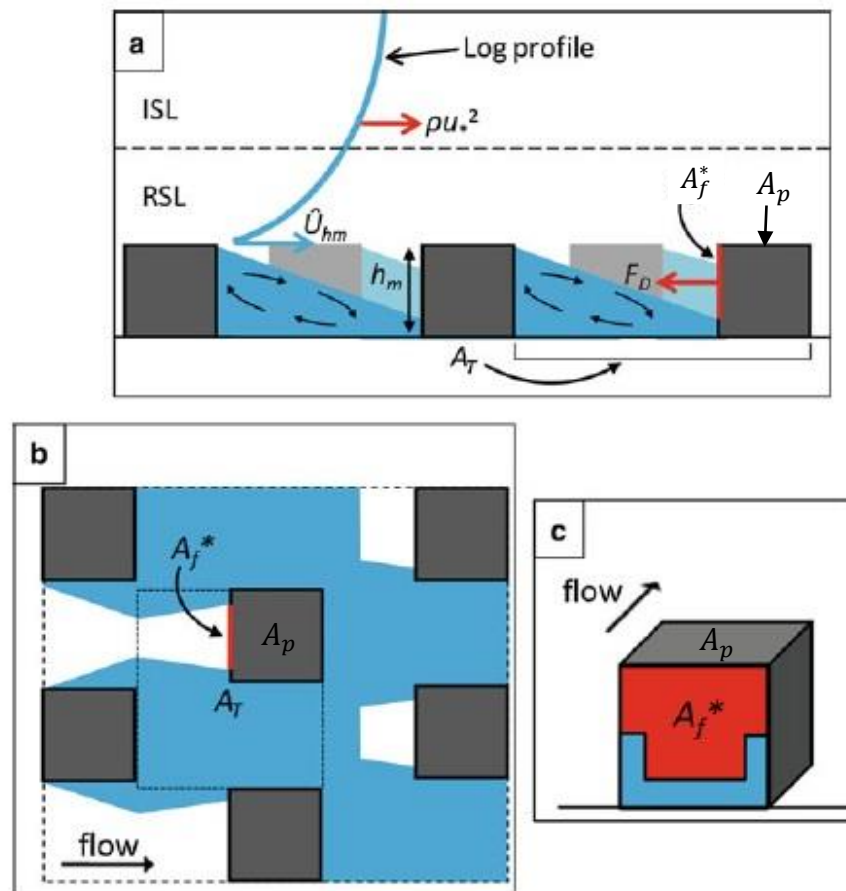
Figure 3.2: Illustration of the log profile and mutual sheltering of the uniform roughness arrays where ISL is the inertial sublayer and RSL is the roughness sublayer. The blue colour shows the total sheltered space that is the sheltering of all the roughness elements and the red region describes the unsheltered frontal area of a single roughness element, (Millward-Hopkins et al., 2011).

The solidity function λ was first defined by Schlichting (1936) which depended on the roughness height and the surface density. This function was defined by Schlichting (1936) as the total projected frontal roughness area per unit wall-parallel projected

area as shown in figure 3.2. This is then classified as two groups, including the ratio of the roughness plane area (A_P) to the ground surface area (A_T), namely $\lambda_P = A_P/A_T$ and the ratio of roughness frontal area (A_f^*) to ground surface area, namely $\lambda_F = A_f^*/A_T$. The roughness effects increase until it reaches a critical value of 0.15. This is in a good agreement by Rouse (1937) who observed the optimum concentration to be between 15-20%. Subsequently this concentration decreases as the roughness effect of the individual elements weakens and the elements begin to shelter each other.

A more apparent difference between fluid flow in a laminar state compared with that of a turbulent one is that turbulent fluid motions are more affected by the presence of surface roughness. This is at once obvious when considering laminar flow through a smooth pipe or channel which is typically accompanied by small scale irregularities at the wall region. The compositions of streamlines in a laminar flow are parallel, leaving the core of the flow where the velocity of the fluid is at its maximum unaffected by small-scale roughness in the vicinity of the wall (e.g. blood flow in human cardiovascular micro-channels)(Kendall, 1990, Okiishi et al., 2006). Turbulent flow, however, is composed of many small eddies, which continuously interact with any roughness present on the pipe inner surface. Chu and Karniadakis (1993)compared the characteristics of the turbulent flow with laminar flow over riblet-mounted wall using a DNS study. Results from this numerical study reported that for laminar flow there is no drag reduction, while the drag reduction exist for turbulent flow.

Further, a similar skin friction profile were found on the riblet wall under both turbulent and laminar flow regimes. Further, the dynamics of turbulent and laminar particle-laden flow were experimented by Baas and Best (2008). For the laminar flow the length of the separation zone were less than in the turbulent flow The suspended sediments also showed a stagnant behaviour in the separation zone for the laminar flow while the entrained sediments were mobile in turbulent flow.

In many studies (Castro, 2009, Tokyay et al., 2011b), bed roughness is described as arrays of elements which disturb the incoming flow. The roughness elements alter the structure of the boundary layer by perturbing the flow near the wall. The effects arising from the perturbations near the wall include the change in momentum, heat and mass transfer rate at the boundary layer bed. The boundary layer of turbulent is thicker than that of laminar boundary layer and for it to develop, the flow must be of sufficiently high Reynolds number. As the roughness height increases, there will be a transition from a hydraulically smooth regime to a critical level where the effect of

the roughness to the turbulent boundary layer begins to take effect. Then, as the roughness height continues to increase, the viscous sub-layer thickness reduces and this weakens the damping effect of the wall to the point where the viscous sub-layer can no longer be maintained. Subsequently, as (Nikuradse, 1933a) noted, with a further increase in the Reynolds number, the roughness effects behave independently of the Reynolds number and becomes proportional to the roughness Reynolds number (h_s^+). Schlichting (1960) introduced an equation for the equivalent sand grain roughness Reynolds number (also known as the roughness Reynolds number) accounting the work of Nikuradse (1933a) as follows:

$$h_s^+ = \frac{u_\tau h_s}{\nu}$$
(3.2)

where U_τ is the friction velocity, h_s is the equivalent sand grain roughness height and ν is the kinematic viscosity. The classification of surface roughness by Nikuradse (1933a) will be discussed in the next section.

3.3 Surface roughness classification

The roughness is characterised either by the grain type roughness or the form type roughness. The form type roughness is referred to a form greater in scale than the sand grain roughness type. For example, a flat bed of coarse sand can be classified as sand grain roughness. Relatively, van Rijn (1984) stated that a composite grain and form type bed roughness occurs in regions such as dune fields. Some investigations have shown that the grain type roughness correlates satisfactorily with the equivalent sand roughness height. However, the suitability of this parameter for characterising the type of roughness is still under discussion. There are debates that reject the idea of having a single value for the form type roughness that results in different values of the Reynolds stress for different types of roughness (Nikuradse, 1933a, Townsend, 1980, Antonia and Krogstad, 2000). This could potentially misrepresent this type of roughness with the outcome of inaccuracies in the flow field. The sand grain roughness model was first introduced by VanDriest (1956), which was defined as follows:

$$\nu_t = (\kappa F y)^2 \left(\frac{\partial U}{\partial y}\right)$$
(3.3)

$$F = 1 - \exp\left(-\frac{y^+}{26}\right) + \exp(-2.3\frac{y^+}{h_s^+}) \tag{3.4}$$

where v_t is the eddy viscosity of the fluid, y is the distance from the wall in vertical direction, $y^+ (= u_\tau y/v)$ is the dimensionless wall distance, v is the kinematic viscosity, u_τ is the shear velocity and F is the damping function.

The damping function has been modified by other authors and the most recent advancement is by Krogstad (1991) who added a new version of the mixing length model for sand grain roughness and this is given as follows:

$$F = 1 - \exp\left(-\frac{y^+}{26}\right) + \exp\left(-\frac{y^+}{26}\left(\frac{70}{h_s^+}\right)^{\frac{3}{2}}\right)\sqrt{1 + \exp\left(-\frac{70}{h_s^+}\right)} \tag{3.5}$$
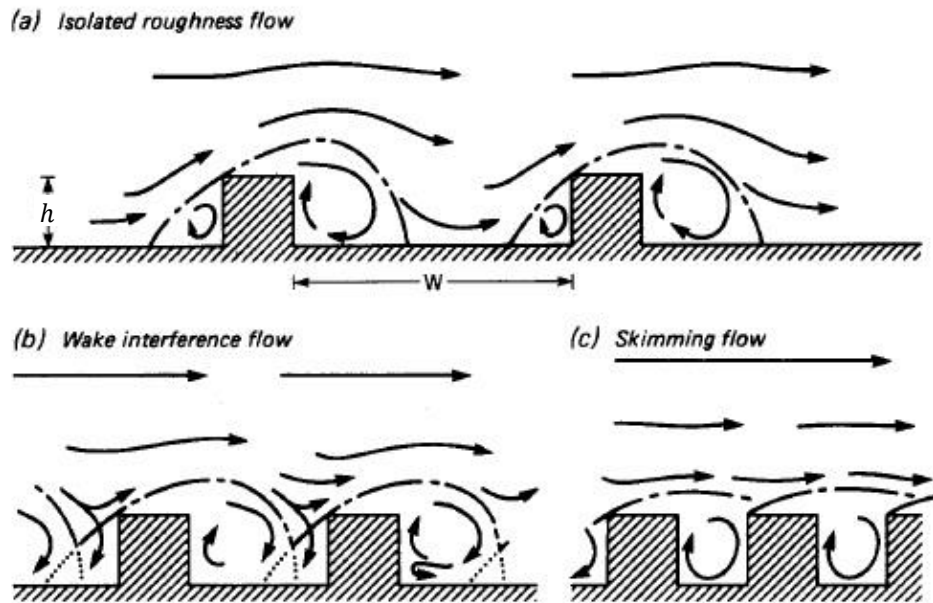
Figure 3. 3: Flow regimes associated with a range of roughness width-to-height ratio (Oke, 1988).

In recent decades, a wide range of experimental and computational studies has been performed to understand the effect of surface roughness on the structure of the turbulent flow. The computational domain and experimental configuration of these studies are typically a two-dimensional or three-dimensional rectangular channel flow with roughness on one or both walls (Tsikata and Tachie, 2013, Lee et al., 2011, Roussinova and Balachandar, 2011, Burattini et al., 2008, Ryu et al., 2007, Cui et al., 2003, Ashrafian and Andersson, 2006, Krogstad et al., 2005, Krogstad et al., 1992, Leonardi and Castro, 2010, Leonardi et al., 2003, Djenidi et al., 1999, Tachie et al.,

2000, Jiménez, 2004). The effect of surface roughness on the flow, as reviewed by Jiménez (2004) and more recently by Antonia and Djenidi (2010), is often separated into three different regimes. Chow (1959) was the first to identify three flow regimes over beam-type roughness as quasi-smooth or skimming flow, wake-interference flow and isolated-roughness flow as shown in figure 3.3. Perry et al. (1969) categorised two distinct types of roughness, namely, "D" and "K" denoting channel height and roughness height, respectively (see below), following from the earlier experimental work conducted by Nikuradse (1933b) on the turbulent flow of fluids in rough pipes. Figure 3.4 shows a schematic of a surface roughness in two-dimensions where h is the average roughness height, y_p is the wall-normal distance form the top of the surfaces element and y_0 is the virtual origin which is the space between y_p and the overall mean velocity distance up to where it becomes zero. Kays and Crawford (1993) suggested that the virtual origin parameter depends on the shape and size of the roughness elements. The relative parameters based on experimental evidence are given by

$$y = y_p + y_0$$

<div align="right">(3.6)</div>
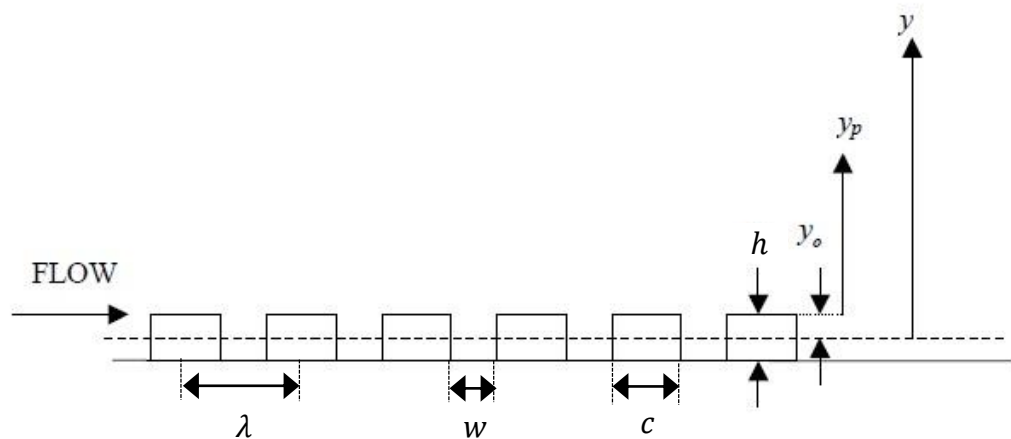
Figure 3.4: Schematic of a two-dimensional rough surface modified from Akinlade (2005).

There are three flow regimes for turbulent flow over rough surfaces including hydraulically smooth, transitionally rough and fully rough flows. This depends on the geometrical size of the elements on the wall relative to the thickness of the viscous sub-layer. Based on the equivalent sand grain roughness, the Reynolds number the rough wall turbulence regimes are described as follows (Jiménez, 2004):

$$\text{Hydraulically smooth wall for } 0 < h_s^+ \leq 5 \tag{3.7}$$

$$\text{Transitionally rough regime for } 5 < h_s^+ \leq 70 \tag{3.8}$$

$$\text{Fully rough regime for } h_s^+ \geq 70 \tag{3.9}$$

The roughness type can be correlated to the spacing to height ratio of a roughness element, w/h. The roughness spacing is differently defined as either the distance between the roughness faces w, or the distance between the roughness-element centre-lines λ; the values differ by unity for square ribs. Therefore one must be careful not to confuse the cavity width to height ratio w/h to the pitch to height ratio λ/h. In addition, for flow over three-dimensional roughness c_z and w_z with $A_f = c_z h$ need to be taken into account.

For a sufficiently low width to height ratio, $w/k \lesssim 2$, or $D-$type roughness, the flow undergoes a "skimming flow" regime and the effective height, y_l above the channel bed where the velocity profile begins to take a logarithmic shape becomes independent of the roughness height, h. In this flow regime there is minor shedding or interaction from the vicinity of the roughness element to the outer flow region (Djenidi et al., 1999, Leonardi, 2004, Leonardi et al., 2007). The $K-$type roughness (isolated-roughness flow regime) is associated with $w/h \gtrsim 4$. The roughness height becomes a crucial parameter for $w/h \gtrsim 4$ when the flow in the roughness cavity begins to interact with the main body of the flow. For this roughness type, the origin of the logarithmic profile, y_l is proportional to the roughness height, h and the flow regimes are characterised by separation occurring at the crest of the first roughness element followed by a reattachment within the distance away from the next adjacent element. The experimental study of Djenidi (1999) suggested a similarity in the quasi streamwise vortices and low-speed streaks of the roughened wall cases, to a flat turbulent boundary layer. Tani (1987) found the demarcation line between the $D-$type and the $K-$type roughness occurs at $w/h = 4$. Cui (2003) observed a similar transition for $w/h = 4$ and named this roughness type as intermediate. This transition flow regime corresponds to wake interference with flow regime classified by Chow (1959). In this regime a weak interaction between the inner and outer roughness layers occurs and the reattachment takes place at the crest of the next roughness element. The direct numerical simulation (DNS) of Leonardi (2004) showed that the intermediate regime appears within the range $3 < w/h < 7$.

In a fully rough flow, the ratio of the product of the roughness height and shear velocity to the kinematic viscosity of the fluid $h^+ = hu_\tau/v$ is greater than ≈ 70 and the pressure drag component of the total drag dominates the viscous drag component. In this flow regime the flow characteristics are only dependent on the roughness spacing to height ratio w/h. Hence, the viscous length scale (v/u_τ) near the wall scale becomes irrelevant (Leonardi, 2010, Castro, 2007).

Orlandi (2006) and Leonardi (2007) found similarity in the vortex shedding distribution between the intermediate and $K-$type roughness. Therefore, they suggested that classification of different roughness types should not be based on the state and intensity of vortex shedding. Instead, they related the transition between $D-$type and $K-$type to the magnitude of the viscous and pressure drags.

Townsend (1980) suggested that, at sufficiently high Reynolds number, if the friction velocity is scaled then both smooth and rough wall turbulent boundary layers have similar structures in the region outside the sub-layer. This was later rejected by Antonia and Krogstad (2000) and Keirsbulck et al. (2002) who proposed that the roughness affects the velocity profiles and changes the fluctuation fields in the outer regions of the turbulent boundary layer. Hence the wall similarity is not valid for the smooth wall. There appears to be a vast number of investigations into the study of rough wall turbulent flows, but there are still uncertainties with regards to the effects of roughness in the near-wall and outer region of the boundary layer (Antonia and Smalley, 2000).

Both LES and DNS numerical modelling of rough-wall flows have proven to be highly accurate in predicting the turbulent kinetic energy and Reynolds stresses in the near-wall region. However, in order to capture most of the flow characteristics within the roughness sub-layer, a higher grid resolution and time step accuracy are required than in a normal smooth-wall case. This makes such approaches expensive, particularly for high Reynolds number flows. Leonardi (2004) used DNS to investigate the effect of the w/h ratio on the turbulence structure near the wall, and its overlying flow by considering two-point velocity correlations. They observed that in the fully rough regime, with the increase in the w/h ratio, the coherence structure becomes less elongated in the streamwise direction, and larger in the spanwise direction as a result of outward jets of fluid at the leading edge of the roughness element. Such coherence structure would appear to be less influenced by the rough wall in the transition regime ($h^+ = 13$), as observed by Ashrafian et al. (2004). The maximum strength of the outward jet and the minimum reduction of the coherence occurred at

the critical value $w/h = 7$. They further found that the influence of roughness can extend up to $2h$ above the roughness crest for $w/h = 3$ and up to $5h$ for $w/h = 7$. The study conducted by Ashrafian and Andersson (2006), for a channel with transverse rib roughness on one wall, suggests a strong interaction between the inner and outer layer roughness for $K-$type roughness.

Numerous authors have performed numerical and experimental analyses to investigate the relationship between the heat transfer and fluid flow behaviour by varying the w/h ratio (Rao and Picot, 1970, Webb et al., 1971, Ichimiya, 1987, Liou et al., 1993). However most of these investigations suffer from a lack of a detailed range of w/h ratio and Reynolds number. The most detailed study was performed experimentally by Furuya et al. (1976) and Okamoto et al. (1993) for boundary layer fluid flow. Okamoto et al. (1993) investigated the maximum resistance of the turbulent boundary layer in a plate roughened by equally spaced wires. They found that the maximum skin drag coefficient, c_f and pressure coefficient, c_p values appear at $w/h = 7$. However the DNS results of Leonardi et al. (2007) suggests that minimum c_f occurs at $w/h = 7$, but agrees with the maximum pressure coefficient c_p occurring at this w/h ratio. The experimental study by (Okamoto et al., 1993) has shown that the maximum heat transfer occurs when the turbulence intensity is maximised. They have shown that the maximum flow resistance occurs between $w/h = 6$ and $w/h = 8$. Chapter 5 aims to explicitly identify where the optimum flow resistance occurs for a more detailed range of w/h ratio as a function of Reynolds number.

3.4 Experimental configurations for gravity driven flows with the inclusion of surface roughness

Extensive research has been performed to investigate the different types of roughness with their effects on pipes, ducts and open channels (Jiménez, 2004). A similar natural occurring flow has been developed in laboratories using lock-exchange or lock release methodologies over a bed consisting of a range of roughness's such as different grades of sand, wire grids, grooves, etc. Maddux et al. (2003a) conducted an experiment to study the dynamics of a turbulent continual flux flow in a flume over a bed of 3D fixed dunes that consisted of coarse sand. There appears to be only a little literatures on performing such experiments for gravity currents but Hallworth et al. (1996) performed an experiment in a tank over a thin layer of granules with a mean grain diameter in of about one millimetre.

The previous studies include a continual flux current over $D-$type beams which were pinned to the bed in a tank (Hallworth et al., 1996). In addition, Kubo (2004) tested the influence of a series of humps on a slope on the sediment deposition in a lock-release particulate gravity current.

More recently, Eggenhuisen and McCaffrey (2012) suggested that field data suggests that the presence of significant bed roughness tends to increase the run out length of turbidity currents. In order to provide evidence for this hypothesis, they investigated the effect of a fixed rough element on the distribution of the sediment within the flow. In the same running experiments velocity profiles were determined for turbidity current propagating over a square roughness element fixed at the bed. It was found that the profiles for the vertical turbulence obtained from the perturbed series showed a distinct dissimilarity to those of the unperturbed turbulence profiles. Eggenhuisen and McCaffrey (2012) concluded from dispersion-diffusion theory, that there is a net distribution of sediments towards the upper region, and this results in a reduced density stratification and an increases in the run-out distance of the flow. One of the main aims of this thesis is to use numerical computations to provide further evidence for or against this hypothesis. Previous work related to this reviewed below.

3.5 Numerical studies of gravity-driven flows over rough surfaces

From numerous encounters in nature, the surface over which gravity currents propagate is far from smooth. The existence of bedforms (such as: dunes, ripples at the bottom of rivers and ocean surfaces), with the addition of topographic bumps in vegetation layers, or simply an array of obstacles significantly affects the dynamics of gravity currents via induced drag. Basically, this acts as a net drag force which provides additional friction to the flow and slows down the gravity current much more than what is observed from the dynamics of the gravity current over smooth surfaces (Tokyay et al., 2011b). The influence of such obstacles on the inner mechanics of smooth bed-manifested gravity currents are, in fact, very similar to what is observed in turbulent constant flow densities which propagate over rougher terrain (Jimenez, 2004).

As regards to the approach taken by both cases above, the existence of large-scale bedforms or obstacles at rivers and ocean bottom channels provides an additional mechanism for energy dissipation. When considering constant density flows, the effects of obstacles manifested from various shapes or bedforms at the bottom of a

channel are legitimately well understood (e.g. (Ikeda and Durbin, 2002, Leonardi et al., 2003, Anderson and Meneveau, 2011). These numerical and experimental studies deliver a systematic discussion on the effects of spacing, shape and dimension of the roughness elements on the mean flow and the structure of turbulence formed in straight horizontal channels.

There have been number of recent works studying the effect of roughness on the gravity currents (Nicholson and Flynn, 2015, Tokyay and Constantinescu, 2015, Tokyay et al., 2011a, Tokyay et al., 2011b, Özgökmen and Fischer, 2008, Ozan et al., 2015). Also, there are recent numerical studies reporting the effect of roughness on the sediment-driven flows (Nasr-Azadani and Meiburg, 2014a, Nasr-Azadani and Meiburg, 2014b). Particular attention has been paid to the synergy of gravity currents and isolated surface-mounted obstacles or ridges. (Armi, 1986) proposed a theoretical framework, which dealt with the study of two-layer flows interfaced with an isolated bottom- mounted long obstacle with a lee side and a smooth variation in the surface slope. By parameterizing the flows by taking into account the internal Froude number for each layer, (Armi, 1986) examined the circumstances for which the subcritical two-layer flow ahead of the obstacle becomes supercritical and passes the crest of the obstacle inside the bottom layer in which the higher density flow is strongly accelerated (Tokyay et al., 2011b).

Gonzalez-Juez et al. (2009) investigated the unsteady drag and lift generated by the interaction of gravity current with a bottom –mounted square cylinder, utilizing high-resolution Navier-Stokes simulations. For the two dimensional simulation (at Re =1000) and three-dimensional simulations at (Re = 10000), it was found that drag coefficient increases exponentially at maximum value; as the current meets the cylinder, which than experiences fluctuations and eventually approaches a quasi-steady value. They also showed that the spanwise variation of the drag determined by gravity currents lobe an cleft structures during the impact phase. Finally, the comparison between gravity-current flows and corresponding constant-density flows shows that the hydrostatic drag component feature of the gravity current and must be considered during obstacle interactions and roughened surfaces. Further work by Gonzalez-Juez et al. (2009) showed the flow of compositional gravity currents past cylinders mounted above a wall. Both two and three-dimensional Navier-Stokes simulations were employed as to measure quantitatively, the force load acting on the cylinders, and the friction velocity at the bottom wall close to the cylinders at relatively low to medium range Reynolds numbers. The results of the two-dimensional simulation findings accurately captured the impact stage, but they overly predicted

the forces and friction velocity fluctuations within the transient stages. They concluded that the friction velocity below the cylinder depends chiefly on the Reynolds number propagated with the gap width and the front velocity. During the impact stage, the maximum friction velocity was 60% larger than what was observed during the quasi-steady stage or constant density flow. The interaction of turbidity currents with a form of Gaussian bump of various heights were investigated by (Nasr-Azadani and Meiburg, 2014a) For the shorter bump the turbidity currents propagated over the obstacles and for the taller bump the current travelled around the obstacle. The effect of settling velocity were investigated by comparing sediment-driven flow with compositional gravity current (no particles in the flow). The influence of the settling velocity on the front velocity of the current was found to be more pronounced than the influence of the obstacle. Although, the Reynolds number in which they simulated turbidity current was Re=2000. Further, smaller bump showed a lower level of current dissipation rate than when turbidity current propagate over flat bed which lead to an increase in current velocity. However, the dissipation of the current was much greater for flow over taller bump than the flat bed case which lead to slower propagating current.

Chapter 4
Turbulence modelling

4.1 Introduction

A wide range of phenomena are associated with turbulent flows which will be discussed in this chapter. Such flows are decomposed into average and fluctuating components, and this is known as Reynolds decomposition. Turbulent flows behave in a chaotic and intermittent manner and can diffuse and dissipate at a certain rate depending on their boundary condition. The presence of velocity fluctuations in such flow regime results in the development of stresses called Reynolds stresses. Turbulent energy containing eddies appear in a wide range of length scales. They can be visualised in a sediment carrying wind. The presence of the kinetic energy in larger eddies results in stretching of smaller eddies and hence the energy is transferred from large to small scales. This process is called vortex stretching. This energy transfer starts as an inviscid process. The process will continue until the viscous effects begin to dominate at the smallest scale, which at this stage energy is dissipated to heat. In comparison to smaller eddies, larger eddies have lower frequency and lower wave number. As the wave number increases the fluctuations begin to behave in an intermittent behaviour. Jiménez (2000) described intermittency as a phenomenon which is a consequence of the energy cascade. This appears in larger eddies rather than smaller ones which have lower wave numbers. Therefore, they are more energetic. The practical limit of eddy scale for which the inertial effect become equal to viscous effect at a particular wave number is called Kolmogorove micro-scale, which is named after the Russian scientist in the 1940s .

4.2 The Navier-Stokes equations

Gravity current flows may occur both in the form of compressible and incompressible flow. Thus, It is important to understand the Navier-Stokes equations in both the fluid states. The equations are named after the Claude-Louis Navier (a French engineer and physicist) and Sir George Gabriel Stokes (an English mathematician and physicist) in the early 1800's. The equations were first derived by them independently which later were used in a combined form.

The Navier-Stokes equations are non-linear partial differential equations which give a mathematical description of a 3D unsteady and steady fluid motion in which the

viscous nature of fluid motion is considered. CFD commercial codes such as ANSYS FLUENT and CFX use the integral conservation form of these equations to resolve the fluid flow in each single control volume of the domain. However, the domain must firstly be divided into a required number of cell to provide the required control volumes. This is achieved with meshing tool softwares such as ANSYS ICEM or Gambit. Then accordingly the CFD solvers can use discretisation techniques to convert the integral equations into a system of algebraic equations which can be solved by an iterative method.

Fundamentally, the Navier-Stokes equations describe the conservation of momentum in the flow, and they are supplemented by mass (continuity) and energy conservation equations. According to the Newton's second law the rate at which a fluid element increases in momentum is equal to the sum of forces exerted to it. In general, there are two types of force acting on the fluid element including surface forces(normal pressure forces, and tangential viscous forces) and body forces (e.g. gravitational, centrifugal and electromagnetic) (Blazek, 2005). The surface forces are included in the three dimensional momentum equation with the addition of body forces as source terms. The continuity equation for the unsteady compressible fluid can be expressed as,

$$\frac{\partial \rho}{\partial t} + \nabla . (\rho \mathbf{u}) = 0 \tag{4.1}$$

In the case of an incompressible fluid such as water, both the density ρ and the velocity vector $\mathrm{u} = (u, v, w)$ are constant and thus, equation (4.1) reduces to the following:

$$\frac{\partial u}{\partial x} + \frac{\partial v}{\partial y} + \frac{\partial w}{\partial z} = 0 \tag{4.2}$$

In order to determine the three components of the momentum, the rate of change of momentum must be set equal to the total of the surface stresses in all three direction with the addition of body force source terms. The net flow into the fluid element per unit volume terms is also included which gives the overall momentum equation as follows:

$$\frac{\partial(\rho u)}{\partial t} + \mathbf{\nabla}.(\rho u\mathbf{u}) = -\frac{\partial P}{\partial x} + \nabla.(\mu\nabla u) + S_{Mx} \tag{4.3}$$

$$\frac{\partial(\rho v)}{\partial t} + \mathbf{\nabla}.(\rho v\mathbf{u}) = -\frac{\partial P}{\partial y} + \nabla.(\mu\nabla u) + S_{My} \tag{4.4}$$

$$\frac{\partial(\rho w)}{\partial t} + \mathbf{\nabla}.(\rho w\mathbf{u}) = -\frac{\partial P}{\partial z} + \nabla.(\mu\nabla w) + S_{My} \tag{4.5}$$

Therefore the momentum equations is given by,

$$\frac{\partial(\rho\mathbf{u})}{\partial t} + \mathbf{\nabla}.(\rho\mathbf{u} \otimes \mathbf{u}) = -\nabla p + \nabla.\tau + \mathbf{S}_M \tag{4.6}$$

The stress tensor which is linked to the strain rate is given by,

$$\tau = \mu\left(\mathbf{\nabla u} + (\mathbf{\nabla u})^{\mathrm{T}} - \frac{2}{3}\delta\mathbf{\nabla}.\mathbf{u}\right) \tag{4.7}$$

4.3 Reynolds-Averaged Navier-Stokes Equations

This method uses time-averaging and mass-weighted time-averaging of the Navier-Stokes equations. The pure time-averaging operation is known as Reynolds averaging. The mass-weighted time-averaging operation is known as Favre averaging. In the equations below, given an instantaneous variable ϕ, its time average is denoted by $\bar{\phi}$, and its Favre average is denoted by $\tilde{\phi} = \overline{\rho\phi}/\bar{\rho}$, where ρ is the fluid density. Dashed quantities ϕ' denote fluctuations from the Favre averaged variable, thus $\phi = \tilde{\phi} + \phi'$ Reynolds averaged variables are suitable for RANS modelling of incompressible flows. However, expressing the time-averaged equations in terms of Favre averaged variables yields RANS equations which are more suitable for compressible flows (Wilcox, 2006).

In RANS models, only the mean Favre average is solved rather than solving the instantaneous values of fluctuating quantities directly. The Favre-averaged continuity equation has the same form as the instantaneous continuity equation:

$$\frac{\partial\bar{\rho}}{\partial t} + \mathbf{\nabla}.\left(\bar{\rho}\widetilde{\mathbf{U}}\right) = 0 \tag{4.8}$$

The time-averaging and Favre averaging of the momentum equations for compressible flows are as follows:

$$\frac{\partial(\bar{\rho}\tilde{U})}{\partial t} + \nabla \cdot \left(\bar{\rho}\tilde{U}\mathbf{U}\right) = -\frac{\partial \bar{P}}{\partial x} + \nabla \cdot \left(\mu\nabla\tilde{U}\right) + \frac{\partial\left(\overline{\rho u'^2}\right)}{\partial x} - \frac{\partial\left(\overline{\rho u'v'}\right)}{\partial y} - \frac{\partial\left(\overline{\rho u'w'}\right)}{\partial z} + S_{Mx} \qquad (4.9)$$

$$\frac{\partial(\bar{\rho}\tilde{V})}{\partial t} + \nabla \cdot \left(\bar{\rho}\tilde{U}\mathbf{V}\right) = -\frac{\partial \bar{P}}{\partial x} + \nabla \cdot \left(\mu\nabla\tilde{V}\right) + \frac{\partial\left(\overline{\rho u'v'}\right)}{\partial x} - \frac{\partial\left(\overline{\rho v'^2}\right)}{\partial y} - \frac{\partial\left(\overline{\rho v'w'}\right)}{\partial z} + S_{My} \qquad (4.10)$$

$$\frac{\partial(\bar{\rho}\tilde{W})}{\partial t} + \nabla \cdot \left(\bar{\rho}\tilde{U}\mathbf{W}\right) = -\frac{\partial \bar{P}}{\partial x} + \nabla \cdot \left(\mu\nabla W\right) + \frac{\partial\left(\overline{\rho u'w'}\right)}{\partial x} - \frac{\partial\left(\overline{\rho u'w'}\right)}{\partial y} - \frac{\partial\left(\overline{\rho w'^2}\right)}{\partial z} + S_{Mz} \qquad (4.11)$$

4.3.1 $k - \varepsilon$ model

The standard $k - \varepsilon$ model is composed of two equations, one for turbulent kinetic energy k and one for the rate of viscous dissipation ε. These are simplified from the exact $k - \varepsilon$ transport equations which include many unknown correlations. Hence, in the standard model the turbulence velocity scale can be defined as $k^{1/2}$ and turbulence length scale l as $k^{3/2}/\varepsilon$, where $k = 1/2(\overline{u'^2} + \overline{v'^2} + \overline{w'^2})$. Turbulent eddies result in momentum transfer which can be modelled with eddy viscosity $\mu_t = \bar{\rho}C_\mu\,k^2/\varepsilon$ where C_μ is a dimensionless constant. The model belongs to the category of the eddy viscosity model which use the eddy viscosity hypothesis to relate the Reynolds stresses to mean velocity gradients as described below.

The Reynolds stresses terms are important to achieve enhanced mixing as these have effective contribution to the mixing as a result of the velocity fluctuation. In other word, with higher velocity fluctuations more mixing could be achieved due to the molecular velocity fluctuations. Using the eddy viscosity hypothesis, also known as the Boussinesq hypothesis, the Reynolds stresses are computed as follows (Versteeg and Malalasekera, 2007):

$$\tau_{ij} = -\overline{\rho u_i' u_j'} = -\frac{2}{3}\bar{\rho}k\,\delta_{ij} + \mu_t\left(\frac{\partial \tilde{U}_i}{\partial x_j} + \frac{\partial \tilde{U}_j}{\partial x_i} - \frac{2}{3}\frac{\partial \tilde{U}_k}{\partial x_k}\,\delta_{ij}\right) \qquad (4.12)$$

The transport equations of the standard $k - \varepsilon$ model for k and ε are respectively as follows (Versteeg and Malalasekera, 2007):

k −equation,

$$\frac{\partial(\bar{\rho}k)}{\partial t} + \frac{\partial}{\partial x_j}\left(\bar{\rho}\,\tilde{U}_j k\right) = \frac{\partial}{\partial x_i}\left[\left(\mu + \frac{\mu_t}{\sigma_k}\right)\frac{\partial k}{\partial x_j}\right] + P_k - \bar{\rho}\varepsilon + P_{kb} \qquad (4.13)$$

ε −equation,

$$\frac{\partial(\bar{\rho}\varepsilon)}{\partial t} + \frac{\partial}{\partial x_j}\left(\bar{\rho}\widetilde{U}_j\varepsilon\right) = \frac{\partial}{\partial x_j}\left[\left(\mu + \frac{\mu_t}{\sigma_\varepsilon}\right)\frac{\partial\varepsilon}{\partial x_j}\right] + \frac{\varepsilon}{k}\left(C_{\varepsilon_1}P_k - C_{\varepsilon_2}\bar{\rho}\varepsilon + C_{\varepsilon_3}P_{\varepsilon b}\right) \qquad (4.14)$$

In the $k - \varepsilon$ transport equations, P_k is the rate of production of turbulence due to shear, which is as follows:

$$P_k = 2\mu_t S_{ij}.S_{ij} \qquad (4.15)$$

Where S_{ij} is the strain rate tensor and is defined as:

$$S_{ij} = \frac{1}{2}\left(\frac{\partial u_i}{\partial x_j} + \frac{\partial u_j}{\partial x_i}\right) \qquad (4.16)$$

The addition of the term P_{kb} is the rate of production due to buoyancy. Its form depends on whether buoyancy is taken account assuming full variations in density, or if the effect of density variations is approximated using the Boussinesq approximation:

Full buoyancy model,

$$P_{kb} = \frac{\mu_t}{\sigma_\rho}g_i\frac{1}{\bar{\rho}}\frac{\partial\bar{\rho}}{\partial x_i} \qquad (4.17)$$

Boussinesq buoyancy model,

$$P_{kb} = \frac{\mu_t}{\sigma_\rho}\rho\beta g_i\frac{\partial\bar{T}}{\partial x_i} \qquad (4.18)$$

Where σ_ρ is the turbulence Schmidt number and T is the static temperature. The buoyancy production term for the ε-equation or $P_{\varepsilon b}$ can also be modelled as follows:

$$P_{\varepsilon b} = C_3.\max(0, P_{kb}) \qquad (4.19)$$

The equations contain five dimensionless empirical constants. The constants are obtained by correlation of 2D experimental data for a variety of turbulent flow cases

as shown in table 4.1. For example, in the case of the $C_{2\varepsilon}$ constant, the value is taken to agree with experimental results on the decay of a homogeneous isotropic turbulence field, where the convection, diffusion and production terms are equal to zero. These constants are adjustable to give better result in specialised circumstances. The production and dissipation terms of ε are proportional to the production and dissipation terms of k as shown in the equations (4.10)-(4.11).

C_μ	C_{ε_1}	C_{ε_2}	σ_k	σ_ε
0.09	1.44	1.92	1.00	1.30

Table 4. 1: Empirical constants values recommended by Launder and Spalding (1972).

The standard $k - \varepsilon$ model is the most widely used turbulence model in industry. This model is applied to the cases where resolving the boundary layer is not as important as resolving of the flow in the free stream. The $k - \varepsilon$ equation restricts integration right to the solid wall due to a singularity in the $\varepsilon -$ equation. Thus, the near-wall $\varepsilon -$ equation must be replaced by logarithmic turbulent wall-functions to overcome this. These are discussed in section 4.3.7.

4.3.2 $k - \omega$ model

In order to understand the near wall behaviour of the turbulence better, it is of importance to compute the physical phenomena, such as boundary layer separation and reattachment accurately. Kolmogorov (1942) developed the first two-equation model of turbulence and referred to ω as the mean turbulence frequency (Junge and Westerhellweg, 2011). Later Wilcox developed the $k - \omega$ turbulence model which solves the turbulence frequency $\omega = \varepsilon/k$ as the turbulence length scale determining variable instead of ε (Wilcox, 1988, Wilcox, 1993). The turbulence length scale for this model is $l = \sqrt{k}/\omega$ and hence the eddy viscosity can be written as $\mu_t = \rho k/\omega$. The buoyancy turbulence term $P_{\omega b}$ is derived by substituting the terms $\varepsilon = \beta' \omega k$ into equations (4.17)-(4.19) and $\alpha = \gamma_l = k/\omega$. In the $k - \omega$ model the Reynolds stresses are also derived using Boussinesq theory of the eddy viscosity hypothesis which are evaluated as follows:

$$\tau_{ij} = -\rho \overline{u'_i u'_j} = -\frac{2}{3}\rho k\, \delta_{ij} + \mu_t \left(\frac{\partial \widetilde{U}_i}{\partial x_j} + \frac{\partial \widetilde{U}_j}{\partial x_i} - \frac{2}{3}\frac{\partial \widetilde{U}_k}{\partial x_k}\, \delta_{ij} \right) \tag{4.20}$$

Hence the Wilcox $k - \omega$ model is defined as follows:

$k-$equation,

$$\frac{\partial(\bar{\rho}k)}{\partial t}+\frac{\partial}{\partial x_j}\left(\bar{\rho}\,\tilde{U}_jk\right)=\frac{\partial}{\partial x_j}\left[\left(\mu+\frac{\mu_t}{\sigma_k}\right)\frac{\partial k}{\partial x_j}\right]+P_k-\beta'\bar{\rho}k\omega+P_{kb} \tag{4.21}$$

$\omega-$equation:

$$\frac{\partial(\bar{\rho}\omega)}{\partial t}+\frac{\partial}{\partial x_j}\left(\bar{\rho}\,\tilde{U}_j\omega\right)=\frac{\partial}{\partial x_j}\left[\left(\mu+\frac{\mu_t}{\sigma_{\omega_1}}\right)\frac{\partial \omega}{\partial x_j}\right]+\alpha\frac{\omega}{k}\,P_k-\beta_1\,\bar{\rho}\omega^2+P_{\omega b} \tag{4.22}$$

This model is more robust near walls than the $k-\varepsilon$ model as it can be integrated to the wall without using logarithmic wall functions. The turbulence frequency ω approaches infinity when the turbulence kinetic energy k is set to zero. In order to avoid this issue, Wilcox (1988) implemented a hyperbolic variation $\omega_p=6\nu/(\beta_1 y_p^2)$ for the grid points near the wall.

This model has proved to be superior to the $k-\varepsilon$ model for the prediction of aerodynamic flows with attached boundary layers. However the model does not perform well for flows with boundary layer separation, as it is too sensitive to free stream values of k and ω (Menter 1992, 1994).

4.3.3 The Baseline BSL $k-\omega$ model

As previously stated, the $k-\varepsilon$ model has an advantage of being less sensitive to free-shear layer flow, but gives poor performance in the near-wall region for boundary layers under high adverse pressure gradients. On the other hand, the $k-\omega$ model over-predicts the set value of ω in the free stream, though gives acceptable values in the near-wall through the integration without using a wall damping function. In the latter case the result is dependent on the value of ω specified at the inlet and hence the variation of the result is undesirable and problematic. Menter (1994) resolved this issue by introducing a hybrid model which transforms the $k-\varepsilon$ to $k-\omega$ near the wall region. In this way a blending function F_1 is introduced which is multiplied by $\omega-$equations which achieved a smooth transition by another multiplication of the $\varepsilon-$equation by $1-F_1$. This function is equal to zero approaching the wall surface and gradually tend to one outside the boundary layer. Hence,

$$\frac{\partial(\bar{\rho}\omega)}{\partial t} + \frac{\partial}{\partial x_j}\left(\bar{\rho}\,\widetilde{U}_j\omega\right) = \frac{\partial}{\partial x_j}\left[\left(\mu + \frac{\mu_t}{\sigma_{\omega_3}}\right)\frac{\partial\omega}{\partial x_j}\right] + (1 - F_1)2\,\rho\,\frac{1}{\sigma_{\omega_2}\omega}\frac{\partial k}{\partial x_j}\frac{\partial\omega}{\partial x_j} + \alpha_3\frac{\omega}{k}P_k - \beta_3\,\rho\,\omega^2 + P_{\omega b} \qquad (4.23)$$

where ω_3, α_3 and β_3 are the linear combination of the corresponding coefficients as follows:

β_1	β_2	β'	σ_{ω_1}	σ_{ω_2}	α_1	α_2	σ_{k1}	σ_{k2}
0.075	0.083	0.09	2	1/0.856	0.44	0.44	2	1

Table 4. 2: Empirical constants values for the $k - \omega$ SST model recommended by Menter (1992) and Versteeg and Malalasekera (2007).

4.3.4 $k - \omega$ SST model

The performance of the BSL model is similar to the standard Wilcox $k - \omega$ model, but avoids the problem of the free stream sensitivity. Menter (1992) developed a new model, the so called Shear Stress Transport model, based on the model of Johnson and King (1985) who acknowledged the importance of the transport of the shear stress in the adverse pressure gradient. In contrast to the $k - \omega$ equation, the new $k - \omega$ shear stress transport model contains one more extra source term to transform the diffusion term in the ε −equation. Computing the eddy viscosity in the standard $k - \varepsilon$ regime in the free stream can potentially interfere with the result of the eddy viscosity in the $k - \omega$ regime near the wall. Numerical instabilities may arise from this, which can be avoided using the blending functions. This modifies the extra cross-diffusion term by using the constants C_1 for the $\omega -$ equations and C_2 for the ε −equation. So,

$$F_1 = F_1(l_t/y\,Re_y) \qquad (4.24)$$

where, $l_t = \sqrt{k}/\omega$, $Re_y = y^2\omega/v$ and y is the distance from the wall. The addition useful terms known as limiters set the eddy viscosity specifically in the adverse pressure gradient condition and limits the turbulent kinetic production to a value suitable at the stagnation points where the velocity is of the fluid is equal to zero. The equation is given in ANSYS manual (Fluent, 2009) as follows: Eddy viscosity limiter,

$$\mu_t = \frac{\alpha_1 k}{\max(\alpha_1\omega, SF_2)} \qquad (4.25)$$

where α_1 is a constant, $S = \sqrt{sS_{ij}S_{ij}}$ which is an invariant measure of the strain rate, $\mu_t = \rho v_t$ and F_2 is a blending function (Fluent, 2009). In addition, the turbulent kinetic energy production limiter can be evaluated as,

$$P_k = \min\left(10\,\beta'\rho k\omega, 2\mu_t S_{ij}.S_{ij} - \frac{2}{3}\,\rho k \frac{\partial U_i}{\partial x_j}\sigma_{ij}\right) \tag{4.26}$$

When considering model applicability, Hesp et al. (2015) has mentioned that the standard $k - \varepsilon$ turbulence model has several advantages over other turbulence models (in particular, the $k - \omega$ SST model, discussed in Sections 4.3.4). One major advantage is that, although the $k - \omega$ SST model is a combination of the $k - \varepsilon$ model (used primarily for high-Reynolds number modelling) and the $k - \omega$ model (for dealing with low-Reynolds number modelling), the difficulty of meeting the y^+ requirements in such large scales, as encountered frequently in geophysics applications, typically results in impaired simulation outcome. Therefore, Hesp et al. (2015) explicitly shows that the $k - \omega$ SST model in contrast with the standard $k - \varepsilon$ model does not satisfy the y^+ requirement during the study of dune validation, as the standard model captures flow separations more accurately.

4.3.5 Reynolds Stress Turbulence models

The earliest developments based on the Reynold's stress model (RSM) was by Rotta (1951) who proposed a closed version of the Reynolds stress transport equations. To pursue the work further, Launder et al. (1975) developed a model to compute the transport equations of Rotta (1951), namely the Reynolds stresses and turbulence energy dissipation rate ε. These models solve the Reynolds averaged Navier-Stokes equations. In the (RSM), the eddy viscosity hypothesis is not being used. In 3D, there are six components of Reynolds stresses which are solved directly and individually as an exact transport equation including the ε. Thus, the closure assumption does not apply to the Reynolds stresses. So, for the mean velocity the Reynolds averaged momentum equation are given by:

$$\frac{\partial(\bar{\rho}\tilde{U}_i)}{\partial t} + \frac{\partial}{\partial x_j}(\bar{\rho}\tilde{U}_i\tilde{U}_j) - \frac{\partial}{\partial x_j}\left[\mu\left(\frac{\partial\tilde{U}_i}{\partial x_j} + \frac{\partial\tilde{U}_j}{\partial x_i}\right)\right] = -\frac{\partial\bar{P}}{\partial x_i} - \frac{\partial}{\partial x_j}\left(\overline{\rho u'_i u'_j}\right) + S_{M_i} \tag{4.27}$$

In general, the transport equations for the Reynolds stresses is of the form:

$$\underbrace{\frac{D\overline{u'_i u'_j}}{Dt}}_{\text{The rate of change of Reynolds stresses}} = \underbrace{P_{ij}}_{\text{Production}} + \underbrace{D_{ij}}_{\text{Diffusion}} - \underbrace{\varepsilon_{ij}}_{\text{Dissipation}} + \underbrace{\Pi_{ij}}_{\text{Strain}} + \underbrace{\Omega_{ij}}_{\text{Rotation}} \qquad (4.28)$$

There are two forms of Reynolds stress models, algebraic and differential (Blazek, 2005). The differential form of the Reynolds stress model is given by:

$$\frac{\partial \bar{\rho}\overline{u'_i u'_j}}{\partial t} + \frac{\partial}{\partial x_k}\left(\tilde{U}_k \bar{\rho}\overline{u'_i u'_j}\right) - \frac{\partial}{\partial x_k}\left(\left(\delta_{kl} + \bar{\rho}C_s \frac{k}{\varepsilon}\,\overline{u'_k u'_l}\right)\frac{\partial \overline{u'_i u'_j}}{\partial x_l}\right) =$$

$$P_{ij} - \frac{2}{3}\delta_{ij}\bar{\rho}\varepsilon + \Phi_{ij} + P_{ij,b} \qquad (4.29)$$

where Φ_{ij} is the pressure-strain correlation and C_s is a constant (Bertolotto et al., 2009). Now, based on the ε −equation, the transport equation for the Reynolds stresses are as follows:

$$\frac{\partial \bar{\rho}\,\overline{u_i u_j}}{\partial t} + \frac{\partial}{\partial x_k}\left(\tilde{U}_k \bar{\rho}\,\overline{u_i u_j}\right) - \frac{\partial}{\partial x_k}\left(\left(\mu + \frac{2}{3}C_s \bar{\rho}\frac{k^2}{\varepsilon}\right)\frac{\partial \overline{u_i u_j}}{\partial x_k}\right) \qquad (4.30)$$

$$= P_{ij} - \frac{2}{3}\delta_{ij}\bar{\rho}\varepsilon + \Phi_{ij} + P_{ij,b}$$

The tensorial production terms due to shear P_{ij} and buoyancy $P_{ij,b}$ have exact equations as follows:

$$P_{ij} = -\bar{\rho}\,\overline{u_i u_k}\frac{\partial \tilde{U}_j}{\partial x_k} - \bar{\rho}\,\overline{u_j u_k}\frac{\partial \tilde{U}_i}{\partial x_k} \qquad (4.31)$$

$$P_{ij,b} = \overline{\rho g_i u_j} + \overline{\rho g_j u_i} \qquad (4.32)$$

The isotropy condition of the turbulence is dependent on the pressure-strain correlation, Φ_{ij}, Blazek (2005). The effects of this correlation is due to the interaction of the eddies with each other and the domain under varying mean velocity gradient. The pressure-strain terms are evaluated as,

$$\Phi_{ij} = \underbrace{\Phi_{ij,1}}_{\text{return}-\text{to}-\text{isotropy}} + \underbrace{\Phi_{ij,2}}_{\text{rapid}} \tag{4.33}$$

There are three ε −based Reynolds stress models, including LRR-IP, LRR-QI and SSG. In the LRR-IP and LRR-QI the pressure-strain correlation is linear whereas the SSG is quadratic (Bou-Zeid et al., 2005, John, 2012).

The ω −equation can be inserted into the original Reynolds stress model to formulate a new omega-based Reynolds stress model or SMC_ω model Blazek (2005). This allows the ω −equation capability to integrate to the wall. The equations for this model can be written as follows,

$$\frac{\partial \rho \omega}{\partial t} + \frac{\partial}{\partial x_k}(\tilde{U}_k \rho \omega) = \alpha \, \rho \, \frac{\omega}{k} \, P_k + P_{wb} - \beta \rho \omega^2 + \frac{\partial}{\partial x_k}\left(\left(\mu + \frac{\mu_t}{\sigma}\right)\frac{\partial \omega}{\partial x_k}\right) \tag{4.34}$$

The BSL Reynolds stress model incorporate the blend in function to transform the coefficients from the ε −based model constants (SMC_ε zone) to the ω −based model constants (SMC_ω zone) near the wall. The stated equation is given by,

$$\frac{\partial \rho \omega}{\partial t} + \frac{\partial}{\partial x_k}(U_k \rho \omega) \tag{4.35}$$

$$= \alpha \, \rho \, \frac{\omega}{k} \, P_k + P_{wb} - \beta \rho \omega^2 + \frac{\partial}{\partial x_k}\left(\left(\mu + \frac{\mu_t}{\sigma}\right)\frac{\partial \omega}{\partial x_k}\right)$$

$$+ (1 - F_1) 2 \, \rho \, \frac{1}{\sigma_2 \omega} \frac{\partial k}{\partial x_k} \frac{\partial \omega}{\partial x_k}$$

4.3.6 Comparisons of Reynolds Stress Components in 2D RANS

As already stated, $k - \varepsilon$ and $k - \omega$ models both use the eddy viscosity hypothesis, which gives the following formula for the Reynolds stresses for incompressible flow:

$$\overline{u'_i u'_j} = \frac{2}{3} k \, \delta_{ij} - \nu_t \left(\frac{\partial \overline{u_i}}{\partial x_i} + \frac{\partial \overline{u_i}}{\partial x_i} \right) \tag{4.36}$$

Where $\nu_t (= \mu_t / \rho)$ is the turbulent kinematic eddy viscosity. Now, in 2D RANS, the 2D assumptions are as follows:

$$\frac{\partial \overline{u}}{\partial z} = \frac{\partial \overline{v}}{\partial z} = \frac{\partial \overline{w}}{\partial z} = 0 \tag{4.37}$$

Putting these into equation (4.36) gives:

$$\overline{u'^2} = \frac{2}{3} k - 2 \nu_t \frac{\partial \overline{u}}{\partial x} \tag{4.38}$$

$$\overline{v'^2} = \frac{2}{3} k - 2 \nu_t \frac{\partial \overline{v}}{\partial y} \tag{4.39}$$

$$\overline{w'^2} = \frac{2}{3} k \tag{4.40}$$

It should be noted that $\overline{w'^2} \neq 0$ and 2D mean flow, there are still 3D fluctuations. Now, if $\left(\overline{u'^2}, \overline{v'^2} \right)$ are both measured experimentally, it is possible to deduce k by adding equations (4.38) and (4.39), as follows:

For incompressible flow, $\frac{\partial \overline{u}}{\partial x} + \frac{\partial \overline{v}}{\partial y} = 0$ and this gives,

$$k = \frac{3}{4} \left(\overline{u'^2} + \overline{v'^2} \right) \tag{4.41}$$

Hence, in equation (4.41) the value of the turbulent kinetic energy k can be compared with the prediction results for the $k - \varepsilon$ and $k - \omega$ models. In addition, if only the $\overline{u'^2}$ measurements are available, then equation (4.38) is used to deduce $\overline{u'^2}$ from $k - \varepsilon$ and $k - \omega$ predictions. Although, if a Reynolds stress model is used then $\left(\overline{u'^2}, \overline{v'^2}, \overline{w'^2} \right)$ are computed automatically and thus, in contrast, the values are less difficult to obtain.

4.3.7 Wall treatment

4.3.7.1 Near-wall treatments.

In order to be able to capture important viscous effects near the wall, the value of y^+ which is a non-dimensional wall variable must be in a certain range near the wall boundary depending on the chosen turbulence model. As stated by Wilcox (2006), the dimensionless wall unit is given by,

$$y^+ = \frac{\rho u_\tau}{\mu} y \tag{4.42}$$

where:

$$\tau_w = \left(\mu \frac{\partial \bar{u}}{\partial y} \right)_w \tag{4.43}$$

$$u_\tau = \sqrt{\frac{\tau_w}{\rho}} \tag{4.44}$$

$$u^+ = \frac{\bar{u}}{\bar{u}_\tau} \tag{4.45}$$

and where τ_w is the shear stress, $\bar{u}_\tau$ is the shear velocity and u^+ is the non-dimesionalised form of the streamwise velocity relative to the shear velocity. In treating the wall for the inclusion of bed roughness within the domain, the law-of-the-wall and the body-fitted approaches appear to be appropriate. The latter method has been adapted successfully in previous studies of single-phase flows (Zanoun et al., 2003). This method changes the mesh to include the roughness on the bed geometry. In contrast, the other approach is the so-called law-of-the-wall allows the inclusion of grain roughness height h_s. It is important to note that this method can be used with a body-fitted approach to develop a composite roughness which includes sand grains and the form roughness on the wall.

In commercial CFD software, the roughness is included by inserting a roughness height which is suitable for the task. Figure 4.4 shows a schematic of the velocity profile which is common in most of the flows which divides into the inner and outer region. The inner region is split into the laminar sub-layer (the viscous sub-layer), buffer layer and the logarithmic layer and the Reynolds stresses near the wall are zero for a no slip wall condition.

In the inner region of the boundary layer, in the viscous sub layer the viscous stresses dominate over the turbulent stresses. Away from the wall towards the outer region, the turbulent stresses dominate. This transition in the Reynolds stresses occurs in the buffer layer, hence it is important to accurately account for both the viscous and turbulent stresses. In the viscous sub-layer region $u^+ = y^+$, and in the logarithmic layer, the u^+ expression is written as follows:
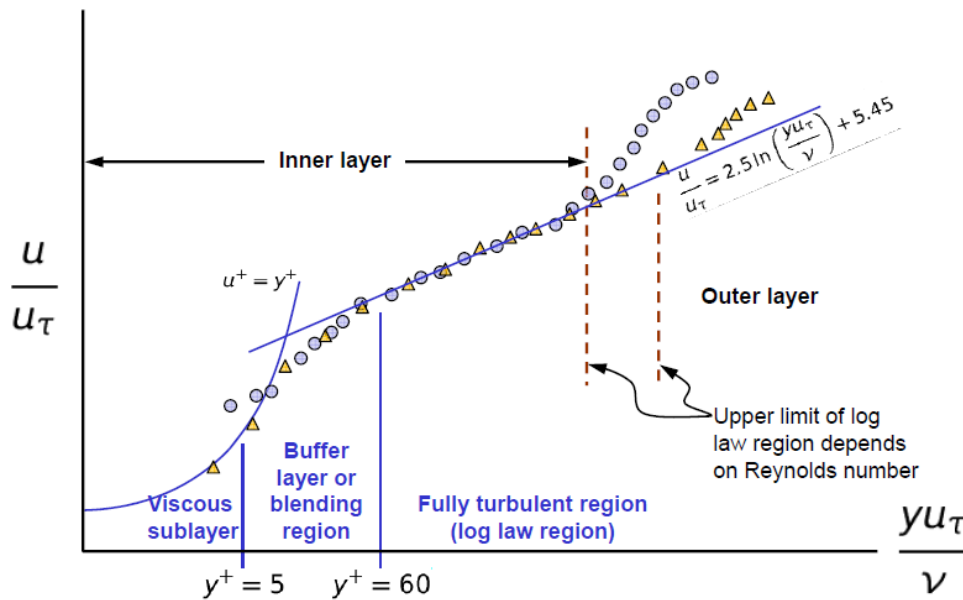
Figure 4.4: Schematic of the universal law of the wall (Wilcox, 2006).

$$u^+ = \frac{1}{\kappa} \ln E y^+ \qquad (4.46)$$

The value of the constant $E = 9.7393$ and Kármán constant $\kappa \approx 0.41$ (Fluent, 2009). In the buffer layer, u^+ switches from the laminar sub-layer to the logarithmic expression, as it approaches the logarithmic layer. In the outer region, the inertial forces dominate and the law-of-the-wall is employed as follows:

$$\frac{\bar{u}}{u_\tau} = \frac{1}{\kappa} \ln \frac{\rho u_\tau}{\mu} y + C_\rho \qquad (4.47)$$

where $\bar{u}$ is the average velocity in the x −direction, $C_p \approx 5$ is a constant, and y is the distance in the y-direction. The values of κ and the integration constant are measured from the correlation of the experimental data over a wide variety of incompressible boundary layer flows in laboratories (Junge and Westerhellweg, 2011, Fluent, 2009, Kline et al., 1969). In the case of rough boundaries, this is given by the addition of the velocity shift due to the bed roughness as follows:

$$\frac{\bar{u}}{u_\tau} = \frac{1}{\kappa} \ln \frac{u_\tau}{\nu} y + B - \Delta B \qquad (4.48)$$

where ΔB is the velocity shift as a result of accounting for the wall roughness, $B = 5.2$ and is a function of the roughness Reynolds number (a function of the dimensionless roughness height) $\Delta B = f(h_s^+)$ (Fluent, 2009). In the case of sand grain roughness, this downshifting is expressed as follows:

$$\Delta B = \frac{1}{\kappa} \ln(1 + 0.3\, h_s^+) \qquad (4.49)$$

In turbulence modelling, it is important to treat the sub-laminar layer as the viscous effects become important. In order to resolve this thin near wall layer, low Reynolds number methods are the most reliable. However, a high mesh resolution is required to solve such models and thus an excessive CPU time is required, particularly in three-dimensional flows. Hence, one common industrial solution is to avoid resolving the viscous layer by adopting a bridge in the near wall region, the so called wall function.

A conventional method of using the wall function is the standard wall function which is valid only in the range $30 < y^+ < 300$. This method positions the first grid point, $y_p^+ \approx 11.225$, at the edge of the log-layer y_p^+ and uses semi-empirical formulae. Hence, if the grid is refined below $y_p^+ \approx 15$, the solver will account for the nodes below this value and therefore this results in a convergence error. In contrast, in the low-Re scheme, this point is positioned at the wall ($y_p^+ = 0$). Thus, alternative expressions for u^+ and y^+ can be evaluated as follows:

$$u^* \equiv \frac{u_p C_\mu^{1/4} K_p^{1/2}}{\tau_w \rho} \qquad (4.50)$$

$$y^* \equiv \frac{u_p C_\mu^{1/4} K_p^{1/2} y_p}{\mu} \qquad (4.51)$$

where u_p is the mean velocity, $C_\mu = 0.09$ and K_p is the turbulent kinetic energy at node p. Scalable wall functions prevent inconsistency in the solution convergence of the out of range grids by setting a limiter in the y^* calculation. This will ignore the nodes below the range and insert a domain boundary at y_p^+. Therefore, y^* for the standard wall function can be replaced by $\tilde{y}^*$ which consists of a limiter as follows:

$$\tilde{y}^* = \max(y^*, y_{limit}^*) \qquad (4.52)$$

where $y_{limit}^* = 11.225$. The scalable wall function is used in conjunction with $\varepsilon -$based models such as the $k - \varepsilon$ model, and the LRR and SSG Reynolds stress models. In contrast, $\omega -$based models such as the $k - \omega$ model and the BSL Reynolds stress model use an automatic near-wall treatment, which switches from wall functions in the coarser mesh region to low-Re near wall formulation where the mesh is fine. The automatic wall treatment in ANSYS CFX is explained in detail by Blazek (2005).

4.4 Large Eddy Simulation (LES)

In LES models, the turbulent flows are defined by decomposing the eddies into large and small length scales. Turbulent flows are highly unsteady and need to be resolved in terms of length and times scales in three-dimensional computations. In developing such models, Kolmogorov's theory of self-similarity has been implemented which states that at a sufficiently high Reynolds number the small eddies are isotropic and have a universal behaviour.

In 1963, Smagorinsky (1963) focused on the energy cascade of the mean flow. He proposed that the anisotropic larger eddies are the ones that characterize the length of the main flow while the isotropic small eddies can be modelled. The large eddies have low-frequency modes in space and hence these can be directly computed. These transport most of the mass, momentum and energy in the mean flow. Resolution of the smaller eddies is not as important as the larger ones which are geometry and boundary condition dependent. However, smaller eddies are responsible for the dissipation of turbulence energy to heat, hence they still need to be modelled.

The size of the eddies which can be resolved are proportional to the size of the mesh. In other words, if the size of an eddy is smaller than the size of the mesh, then it is not being resolved. Nevertheless, this is limited to the available computational resources and the domain complexity.
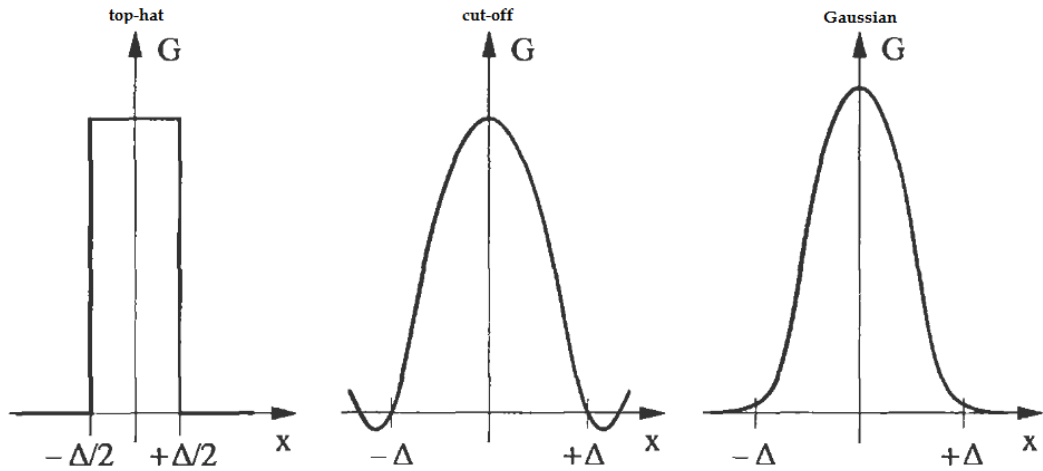
Figure 4.1: The common filter functions in LES (Blazek, 2005).

A border line can be defined as l_{EI}, which separates the regions of large scale anisotropic eddies from the small scale isotropic eddies. In most of the flows high Reynolds numbers, this length scale has been estimated as $l_{EI} \approx l_0/6$, where $l_{aniso} > l_{EI}$, $l_{iso} < l_{EI}$ and l_0 is the turbulent length predicted by RANS model. In order, to separate these eddies, a spatial filtering technique is used which replaces the conventional time-averaging method. Thus, a cut-off width is specified to distinguish the large scale from the small scale eddies. In order to take account of the small eddies behaviour, an SGS (sub-grid scale) model can be introduced. This adds the SGS stresses of the small eddies to the normal stresses of the spatial filtered eddies when solving the flow equation over several control volumes in the computational domain. Therefore a spatial filtering operation can be evaluated as Versteeg and Malalasekera (2007) using a filter function as follows:

$$\bar{\Phi}(\mathbf{x}, t) = \int_{-\infty}^{\infty} \int_{-\infty}^{\infty} \int_{-\infty}^{\infty} G(\mathbf{x}, \mathbf{x}', \Delta) \Phi(\mathbf{x}', t) dx_1' dx_2' dx_3' \tag{4.53}$$

where, $G(\mathbf{x}, \mathbf{x}', \Delta)$ is the spatial filter and Δ is the filter cut-off width. The common examples of filter function in LES models are Top hat filter, Gaussian filter and

spectral cut-off filter, as shown in figure 4.1. In the finite volume method, the Top hat or box filtering is used. So, the filtered LES continuity equation is given by,

$$\frac{\partial \rho}{\partial t} + \nabla.(\rho \bar{\mathbf{u}}) = 0 \tag{4.54}$$

The filtered convective term can be expanded as follows:

$$\nabla.(\rho \overline{\phi \mathbf{u}}) = \nabla.(\bar{\phi} \bar{\mathbf{u}}) + \left(\nabla.\left(\rho \frac{\bar{\phi}}{\mathbf{u}} \right) - \nabla.(\bar{\phi} \bar{\mathbf{u}}) \right) \tag{4.55}$$

So, analogous to the RANS, the LES filtered moment equations can be written as follows:

$$\frac{\partial(\rho \bar{u})}{\partial t} + \nabla.(\rho \bar{u} \bar{\mathbf{u}}) = -\frac{\partial \bar{p}}{\partial x} + \mu \nabla.\left(\nabla(\bar{u}) \right) - \nabla.\left(\rho \overline{u\mathbf{u}} - \nabla.(\rho \bar{u} \bar{\mathbf{u}}) \right) \tag{4.56}$$

$$\frac{\partial(\rho \bar{v})}{\partial t} + \nabla.(\rho \bar{v} \bar{\mathbf{u}}) = -\frac{\partial \bar{p}}{\partial x} + \mu \nabla.\left(\nabla(\bar{v}) \right) - \nabla.\left(\rho \overline{v\mathbf{u}} - \nabla.(\rho \bar{v} \bar{\mathbf{u}}) \right) \tag{4.57}$$

$$\frac{\partial(\rho \bar{w})}{\partial t} + \nabla.(\rho \bar{w} \bar{\mathbf{u}}) = -\frac{\partial \bar{p}}{\partial x} + \mu \nabla.\left(\nabla(\bar{w}) \right) - \nabla.\left(\rho \overline{w\mathbf{u}} - \nabla.(\rho \bar{w} \bar{\mathbf{u}}) \right) \tag{4.58}$$

The last term of equations (4.56)-(4.58) is given by,

$$\nabla.(\rho \overline{u_\iota \mathbf{u}} - \rho \bar{u}_\iota \bar{\mathbf{u}}) = \frac{\partial \tau_{ij}}{\partial x_j} \tag{4.59}$$

Hence, the LES stresses can be written as follows:

$$\tau_{ij} = \rho \overline{u_\iota \mathbf{u}} - \rho \bar{u}_\iota \bar{\mathbf{u}} = \rho \overline{u_\iota u_j} - \rho \bar{u}_\iota \bar{u}_j \tag{4.60}$$

Now, decomposing $\rho \overline{u_\iota u_j}$ gives the final sub-grid-scale stresses as follows:

$$\tau_{ij} = \rho \overline{u_\iota u_j} - \rho \bar{u}_\iota \bar{u}_j = \underbrace{\left(\rho \overline{\bar{u}_\iota \bar{u}_j} - \rho \bar{u}_\iota \bar{u}_j \right)}_{Leonard\ stresses} + \underbrace{\left(\rho \overline{\bar{u}_\iota u_j'} + \rho \overline{u_\iota' \bar{u}_j} \right)}_{cross-stresses} + \underbrace{\left(\rho \overline{u_\iota' u_j'} \right)}_{LES\ stresses} \tag{4.61}$$

Leonard stresses (L_{ij}), correspond to the interaction between the large scale eddies. The cross-stresses (C_{ij}), are for the interaction between the large and small scale eddies. In addition, the interaction between the SGS eddies is considered by the term LES Reynolds stresses (R_{ij}).

4.4.1 Smagorinsky-Lilly SGS model

As stated in the previous sections, the small turbulent eddies tend to be almost isotropic at certain range of Reynolds number. Smagorinsky (1963) considered this behaviour and suggested that the Boussinesq hypothesis may be used to describe the effects of the smaller eddies. The Smagorinsky-Lilly SGS model is based on Prandtl's mixing length model which is one of the earliest developed turbulence models. The Prandtl's mixing model is evaluated as follows:

$$\mu_t = \rho C_\mu L_s^2 \left(2\bar{S}_{ij}\bar{S}_{ij}\right)^{1/2} \tag{4.62}$$

where,

$$L_s = \min(k, C_s\Delta) \tag{4.63}$$

where Δ is the filter cut-off width which is computed as $\Delta = \sqrt[3]{V}$, and C_s is the Lilly-Smagorinsky constant. Lilly (1967) analytically derived C_s to a value in the range 0.17 and 0.21, by analysing the three-dimensional homogeneous isotropic turbulence in the inertial sub-range of the energy spectrum. The value of this constant is still not universal and under much discussion. (Deardorff, 1970) suggested that this value is too large in the case of LES study of turbulent channel flow, causing motions to damp, leading to excessive mean shear in the sub-grid scales. Hence, he suggested that a value of C_s = 0.1 gives the best result and avoids the turbulent motions becoming excessively large.

4.4.2 Dynamic Smagorinsky-Lilly model

As already stated, the value of C_s must be adjusted case-by-case to give an optimum result. Thus, this procedure requires many simulations runs and is computationally expensive. Germano et al. (1991) proposed a method in which the local value of C_s can be dynamically computed using the resolved structure properties of the flow field. The Dynamic Smagorinsky-Lilly model (DSGS model), requires different forms of turbulent stresses to calculate C_s per time-step by two different filtering operation with cut-off widths of Δ and $\widehat{\Delta}$. The cut-off width Δ or the test filter is twice the $\widehat{\Delta}$ or the original filter width. Hence, difference of the SGS stresses of the two resolved fields is therefore given by,

$$T_{ij} = \overline{\rho \widehat{u_i} \widehat{u_j}} - \overline{\rho \widehat{u_i} \rho \widehat{u_j} \widehat{\rho}} = -2C\bar{\rho}\widehat{\Delta}^2 \left|\widehat{\bar{S}}\right| \left(\widehat{\bar{S}}_{ij} - \frac{1}{3}\widehat{\bar{S}}_{kk}\delta_{ij}\right) \tag{4.64}$$

$$\tau_{ij} = -2C\bar{\rho}\Delta^2 |\bar{S}| \left(\bar{S}_{ij} - \frac{1}{3}\bar{S}_{kk}\delta_{ij}\right)$$

where, $C = C_s^2$ and this is assumed to be the same for both of the filtering operation. Hence,

$$L_{ij} = T_{ij} - \hat{\tau}_{ij} = \bar{\rho}\widehat{\bar{u}_i}\bar{u}_j - \frac{1}{\widehat{\bar{\rho}}}\left(\widehat{\bar{\rho}\bar{u}_i}\ \widehat{\bar{\rho}\bar{u}_j}\right) \tag{4.65}$$

and using the least-squares method of Lilly (1992) the constant C can be evaluated as follows (Sagaut, 2013):

$$CM_{ij} = L_{ij} - \frac{1}{3}L_{kk}\delta_{ij} \tag{4.66}$$

where,

$$M_{ij} = -2\left(\widehat{\Delta}^2\widehat{\bar{\rho}}\left|\widehat{\bar{S}}\right|\widehat{\bar{S}}_{ij} - \Delta^2\bar{\rho}\left|\widehat{\bar{S}}\right|\bar{S}_{ij}\right) \tag{4.67}$$

In addition, numerical instability can be avoided by an averaging procedure based upon $\widehat{\Delta}$, as follows:

$$C = \frac{\langle L_{ij} M_{ij} \rangle}{\langle M_{ij} M_{ij} \rangle} \tag{4.68}$$

It is important to note that there is an excessively high resolution requirement for the above two models in order to resolve the wall boundary layer. Hence it can only be applied to simple geometries and it is not recommended for the complex geometries where the boundary layer flow is important. Alternatively, a Dynamic Global coefficient Eddy-Viscosity model was developed by You and Moin (2007) that requires only a single test filter. This is more suitable for complex geometries since it avoids the necessity of the second filter as in the previous proposed models. The other industry suited model which avoids the grid resolution near the wall is the algebraic Wall-Modelled LES (WMLES). This model uses RANS in the logarithmic part of the boundary layer and then switches to the LES to resolve the eddies larger than the filter width. In contrast to the standard Smagorinsky model, which are limited only to low Reynolds number flows and analogues to normal RANS behaviour near the wall, the WMLES model is Reynolds number independent.

4.5 Direct Numerical Simulation (DNS)

A direct numerical simulation method solves the full Continuity and Navier-Stokes equations of an unsteady flow in 3D. This method is useful for understanding the properties and structure of turbulent flow in situations where it is impossible to measure these quantities using an experimental method. The spatial and temporal scale of the turbulence increase with the increasing Reynolds number and subsequently induce smaller and smaller eddies. Hence, this method can only be used for low Reynolds numbers to avoid excessively high usage of CPU time and memory (RAM). Consequently, this method is currently only appropriate for research purposes and is not feasible for industrial applications (Moin and Mahesh, 1998). For example, in the case of a channel the channel height must be sufficient so that larger eddies are also captured within the domain. In addition, the mesh has to be sufficiently fine to resolve the smallest scale eddies in order of $\eta = (\nu^3/\varepsilon)^{1/4}$. The number of time-steps increases with increasing Reynolds number and has to be of the same order as the Kolmogorove time scale, $\eta = \tau = (\nu/\varepsilon)^{1/2}$. As figure 4.2 shows,

the energy scale is divided into three ranges of energy containing range, inertial sub-range and dissipation range (Kolmogorov length scale). Thus, assuming that $e_\tau = \frac{u_\tau H/2}{\nu}$, the total number of grid points for uniform spacing and the time-step in the computation are $N_{uniform} \approx (3\ Re_\tau)^{9/4}$ and $\Delta t \approx \frac{0.003}{\sqrt{Re_\tau H/u_{tau}}}$, respectively (Junge and Westerhellweg, 2011, Moser Jr, 1984, Kim et al., 1987).The spatial discretisation of the DNS simulation can be performed using spectral, spectral element and higher-order finite difference methods. The spectral method can only be performed in simple domains, and has been reported to give good convergence performance in the case of the channels with roughness elements (Orszag and Patterson Jr, 1972). A modified version is the spectral element method, which is a combination of finite element and spectral methods. The more updated version of the DNS methods which was performed by Patera (1984) is the higher-order finite difference methods which is applicable to more complex geometries.
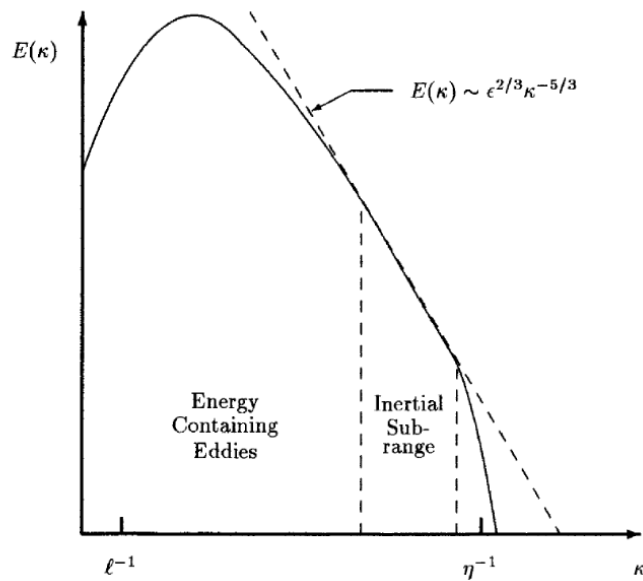
Figure 4.2: Energy spectrum for a turbulent flow on a log-log scale (Wilcox, 2006).

4.6 Conclusions

Accurate computational fluid dynamics simulations are essential for a wide variety of turbulent flows including sediment dispersion and deposition. The purpose of this chapter was to understand the capability of turbulence models in predicting the turbulence characteristic of flow for turbidity currents. For the Reynolds Averaged Navier-Stokes (RANS) method, the $k - \omega$ SST model appears to be the most efficient modelling approach for the purpose of this project, as it uses automatic wall function to resolve the flow both in the free stream and viscous sub-layer. Predicting the evolution of turbulent sedimentary flows using a Large-eddy simulation method is of great interest as it directly resolves the large eddies and this gives a detailed understanding of the turbulence structure with its capacity to carry sediments. However, its computational expense prohibits its use as a tool for wide-ranging parametric studies. Thus, in the next chapter the goal will be to choose the most computationally efficient modelling approach to enable the detailed study and analysis of turbulent flows over rough beds.

Chapter 5
Optimised mixing and flow resistance during shear flow over a rib roughened boundary

This chapter is concerned with properties of various roughness types and the effect of such roughness on the turbulence characteristics relative to a smooth wall. The work has implications for geophysical flows over rough beds, and for engineering applications. In both cases, we are interested in determining an optimum arrangement of roughness elements to maximise the amount of turbulent mixing in the flow. For geophysical flows, this is expected to contribute to the ability of the flow to keep particles in suspension, and hence potentially increase run out lengths of turbidity currents. Previous studies suggested similarity between the flow structure of turbidity currents from the velocity maximum to the lower surface and single-phase shear flow from the boundary layer thickness to the bed. For engineering flows, this is expected to contribute to the design of rib-roughened channels which optimise the rates of heat transfer due to turbulent convection. In summary, the aims of this research are to better constrain optimum conditions for turbulent mixing, and to assess lower boundary roughness effects on turbidity current turbulence generation, flow depletion and run-out.

Two-dimensional models will be employed to study the turbulence intensities and velocity components of the flow through a rib-roughened straight channel. Previously published numerical and experimental data will be used to validate the existing numerical methodologies and to choose the most computationally efficient modelling approach to achieve our objectives.

In the present study, we employ a variety of RANS turbulence models to simulate turbulent flow in a two-dimensional channel with an asymmetric two-dimensional rough lower boundary for a wide range of Reynolds numbers and width-to-height ratios w/h, where h is the height of the roughness elements, and the width w is the distance between roughness elements, as discussed in section 3.3. In this chapter, we attempt to accurately constrain the critical w/h ratio for an optimum turbulence enhancement, mixing and resistance to the flow. For this purpose, we evaluate the dependence of eddy viscosity and friction factor on Reynolds number for a series of w/h values.

5.1 Numerical method

This section describes and provides a literature review of the numerical methodology used to capture the structure of flow over surface roughness. Suitability of various turbulence models is discussed in predicting the characteristics of the flow near the bed and in the outer flow region in a confined channel with a lower rough boundary.

5.1.1 Turbulence modelling

Steady state CFD simulations have been performed using the commercial code, ANSYS CFX 14.0. This code uses a finite volume method to solve the Reynolds time averaged Navier–Stokes equations by a coupled velocity-pressure solver. Furthermore, the fluid is assumed to be incompressible and Newtonian. Numerous turbulence models were employed for comparisons against experimental and numerical results in the literature. The Shear Stress Transport (SST) turbulence model was initially identified as the model of choice, motivated by the work of Milnes et al. (2012) on deep cavities. This model uses "Automatic Near Wall Treatment", which switches between the low-Re formulation and wall function depending on the resolution of the mesh near the wall (ANSYS, 2009, Menter et al., 2003, Esch and Menter, 2003). Other turbulence modelling choices included the standard $K - \varepsilon$ model, the $\varepsilon -$ based Reynolds stress models due to Launder, Reece and Rodi (LRR) and Sarkar, Speziale and Gatski (SSG), and the $\omega -$ based BSL Reynolds stress turbulence model. The $\varepsilon -$ based models used a scalable wall function to avoid problems in resolving grid points in the viscous layer (ANSYS, 2009). These models have been used extensively, and have been shown to be reliable in terms of robustness and accuracy (Menter et al., 2003, Menter, 1994). The Reynolds stress models are not based on the eddy viscosity hypothesis but instead directly solve the transport equation for the individual stress components per time step. The BSL and LRR Reynolds stress models use a linear pressure–strain correlation whilst SSG uses a quadratic relation (ANSYS, 2009, Speziale et al., 1991, Hanjalic and Launder, 1972).

In total, 28 geometries with varying width to roughness height ratio have been meshed using the Hexa mesh method as employed in ANSYS ICEM. The geometry and mesh are illustrated in figure 5.1 for $w/h = 9$. Preliminary mesh independence studies were carried out in order to verify that the solutions were grid independent. The first wall node was positioned at $y^+ \approx 1$ for the SST model and at least 15 further nodes were placed inside the boundary layer in order to resolve the viscous layer.

The variable y^+ is the dimensionless distance which is based on the height of the first node from the wall and wall shear stress (yu_τ/ν). For models that use the scalable wall function, at least 10 nodes were placed in the boundary layer in the direction normal to the wall to achieve $y^+ \approx 11$. A non-dimensional residual target of 1×10^{-06} was chosen, as the convergence criterion for all the quantities and simulations.
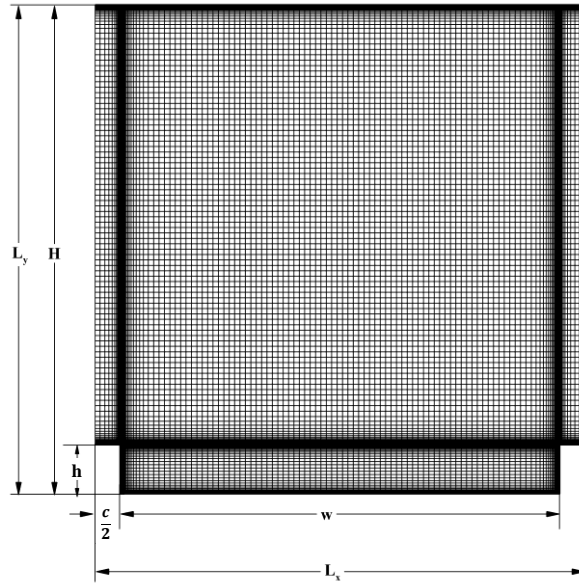
Figure 5. 1: Computational domain and hexahedral grid system of the channel flow with surface roughness showing the parameters for $w/h = 9$.

5.2 Flow configuration

Figure 5.1 shows the computational domain with its co-ordinate system and the roughness element shape. The domain size is $(L_x, L_y) = (w + c, H)$. The roughness element is in a non-staggered, two-dimensional transverse square arrangement, with a cross section $h \times h$, positioned on the lower boundary. Periodic boundary conditions are used in the streamwise direction and a symmetry condition is applied in the spanwise direction. A no-slip boundary condition was applied to the upper and lower walls. A mean pressure gradient is imposed as a source term in the U −momentum equation. The Reynolds number is determined based on the shear velocity u_τ and the half-channel height, $\mathrm{Re}_\tau = (H/2)\, u_\tau/\nu$. The width-to-height ratio w/h was varied from 0.12 to 402 (0.12, 0.27, 0.51, 0.75, 1, 2, 3, 4, 5, 6, 7, 8, 9, 10, 11, 12, 18, 24, 30, 42, 54, 63, 75, 87, 96, 204, 300, 402). Turbulent flow over surface roughness can experience either a hydraulically smooth wall regime, a transitional-roughness regime, or a fully rough flow regime depending on the value of h^+

(hydraulically smooth wall: $0 \lesssim h^+ \lesssim 5$, transitional-roughness regime: $5 \lesssim h^+ \lesssim 70$ and fully rough flow: $h^+ \gtrsim 70$). For the original simulations reported here, the roughness element height is $0.05 \, H$, where H is the channel height, and the dimensionless roughness height, and the dimensionless roughness height are in the range of the fully rough regime, $h^+ \geq 70$. The simulations have been performed for 28 domains for values of dp/dx equal to 1×10^{-4}, 5×10^{-4}, 1×10^{-3}, 2×10^{-3}, 3×10^{-3}, 4×10^{-3} and $5 \times 10^{-3} \, \mathrm{kgm^{-2}s^{-2}}$.

5.3 Validation

In order to validate the solution, the experimental results of Okamoto et al. (1993), Djenidi et al. (1999) and the LES computations of Cui et al. (2003) are compared to the present data. In this work, the computational geometry is set to match that of Cui et al. (2003), i.e., $0.1 \, H$. The mean pressure gradient, dp/dx is varied to obtain the Reynolds number, Re_b close to the experimental and LES data.

The Figure 5.2(a)–(d) shows the streamwise velocity profiles normalised by the maximum streamwise velocity obtained from the turbulence model solutions for w/h = 1, 4, 8, 9. The velocity profiles are displayed with a line located at the centre of the channel in the cavity from the upper to the lower wall boundaries. Overall for all the turbulence models, the velocity profiles overall show a reasonable agreement with the previous numerical and experimental data. The $K - \varepsilon$ model shows the best agreement compared to the available data. To further support this validation, the present $K - \varepsilon$ model has been compared to the experimental data for w/h = 8 and w/h = 9, respectively in Figure 5.2 (c) and (d).

The normalised streamwise turbulence intensity U_{rms} at the centre of the cavity is also compared for $w/h = 1, 4$ with previous experimental and numerical data in Fig 5.2. The streamwise turbulence intensity U_{rms} is defined by $\left(\sqrt{\overline{u_i' u_j'}} \right)$, which is the root mean square of the Reynolds stress uu, $R_{ij} = -\rho \overline{u_i' u_j'}$, normalised by the maximum velocity, U_{max}. The normalised turbulence intensity results are more sensitive and show discrepancies. As illustrated by Fig 5.2(e)–(f), RANS models shows poor prediction of the turbulence intensities for both w/h = 1 and w/h = 4. On the other hand, the discrepancies for the standard $K - \varepsilon$ model appear to be less severe than those of the other RANS models.
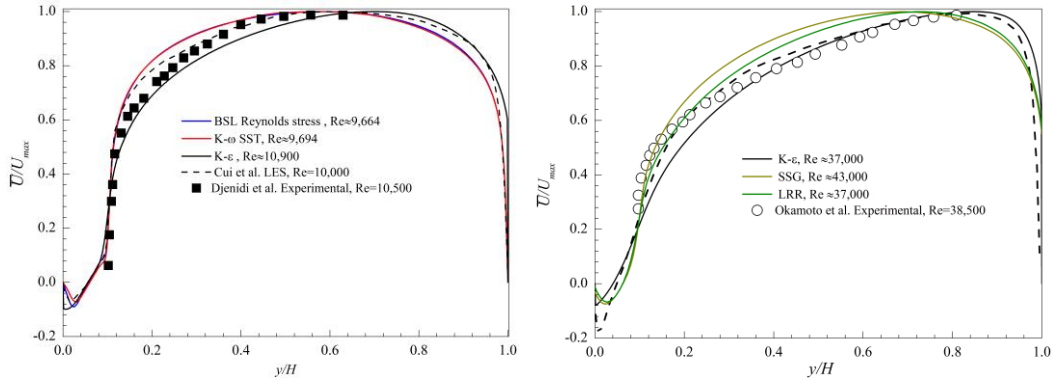
(a) $w/h = 1$

(b) $w/h = 4$
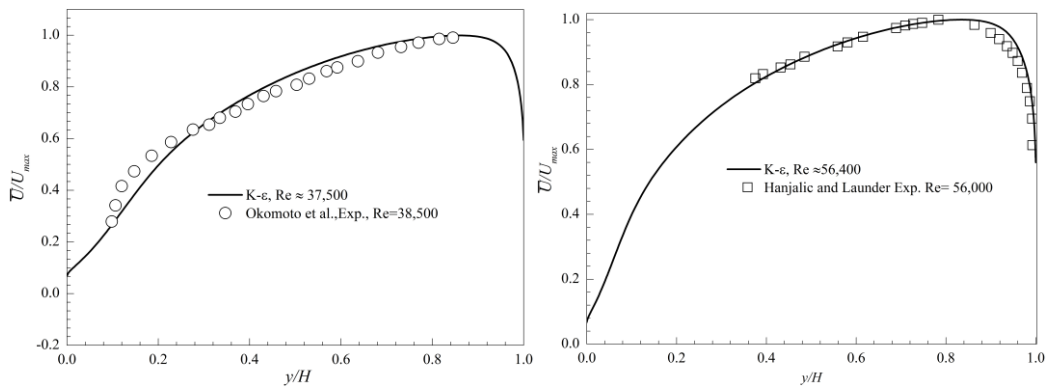
(c) $w/h = 8$

(d) $w/h = 9$
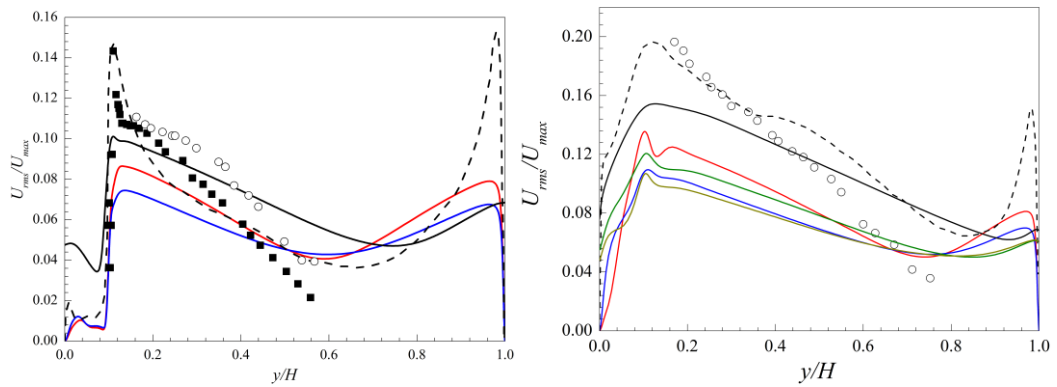
(e) $w/h = 1$

(f) $w/h = 4$

Figure 5. 2: Plots of the computed velocity profiles of various turbulence models on the line inserted at the centre of the computational domain from $y = 0$ to $y = H$ for (a) $w/h = 1$, (b) $w/h = 4$, (c) $w/h = 8$ at Re $\approx 56,000$ (d) $w/h = 9$ at Re $\approx 37,000$ and (e) Turbulence intensity at $w/h = 1$ (f) Turbulence intensity at $w/h = 4$, with the result of (Hanjalic and Launder, 1972, Okamoto et al., 1993),(Djenidi et al., 1999) and LES of (Cui et al., 2003).

Figure 5.3 shows the wall pressure drag distribution along a line positioned at the bottom of the cavity for w/h = 9. This distance is normalised by the roughness height "h" and $K - \varepsilon$ model is tested for validation. The agreement between the Cp computation and LES of Cui et al. (2003)is satisfactory. The zero pressure drag due to the recirculation region at the back face of the rib predicted by the $K - \varepsilon$ model shows a close resemblance to that obtained with the LES result. The pressure coefficient is defined as

$$C_p = \frac{p - p_0}{\frac{1}{2}\rho\overline{U}^2} \tag{5.1}$$
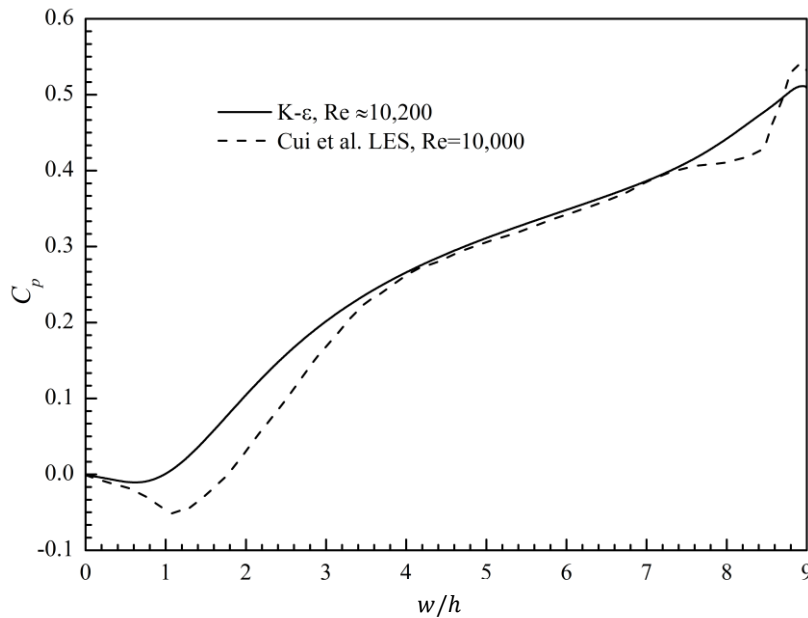
Figure 5. 3: The pressure coefficient profile at $w/h = 9$.

Figure 5.4 shows the mean averaged velocity profiles for the pitch ratio $w/h = 1,4$. Turbulence intensities are obtained from the results obtained using the Reynolds stress BSL model. These can also be obtained from the results of other turbulence models, see Section 4.3. The turbulence intensities (root-mean-square) U_{rms} and V_{rms} for the BSL model are defined as $\sqrt{(\overline{u}')^2}$ and $\sqrt{(\overline{v}')^2}$ respectively. The streamwise and vertical turbulence intensities for pitch ratio of 1 and 4 ($w/h = 1,4$) at the cavity and rib can be observed in figure 5.5 for the Reynolds stress BSL model. The magnitude of U_{rms} is small in the cavity and increases sharply to a value 0.08. At short distance away from the roughness elements the value of U_{rms} decreases gradually in the middle of the channel in the y-direction and peaks rapidly close to the top of the channel where it starts to decrease again. The first peak appears to be

higher in magnitude than the second peak and this is due to the presence of the roughness elements. The value of U_{rms} still behaves in the same way as the top wall, however the first peak is higher in magnitude than the second peak close to the top wall. The magnitude of the V_{rms} peak is smaller than those of the U_{rms} values for both pitch ratios 1 and 4.

In a similar trend to those for the V_{rms} values, the U_{rms} values have two peaks. They are less sharp than those for U_{rms}. The streamwise turbulence intensities increase as the pitch ratio increases. Figures 5.6-5.7 show the contours for turbulence intensities for pitch ratios of 1 and 4 ($w/h = 1,4$) normalised by the bulk velocity for the Reynolds stress BSL model. The contours show a small magnitude of U_{rms} and V_{rms} at the cavity. These values are the smallest close to the wall and maximum slightly above the crest of the square bars. The peak in the magnitude of these values at the crest is due to the presence of the strong shear. The peak of the U_{rms} and V_{rms} are higher in $w/h = 4$ than $w/h = 1$.

For the vertical turbulence intensity V_{rms} at a pitch ratio of 4 ($w/h = 4$), the peaks occur slightly above the crest at the centre of the channel and at the crest of the next rib. Figure 5.7 shows the contours of the turbulence intensity $\overline{-u'v'}$ for $w/h = 1, 4$ which is normalised by the bulk velocity for the Reynolds stress BSL model. For $w/h = 1$, the Reynolds shear stress in the cavity is zero, as can be observed in the contour, and the peak occurs slightly above the crest of the ribs. In the $w/h = 4$ case, the Reynolds stresses are zero close to the wall and begin to increase slightly above the floor. The peaks in turbulence intensity occur at the circulation above the height of the cavity and at the crest of the next adjacent rib.
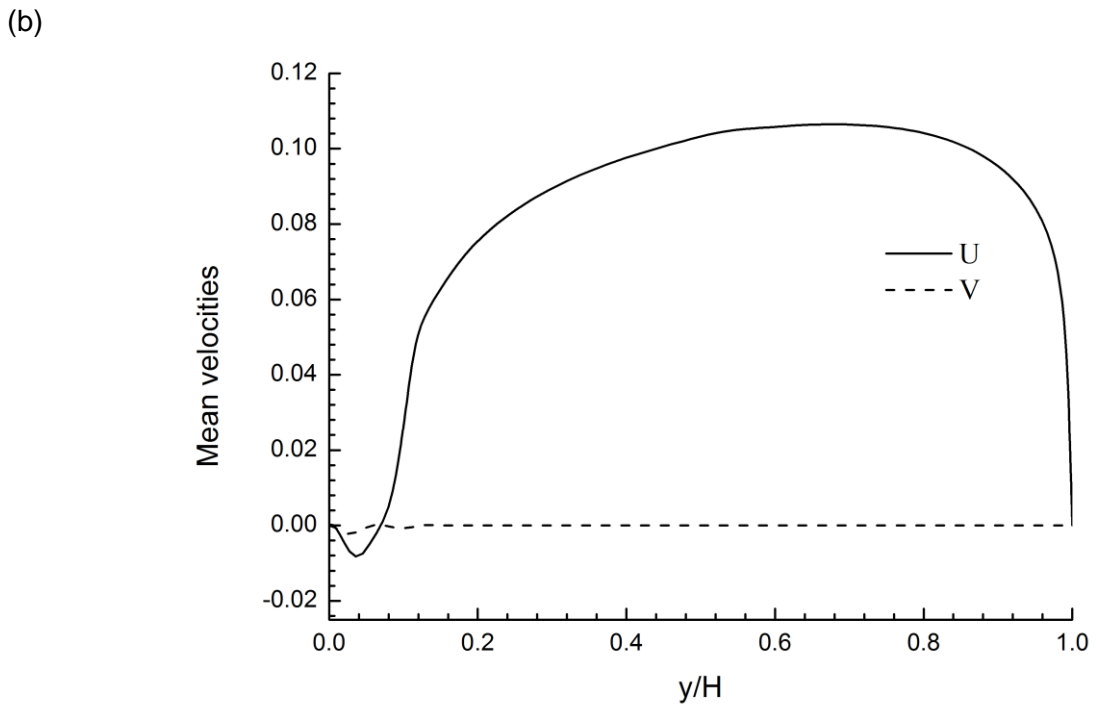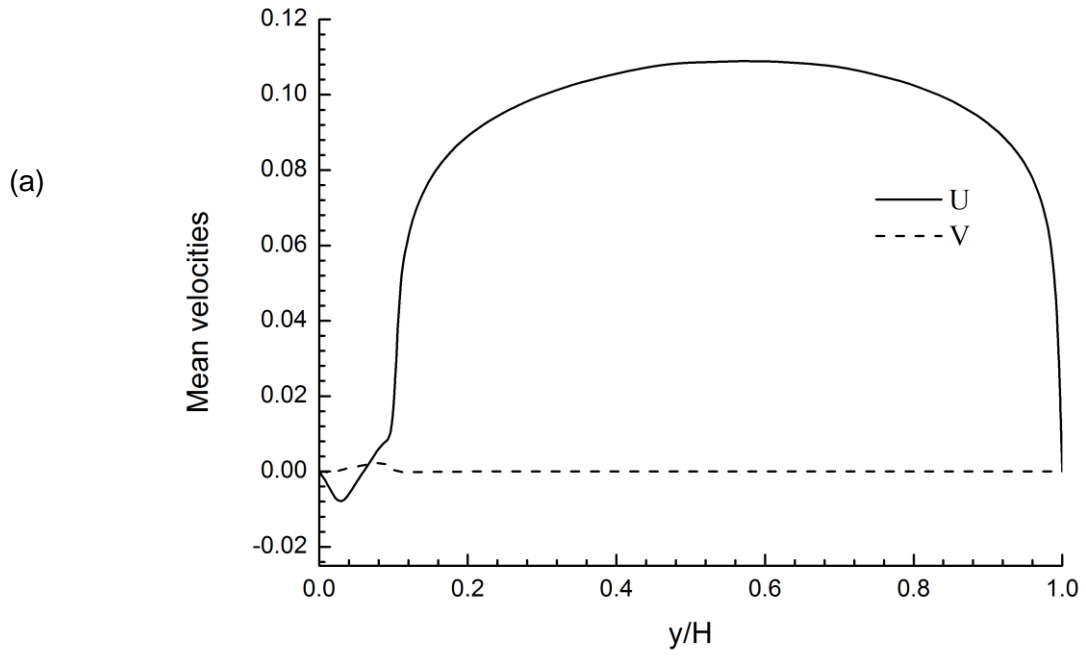
Figure 5. 4: Averaged mean velocity profiles for pitch ratio: (a) $w/h = 1$ and (b) $w/h = 4$.

(a)

(b)
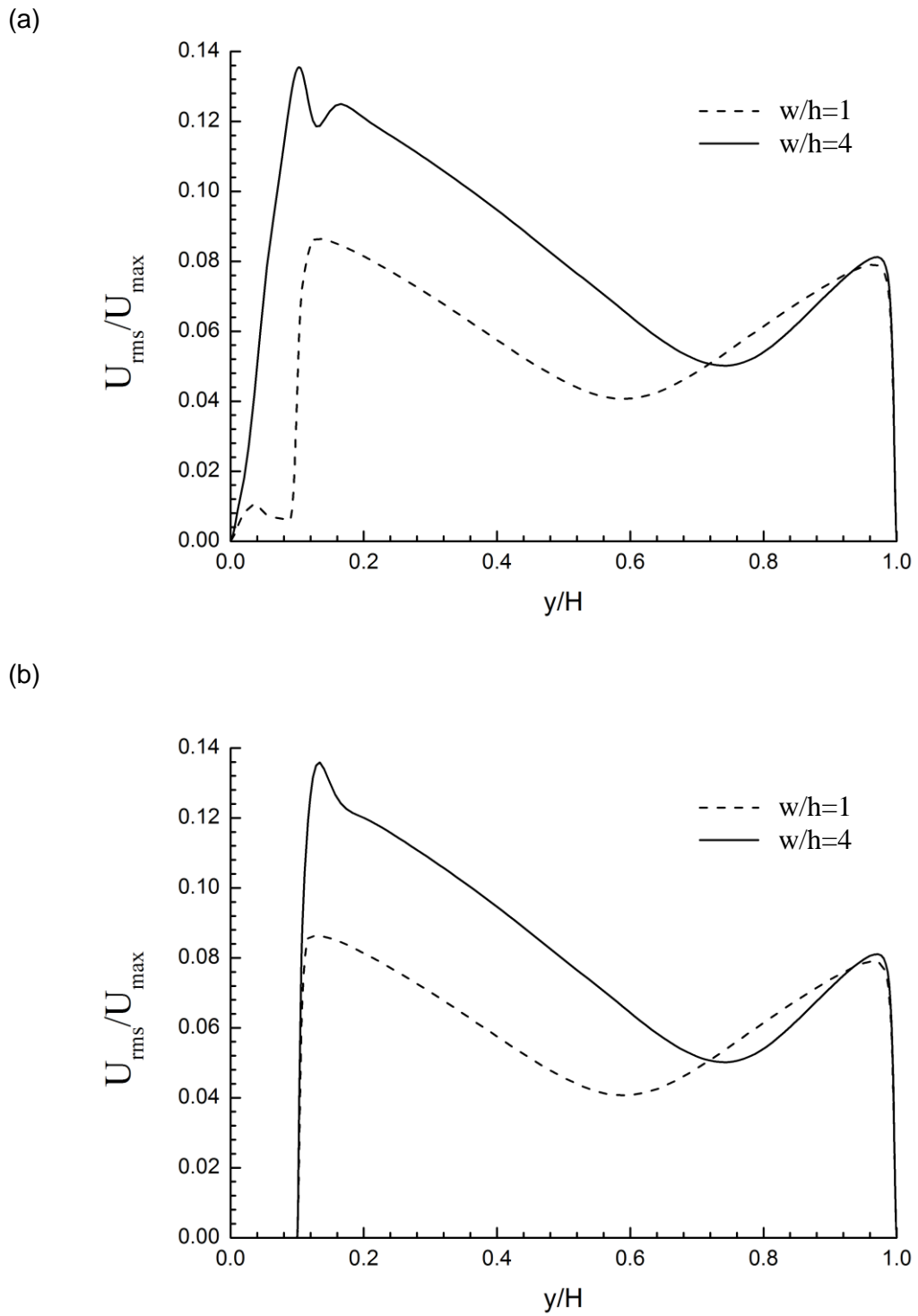
Figure 5. 5: Mean streamwise turbulence intensities at (a) cavity and (b) rib for different pitch ratio in a rectangular channel.
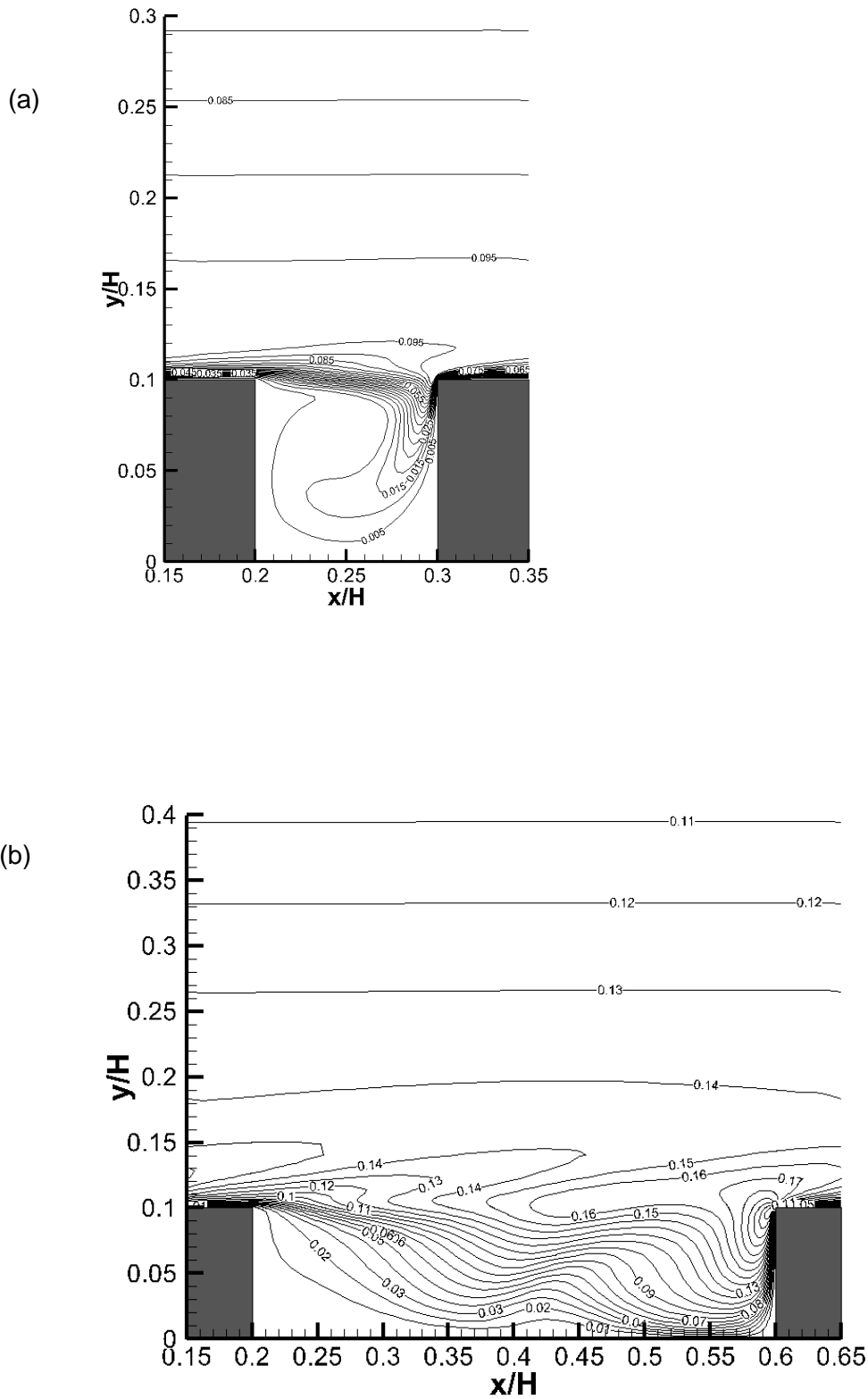
Figure 5. 6: U_{rms}/U_b contours for pitch ratio (a) $w/h = 1$ and (b) $w/h = 4$ in a rectangular channel.

(a)
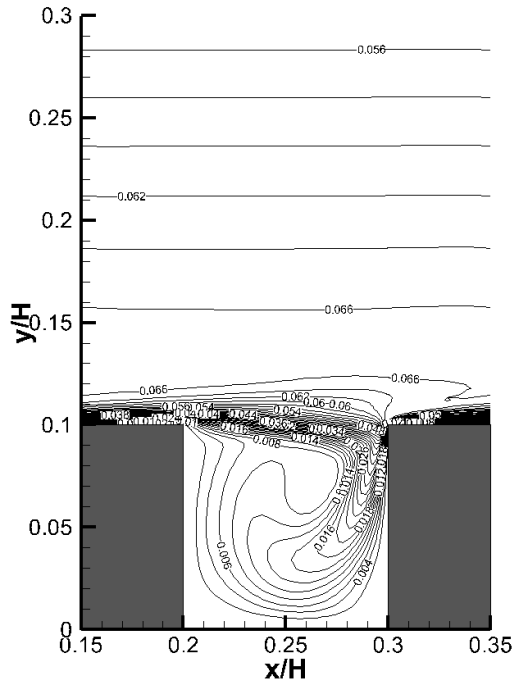
(b)
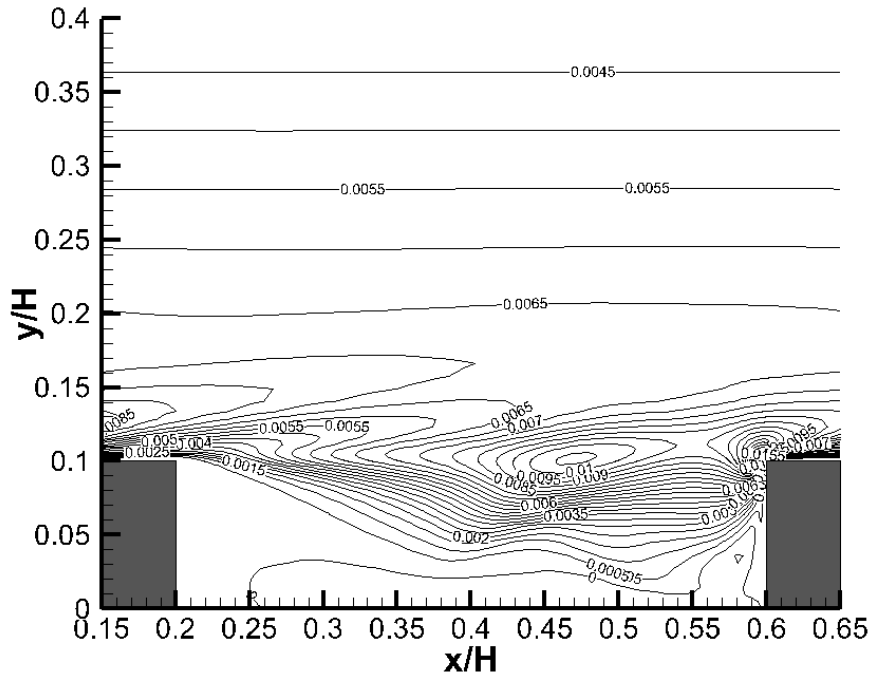
Figure 5. 7: V_{rms}/U_b contours for pitch ratio (a) $w/h = 1$ and (b) $w/h = 4$ in a rectangular channel.

Figure 5. 8: $\sqrt{\overline{u'v'}/U_b}$ contours for pitch ratio (a) $w/h = 1$ and (b) $w/h = 4$ in a rectangular channel.

Out of the turbulence models examined, the standard $K - \varepsilon$ turbulence model appears to give the best agreement in capturing mean velocity profiles. Therefore, the predictions of the eddy viscosity must be reasonably accurate, as the influence of turbulence on the flow field is largely governed by the eddy viscosity term in equation (4.36). Moreover, turbulent dispersion of heat and small particles may be modelled using an eddy diffusivity which is proportional to the eddy viscosity. Therefore, the $K - \varepsilon$ model has been used to further examine the characteristics of the roughened wall flow over a range of aspect ratios. Note that, somewhat surprisingly, this is different to our initial expectations that the SST model would produce the most accurate comparisons.

Before commencing our parametric study with the chosen turbulence model, a grid independence study was conducted at $w/h = 1$, by using a coarse (14919 cells), medium (53874) and fine (253444) mesh. As figure 5.9 shows, the solution becomes independent of the grid for the medium to fine mesh. Thus, the medium mesh is chosen for future calculations. Further, the convergence is checked by monitoring the mass flow rate, maximum velocity u and y^+, as shown in figure 5.10.
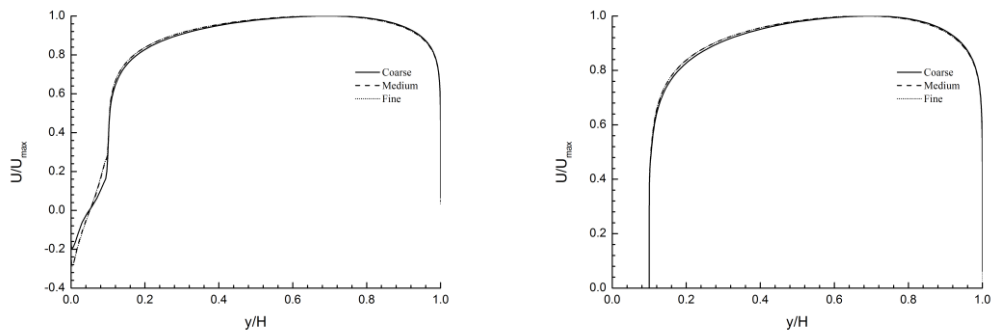
Figure 5. 9: Grid independence study of the mean streamwise velocity profile at top rib $w/h = 1$.
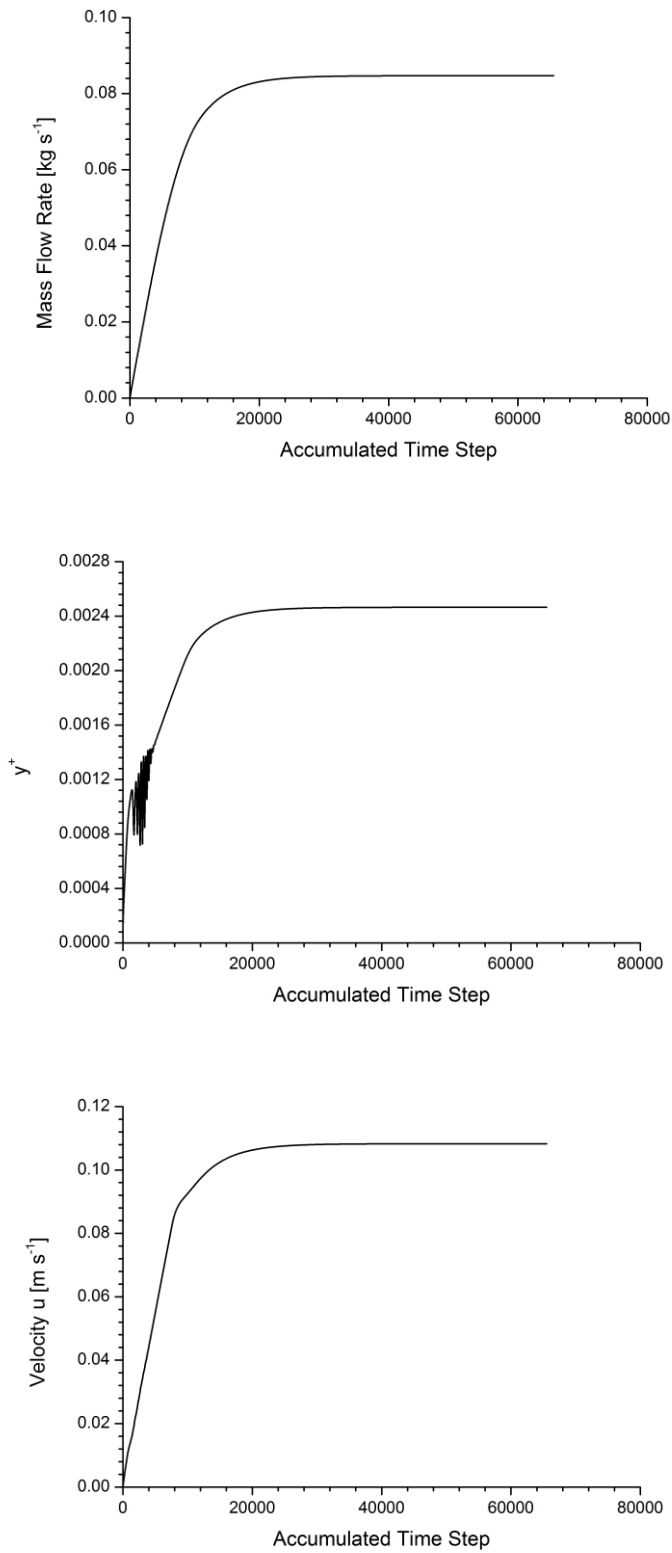
Figure 5. 10: Monitoring of mass flow rate of the fluid as a function of number of time steps.

5.4 Results

In total, 196 RANS modelling simulations were performed to study turbulent flow over two-dimensional square roughness elements for various Reynolds numbers and w/h ratios. The w/h ratio lies between 0.12 and 402 whilst the Reynolds number range from 6.3×10^3 to 4.5×10^4. The streamlines and reattachment length of the averaged two-dimensional velocity field of the results are presented. The flow is over form-type roughness as roughness Reynolds number $h^+ (= Re_\tau \frac{2h}{H})$ is well beyond the critical range for the form roughness $h^+ \geq 50 - 100$ suggested by Jiménez (2004). Thus, the viscous effect of the wall will be negligible relative to the pressure drag produced by the rib.

The trend in which the velocity profile $\bar{U}/U_{max}$ changes has been examined with respect to Reynolds number for different classes of rough wall. The results are compared with the effect of Reynolds number on a typical turbulent layer profile over a flat plate. The direction in which the velocity profile changes as a result of the increase in Reynolds stresses through a rise in perpendicular mass interchanges between the inner and outer fluid layers. The direction in which the velocity profile changes for the D−type roughness is similar to the flow over flat plates. However, it is interesting to note that this change occurs at a lower rate compared to the flat cases. Two interesting observations can be made for w/h = 3 and w/h = 4 velocity profiles in figure 5.11. Firstly, the effect of Reynolds number on the flow velocity profiles is insignificant for intermediate type roughness. Secondly, for both the flat plate and D−type ($w/h < 2$) roughness the direction of change in velocity profiles (indicated by arrows in figure 5.11) effected by the increase in Reynolds number in the lower boundary is opposite to what is observed for intermediate and k-type roughness. In contrast the velocity profiles close to the upper boundary show the same trend with the increase in Reynolds number in various roughness type. The trend for K−type roughness has previously been extracted by Leonardi et al. (2006) and Bandyopadhyay (1987) which agrees with the present study. The key point to take away from this comparison is the critical transition point in terms of Reynolds number effect, the ratio w/h = 3, between D−type and K−type. Figure 5.11 shows a more pronounce resistance effect near the roughness element as the spacing between the roughness element increases. This leads to the up-lifting of the U_{max} towards the upper flat wall. This effect is more apparent for w/h = 8 and w/h = 9. Finally, to further characterise the bed roughness, flow resistance and eddy

viscosity variation are evaluated. The dependence of these results on the Reynolds number as a function of width-to-height ratio will be discussed .

(a) Flat

(b) $w/h = 1$

(c) $w/h = 3$

(d) $w/h = 4$

(e) $w/h = 7$
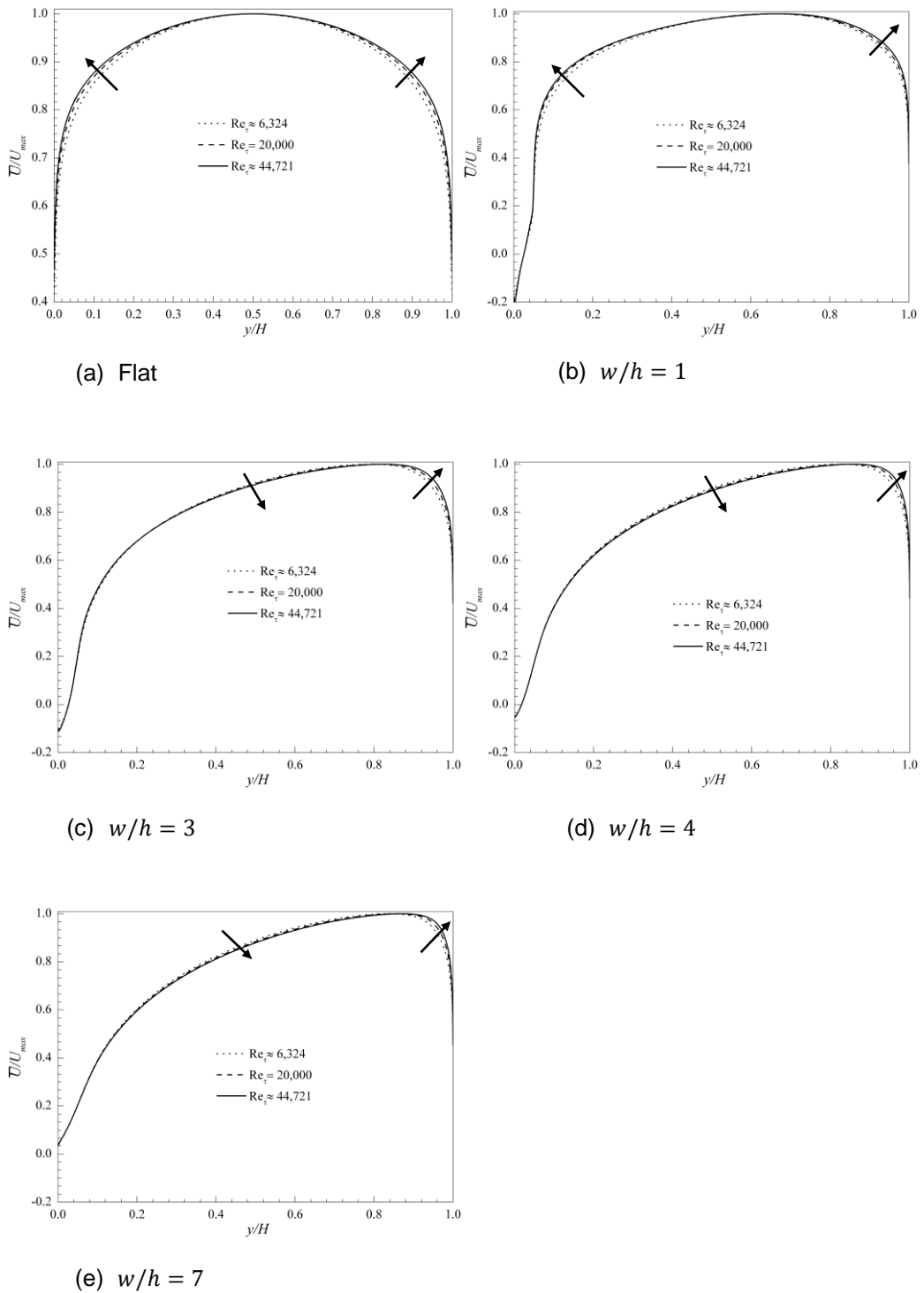
Figure 5. 11: The velocity profiles inserted vertically in the middle of the channel with roughness elements of various aspect ratios.
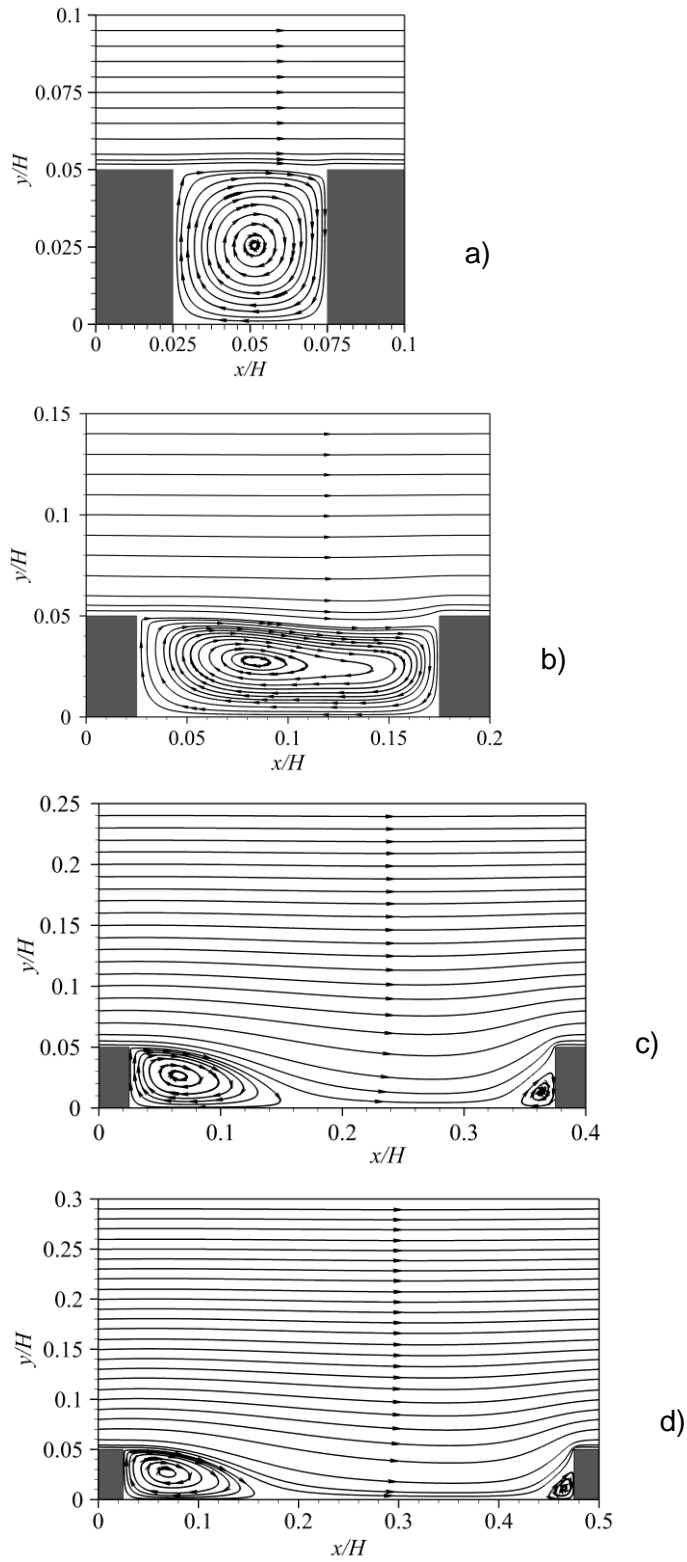
Figure 5. 12: Distribution of mean streamlines velocity for (a) $w/h = 1$, (b) $w/h = 3$, (c) $w/h = 7$ and (d) $w/h = 9$.

5.4.1 Reattachment length and streamlines

Two-dimensional mean velocity streamlines are created to illustrate the flow distribution in the inner and outer roughness elements. In this section the effect of the w/h variation on the flow pattern is considered. The separation and reattachment region for different roughness types are similar to the flow behaviour observed by Cui et al. (2003) and (Leonardi et al., 2007). Figure 5.12 shows the change in flow pattern from w/h = 1 to w/h = 9. The vortices are seen to become elongated from w/h = 1 to w/h = 3 and the reattachment still occurs at the leading edge of the neighbouring element as shown in figure 5.12 (a)–(b). As the w/h ratio increases further the vortices stretch until they split and the flow reattaches on the lower boundary between adjacent roughness elements, as observed in figure 5.12 (c). For $w/h = 7$ and $w/h = 9$ a vortex is formed in the corner of the next roughness element as a result of the flow reattachment at the cavity. This behaviour cannot be observed for $w/h = 1$ and $w/h = 3$, although small flow rotations was found to occur in both corners of the roughness element which were visible by flow vectors. Ashrafian et al. (2004) found that in the transitionally rough flow regime at w/h = 7, the apparent reattachment does not occur at the channel bed. However, Leonardi et al. (2003) reported that for w/h = 7, in the fully rough regime, the flow reattaches on the bottom of the channel between the roughness elements. In the transitionally rough regime the flow becomes dependent on the Reynolds number (Bandyopadhyay, 1987) and therefore the reattachment location may become sensitive to the roughness height.

The reattachment location is determined by the point at which the non-dimensionalised wall-shear stress vanishes, for a selection of w/h ratios where the reattachment occurs at the cavity, as shown in figure 5.13 (a) The reattachment length x_r is measured from the step and normalised by the roughness height, h. Figure 5.13 (a) shows that the value of reattachment length increases with an increase in the ratio, w/h. The reattachment point for each of the selective w/h ratios is plotted and a quadratic polynomial curve can be fitted to the data, as illustrated in figure 5.13 (b).
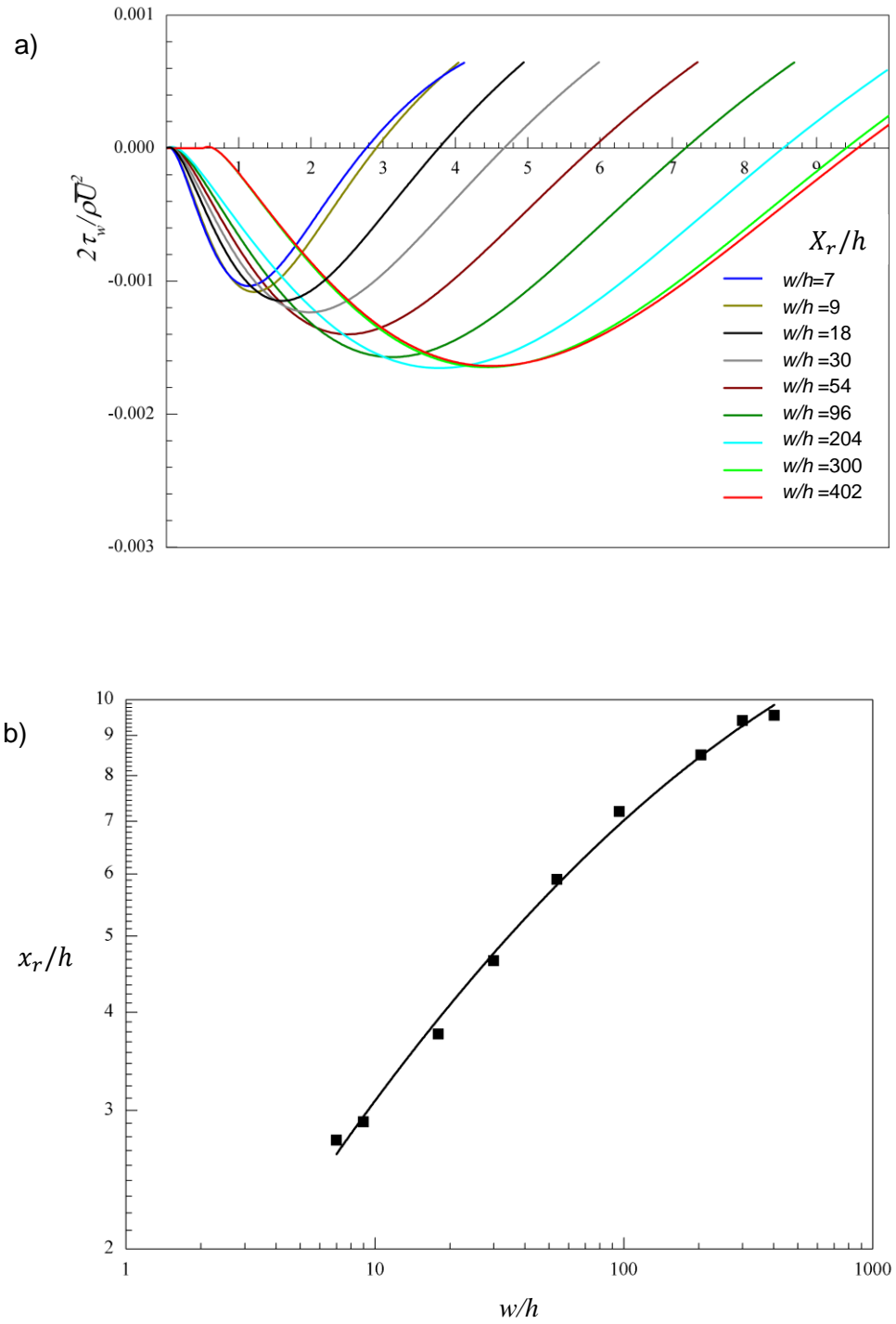
Figure 5. 13: (a) The normalised wall shear stress versus the normalised distance between the adjoining ribs and the (b) graph of the reattachment point with varying width-to-height ratio.

5.4.2 Flow resistance

The loss of energy from a flow needed to overcome a rugose surface is commonly evaluated using the skin-friction drag and form drag which sum to the total drag. The ratio of the form drag to skin drag increases with the w/h ratio. The friction factor for the turbulent flow structure obtained near the roughness element is a function of the ratio w/h and the Reynolds number, Re_τ. Since the value of the form drag for higher values of the ratio w/h is significantly greater than the value of the skin-frictional drag, then the entire flow resistance as a function of w/h occurs in the form of the pressure drag. The Darcy friction factor equation is defined as

$$f = \frac{(H/2)(-dp/dx)}{0.5\,\rho\bar{U}^2} \qquad (5.2)$$

where dp/dx is the main driving force against the wall shear stress τ_w and $\bar{U}$ is the area-weighted average streamwise velocity. In the transitionally rough regime, the friction factor varies with the Reynolds number and the roughness height, as the roughness elements begin to distort the laminar-sub layer (Jiménez, 2004, Schlichting et al., 2000, Busse and Sandham, 2012). The present results correspond to the fully rough regime where the viscous cycle is completely distorted by the roughness element and hence the friction factor becomes independent of the viscosity. The variation of the friction factor with the Reynolds number and the width-to-height ratio are shown in figure 5.14. Maximum resistance to the flow occurs at $w/h \approx 7$, for the lowest Reynolds number, $\mathrm{Re}_\tau = 6,325$. This optimum flow resistance value agrees well with the DNS result of Leonardi et al. (2003) and the experimental result of Furuya et al. (1976) on plates roughened by wires. For all the roughness type classes investigated, the resistance decreases with increasing Re_τ.

A cubic polynomial curve can be fitted to the friction factor data as shown in figure 5.14. The results are in accordance with the conclusion of Saito et al. (2012), who suggest that in the fully rough regime the average turbulence intensity is proportional to the friction factor. The equation for the polynomial curve is given by,

$$f = 0.005 + 0.01(w/h) + (w/h)^2 + 0.003\,(w/h)^3, 0.12 \lesssim w/h \lesssim 7 \quad (5.3)$$

A fitted cubic polynomial curve indicates a rapid rate of friction enhancement up to $w/h \approx 7$ as described in equation (5.3). For $w/h \gtrsim 7$, an exponential decay function can be described by fitting a curve to the data as illustrated in figure 5.14, with the exponential curve given in equation (5.4). Figure 5.14 demonstrates that the decay rate of the flow resistance is slow with respect to the varying w/h ratio equation (5.4) indicates it is $\approx 1/41$.

$$f = 0.02e^{-\frac{w/h}{41.03}} + 0.005 \; w/h \gtrsim 7 \tag{5.4}$$
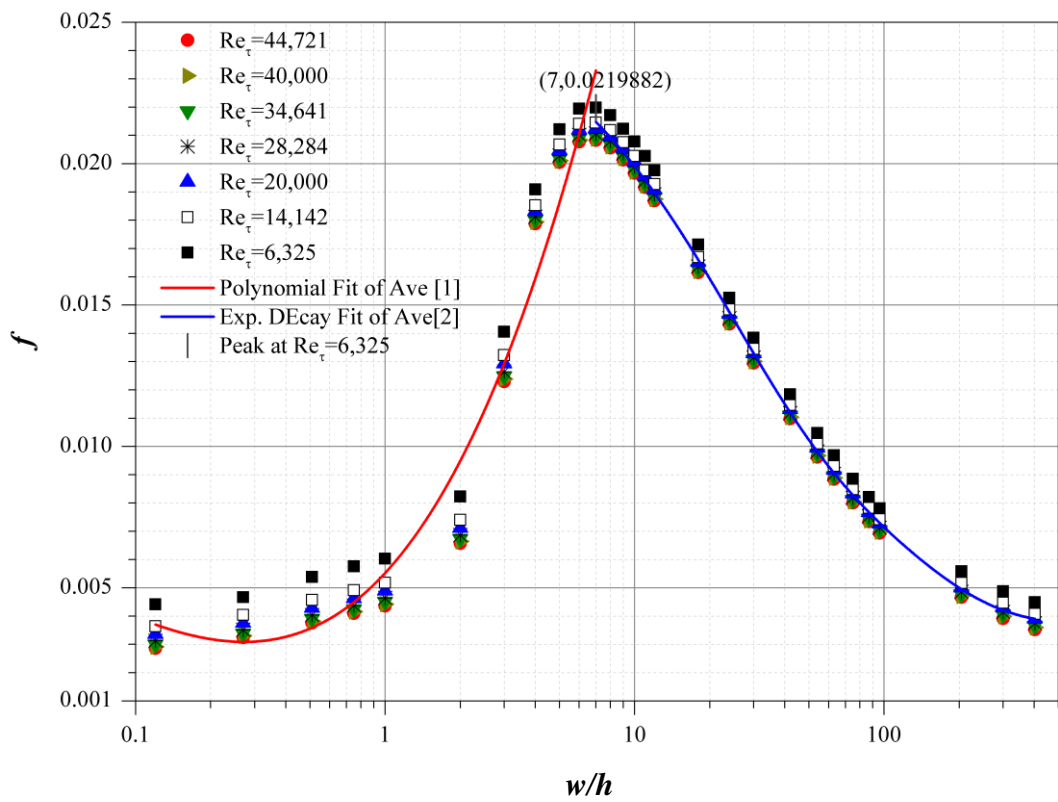
Figure 5. 14: Scatter plots of the area-weighted average friction factor as a function of w/h for a range of Reynolds numbers.
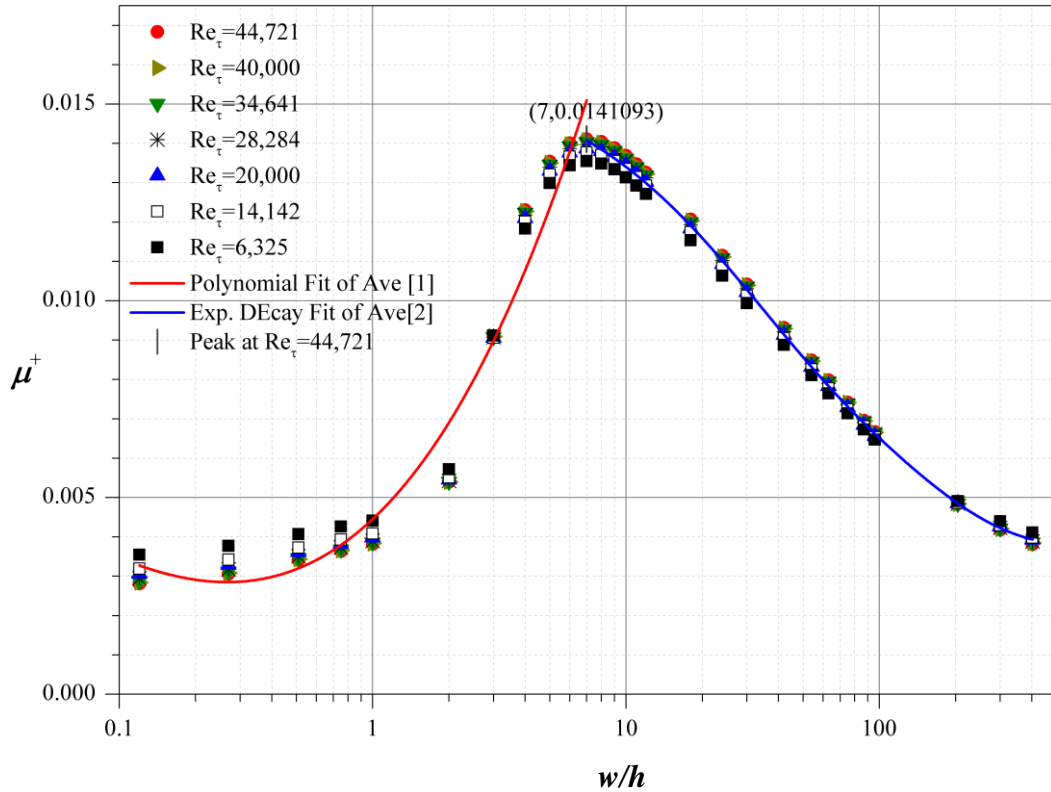
Figure 5. 15: Scatter plots of the area-weighted average eddy viscosity as a function of w/h for a range of Reynolds numbers.

5.4.3 Eddy viscosity

Eddy or turbulent viscosity μ_t is associated with the transfer of momentum caused by turbulent eddies and contributes to the local state of turbulence (Nielsen and Teakle, 2004). The eddy viscosity depends on the turbulent energy per unit mass of the fluid K, and the dissipation rate ε. The eddy viscosity μ_t is computed in a non-dimensional format which can be expressed as,

$$\mu^+ = \frac{\mu_t}{\rho \bar{U}(H/2)} \tag{5.5}$$

The optimal values of the w/h ratio and Reynolds number to maximise mixing enhancement can be constrained. Figure 5.15 shows that the value of μ^+ is maximised at $w/h = 7$ for the highest Reynolds number at $\mathrm{Re}_\tau = 44,721$. It is observed that the rate of eddy viscosity enhancement and decay is similar to the flow resistance. In this case the data is described by a polynomial curve given by

$$\mu^+ = 0.004 + 0.006 \left(\frac{w}{h}\right) + 0.006 \left(\frac{w}{h}\right)^2 + 0.001 \left(\frac{w}{h}\right)^3, \qquad (5.6)$$

$$0.12 \lesssim w/h \lesssim 7$$

and an exponential decay equation

$$\mu^+ = 0.01 e^{-\frac{w/h}{56.13}} + 0.004 \; w/h \gtrsim 7 \qquad (5.7)$$

The normalised eddy viscosity is maximised in the range of $7 \lesssim w/h \lesssim 10$. As figure 5.15 illustrates, a polynomial curve can be fitted to the normalised eddy viscosity data for $w/h \lesssim 7$. The eddy viscosity immediately enhances up to $w/h \approx 7$ and decays exponentially at a rate of $\approx 1/56$ order of magnitude. For $w/h \lesssim 1$, the value of μ^+ decreases with increasing Reynolds number. For the intermediate type roughness, or $w/h = 3$, μ^+ becomes independent of the Reynolds number. As the flow separates and reattaches in the bed at $w/h = 7$, the eddy viscosity begins to change behaviour and increases with increasing Reynolds number. This phenomenon continues up to $w/h \approx 200$ where μ^+ once again becomes independent of the Reynolds number behaviour inclusive to the intermediate type roughness behaviour. For $w/h > 201$, μ^+ starts to decrease with an increasing Reynolds number in a similar manner observed for the D −type roughness, as the width expands towards the smooth wall limit.
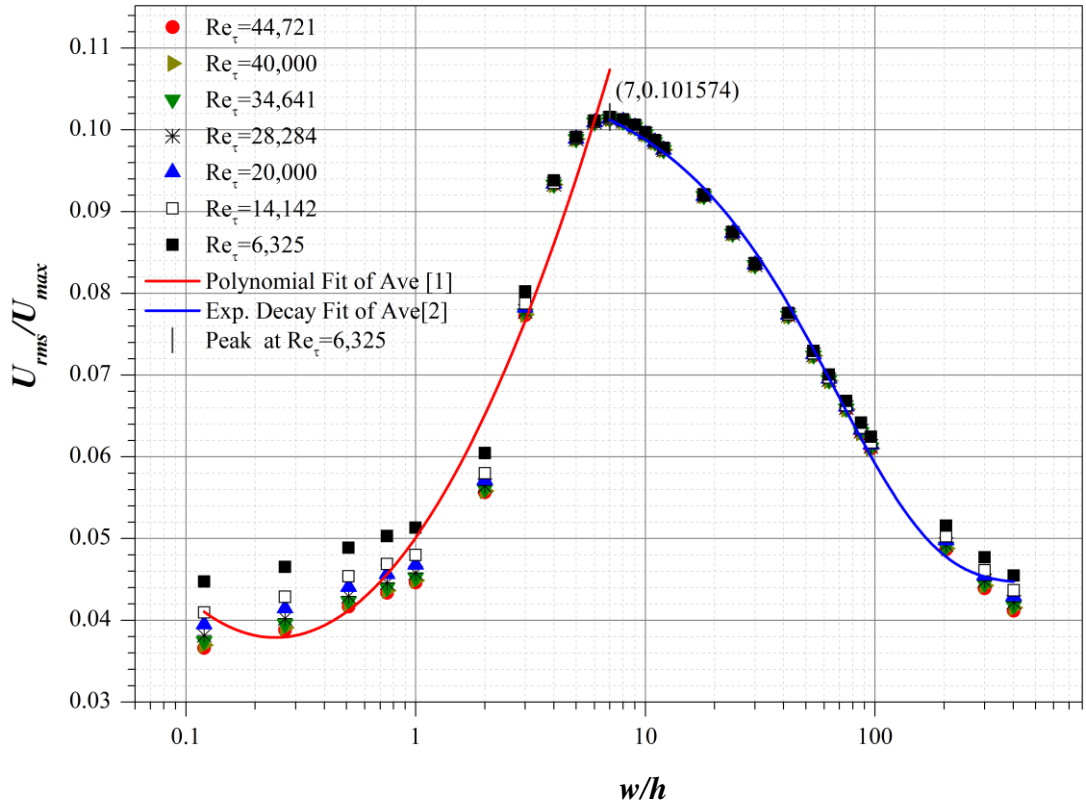
Figure 5. 16: Turbulence intensity as a function of aspect ratio w/h and Reynolds number.

5.4.4 Turbulence intensity

The wall roughness produces a favourable and adverse pressure gradient due to separation and stagnation points. This increases the ejection and influx of the flow towards the wall. As a consequence, the value of the $x-$ and $y-$ components of turbulence intensity increases with respect to cases approaching the flat wall. The area-weighted average of root mean square of the turbulence intensity in the $x-$direction U_{rms}/U_{max} is illustrated in figure 5.16 for the different values of Reynolds number Re_τ and as a function of dimensionless distance w/h. The turbulence intensity data show a similar evolution to eddy viscosity and friction factor and thus the data fits both the polynomial and exponential decay curves. The equation for polynomial curve for the average of turbulence intensity of various Re_τ is given by,

$$\frac{U_{rms}}{U_{max}} = 0.04 \left(\frac{w}{h}\right) + 0.03 \left(\frac{w}{h}\right)^2 + 0.050, \quad 0.12 \lesssim w/h \lesssim 7 \qquad (5.8)$$

and for the exponential curve is given by,

$$\frac{U_{rms}}{U_{max}} = 0.06e^{-\frac{w/h}{68.75}} + 0.004, \qquad w/h \gtrsim 7 \qquad (5.9)$$

Similar to the friction factor data the peak, in U_{rms}/U_{max} was obtained at the lowest value of Reynolds number, $\mathrm{Re}_\tau = 6{,}325$. The maximum value of turbulence intensities were observed close to the surface of the rib crest for all aspect ratios. In this region, a shear layer is formed as the flow separates from the top surface of the leading edge of the roughness element. Here it is evident that the square ribs enhance the U_{rms}/U_{max} compared to cases approaching a smooth wall. Further the current data provide evidence that the streamwise Reynolds stresses normalised by the maximum value of the free stream velocity depend on the w/h ratio. The higher value of the streamwise Reynolds stress at ratio $w/h = 7$ leads to enhanced mixing. Here the data for turbulence intensity are shown for reporting purposes and cannot be considered reliable since the earlier comparison with experimental data was not satisfactory.

5.4.5 Turbulence Kinetic Energy Production

The turbulent kinetic energy (TKE) production and dissipation rate of the flow depends only on the scale of the velocity u_e and spatial distribution l_e of the energy containing turbulent eddies. The scales of u_e and l_e are typically smaller than that of the mean flow. Figure 5.17 shows the scatter plot for the rate of production of non-dimensional area-weighted turbulence kinetic energy $\bar{P}^+(= P_{rough}/P_{flat})$ for various Re_τ and w/h. It should be noted that for non-dimensionlisation the flat bed case uses the same Re_τ as the rough bed case.

Figure 5.17 demonstrates an enhancement in production rate $\bar{p}^+$ with extension of w/h up to $w/h = 10$. At ratio $w/h = 10$, $\bar{p}^+$ attains its maximum value and in this section it is referred to as the critical production ratio $\bar{p}_{cr}^+$. From $w/h = 10$ onwards the rate of production decays gradually up to the last aspect ratio. Further observations indicates that the dependence of the $\bar{p}^+$ to Re_τ is weaken more towards the flat cases (before and after $\bar{p}_{cr}^+$). The turbulence kinetic energy $\bar{p}^+$ appear to be almost independent of the of Re_τ for the $D-$type roughness element cases for $w/h < 1$. For $w/h = 0.27$ at $\mathrm{Re}_\tau = 6,325$ the value of $\bar{p}^+$ is maximum compared to intermediate and $K-$type roughness where $\bar{p}^+$ is maximum for the highest Reynolds number $\mathrm{Re}_\tau = 44,721$. For all the Reynolds numbers $\bar{p}^+$ showed a peak at $w/h = 12$ except for $\mathrm{Re}_\tau = 6,325$ where the peak occurred at $w/h = 9$.

In figure 5.17 (b), the non-dimensional maximum value of TKE production P_{max}^+ $(= P_{rough,max}/P_{flat,max})$, for the entire channel is compared for various Re_τ and w/h. P_{max}^+ show an increase with the increase in aspect ratio up to $w/h = 1$, followed by a decrease up to $w/h = 3$ and lastly a sudden increase from $w/h = 5$ to $w/h = 402$. Contrary to figure 5.17 (a), P_{max}^+ do not exhibit much dependence on Re_τ. Only minor dependence appear to be attributed to $\mathrm{Re}_\tau = 6,325$ from $w/h = 1$ to $w/h = 0.1$ and from $w/h = 10$ to $w/h = 96$. For larger w/h ratio (from $w/h = 96$ onwards) P_{max}^+ start to be slightly dependent on the Re_τ. Furthermore, for $w/h = 300$ and 400 the peak in P_{max}^+ is seen for $\mathrm{Re}_\tau = 40,000$.

The relative contour plots of turbulent kinetic energy for a selection of ratio w/h as a function of Re_τ values are shown in figure 5.18. As the contour plots suggest, a shear layer is generated by the impact of the flow on the leading edge of the roughness element for all cases. Further growth in length of the shear layer with the increase in ratio w/h is evident downstream of the top surface of the rib. This is causes by the turbulent diffusion which is distinctly different for between the cases with various aspect ratios.

The region of the shear layer is also associated with higher value of turbulent kinetic energy than other region of the channel. It is clear that the strength of the shear layer is weakened with the decrease in Re_τ values as illustrated by the contours. For rough surfaces, turbulent kinetic energy appears to be produced some height above the bed which is then directed towards the wall region where it is dissipated. For such cases the production of turbulence kinetic energy is determined by the sum of the turbulent diffusion and the dissipation rate. In the case of the flat bed, the dissipation of the energy effectively depends on the viscous diffusion. A significant loss in turbulent kinetic energy by diffusion is seen in the near wall region for all aspect ratios compared with the gain in transfer of energy and momentum flux over the two-dimensional rib-roughness. The loss in turbulent energy is more pronounced in zones associated with flow recirculation. This is more apparent in the cavity region of $w/h = 1$ comprising of stable vortices. These observations verify that the turbulent transport mechanism in the inner and outer region of the flow strongly controlled by the surface geometry.
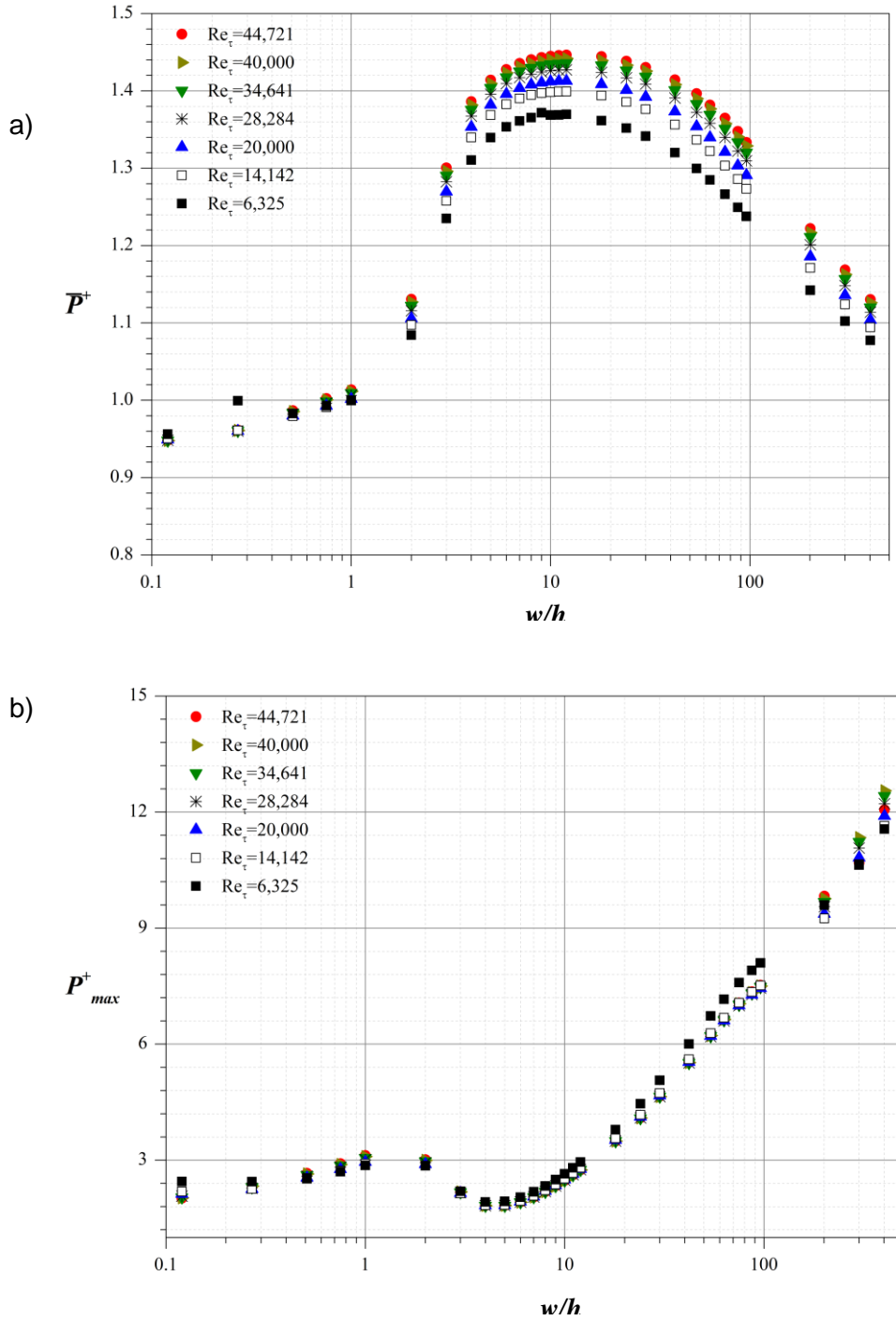
Figure 5. 17: The turbulence kinetic energy plot: (a) the area-weighted average turbulence kinetic energy and (b) the maximum turbulence kinetic energy over the entire domain.

Figure 5. 18: Turbulent kinetic energy contours for various w/h ratio and Reynolds number.

a)

b)

Figure 5. 19: The effect of the variation of the roughness height on (a) friction factor (b) eddy viscosity.
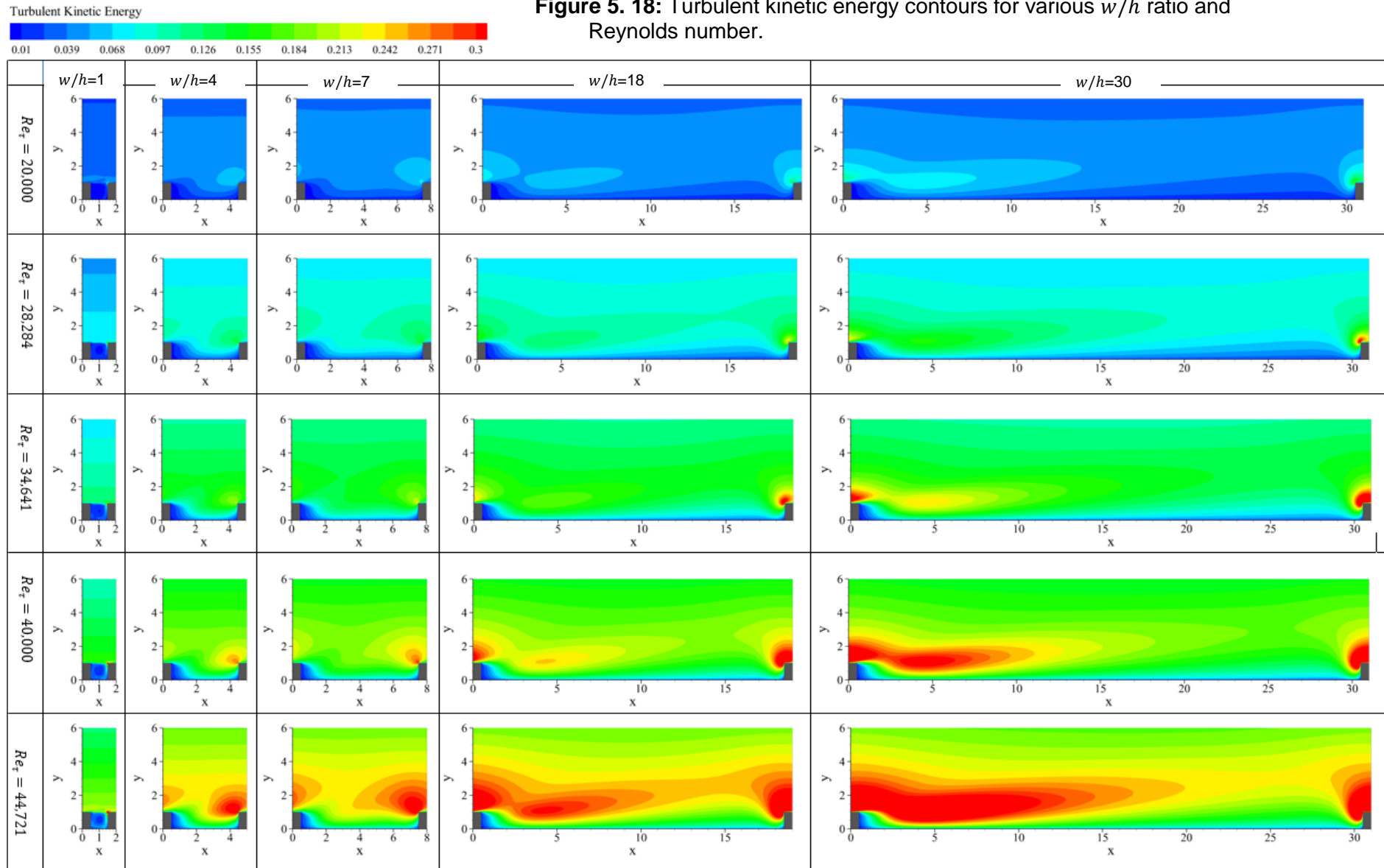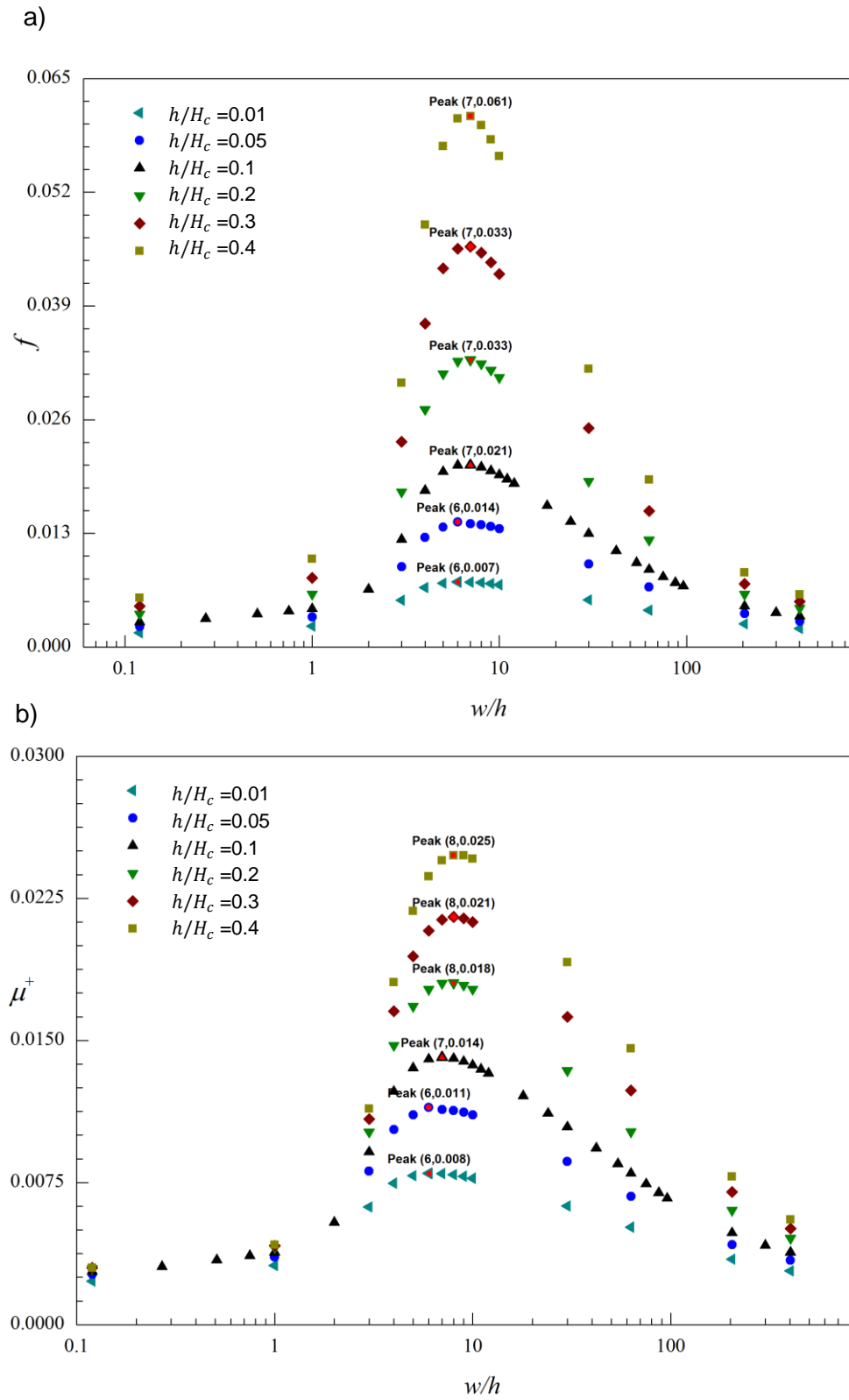
5.5 Effect of roughness height

This section examines the effect of the height of the surface roughness on turbulent mixing and flow resistance, as a function of ratio w/h at a fixed Reynolds number ($\mathrm{Re}_\tau = 44{,}721$). Thus, further simulations were conducted for a range of roughness height to half channel height, h/H_c. Profiles of the friction factor for various rib heights and aspect ratios are presented in figure 5.19 (a). The increase in obstacle height lead to severe changes in the original wall flow dynamics as the roughness ~~is~~ now covers larger region of the boundary layer. As expected, the maximum flow resistance is observed for the largest ratio h/H_c. Despite the change in the ratio k/H_c, the peak value in f stays almost the same around the ratio $w/h = 7$. Although, for lower ratio h/H_c =0.05-0.01, the peak in f is observed to occur at $w/h = 6$. Figure 5.19 (b) shows the profiles of non-dimensional eddy viscosity for a range of ratio h/H_c. Interestingly, μ^+ enhances with the increase in the ratio h/H_c. Similarly to the friction factor profile, the peak in μ^+ weakly decreases as the ratio h/H_c reduces. Thus, the present analysis of turbulent channel flow suggests that increasing the roughness element height would have a pronounced effect on the turbulent mixing and flow resistance, however it does not significantly influence the critical w/h ratio at which the peak in these variable occurs. Moreover, the current data suggest that the influence of roughness on eddy viscosity and friction factor is almost independent of the roughness height for $D-$type surfaces. For the intermediate surface roughness μ^+ an f become essentially dependent on the ratio h/H_c. In contrast for the $K-$type surfaces distinctively these variables become fully dependent on the eddy viscosity and flow resistance.

5.6 Discussion

The new results confirm that the optimum spacing of the roughness elements to maximise friction and eddy viscosity within the flow occurs at $w/h = 7$. The rate of turbulence enhancement increases rapidly up to this critical spacing and the rate of perturbation decay is slow thereafter, such that the effect of turbulence perturbation does not change significantly with the increasing aspect ratio. In turbulent pipe flows it normally takes around 100 pipe diameters for the velocity profile to become fully developed (Patel, 1974, Lien et al., 2004), and this value is similar to the modelled roughness case investigated here, in which the flow does not becomes fully developed until a distance of about 100 roughness heights downstream of a roughness element.

Okamoto et al. (1993) concluded that optimal heat transfer occurs when the turbulence of the free stream is maximised. Similarly, Ryu et al. (2007) found that the maximum heat transfer occurs when the flow resistance attains its maximum value. The conditions associated with optimum turbulence enhancement and the flow resistance in the present work suggest, therefore, that heat transfer enhancement is maximised during flow over roughness elements with spacing $w/h \approx 7$, but that close to optimal transfer can occur with much wider roughness spacings. This result may guide efforts to optimise heat transfer in engineering applications.

The present results are pertinent to analyses of environmental flows over rough surfaces, here explored with reference to dilute, particulate, density-driven flows in deep marine setting (i.e., turbidity currents; (Meiburg, 2010). Horizontal velocities within such flows tend to zero near the flow-ambient fluid interface and at the lower boundary, with an internal velocity maximum beneath which the flow can be well approximated as a shear layer (Kneller, 2000). Turbidity currents may flow over substrates that are dynamically rough, either through erosion of substrate to leave a rugose lower boundary(Wynn and Stow, 2002, Eggenhuisen et al., 2010, Macdonald et al., 2011), or via the construction of aggradational bed forms autoregulated by flow conditions (Wynn and Stow, 2002). Flow over erosional roughness may operate in addition to or instead of the commonly invoked hydraulic jump mechanism (Komar, 1971, Mutti, 1987 and Normark, 1979) to cause enhanced turbulence and thereby sediment carrying capacity at locations such as submarine channel to lobe transitions. Turbidity current run-out length is controlled by the balance of potential to kinetic energy conversion vs. the rate of energy dissipation through drag, diffusion and viscous dissipation. The potential energy is controlled by balance of turbulent particle diffusion to gravitational settling (Rouse, 1938). Classical mixing length theory describes the turbulent diffusion of particulate material using an eddy diffusivity (which is proportional to the eddy viscosity, as described above (Menter1994, Shih1995). Thus maximising flow turbulence will increase eddy diffusivity, the potential energy of the flow and hence promote greater run out (Straub et al., 2011, Tokyay et al., 2011b, Eggenhuisen and McCaffrey, 2012); it will also increase resistance to the flow, through drag, promoting decreased run out. Uncertainly over the relative magnitudes of these effects makes it unclear whether greater flow run-out will be promoted during flow over rugose substrates of width to height ratio $w/h \approx 7$; similar decay rates of drag and turbulent diffusion for $w/h > 7$ further suggest there may be no optimal higher w/h ratio over which a flow might experience maximal run-out; both these question await further work.

Moreover, the current results have implications in turbulent particle-laden flows of engineering interest with lower rough boundaries. Seeding particles in the flow is still used as a heat transfer augmentation technique in heat-exchangers and fluidized beds (Michaelides, 1986, Rajan et al., 2008). The enhancement of the eddy viscosity by surface roughness, suggests effective mixing and entrainment of the particles within the channel. Therefore, it would be anticipated that at $w/h \approx 7$ the dispersion and fluctuating velocities of particles are maximally modified, which leads to an increase in the mean distribution of the particles throughout the channel.

5.7 Conclusions

We report the results from a RANS-based numerical modelling study of flow over lower boundary roughness elements, conducted over a wide range of Reynolds numbers. A critical width-to-height ratio of $w/h \approx 7$ is confirmed to be associated with maxima in each flow resistance and eddy viscosity for over-passing flow. A linear rate of turbulence enhancement is seen up to $w/h = 7$, followed by an exponential rate of perturbation decay beyond this critical ratio, with no significant dependence on flow Reynolds number. The results have implications for the optimised engineering designs to enable maximum enhancement of heat transfer. The critical pitch ratio value of $w/h \approx 7$ was for length $L_x = w + c$ where $c/h = 1$, further work can be done to investigate the optimised mixing and flow resistance as a function of ratio c/h. Flow over erosional roughness is a source of turbulence generation for turbidity currents, but further work to constrain the interplay between drag enhancement and particle diffusion is required to clarify the implications for flow propagation.

Chapter 6
Flow over Dunes and Scours: Turbulent Mixing and Flow Resistance

6.1 Motivation

Flows in both submarine and fluvial channels are subject to lower boundary roughness. Lower boundary roughness occurs as frictional roughness suffered by the flow as it moves over the bed (skin friction) or drag suffered by the flow as it moves past a large obstacle (form drag)(Smith and McLean, 1977, Gust, 1988, Grant and Madsen, 1982). Critically, to overcome such roughness the flow must expend (lose) energy and momentum. However, whilst overcoming bed roughness the degree of turbulent mixing in the flow may be enhanced, thus increasing the potential energy of the flow due to the increased capacity required to keep particles in suspension. This is of key importance to density driven flows as the balance between kinetic energy lost and potential energy gained (through turbulent diffusion of suspended particulate material) may critically affect the criterion for auto-suspension. Moreover, this effect of lower boundary roughness may go as far as helping to explain why, even on shallow slopes, channelized submarine density currents can run out over ultra-long distances. Such effects are also important in fluvial systems, where they will be responsible for maximizing or minimizing sediment capacity and competence in different flow environments.

The previous chapter presented data from the characteristics of flow resistance and turbulent mixing over periodic rectangular two dimensional roughness elements. This was to provide a better constraint on the interplay between turbulent mixing and flow drag, in order to develop a better informed understanding of the factors controlling turbidity current run-out. Further, cases with varying aspect ratio and distance were considered to identify which aspect ratio produced the maximum turbulence enhancement. This chapter studies how resistance and mixing vary with bed form shape and aspect ratio keeping the distance between bedforms fixed at the same height-to-distance ratio as was found to optimise turbulence during flow over rectangular ribs. This will be with a view towards studying bedform stability in the following chapter.

6.2 Introduction

Surface roughness plays an important role in the interaction between flow, particle transport and the structure of the bed over erodible beds in many natural systems. The study of the evolution of the seascape and landscape as a result of interaction between the flow and the topography is known as morphodynamics (Parker and García, 2006). As particles are set in motion by near-bed fluid forces, the resulting erosion and deposition processes lead to small changes in bed elevation. Such processes continue under a certain flow regime until various surface features called bedforms are developed. A bedform is a geological term given to form-type roughness developed on the bed surfaces by the interaction between the flow and sediment in motion (Simons and Richardson, 1963). Bedforms preserved in rock records (strata) provides detailed information about the flow structure, depth and more importantly, the transportation of sediment concentration (Shanmugam, 2000). Understanding the morphodynamical mechanics of bedforms is difficult as it involves capturing different components of the flow and near-bed flow conditions. This study deals with CFD modelling of turbulent flow over a range of idealized deep marine bedforms with applications to bedforms found in fluvial and deep marine systems.

6.3 Background

Bedforms can be classified based on the flow regime, scale and morphology (Simons and Richardson, 1963, Ashley, 1990, Davies, 1982). Bedforms categorization depends on the properties of the bed material including grain size, slip velocity and the Reynolds number of particles. Bedforms with complex topography are developed under different range of scales and flow regimes in fluvial, alluvial and deep marine systems. Bedforms in fluvial and coastal environments are formed under shallow water, influenced by the boundary with the atmosphere, whilst those in deep marine systems lie under a deep water column. In such systems bedforms vary in size and are grouped into upper and lower flow regimes. Athaullah (1968) used Froude number values of flow over bedforms to identify bedforms in lower and upper flow regimes. The upper flow regime is associated with supercritical condition (Fr>1) and in fluvial systems, dune bedforms (see below) are in phase with free-surface undulation. Dune bedforms in the lower flow regime form under subcritical conditions (Fr<1) and are out of phase with the fluid surface waves (Simons and Şentürk, 1992).

Two characteristic scales of bedform are commonly developed: dunes and ripples. Rippled topographies comprise small-scale sand waves which are triangular

(Tucholke, 1982) to nearly sinusoidal (Mutti, 1977) in shape and can either be symmetric and asymmetric (Wiberg and Nelson, 1992b). Their sizes vary depending on grain size and shear stress. Ripples typically have a height to length ratio (h/l) greater than 0.05 (Khosronejad and Sotiropoulos, 2014, Lacy et al., 2007, Seminara et al., 1996, Venditti and Bennett, 2000, Wiberg and Nelson, 1992b, Venditti et al., 2005a, Venditti et al., 2005b, Venditti et al., 2005c). Dunes are large-scale bedforms and have greater length to height ratio than ripples, although ripples are steeper than dunes. In fluival and coasal envioments, their wave length is from 1-100 m with amplitude ranging from 0.1-3m (Sohn, 2000, Venditti and Bauer, 2005, Hiscott, 1994, Venditti et al., 2005a). Dunes can form both in symmetric and asymmetric shape (Kostaschuk and Villard, 1996, Carling et al., 2000). As found by Best and Kostaschuk (2002) symmetric dunes in rivers have equal lee and stoss sides typically with slope angles of less than < 8 degrees. Asymmetric dune have stoss side length scale greater than the lee side with slope angle of up to 19º and they carry superimposed smaller dunes on the stoss sides (Best et al., 2004). The crests of symmetric dunes are commonly sharp, and asymmetric dunes rounded (Kostaschuk and Villard, 1996, Kostaschuk, 2000). Moreover the symmetric dunes are developed under suspended load dominated regimes and asymmetric dunes in bed-load dominated regimes (Maddux et al., 2003, Yalin, 1964, Best and Kostaschuk, 2002).

Figure 6.1 shows a schematic of a range of deep-water bedforms as a function of velocity and grain size. In deep water, the substrate over which sediment gravity flows travel are commonly dynamically rough due to the effect of both erosional and depositional processes on the sea floor producing, e.g. erosional scours and aggradational bedforms, respectively (Eggenhuisen and McCaffrey, 2012, Eggenhuisen et al., 2010, Meiburg and Kneller, 2010, Normark, 1991). Such large-scale features have different morphology and dimensions (Wynn and Masson, 2008). Their height commonly ranges up to several metres, and their spacing from a few meters to several kilometres in the extreme case (Wynn et al., 2002, Lastras et al., 2009). Their headwall and sidewall slopes generally range from 6-50°(Macdonald et al., 2011). Giant sediment waves formed by turbidity currents are depositional bedforms (Wynn et al., 2000). Such features have a wave length in km and amplitude of 10-80m and are made from either fine grain (mud and slit) or coarse grain (sand and gravel) (Wynn et al., 2000, Wynn and Stow, 2002). Other bedforms such as anti-dunes have been reported to be formed under supercritical flow condition over erodible beds, and migrate upstream (Hand, 1974). There is a little direct information about the development of such features due to challenges in deep-sea field surveying.
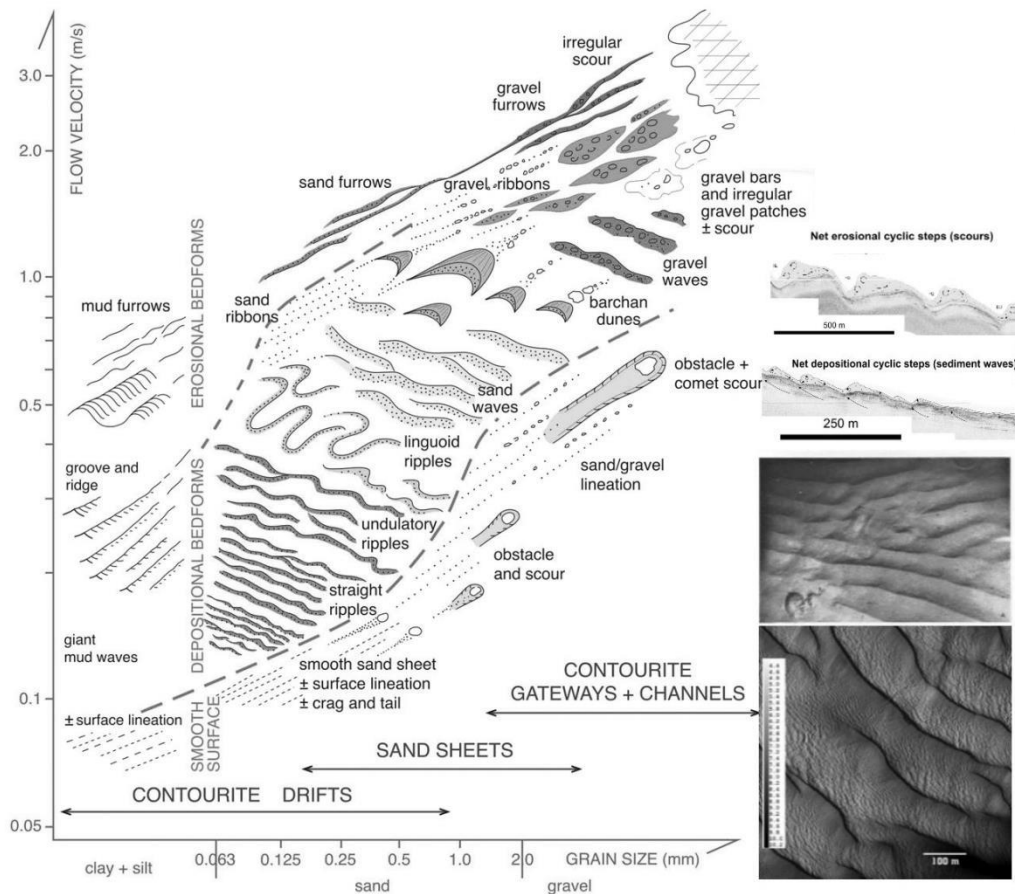
Figure 6. 1: Schematic of seafloor bedforms as a function of grain size and flow velocity reproduced from work by Rebesco et al. (2014) and Stow et al. (2009). Images are modified from Parsons et al. (2005), Heezen and Hollister (1964) and Tubau et al. (2015).

Flows over bedforms are commonly associated with flow acceleration, separation and re-attachment depending on flow Reynolds number and geometrical characteristics of the bedforms. A bed form that develops from a flatbed becomes unstable to perturbation as the shear stress produced by the flow becomes sufficiently large to lift the sediments upwards from the bed (Nelson et al., 1993). The turbulent flow field above bedforms is effected by the geometry of the bedform and in a two-way coupling evolves the shape of the bedform via transporting sediments. Thus, flow erosion and deposition over bedforms effectively constitutes a transport mechanism which changes the geometrical characteristics of the original bedform shape and leads to bedform migration (Van den Berg, 1987). Therefore knowledge of flow field over bedforms is required to understand the relation between flow, sediment flux and bedform development. Initially a number of studies focused on flow characteristics over a fully developed bedforms (Nelson et al., 1993, Wiberg and Nelson, 1992a, McLean et al., 1994, Lyn, 1993, Raudkivi, 1966, Fernandez et al., 2006, James and Cottino, 1995). However, to the author's knowledge there is only a

little information about modelling of flow over various fixed bed geometries (e.g., Orlandi et al., 2006) in order to study bed form development.

The prediction of the sediment flux over bedforms requires the total shear stress to be split into pressure and frictional stresses (Smith and McLean, 1977, Bennett, 1995, Le Bouteiller and Venditti, 2015), although, the total sediment transport is based on computing the total shear stress from the lower boundary of bedforms (Engelund and Hansen, 1967, Brownlie and Brooks, 1982). The partitioning of the skin friction from the total drag is also applied in bed load transport studies (Frank and Jørgen, 1976, Niño and García, 1998). Various authors have used different partitioning methods of the total shear stress . For example, Raupach (1992) partitioned the drag using the atmosphere boundary layer over rough surfaces. This methodology considered the effective shelter area and effective shelter volume generated by the flow shear stress on the vicinity of the roughness elements. The length scale of the pressure field on the bedform surfaces is greater than the scale of pressure on the individual grain and hence the effect of form drag on the bed load transport would be insignificant (Maddux et al., 2003). The mixing of the sediments in suspension is determined by turbulence, which is mainly produced by shear in the bottom boundary layer and free shear layers. In flow over bedforms pressure forces contribute more than viscous forces to the total drag and therefore they have a greater influence in mixing .

This study investigates the changes in bed resistance to flow over idealized bedforms found in deep-sea floors. The run-out distance of the turbidity currents may be affected by the type of lower boundary roughness. Enhanced turbulent mixing will increase the potential energy of the flow, thus promoting longer run-out, whereas the associated increases in drag may reduce run-out. To assess the balance of these effects, a Reynolds Averaged Navier-Stokes (RANS) was performed following the technique of (Arfaie et al., 2014) to assess the changes to turbulent mixing and drag across a range of lower boundary roughness configurations.

6.4 Assumptions and Model Set up

There is strong evidence that the inner wall region of sediment gravity flows (below peak velocity) resembles those corresponding to open-channel flows (Altinakar et al., 1996, Eggenhuisen and McCaffrey, 2012, Kneller, 2003, Kneller et al., 1999, Sequeiros et al., 2010). Thus, the present CFD code can be regarded as a simplified model for the inner region of the turbidity currents. By adopting this simplified model, we can gain insight on the effect of different bedform shapes on the turbulent flow field and the sediment carrying capacity of turbidity currents. Here, only the flow of pure seawater over the idealised bedforms is considered. In the next chapter, this work is extended to examine the effects of the flow on particle transport. Further it is assumed that the particle concentrations are sufficiently small that they do not have a significant influence on the flow fields studied here.

The rib type roughness elements studied in the previous chapter ($S1$) are generalised in $S2 - S4$ to represent idealised symmetric bedforms, anti-dunes and dunes ($S2 - S4$) respectively (Figure 6.2); in $S5$ to $S7$, the simple shapes $S1 - S4$ are combined to approximate more realistic natural lower boundary rugosities of symmetric dunes, anti-dunes and normal dunes, respectively.
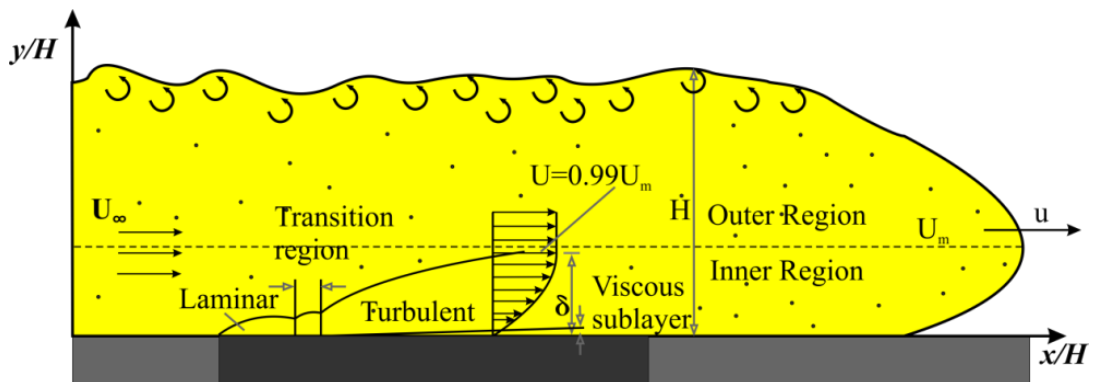
Figure 6. 2: The structure of turbidity currents modified from the work by Kneller and Buckee (2000). Note: the velocity profile below the velocity maximum approximates that of a shear flow.
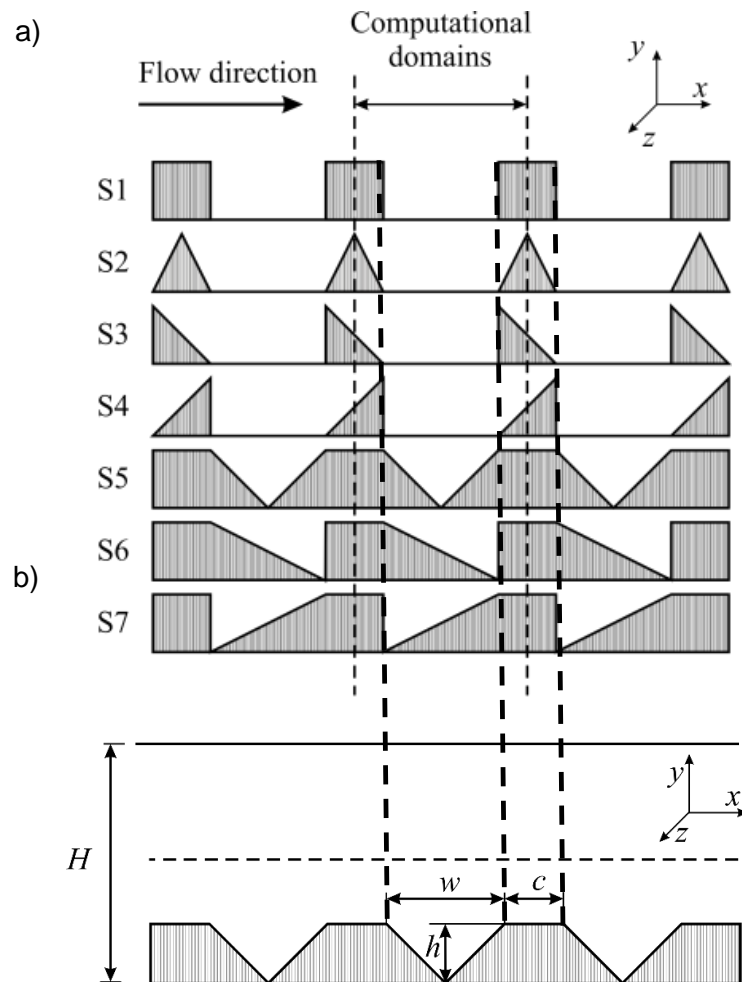
Figure 6. 3: (a) Schematic illustration of the computational domains shown by the dashed lines for pressure driven flow over idealized bedforms under a periodic condition. (b) Channel flow configuration with roughness segment S5 positioned at the solid bed.

6.5 Numerical modelling

CFD simulations were conducted for fully-developed turbulent flow over a range of idealized bedforms, which are periodically repetitive in the stream-wise direction. Figure 6.3 describes the aligned flow rugosity for seven different bed roughness forms, $S1-7$. As well as rugosity studies of both the effect of the ratio of axial roughness length to height ratio (c/h) was conducted. The upper flat surface length

of the roughness element c is varied while the roughness element height is remained fixed to aspect ratio $c/h = 1, 2, 4$ and 8 for each of the bed geometries.

In order to model fully-developed Newtonian, incompressible flow over regularly spaced roughness element shapes a steady state $K - \varepsilon$ model was used, closed by a periodic boundary condition in the direction of mean flow, as described in earlier chapters. The lower boundary was comprised a hydraulically rough bed, in one of forms S1-7, whilst the upper boundary was flat. The flow was driven by a constant mean pressure gradient $\frac{\overline{\partial p}}{\partial x} = 0.5$ kg m^{-2} s^{-2}, added as a source term in the x$-$momentum equation (4.9). The flow has a friction Reynolds number $\mathrm{Re}_\tau \approx 10^5$, where $\mathrm{Re}_\tau (= \mathrm{u}_\tau H/2\,\nu)$ is based on the shear velocity $\mathrm{u}_\tau \left(= \sqrt{H/\rho \frac{\overline{\partial p}}{\partial x}} \right)$ and half-channel height $H/2$. Flow was of density of 1027 (kg m^{-3}) and kinematic viscosity of 1.36×10^{-6} m^2 s^{-1}.
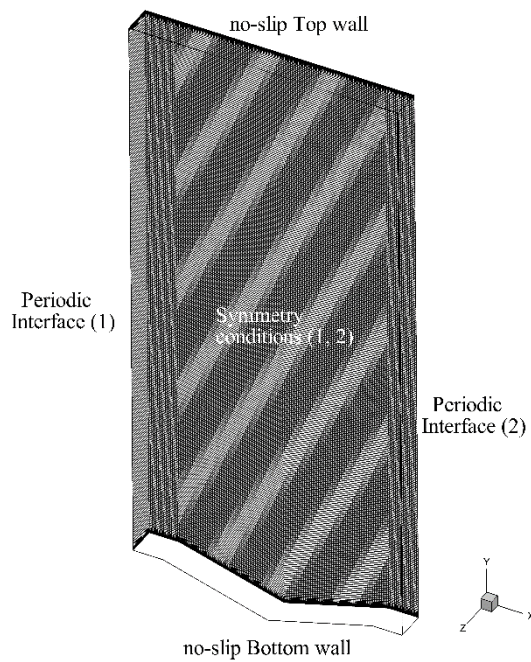
Figure 6. 4: Computational grid and boundary conditions for $S5$ with aspect ratio $c/h = 2$.
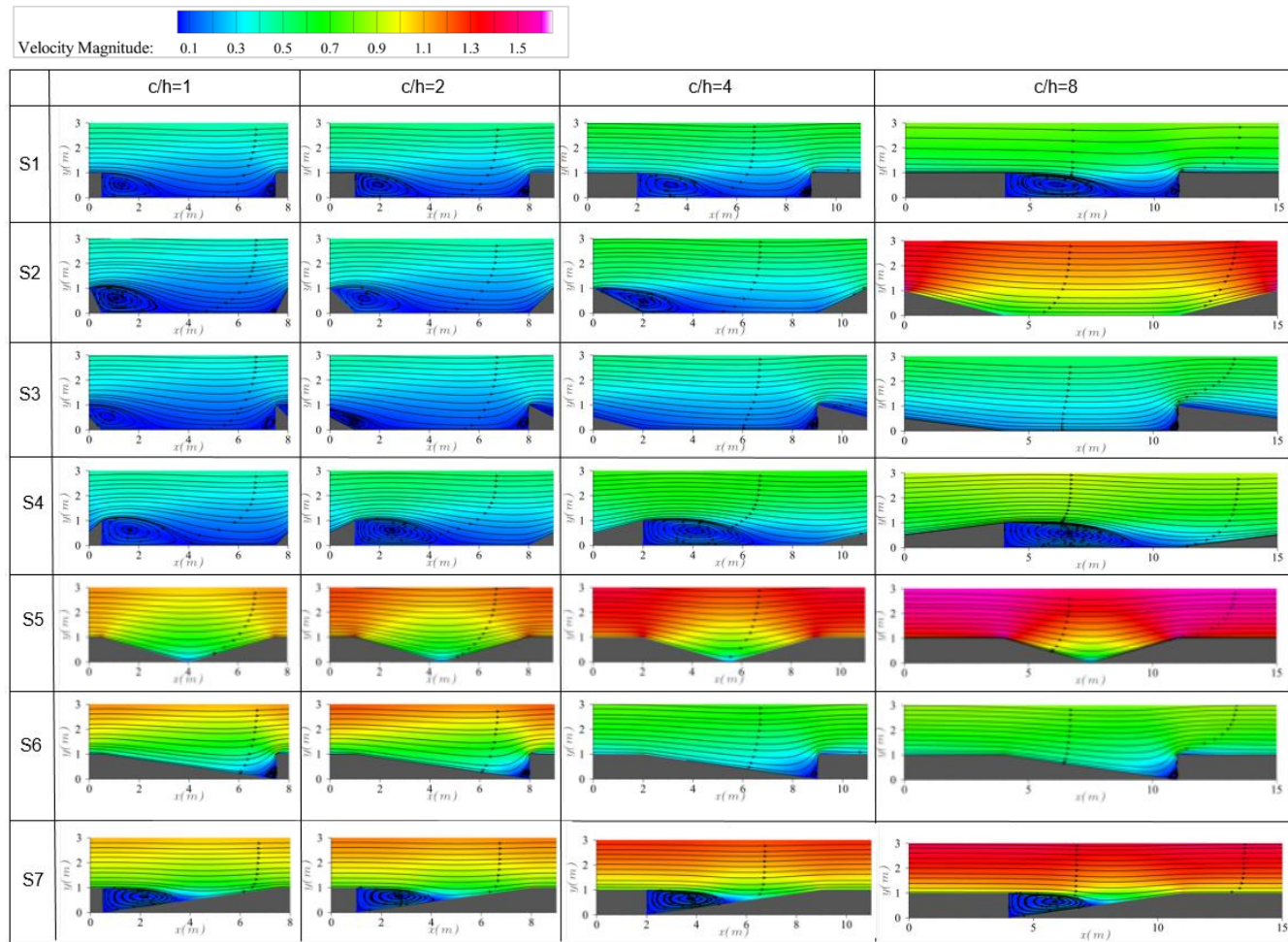
Figure 6. 5: Matrix view of the velocity magnitudes with flow streamlines over various bedforms with varying aspect ratio c/h.

6.6 Model solutions

The results for flow resistance and turbulent mixing are obtained for unidirectional turbulent flow over fixed two-dimensional bed forms at a high Reynolds number. Below, the effect of the bed slope angle on the flow drag and the eddy viscosity is discussed. In addition the average skin friction and form drag is computed to provide insights into predicting sediment transport rate.

6.6.1 Mean velocities

Here we analyse how typical well-developed bedforms modulate the flow velocity field. The relative positioning of the two adjacent bedforms and shapes are shown in figure 6.3. Figure 6.5 displays a matrix view of velocity magnitude contours as a function of bedform topography and aspect ratio. Shapes 1-4 behave as K−type roughness element as the cavity length w is larger than the height h ($w/h \approx 7$).

The D−type surfaces ($S5 - S7$) are arguably closer to the flat wall case and consequently are less effective at slowing down the flow than the K−type surfaces. Therefore, D−type bedforms are expected to result in greater streamwise wall shear stress than K−type bedforms. This is due to the higher shear velocity exerting more forces over the boundaries of D−type surfaces than the K−type surfaces. Thus, more sediments are likely to be eroded from the D−type surfaces into suspension. For D−type cases, the flow separation can only be observed for shape $S7$ as can be seen by the mean flow streamlines. For this shape the cavity is filled with a vortex bubble.

Small secondary recirculating regions are observed behind the downstream edge of shapes $S1$, $S2$, $S3$, $S4$ and $S7$. Such vortices appear to be a function of the fluid-facing slope angle. For example shapes $S1$ and $S4$ with downstream edges at 90 degree angle produce larger vortices compared to shape $S2$. This is further confirmed with shape $S5$ which has no recirculation region at all. The comparison of the streamlines for shape $S3$ and $S6$ indicate that the development of the secondary vortex on the slope facing bedforms does not depend on the spacing between two bed forms. In the previous section, it was observed that for the D−type cases the focal points of the recirculation region were located at the center of the cavity and had a circular shape. However, for shape $S7$ the vortices are shifted towards the leading slope of the downstream bedform and behave similarly to intermediate type roughness.

In Chapter 5, we observed that for both intermediate and $D-$type surfaces the vortices cover the entire cavity as also observed with shape $S7$. Further, the streamlines in shape $S7$ are distributed more closely to parallel when approaching the cavity. Therefore, less intense interaction of the flow within cavity with the overlying shear layer is seen compared to $K-$type cases. In figure 6.5 shapes $S1 - S4$ ($K-$type roughness) are characterized by unstable eddies with length scale of order h or bedform height formed in the cavity between the roughness elements. The flow streamlines in figure 6.5 shows that for $K-$type roughness the flow separates near the bedform crest, followed by reattachment of the flow on the flat bed next to the adjacent bedforms. Moreover, the streamlines of shape $S1$ show that as the c/h value increases the focal point of the recirculation region shifts more towards the leading face of the downstream rib, approaching intermediate type roughness behavior. This behavior is also apparent for shape $S4$ where the streamlines become more parallel from $c/h = 1$ ratio to $c/h = 8$.

Figure 6.5 further illustrates how the velocity flow field behaves as a function of aspect ratio c/h over fixed bedforms. From figure 6.5 it is obvious that the velocity increases with increase in ratio c/h . Also, the re-attachment length appear to increase for all $K-$type bedforms with the increase in ratio c/h. Previous authors also found the length of the recirculation region increases with the windward slope of the aeolian sand dunes (Faria et al., 2011, Qian et al., 2009, Parsons et al., 2004). The behavior in reattachment is attributed to a reduced turbulence intensities and turbulence diffusivity at space between the recirculation region and the next roughness element. However it appears to remain constant for $S7$ ($D-$type case). Further, no recirculation is seen for $c/h = 8$

The normalized stream-wise velocity $\overline{U}_{rough}/\overline{U}_{flat}$ is plotted against ratio c/h for all lower roughness boundary in figure 6.6. Here the area-weighted average velocity over the flat bed $\overline{U}_{flat}$, is used to normalize $\overline{U}_{rough}$ which is the area-weighted average velocity in $x-$direction for rough bed cases. Figure 6.6 shows that the maximum average velocity across all aspect ratios is seen for shape $S5$ and the minimum for shape $S3$. Shape $S2$ is noted to have a greater velocity gradient with the change in aspect ratio c/h compared to other bed shapes. In addition, figure 6.6 shows there is an upward shift in velocity between $D-$type and $K-$type case. However, the magnitude of this shift decreases with the increase in aspect ratio c/h. As can be seen in figure 6.6 , the value of U_{rough}/U_{flat} in $S4$ (or idealized asymmetric dune) is greater than in $S2$ (or idealized symmetric dune). This agrees with the wind

tunnel study of Faria et al. (2011) for the stoss slope effect on the aeolian sand dunes where the author observed a greater friction velocity for asymmetric than symmetric aeolian dunes. Previous authors have shown a direct comparison of flow over symmetric and asymmetric dunes in subaqueous environments (Villard and Kostaschuk, 1998, Kostaschuk and Villard, 1996). For these studies natural subaqueous symmetric dunes showed greater mean flow velocity and sediment transport rate than the asymmetric dunes. However, the natural asymmetric dunes had superimposed small dunes on their stoss sides. The comparison in the present study ascertains that the form drag from the superimposed dunes have quite a considerable effect in reducing the shear velocity of the flow and future studies should therefore include small superimposed dunes on the stoss side.
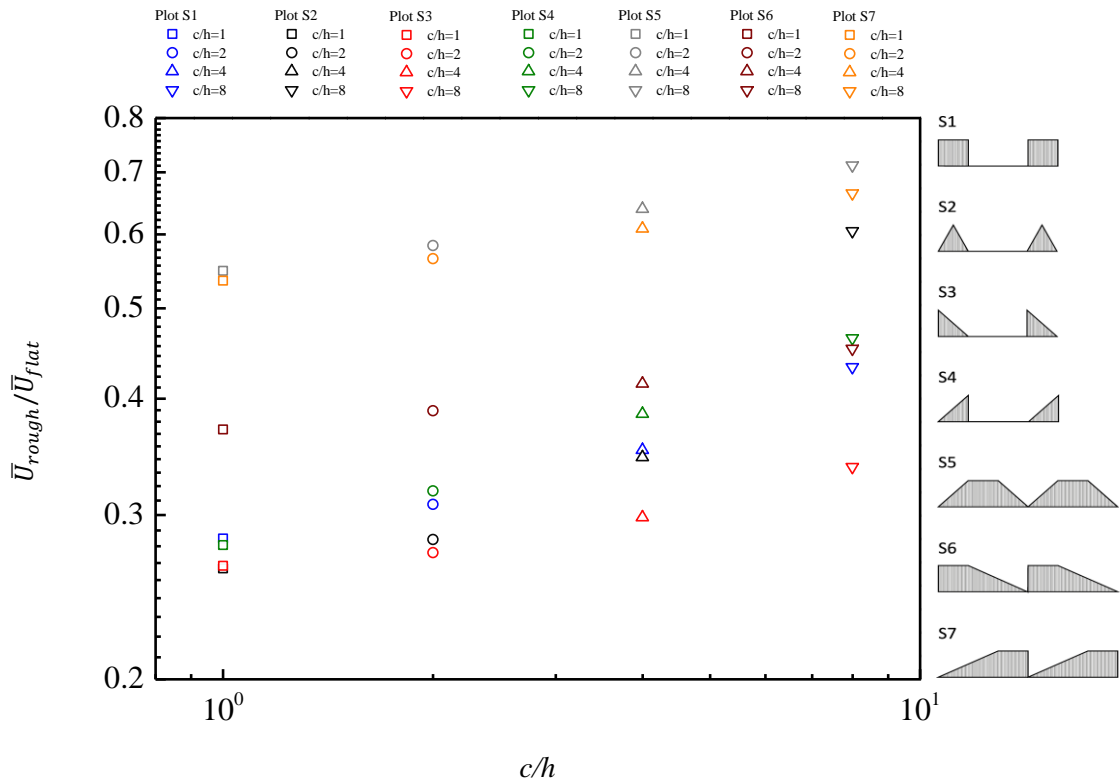
Figure 6. 6: Normalised stream-wise velocity as a function of aspect ratio for all bed roughness cases.

6.6.2 Flow resistance

The transport of fluid over bedforms is associated with energy losses (in both kinetic and potential energy). The resistance to flow over various bed geometries is computed using the Darcy-Weisbach f equation (5.2) which is a function of Reynolds number and roughness height to flow depth ratio (h/H). The friction factor is

computed based on the same fixed pressure gradient, which is equal for all bed roughness shapes, and on the area-weighted average stream velocity of the individual bedforms. The results in figure 6.7 show that the flow energy losses decrease with the increase in ratio c/h for all bedform shapes. The maximum head losses or flow resistance occurs for the transport of fluid over shape $S3$ and the minimum head losses occurs for shape $S5$. The friction factor (flow energy loss) is greater for $K-$type (with spacing) roughness elements than $D-$type (without spacing) cases. In general, lower energy losses of the flow were observed for bedforms with low-angle (or higher ratio c/h) for a constant flow depth.
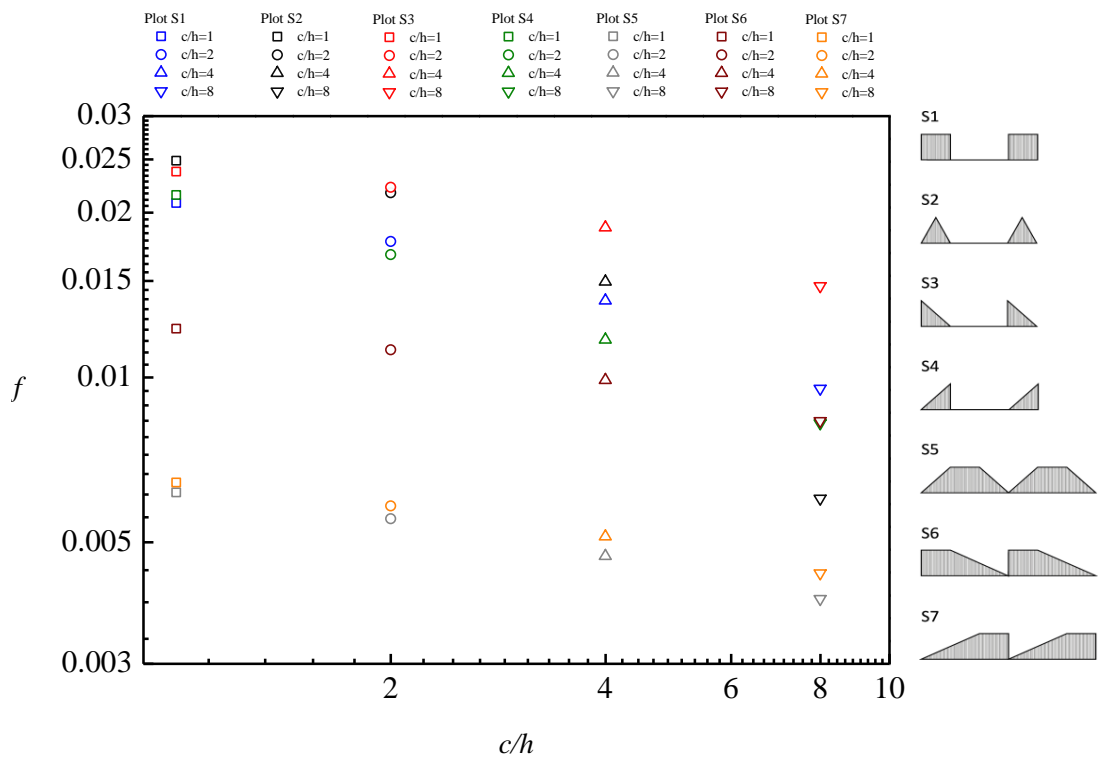
Figure 6. 7: Darcy-Weisbach friction factor as a function of aspect ratio for flows over different roughness elements.

6.6.3 Skin friction and form drag

The total shear stress of the flow acting on the roughness shapes can be partitioned into skin friction and form drag (Einstein, 1950) as follows:

$$\tau = \tau_f + \tau_s \tag{6.1}$$

where τ total shear stress is, τ_f is the shear stress due to pressure and τ_s is the stress due to friction on the boundary. Figure 6.8 shows the computed skin friction and form drag of roughness shapes as a function of aspect ratio. The viscous force can be obtained from the integral of the wall shear stress as

$$\overline{F_v} = \int_w \tau_w \vec{s}.\vec{x}ds \qquad (6.2)$$

To calculate skin friction, the viscous force is normalised by

$$D_s = \frac{\overline{F_v}}{1/2\rho u_f^2 A_w} \qquad (6.3)$$

where u_f is the area-weighted average velocity of a fully developed flow at the outlet of the flat bed case, ds is the area of the surface, $\vec{s}$ is the unit tangent vector and $\vec{n}$ is the unit normal to surface. The wetted areas A_w for aspect ratios $c/h = 1, 2, 4, 8$ are $A_w = 9, 11, 15, 23 \text{ m}^2$. The pressure forces are computed as the integral of the pressure distribution along the bottom boundary as follows

$$\overline{F_p} = \int_w p\vec{n}.\vec{x}ds \qquad (6.4)$$

Therefore form drag can be written in a non-dimensionalised form as

$$D_f = \frac{\overline{F_p}}{1/2\rho u_f^2 A_p} \qquad (6.5)$$

where the projected area A_p is equal to 1 m^2 for all bedform simulations. Figure 6.8 shows the results for partioning the total shear stress into form drag and skin friction for non-uniform lower boundary surfaces.

Both skin friction and form drag are found to increase with increase in ratio c/h. The increase is due to the integral of the pressure and viscous forces for the extended surface produced by the increase in aspect ratio c/h. This agrees with the wind tunnel experiments on dunes by Faria et al. (2011) and Qian et al. (2009) where the total value of wall shear stress increased with increased windward slope angle. Further, figure 6.8 indicates that the value of skin friction is greater for D −type than K −type bedforms. This is primarily due to either the lack of flow separation ($S5$ and $S6$) or flow separation with reattachment on the downstream sloped edge next adjacent element ($S7$) leading to a low pressure gradient. Also, the value of form drag is greater for the K −type than D −type bed roughness configurations. Therefore, as can be noted in figure 6.8, the cases with no horizontal spacing between the two roughness elements, produce a lower value of form drag D_f leading to higher value of skin friction compared for cases with spacing between the roughness elements (see shape $S5 − S7$). In general the value of averaged stream wise pressure drag is greater than the

averaged streamwise skin friction for all bedforms and aspect ratios. This agrees with the result of McLean and Nikora (2006) for turbulent unidirectional flow over sand dunes. Moreover, the difference between the form drag and skin friction reduces with the length of cavity between two adjacent bedforms. A negative value of area-weighted average streamwise wall shear stress was obtained for shape $c/h = 1$. Figure 6.8 shows an absolute value of the skin friction for this aspect ratio. This suggests that the recirculation vortices apply a greater force in the upstream direction to the boundary of the bed than the force applied by the streamlines in the downstream direction. A local maxima is produced by shape $S3$ at $c/h = 4$ which appears to result from the absence of recirculation vortices inducing a sudden change of pressure at this ratio.

The rate of sediment entrainment is a function of the skin friction. However the total sediment concentration is controlled by the total averaged shear stress on the bedform boundary, as discussed earlier in this section. Figure 6.8 predicts that the sediment entrainment rate is greater for bed form $S5 - S7$ (D −type) than $S1 - S4$. The results also predict that the suspension of the sediment should be greater for K −type than D −type surfaces. Both the sediment suspension and entrainment rate are predicted to increase with the decrease in slope angle.
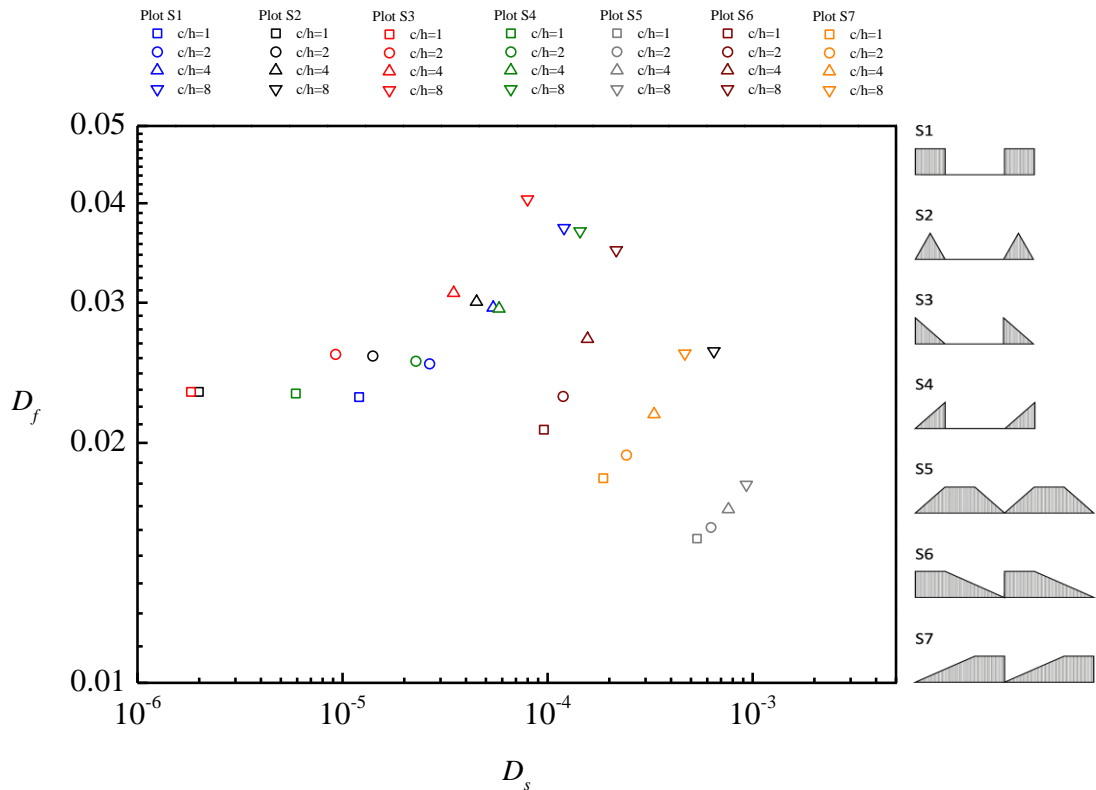
Figure 6. 8: Pressure drag versus skin friction over bedforms normalised by the bulk velocity u_f.

6.6.4 Turbulent mixing

A simple closure for the upward mixing of suspended sediment in turbulent flow was introduced by Rouse (1937). Here we compute the non-dimensionalised eddy viscosity μ^+, in the momentum equation to evaluate mixing of different bed geometries. The transport of sediment concentration in the vertical direction can be described by,

$$w_s \phi - \varepsilon_s \frac{\partial \phi}{\partial y} = 0 \tag{6.6}$$

where w_s is the sediment settling velocity, ϕ is the volumetric sediment concentration and ε_s is the eddy diffusivity. Here the sediment dispersion coefficient (or eddy diffusivity) is proportional to the turbulence dispersion coefficient (or eddy viscosity). Figure 6.9 plots the μ^+ as a function of c/h for all bed geometries. The overall results suggest that bedforms with high flow resistance result in high turbulent mixing. The data further shows that μ^+ is reduced when the aspect ratio of the bedforms is increased. The lowest turbulent mixing belongs to bed form shapes with closed spacing for shapes $(S5-7)$ and the highest to bed form $(S1-S4)$. The comparison of figure 6.8 and 6.9 suggests that turbulent mixing depends on form drag rather than skin friction. In general the present data show that turbulent mixing is a function of bedform shape and bed roughness slope.
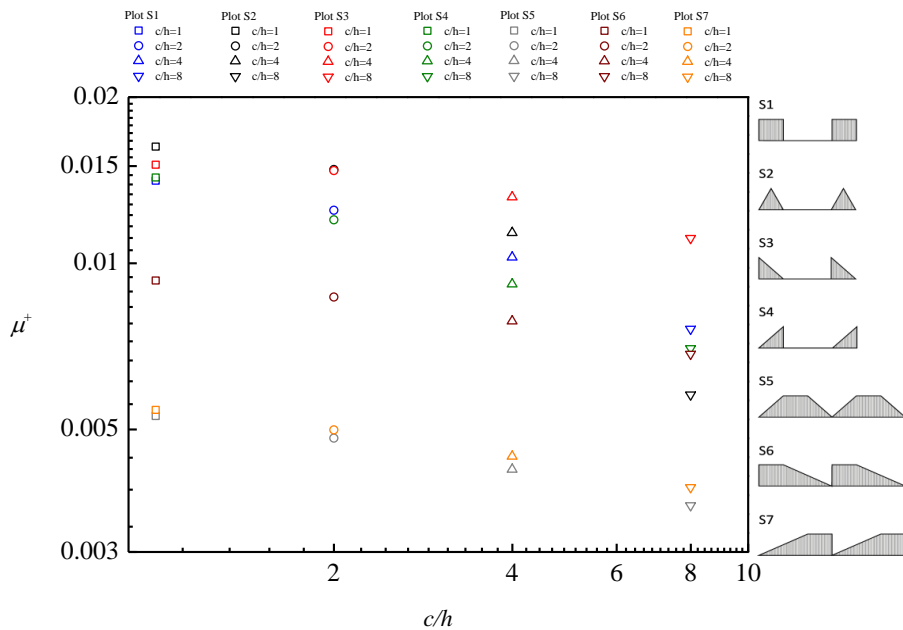
Figure 6. 9: The normalised eddy viscosity as a function of aspect ratio c/h.

6.7 Discussion

Turbidity current run-out length is controlled by the balance of potential to kinetic energy conversion as a function of the rate of energy dissipation through drag, diffusion and viscous dissipation. The potential energy is controlled by the balance of turbulent particle diffusion to gravitational settling. Thus maximizing flow turbulence will increase the eddy diffusivity, the potential energy of the flow and hence promote greater run out (Straub et al., 2011, Tokyay et al., 2011b, Eggenhuisen et al., 2011); it will also increase resistance to the flow leading to loss in kinetic energy of the flow, through drag, thus promoting decreased run out. Figure 6.10 shows the relation between flow resistance and turbulent mixing as a function of aspect ratio and bedform shapes.

Shape $S5$ produces the least flow resistance and eddy viscosity. The low value of vertical mixing in $S5$ appears to be caused by the lack of flow separation and the closed gap between two adjacent bedforms. Low value of potential energy for this bedform compared to other case implies that turbidity currents may experience shorter run-out length during flow over lower boundaries of this character. However, the low value in friction factor suggests that the flow experiences lower loss in kinetic energy promoting longer run-out length. The linear trend in friction factor versus eddy viscosity make it unclear whether the friction factor dominates over eddy viscosity or vice versa (see figure 6.10) in predicting runout.

Moreover, the results indicate that flow separation has an insignificant effect on the value of upward sediment mixing for the skimming flow type ($S5 - S7$), where the flow reattaches on the slope of the downstream roughness element. Figure 6.10 further illustrates that the blunt facing bedforms $S5$ and $S7$ achieve a higher turbulent mixing than the slope facing bedform $S6$. $K-$type surfaces also show an increase in μ^+ and f with the orientation of the downstream facing flow (or stoss side). For instance, shapes $S2$ and $S4$ lead to reductions in the values of mixing and flow resistance compared to shape $S1$ and $S2$ (with $90°$ side facing flow angle). For the $K-$type surfaces the effect of flow separation on the flow resistance and turbulent mixing is also weak. This effect is described for shape $S3$ at $c/h = 2$ (with flow separation) and $c/h = 3$ (with absence of flow separation) in figure 6.5 and 6.10.
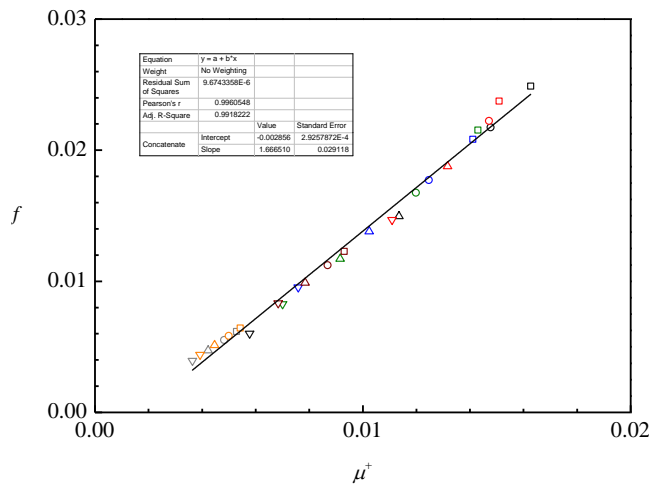
Figure 6. 10: Flow resistance as a function of eddy viscosity for all bedforms.

6.8 Conclusions

Numerical simulations have been performed at a high Reynolds number for shear flow over a series of lower boundary roughness elements comprising a range of idealized bedform shapes, of varying crestal length to height ratio c/h at a fixed width to height ratio (w/h). The total basal shear stress is split into skin friction and form drag and to show how the respective magnitudes vary as a function of bedform shape and scale. Moreover the present results demonstrate how bedforms affect the balance of energy lost (through frictional) as a function of the potential energy gained (through turbulent mixing).

The drag coefficient results demonstrate that the total flow resistance decreases with the increasing aspect ratio c/h. This suggests that the turbidity current may expend less energy in overcoming the obstacles and hence promoting increased run-out distance. On the other hand, the dimensionless eddy viscosity, which represents turbulent mixing of the flow, decreases with the increasing ratio c/h. As a consequence the potential energy of the turbidity current reduces, promoting shorter run-out. Remarkably, figure 6.10 indicates that the relation between flow resistance to eddy viscosity collapses to a single monotonically increasing linear function for all bedforms considered.

This, as we found in Chapter 5, we cannot conclude that any of the shapes considered definitively promote or reduce runout length. To elucidate bed form roughness effects on the potential run-out distance of turbidity currents, further work is needed to investigate the change in kinetic and potential energy through increased drag and decreased mixing or decreased drag and increased mixing.

Chapter 7
Flow over Dunes and Scours: Particle Transport

7.1 Motivation

In the two preceding chapters, resistance and turbulent mixing in constant density flows over idealised bedforms were studied. In this chapter, the analysis is significantly extended to study details of sediment transport over idealised bed forms.

The pathways of sediment gravity flows in deep sea basins are typically covered with large-scale bedforms, developed by erosional and depositional processes (Rebesco et al., 2008, Wynn and Masson, 2008). Predicting the turbidity current flow dynamics and bed interactions is of immense value in understanding whether or not there is a coupling between flow dynamics and the substrate, which might affect the flow run out, and to identify the location of deposits. Observing bed form evolution and measuring the turbulence flow field around prototype roughness features, especially close to the wall region, is often not practical. Hence, a numerical approach is useful to investigate such cases. Accordingly, this study focuses on:

(i)   Modelling the two-way coupling between turbidity currents and bed forms.
(ii) Adopting a computational fluid dynamics approach to couple the hydro- and morpho-dynamical models.
(iii) Linking bedforms development with properties of the overpassing flow.

The study begins in this chapter by modelling quasi-steady flow over stationary bedforms (one-way coupling). This is justified because bed form evolution takes place over very long time scales compared to hydrodynamic timescales. The interaction between flow and bedform is modelled subsequently using specified mass flux boundary conditions on the lower boundary that are based on erosion and deposition models.

An algebraic slip model (Manninen et al., 1996) has been employed to compute the relative motion of sediments and water in the liquid mixture. Full details of this model are presented in Section 7.4. As in previous chapters, the model considers flow below the velocity maximum. Although the original focus of the thesis was on turbidity currents, the work considered here is expected to be relevant to flows in more general geophysical contexts, such as bedforms in rivers and in both shallow and deeper marine environments. The analysis is considered essentially to model the main body of the turbidity currents (not the head nor the tail), below the velocity maximus, since

most morphodynamic work is done by the body, and the lower part of the turbidity currents is well approximated by shear layer flow (i.e. the modelled scenario).

The study concludes in Chapter 8 by modelling unsteady flow over moving bedforms. The bedform motion is modelled using a deforming mesh whose boundary deformation velocity is based on the mass flux boundary conditions previously employed for the quasi-steady studies. For this work, element initial simulations are conducted for an unsteady shear flow over low-angled periodic symmetric dunes to investigate the inherent evolution of systems under a high stream flow condition, $\mathrm{Re_f} \approx 10^7$. The computed eroded substrate topography is analysed and compared with published field data.

These results have implications for both turbidity current flow competence and flow capacity, and hence the run-out length. Uncertainty over the relative magnitudes of these effects makes it unclear whether the greater flow run-out will be promoted by enhanced mixing by flow over rugose substrate or depleted by the loss in energy budget.

7.2 Introduction

In some cases, suspended sediments have no significant effect on the flow turbulence and hence may be studied independently of the presence of the sediments within the flow (Muste and Patel, 1997). However, in many cases the suspended sediment may have a significant influence on the turbulence structure. For example it is the turbulence which determines the local erosion and deposition in the river-bed and sea-bed leading to instability of bed surfaces (Coleman et al., 2003, McCave, 1984, Faraci and Foti, 2002, Gust and Walger, 1976, Gust, 1976). Thus despite a significant research effort (Best, 1993, Leeder, 2009a, Perillo et al., 2014, Van Rijn et al., 1990), a key challenge in modern sedimentology remains linking the hydrodynamic processes of sediment-laden flow interaction with lower boundaries and the evolution of resultant morphodynamic products, i.e., bedforms. Such flow processes play a crucial role in the geomorphic evolution of riverbeds, sea-beds, estuaries and coasts. Therefore, the interaction between turbulence, suspended sediment and the lower boundary is of great importance to river and coastal engineers, and to geologists, as it plays a key role in modulating the transport and deposition of sediment in shallow- to deep-water environments.

Computational fluid mechanics is a convenient and effective method of studying sediment transport over topography; the RANS equations (see Chapter 4) are

commonly used to provide the turbulence closure model of the flow field. The flow and the sediment transport and the bed deformation equations are either solved discretely or simultaneously. Models may be depth-resolved or depth averaged. For the depth-resolved models, it is essential to describe mathematically the exchange between the flow and the sediments near the bed. On the other hand the depth-averaged models are defined based on depth averaged equations, incorporating the Boussinesq, shallow-water and Saint-Venant equations. The vertical sediment motion for suspended load is included in the convection-diffusion equation. Therefore the depth-averaged models are another modelling approach which are useful for modelling the grain transport and morphological changes in geophysical flows.

7.3 Literature review

Sediment transport is commonly treated in geophysical modelling (Blazek, 2005, Launder and Spalding, 1972, Kolmogorov, 1942, Hesp et al., 2015, Wilcox, 1988). Turbulence is responsible for the transporting of the sediments, and in turn, sediments in suspension affect the turbulence characteristic in the flow (Wilcox, 1993); the associated coupling mechanism between the sediment and turbulence is of fundamental importance in the physics of the sediment transport. However, there is no consensus as to whether the turbulence is enhanced or attenuated by suspended particles, depending on the particle size and turbulence length scale (Menter, 1994, Menter, 1992, Fluent, 2009, Rotta, 1951, Launder et al., 1975, Cao et al., 2003). In previous experimental studies, authors found that the von Karman constant k, which is a function of the logarithmic mean velocity profile, is decreased for the sediment-laden flow compared to that of free particle flow (Einstein and Chien, 1953), (Middleton and Southard, 1984). Coleman (1981) introduced a model in which the von Karman constant remained fixed when an extra term due to the effect of suspended was added to the original logarithmic distribution. Previous studies which focus on the effect of density stratification by suspended sediment on the sediment laden flow are (Smith and McLean, 1977, Soulsby and Wainwright, 1987, Villaret and Trowbridge, 1991).

van Rijn (1984) conducted an experiment to estimate a function for the sediment entrainment rate. Furthermore, van Rijn (1985) implemented a mathematical model to obtain concentration profiles for net-erosion vs. deposition processes over uniform and non-uniform lower boundaries. Later research focused on introducing empirical expressions for the sediment entrainment rate (Garcia and Parker, 1991, Pizzuto, 1987, Cao, 1997). Celik and Rodi (1985) developed a mathematical model for the

transport of sediment concentration in open channel flow. A net boundary condition flux for sediment concentration was defined near the bed which described the net erosion and deposition from the bed.

The capacity of the flow is the maximum mass of the sediment that the flow can carry in suspension (Hiscott, 1994, Leeder, 2011). Sedimentary equilibrium condition is reached as the flow transports sediments at capacity (Manville and White, 2003) . Under such conditions, the sediments which have been deposited can readily be exchanged by eroded sediments. At capacity, any sediments entering the system will be deposited on the bed with no influence on the suspended sediment concentration (Govers and Rauws, 1986). A "non-capacity condition" occurs when there is no active layer sediment layer on the bed. In this condition all the sediments within the flow remain suspended (Cao et al., 2006). New sediments added to the flow will result in an increase in sediment concentration but with no deposition on the lower boundary. Cellino and Graf (1999) experimentally determined the suspended load component of sediment transport in open channel flow under capacity and non-capacity conditions. The carrying capacity is linked to the energy of the turbulent motion that keeps the particles in suspension. Cellino and Graf (1999) suggested that deposition is controlled mainly by a decrease of capacity through reduction in shear for mono-dispersed particles. Dorrell et al. (2013b) developed a polydisperse model for the erosional-depositional flow processes over erodible and non-erodible beds. The model demonstrated that loss in flow capacity is the main driver for deposition of polydisperse sediments.

The present study aims to provide further insight into the interaction of particle-laden flow with a range of idealized bedforms. We employ the previously validated computational code to perform numerical modelling simulations of particulate flow interacting with geometrical bed features in geophysics known as bedforms. The modelling solutions of flow over roughness are compared with the flow over a flat surface. We investigate the relationship between the mass of suspended sediment, grain size and the bed irregularities.

7.4 Mathematical modelling

7.4.1 Multiphase modelling of sediment-water mixture

Particle transport is commonly modelled as a scalar advection diffusion equation, with an additional advective term to take account of the downwards particle mass flux due to non-zero settling velocities (Celik and Rodi, 1988, Celik and Rodi, 1991, Rouse, 1937, Huang et al., 2007, Huang et al., 2005, Stacey and Bowen, 1988b, Necker et al., 2005):

$$U\frac{\partial C}{\partial x} + V\frac{\partial C}{\partial y} = \frac{\partial}{\partial y}(\Gamma_s\frac{\partial C}{\partial y} + w_s C) \qquad (7.1)$$

Where w_s is the particle settling velocity and C is the time-averaged mean particle concentration, Γ_S is the turbulent transport coefficient of the suspended particles, U and V are the velocities in x- and y-direction respectively. However, most commercial CFD packages such as ANSYS Fluent and ANSYS CFX offer a more generally applicable model, known as the Algebraic Slip Model (ASM) in ANSYS CFX, or the Mixture Model in ANSYS Fluent. The model was first formulated by Ishii (1977), where it was called the Drift Flux Model. In this form it was applied mainly to multiphase flow problems in one spatial dimension, as described in the book by Wallis (1969). Later, the model was described in three spatial dimensions by Manninen et al. (1996). This paper forms the basis of the model implementation in ANSYS Fluent and CFX. The approach was called the equilibrium Eulerian approximation, and followed the same formulation as was found earlier by Carrier (1958) and later advanced by Marble (1970), who used the model to deal with particle-laden flows for compressible fluids in the Dusty Gas approach. The model considered the particle-laden flow as a single phase in which the density depends on the local concentration of the particles in suspension. Further, the model assumes that the size of particles is small enough that their motion is controlled by the ambient fluid. This occurs when the time for the particles to achieve their terminal velocities is negligible compared to inertial time scales. The ratio of these time scales is called the Stokes number, so the model is valid when Stokes number is small (Balachandar and Eaton, 2010) - see also below. The model has been derived in a mathematically more rigorous way, and extended to account for the effects of interfacial forces other than the drag force, such as the lift and virtual mass forces (Ferry and Balachandar, 2001, Ferry and Balachandar, 2002, Bagchi and Balachandar, 2002). The equilibrium Eulerian approximation method was found to be accurate for low value of Stokes number for

determining the particles velocity for turbulent flow $St \leq 0.2$ (Shotorban and Balachandar, 2006).

The accuracy of the mixture model has been verified in the literature (Hanzevack and Demetriou, 1989, El-Batsh et al., 2012, Pericleous, 1987, Altway et al., 2001, Lin and Ebadian, 2008). For example Lin and Ebadian (2008) conducted a numerical study on the development of the slurry flow (sediment-water mixture) in a pipeline geometry. He found the mean pressure gradient solution to be in a good agreement with experimental data of Skudarnov et al. (2001) and Newitt et al. (1955).

The mixture model has been employed recently to model two-dimensional sediment-driven gravity flows by An and Jia (2010) and Yam et al. (2011). An and Jia (2010) investigated the plunging characteristics of turbidity currents using an algebraic slip model. The ASM model was found to be in a good agreement in capturing the reflux and backflow by the plunging of density currents. Yam et al. (2011) used the ASM model with the inclusion of turbulence dispersion model to investigate the evolution of turbidity currents. He suggested an accurate turbulence dispersion model is necessary for correct prediction of the flow of mono-dispersed and poly-dispersed lock release turbidity currents.

7.4.2 Algebraic Slip Model

The algebraic slip or mixture model as presented by Manninen et al. (1996) is a homogenous multiphase flow model applied to describe the interaction between dispersed particulate phases and a continuous fluid phase in general three-dimensional geometries. The model solves a lower number of equations than the full Eulerian approach and therefore it is computationally less intensive. The derivation of the model is from the transport equations of the full Eulerian multiphase model. In Eulerian-Eulerian approach to multiphase flow, individual equations of mass and momentum are solved for each phase that is present in the problem. In the mixture model, the individual momentum equations are added together and simplified to provide a single momentum transport equation for the mass averaged mixture velocity. In order to obtain the individual phase velocities from the mixture velocity, a fundamental assumption is made. Namely, that the time taken for particles to reach their asymptotic slip velocity relative to the flow is much smaller than the hydrodynamic time scale. The former time scale is known as the particle relaxation time, and its ratio with the hydrodynamic time scale is a dimensionless quantity known as the Stokes number. The formula for the Stokes number is given by:

$$S_t = \frac{\tau_p}{\tau_f} = \frac{\rho_p d_p^2}{18\,\mu_f} \frac{U}{L} \tag{7.2}$$

where τ_p is the particle relaxation time, τ_f is a typical flow time scale, d_p is the particle diameter and L denotes a typical flow length scale. Thus the ASM is only valid at low Stokes numbers. The low Stokes number assumption permits the slip velocity of each dispersed phase to be determined from a balance between interfacial forces such as drag force, with external forces due to gravity and particle acceleration. Thus, if the full Eulerian model contains N phases, the N momentum transport equations are reduced to a single momentum transport equation for the mixture velocity, and $N-1$ algebraic equations for the dispersed phase slip velocities. The model still contains N mass transport equations to be solved. These can be used to determine the mass fractions of each phase, as in ANSYS CFX, or the volume fractions of each phase, as in ANSYS Fluent. These can be reduced to $N-1$ equations by replacing one of them by the ballast equation which constrains either the mass fractions or the volume fractions to sum to one.

The full multi-fluid model equations are given as follows:

Continuity:

$$\frac{\alpha(\rho_\alpha r_\alpha)}{\partial t} + \frac{\partial\left(\rho_\alpha r_\alpha u_\alpha^i\right)}{\partial x^i} = 0 \tag{7.3}$$

Momentum:

$$\frac{\partial\left(\rho_\alpha r_\alpha u_\alpha^i\right)}{\partial t} + \frac{\partial\left(\rho_\alpha r_\alpha u_\alpha^j u_\alpha^j\right)}{\partial x^j} = -r_\alpha \frac{\partial p}{\partial x^i} + \frac{\partial\left(r_\alpha \tau_\alpha^{ji}\right)}{\partial x^j} + \rho_\alpha r_\alpha g^i + M_\alpha^i \tag{7.4}$$

Where r_α is the volume fraction of phase α the index α which runs from 1 to N, ρ_α is the phase density (mass per unit volume of phase α) .

The bulk equations are derived by summing the phasic equations for continuity and momentum:

$$\frac{\partial \rho_m}{\partial t} + \frac{\partial\left(\rho_m u_m^i\right)}{\partial x^i} = 0 \tag{7.5}$$

$$\frac{\partial(\rho_m u_m^i)}{\partial t} + \frac{\partial(\rho_m u_m^j u_m^i)}{\partial x^j} = -\frac{\partial p}{\partial x^i} + \frac{\partial(\tau_m^{ji} + \tau_D^{ji})}{\partial x^j} + \rho_m g^i \qquad (7.6)$$

where:

$$\rho_m = \sum_\alpha r_\alpha \rho_\alpha \qquad (7.7)$$

$$\rho_m u_m^i = \sum_\alpha r_\alpha \rho_\alpha u_\alpha^i \qquad (7.8)$$

$$\tau_m = \sum_\alpha r_\alpha \tau_\alpha \qquad (7.9)$$

$$\tau_D^{ji} = -\sum_\alpha r_\alpha \rho_\alpha (u_\alpha^i - u_m^i) u_\alpha^j \qquad (7.10)$$

The volume fractions are solved by the transport equation of the particles phase which are assumed to be dispersed in the saline water continuous phase. The relative phasic velocities between continuous and dispersed phases are solved by the Algebraic Slip Model in which the slip and drift velocity are defined and related as follows:

$$u_{s\alpha}^i = u_\alpha^i - u_c^i \qquad (7.11)$$

$$u_{D\alpha}^i = u_\alpha^i - u_m^i \qquad (7.12)$$

$$u_{D\alpha}^i = u_{s\alpha}^i - \sum_\alpha Y_\alpha u_{s\alpha}^i \qquad (7.13)$$

where $u_{s\alpha}^i$ is the slip velocity, u_c^i is the velocity of the continuous phase, Y_α is the vertical distance of phase α and $u_{D\alpha}^i$ is the drift velocity. The computational effort is reduced as the velocity in each of the dispersed phase is predicted by the algebraic equations. The model assumes that the dispersed sediment phase at the terminal velocity $u_{s\alpha}^i$ is relative to continuous phase water. Further, the turbulent dispersion

is modelled using a standard gradient diffusion hypothesis in the transport equation of phase mass fraction. The turbulent dispersion equation is given by,

$$\rho_\alpha \overline{Y_\alpha'' u_\alpha^{\iota}{}''} = \frac{\mu_t}{\mathrm{pr_t}} \frac{\partial Y_\alpha}{\partial x^i}$$ (7.14)

7.4.2.1 Assumptions and derivation

The pressure gradient term can be eliminated by combining equations (7.3) and (7.4) as follows:

$$M_\alpha^i = r_\alpha \left(\rho_\alpha \frac{\partial u_{D\alpha}^i}{\partial t} + (\rho_\alpha - \rho_m) \frac{\partial u_m^i}{\partial t} \right) + r_\alpha \left(\rho_\alpha u_\alpha^j \frac{\partial u_\alpha^i}{\partial x^j} - \rho_m u_m^j \frac{\partial u_m^i}{\partial x^j} \right)$$ (7.15)
$$- \frac{\partial (r_\alpha \tau_\alpha^{ji})}{\partial x^j} + r_\alpha \frac{\partial (\tau_m^{ji} + \tau_D^{ji})}{\partial x^j} - r_\alpha (\rho_\alpha - \rho_m) g^i$$

The assumptions for approximating the slip velocity in the algebraic slip model are as follows:

i. The terminal velocity is instantly attainable by the dispersed phase and therefore the transient term of the drift velocity can be neglected:

$$\frac{\partial u_{D\alpha}^i}{\partial t} = 0$$ (7.16)

i. The approximation describes that:

$$u_\alpha^j \frac{\partial u_\alpha^i}{\partial x^j} \approx u_m^j \frac{\partial u_m^i}{\partial x^j}$$ (7.17)

ii. The stresses for the viscous and diffusion effects are negligible (in the CFX ASM model):

$$M_\alpha^i = r_\alpha (\rho_\alpha - \rho_m) \left(\frac{\partial u_m^i}{\partial t} + u_m^j \frac{\partial u_m^i}{\partial x^j} - g^i \right)$$ (7.18)

Assuming that only the drag controls the momentum between two phases and that particles are spherical then,

$$M_\alpha^i = -\frac{3}{4}\frac{r_\alpha \rho_i}{d_p} C_D |u_{S\alpha}| u_{S\alpha}^i \qquad (7.19)$$

Thus, the slip velocity can be written as,

$$|u_{S\alpha}| u_{S\alpha}^i = -\frac{4}{3}\frac{d_p}{\rho_i C_D}(\rho_\alpha - \rho_m)\left(\frac{\partial u_m^i}{\partial t} + u_m^j \frac{\partial u_m^i}{\partial x^j} - g^i\right) \qquad (7.20)$$

The Schiller and Naumann (1935) drag law is employed in ANSYS-CFX to resolve the drag force acting on the particles. The drag coefficient is a function of the particle Reynolds number $\mathrm{Re_p}$ and can be expressed as:

$$C_D = \frac{24}{\mathrm{Re}}(1 + 0.15\mathrm{Re}^{0.687}), \qquad \mathrm{Re_p} \le 1000 \qquad (7.21)$$

7.4.3 The hydro-morphodynamic model

This section describes the governing equations for the deposition and erosion processes over bedforms. Thus a hydrodynamic model is adapted here for calculating the transport of sediment under a unidirectional flow in a channel with a variable lower bed configuration. At a condition of the flow above the threshold of the motion sediments are entrained from the bed into suspension. The suspended sediments are carried at the same velocity as the flow, plus a correction due to the finite slip velocity under gravity. This study only considers the suspended load and the bed load transport is assumed to be negligible. The suspended load model models the interaction of the flow with the particles on the bed surface which results in the erosion of the particles into suspension and settling of the particles from suspension.

The sediments on the surface of the bedforms remain immobile for flows with low Reynolds number. At higher Reynolds number the flow exerts enough shear stress on the sediments to begin to move them. This is known as the incipient motion or the threshold of motion. Therefore, a critical area-weighted averages velocity $\bar{U}_{cr}$ is required to result in motion of sediments of diameter d on the surface boundary of the bedform over a sea water depth H. Wall shear stress can be non-dimensionalised

by sediment diameter and density to give the Shields parameter, θ as follows,

$$\theta = \frac{\tau}{g(\rho_s - \rho)\phi} \tag{7.22}$$

$$\theta = \frac{u_*^2}{g(s - 1)\phi} \tag{7.23}$$

$$u_* = \sqrt{(\tau / \rho)} \tag{7.24}$$

where τ = shear stress tangential to the bed

   u_* = shear velocity

   g = sediment gravitational acceleration= 9.8 m s^{-1}

   ρ_s = sediment density

   ρ =sea water density

   $s = \rho_s/\rho$ = the ratio of sediment density to fluid density

   ϕ =sediment diameter

Further, the threshold of the motion relative to the lower boundary shear stress is given by,

$$\theta_{cr} = \frac{\tau_{cr}}{g(\rho_s - \rho)\phi} \tag{7.25}$$

The critical shields parameter for the flat bed case was based on the modified formula of Soulsby (1997),

$$\theta_{cr} = \frac{0.30}{1 + 1.2D_*} + 0.055[1 - \exp(-0.020D_*)] \tag{7.26}$$

The dimensionless grain size D_* (Soulsby, 1997) is given by,

$$D_* = \left[\frac{g(s-1)}{v^2}\right]^{1/3} d \tag{7.27}$$

where v is the kinematic viscosity of sea water with the value of $1.36 \times 10^{-6} \text{ m}^2 \text{ s}^{-1}$.

For two-dimensional bedforms with transverse bed slopes equation (7.26) is modified as:

$$\theta_\beta = \theta_{cr} \frac{\sin(\phi \pm \beta)}{\sin(\phi)} \tag{7.28}$$

The sign for the local bed slope angle β is negative when the flow travels up the slope and negative when the flow is directed down the slope. The local angle β is described by:

$$\beta = \tan^{-1} \left|\frac{\hat{n}_x}{\hat{n}_y}\right| \tag{7.29}$$

Where n_x and n_y are the normal components of the vector to the bed.

The equation for the bed-growth rate can be written in the following form (Soulsby, 1997, Dorrell et al., 2013b):

$$\frac{\Delta\eta}{\Delta t} = \frac{D - E}{\phi_m - \phi_c} \tag{7.30}$$

ϕ_m is the maximum packing concentration of the bed and ϕ_c is the reference concentration. Garcia and Parker (1991) compared various relations in the literature for predicting sediment concentration close to the bed. The formulas for predicting the near-bed sediment concentration are collected by :

Smith and McLean (1977):

$$C_a = \frac{0.00156 T_s}{1 + 0.0024 T_s} \tag{7.31}$$

$$T_s = \frac{\tau - \tau_{cr}}{\tau_{cr}} \tag{7.32}$$

The reference height z_a for this formula is expressed as follows:

$$Z_a = 26.3 \frac{\tau_{cr} T_s}{\rho g(s-1)} + \frac{d_p}{12} \tag{7.33}$$

Rijn (1984) at $z_a = \Delta_s/2$:

$$C_a = \frac{0.0015 d_p T_s^{3/2}}{z_a D_*^{0.3}} \tag{7.34}$$

$$\Delta_s = \begin{cases} 0 & \tau < \tau_{cr} \\ 0.11h\left(\frac{d_p}{h}\right)^{0.3}(1 - e_s^{-0.5T_s})(25 - T_s) & \tau_{cr} < \tau_{0s} < 26\tau_{cr} \\ 0 & \tau > 26\tau_{cr} \end{cases} \tag{7.35}$$

Zyserman and Fredsøe (1994) at $z_a = 2d_{50}$:

$$C_a = \frac{0.331(\theta - 0.045)^{1.75}}{1 + 0.720(\theta - 0.045)^{1.75}} \tag{7.36}$$

Cacchione et al. (2008):

$$C_a = 0.00086 Z^{1.08} \rho_s \tag{7.37}$$

$$Z = \frac{u_*^2 v}{w_s(s-1)g d_{50}^2} \tag{7.38}$$

where C_a is the near-bed concentration, Δ_s is the bedform height, d_{50} is the median grain diameter γ is the fluid gravity, and γ_s is the sediment gravity.

Equations (7.31) through to (7.38) provide a wide range of models for the sediment concentration at a reference height. These models give a wide range of predictions for the value of C_a. Because of this, and because of the ambiguity in the specification of the reference height z_a, none of these models are utilized in this work. Rather, the

reference concentration ϕ_c in equation (7.30) is determined from the solution of the CFD model at cell vertices adjacent to the wall. These are determined by the use of logarithmic wall functions within the CFD model.

The settling of the sediments is described by the volumetric settling rate D_v, which denotes the volume of sediment settling out of the flow per unit bed area per unit time, hence has units of velocity. It is modeled as (Celik and Rodi, 1991, Dorrell et al., 2013a, Soulsby, 1997):

$$D_v = \phi_c \ w_s$$

(7.39)

where w_s denotes the settling velocity of the sediments.

Similarly, the erosion of particles into suspension is described by the volumetric erosion rate E_v (Celik and Rodi, 1991, Dorrell et al., 2013b, Soulsby, 1997, Partheniades, 1965, van Rijn, 1984). This has the same dimensions as D_v, and it is modelled as follows,

$$E_v = \begin{cases} m(\theta - \theta_{cr})^n & \text{if } \theta \geq \theta_{cr} \\ 0 & \text{if } \theta < \theta_{cr} \end{cases}$$

(7.40)

The exponent n depends on grain material and here it is equal to 1.5 (Garcia and Parker, 1991, Garcia and Parker, 1993, van Rijn, 1984, Dorrell et al., 2013b). The constant m (m s^{-1}) is a function of particle diameter, density and gravity and can be written as,

$$m = \alpha \sqrt{g\left(\frac{\rho_s}{\rho} - 1\right)\phi}$$

(7.41)

Where the coefficient constant α is 0.02.

7.4.4 Simulation details

Quasi-steady simulations were performed for sediment-laden flow over bedforms in a two-dimensional channel by using an algebraic slip model. The sediment-laden flow is assumed to be periodic at both ends of the channel. This setting was used to approximate the situation with an infinitely long channel comprising bedforms in the lower wall boundary. As described in the previous chapter, the standard $k - \varepsilon$ model was used to solve the turbulence behavior in the continuous saline water phase which

in here was set as a constraint. The scalable wall function was used for the modelling of the flow close to wall boundary. The particle flow phase was simulated by the ASM model which contained additional transport equations for the adapted morphodynamic model. The solutions for single-phase saline water flow over bedforms were used as the initial condition to simulate particle-laden flow. The details of the boundary conditions for the flow are given in chapter 5.

It is possible in ANSYS CFX to switch off the solution of the fluid flow equations, and to just solve the scalar transport equations on a fixed fluid flow field. This one-way coupled method was used initially, as it permitted the use of large time steps to obtain solutions to several problems using a very small amount of CPU time. The solutions of the one-way coupled problems were subsequently used as initial fields to fully two-way coupled simulations, which took into account the effect of the particle concentration fields on the flow field. The influence of the sediments on the flow turbulence was also taken into account.

The effect of lower boundary deposition and erosion on the flow field was taken into account using the Boundary Sources feature in ANSYS CFX. This feature permits the user to specify boundary fluxes of any transported variable at any flow boundary. The user specified fluxes are integrated across control cell boundaries adjacent to the surface, and the resulting sources are the distributed inside the half-control cells adjacent to the boundary. In order to apply this feature to the transport equation for particle mass fractions, it is necessary for the net erosional and depositional fluxes to specified as particle mass fluxes.

The particle mass fluxes are expressed as (Dorrell et al., 2013b):

$$S_\phi = (E_m - D_m)$$
(7.42)

$$D_m = D_v \times \rho_s$$
(7.43)

$$E_m = E_v \times \rho_s$$
(7.44)

where S_ϕ is the source term used as the flux boundary source, D_m is the deposition rate mass flux, D_v is the deposition rate volume flux, E_m is the erosion rate mass flux and E_v is the erosion rate volume flux.

The details of the numerical experiments conducted are given in Table 7.1. Simulations were performed for a range of aspect ratio and particle diameter. Mono-

disperse particles with diameter size $\phi = 50,\ 100,\ 200,\ 400\ \mu$m were investigated which represented, respectively, the sediment size range from fine to coarse grained. The particles density ρ_s has the particle density of quartz grains (2650 kgm^{-3}). Quartz grains have nearly spherical shape. The kinematic viscosity of saline water which is equivalent to $1.36 \times 10^{-6}\ \mathrm{m}^2\mathrm{s}^{-1}$ was used for computing the dimensionless diameter D_*. The ASM model solutions for vertical sediment slip velocity were used to substitute for settling velocity of sediments w_s. The maximum packing concentration of the particles was given a fixed value equivalent to 0.6. For the near-bed concentration ϕ_c we have not used any of the given formulas in the literature but computed as a part of the solution, as described above. To do this, the solution for sediment volume fraction was used as an input for ϕ_c. The local wall shear $\tau_w =$ $\sqrt{\tau_x^2 + \tau_y^2}$ over the entire lower surface boundary was used to calculate the Shields parameter θ.

No. Runs	Bedforms	Roughness type	c/h	ϕ (μm)	$\partial p/\partial x$	(kg m $^{-2}$ s $^{-2}$)
16	Shape 1 (S1)	K-type	[1,2,4,8]	[400,200,100,50]	0.5	
16	Shape 2 (S2)	K-type	[1,2,4,8]	[400,200,100,50]	0.5	
16	Shape 3 (S3)	K-type	[1,2,4,8]	[400,200,100,50]	0.5	
16	Shape 4 (S4)	K-type	[1,2,4,8]	[400,200,100,50]	0.5	
16	Shape 5 (S5)	D-type	[1,2,4,8]	[400,200,100,50]	0.5	
16	Shape 6 (S6)	D-type	[1,2,4,8]	[400,200,100,50]	0.5	
16	Shape 7 (S7)	D-type	[1,2,4,8]	[400,200,100,50]	0.5	
4	Flat	none	none	[400,200,100,50]	0.5	

Table 7. 1: The Simulation tests performed for particle-laden flow over various idealised bedform shapes.

7.5 Results

7.5.1 Particulate flow dynamics

Profiles of $\bar{u}$ were compared for the case Shape 4 (denoted by $S4$) at $c/h = 8$ (denoted by $U8$) for different particle diameter are shown in figure 7.1. This bed geometry was specifically chosen as converged solutions were obtained for all simulations. The values of particle mass fraction for different bed shapes and particle diameter are shown in Table 7.1. For all cases, the $\bar{u}$ profile show an enhancement in flow velocity profile mainly towards the outer region of the flow with an increase in particle diameter, except for case with $\phi =50$ μm. Thus, the velocity profiles appear to be dependent on the flow concentration field. This will be discussed further in following sections.

Two-dimensional mean flow velocity contours are plotted in figures 7.2-4 to compare the flow field over bedforms in particle-laden flow with pure sea-water in the previous chapter. No significant change is seen in the mean flow field from the contours between the flows with particle diameter size $\phi = 100 - 400$ μm and the case with pure saline water flow. Thus, in order to closely look at the influence of sediments on the flow field, the centre-line velocity $\bar{u}$ for $\phi =200$ and 400 μm were compared to the flat case. Only a minor decrease in the $\bar{u}$ profile was observed for 400 μm. However, a more pronounced decrease was obtained for $\phi = 200$ μm. The reason for this decrease may be due to the difference in the concentration of the sediments in each type of particle-laden flow field, as the flow with higher concentration leads to higher flow resistance.
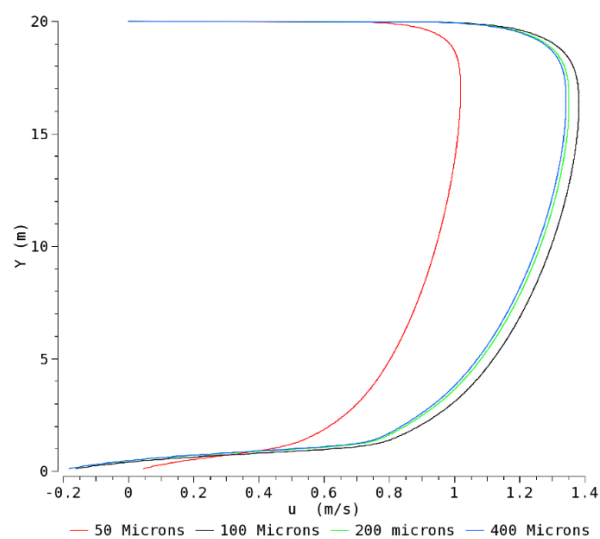
Figure 7. 1: The centre line velocity profile for different particle diameters.

Figure 7. 2: Matrix view of the velocity magnitudes for $\phi = 400$ μm with flow streamlines over various bedforms with varying aspect ratio c/h.
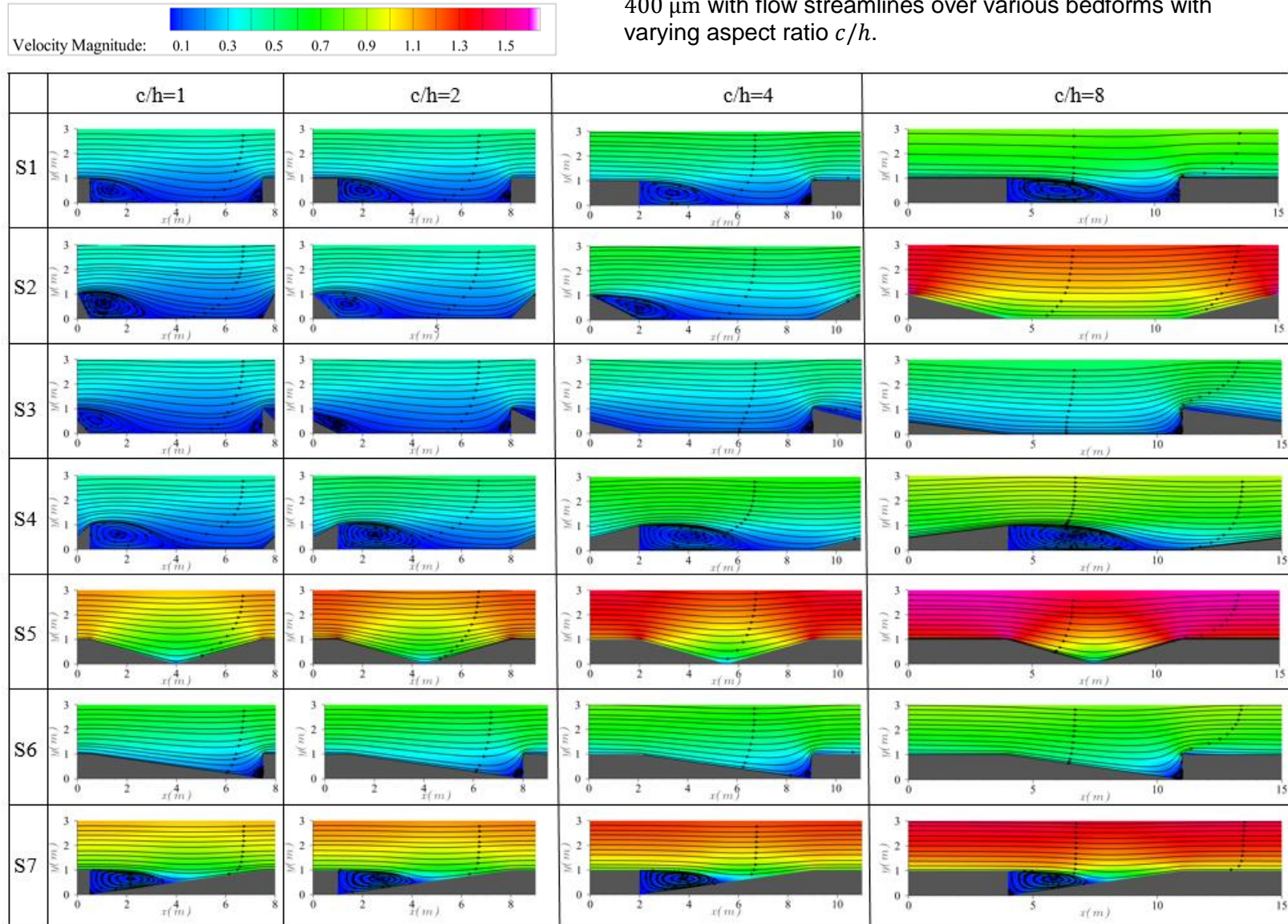
Figure 7. 3: Matrix view of the velocity magnitudes for $\phi = 200\ \mu m$ with flow streamlines over various bedforms with varying aspect ratio c/h.
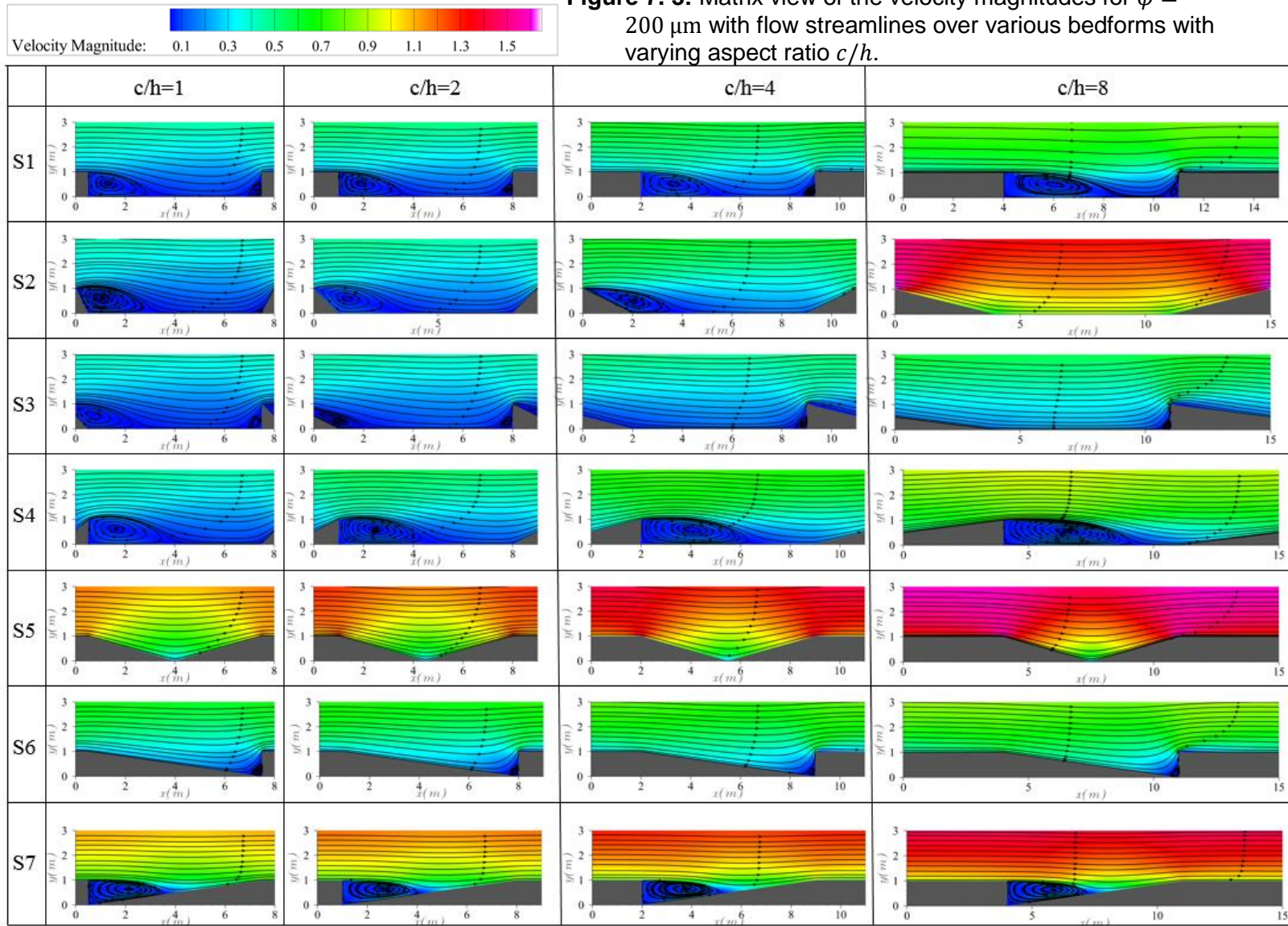
Figure 7. 4: Matrix view of the velocity magnitudes for $\phi = 100\ \mu m$ with flow streamlines over various bedforms with varying aspect ratio c/h.
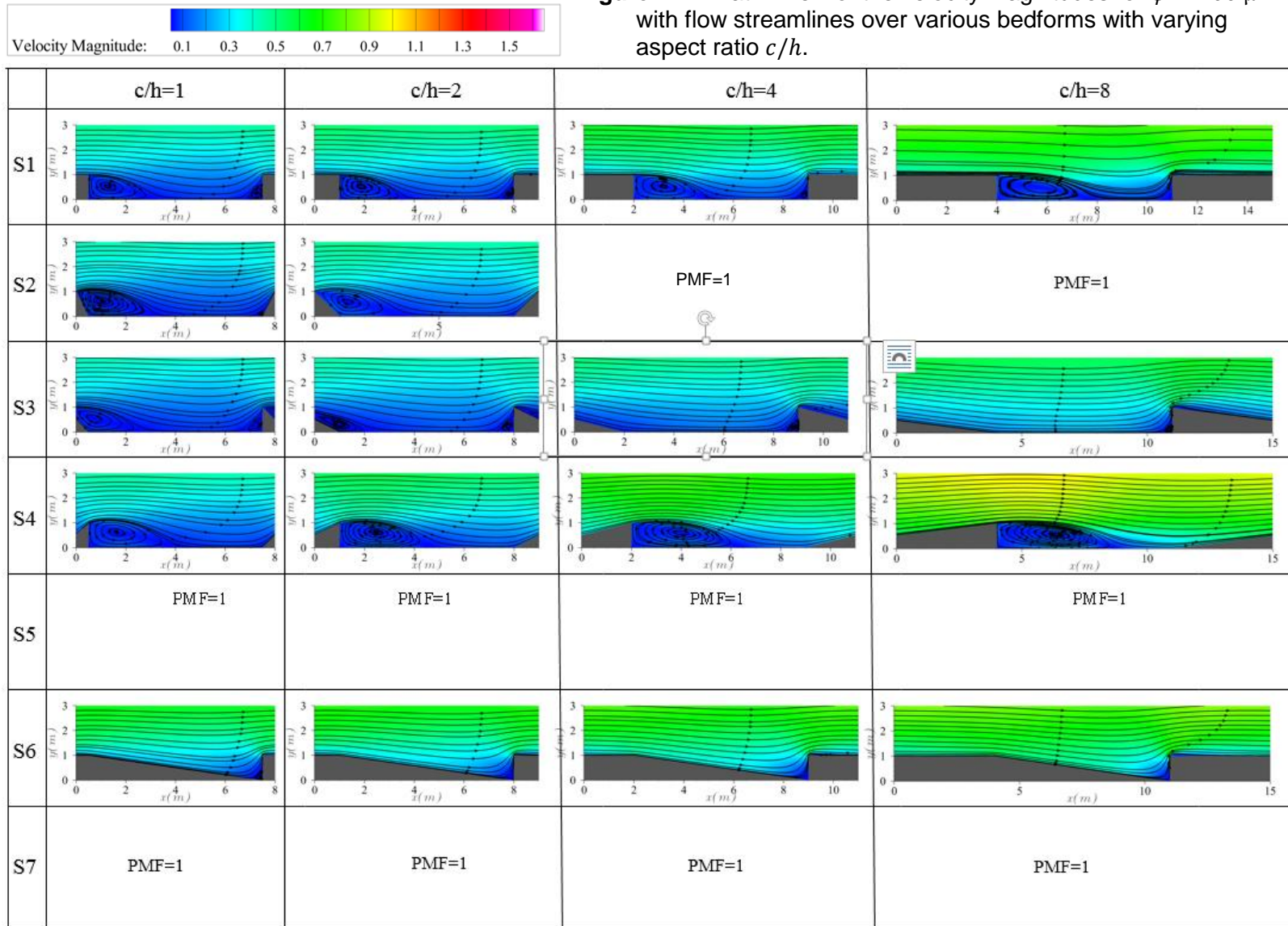
Bed geometry	PMF % ($\phi = 400$ μm)	PMF % ($\phi = 200$ μm)	PMF % ($\phi = 100$ μm)	PMF % ($\phi = 50$ μm)
S1U1	1.56E-05	1.54E-03	0.0711742	1.24159
S1U2	3.02E-05	3.65E-03	0.180612	3.1243
S1U4	6.96E-05	9.25E-03	0.497354	8.50238
S1U8	1.64E-04	2.24E-02	1.35098	21.5928
S2U1	1.78E-05	8.96E-04	0.0272706	0.538849
S2U2	7.60E-05	2.73E-03	0.0890758	1.90729
S2U4	1.38E-04	7.74E-03	0.430315	10.1401
S2U8	2.69E-03	3.09E-01	100	100
S3U1	4.67E-06	3.26E-04	0.0122998	0.32652
S3U2	7.80E-06	4.97E-04	0.017385	0.423649
S3U4	1.82E-05	1.23E-03	0.0730697	2.02838
S3U8	5.46E-05	6.13E-03	0.44919	12.3713
S4U1	6.13E-06	8.86E-04	0.0387756	0.890738
S4U2	2.87E-05	4.44E-03	0.208891	4.25952
S4U4	3.87E-04	1.75E-02	0.912859	17.316
S4U8	1.21E-04	2.81E-02	2.74292	65.1221
S5U1	1.54E-03	2.14E-01	100	100
S5U2	1.62E-03	2.45E-01	100	100
S5U4	1.66E-03	2.83E-01	100	100
S5U8	1.56E-03	3.10E-01	100	100
S6U1	7.66E-05	1.01E-02	0.711843	16.4273
S6U2	1.02E-04	1.42E-02	1.02917	25.4943
S6U4	1.70E-04	2.09E-02	1.57581	100
S6U8	2.40E-04	3.08E-02	2.47489	100
S7U1	3.38E-04	4.76E-02	100	100
S7U2	3.77E-04	5.66E-02	100	100
S7U4	4.21E-04	6.80E-02	100	100
S7U8	4.68E-04	8.17E-02	100	100
Flat Case	1.30E-03	2.47E-01	100	100

Table 7. 2: Table of the particle mass fraction in percentage for different bedform shapes.

7.5.1.1 Sediment effect on skin friction and form drag

Here the results for the model solution case $S4U8$ are considered, to evaluate the effect that particle laden flow has on the skin friction and form drag. Figure 7.5 plots the pressure drag against skin friction for the flow with different particle sizes compared to the pure single-phase flow for the bed roughness case $S4U8$. In general, the value of skin friction increased for finer particle diameters. A sudden increased in skin friction is observed from $\phi = 100\ \mu m$ to $\phi = 50\ \mu m$ which is explained by sudden increases in particle mass concentration (Table 7.2). It should be noted that the particle mass fraction percentage $\approx 2.8\%$ is obtained for $\phi = 100\ \mu m$ and for $= 50\ \mu m \approx 65\%$ in Table 7.2.

Pressure drag shows a decrease in value for finer particle size up to $\phi = 100\ \mu m$ at which a local minima is achieved followed by a significant increase at $\phi = 50\mu m$. In other words, once ϕ has fallen beyond a critical form drag value at $\phi = 100\ \mu m$, the flow becomes immediately exhausted. This is likely because the intensity of the recirculation reaches its minimum value at $\phi = 100\ \mu m$ which then leads to a weak pressure gradient across the roughness elements. Note, the size of the recirculation and reattachment reduced for all particle diameters, including $\phi = 50\ \mu m$.
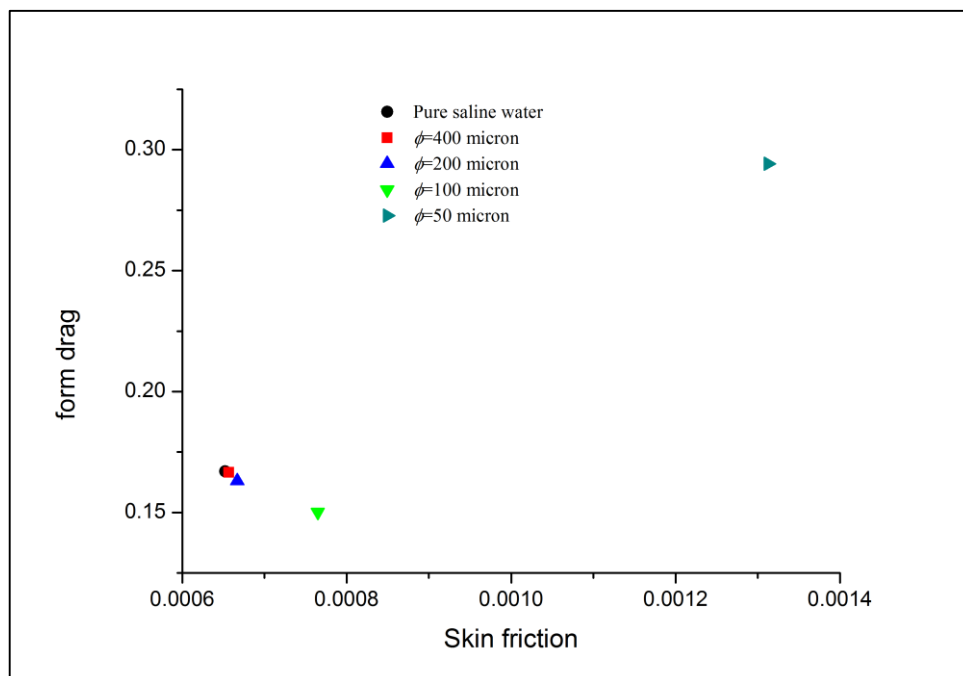
Figure 7. 5: Form drag as a function of the skin friction for different particle diameter and pure saline water.

- 138 -

Figure 7. 6: Matrix view of the particle mass fraction for $\phi = 400$ μm for flow over various bedforms with varying aspect ratio c/h.

Figure 7. 7: Matrix view of the particle mass fraction for $\phi = 200$ μm for flow over various bedforms with varying aspect ratio c/h.

Figure 7. 8: Matrix view of the particle mass fraction for $\phi = 100\ \mu m$ for flow over various bedforms with varying aspect ratio c/h.

7.5.1.2 Near-bed sediment concentration

In order to investigate the effect of bedforms on dilute particle-laden flow, in figure 7.6-8, sediment mass fraction contours are shown for different particle sizes. In this section, the intensity of the vortex is referred to the area-weighted average wall shear stress τ_w, produced in the recirculating streamlines. The obtained results indicate the entrainment of the sediment into suspension depends on the value of the skin friction $\overline{D_s}$ which is a function of $\overline{\tau_w}$. In the last chapter we showed, the value of $\overline{D_s}$ increased with the c/h value for all cases. It should be note that the form drag $\overline{D_f}$ does not play an important role in the sediment distribution as it also increases with the ratio c/h.

For shape $S1$ in figure 7.6, the contour lines show a relatively high suspended sediments concentration on the rib crests (here the crest is referred to as the horizontal region located on the top of roughness element). This can be explained by the high value of $\overline{\tau_w}$ on this region. Consequently, the strong forces exerted on the sediments by the flow will transport the sediments from the crest into the vortex zone. The value of $\overline{\tau_w}$ is strongest at the largest c/h value. In the cavity region, the maximum $\overline{\tau_w}$ value is located at the centre of the recirculation zone although it is much lower than the value on the crest.

In figure 7.6 the focal region of the vortex is seen to be erosional as the Shields parameter θ goes above its critical value θ_{cr} for entraining sediments from the bed. The value by which θ exceeds θ_{cr} in the focal region is greater for higher aspect ratio. The particles eroded upstream of the vortex zone tend to be deposited inside the recirculation zone. Note also how the sediment distribution is shifted towards the face of the downstream rib with the increased ratio c/h and the increased reattachment length. Further, the particle mass fraction (PMF) contour lines are more parallel on the horizontal surface of the ribs crest and become disturbed by the flow streamlines in the cavity.

The intensity of the secondary recirculation appears to be inversely proportional to the primary vortex. The localised sediment suspension appear to be absent in the trailing corner of $S2$ at $c/h = 2$ to 4 and $S4$ due to the lack of the secondary recirculation. This confirms that the secondary vortex downstream is responsible for the small amount of sediment suspension around the corner of the roughness elements. As intuitively expected, $S1$ showed a decrease in the sediment concentration for smaller ϕ. This is because a higher value of θ is achieved for finer sediments and thus the flow is able to erode a greater amount of sediment from the

bed. In $S2$, the reattachment length decreases with the increase in aspect ratio up to $c/h = 4$. Therefore the focal point of the vortex shifts backwards towards the leading face of the geometry. The erosion effect in the focal region of the $S2$ is weaker than $S1$. This is due to the back stretching of the vortex from a perpendicular to an inclined position. Thus, this suggests the intensity of the vortex reduces towards a more parabolic shape. However, for higher values of c/h $S2$ shows an increase in $\overline{\tau_w}$. This is as a result of extra surface added by the increase in c/h value which results in minor additional production of $\overline{\tau_w}$.

In the distance between the reattachment point and the next roughness element, the bed is exposed to a strong incoming flow over the vortex streamlines which produce a high region of $\overline{\tau_w}$. At this region for $c/h = 4$, θ was slightly above θ_{cr} which resulted in minor erosion. Note, θ was lower than θ_{cr} for $c/h =$ 1 to 4 and thus no erosion occurred. At $c/h = 8$ for $S2$, the concentration of suspended sediment significantly increased due to no flow recirculation. For this aspect ratio θ exceeded θ_{cr} for the entire bed surface. It should be noted that the flow streamlines are less parallel for $S1$ at $c/h = 8$ with flow recirculation compared to $S2$ with a little flow separation. The small amount of sediment suspension on the leading edge of the $S2$ corresponds to a small recirculation which was identified by the zoomed in vector field.

The lowest sediment suspension concentration field compared to other bedforms was observed for S3. As was noted in the last chapter, $S3$ produced the highest form drag. Further it was noted that the re-attachment length decreased and with the focal point of the vortex shifting upstream similar to $S2$ case for $c/h = 1$ and 2. This allowed a lower intensity vortex to be generated for $S3$ at $c/h = 1$ than c/h=2. Thus this allowed the skimming flow above the recirculation region to produce a higher amount of $\overline{\tau_w}$ downstream of the reattachment point for $c/h = 2$ than $c/h = 1$. Comparing $S3$ and $S2$ at $c/h = 8$ further approves that the suspension concentration of sediment does not depend on the flow separation but rather on the shape of the geometry. Thus, the bed geometry with blunt downstream inclined edges suspend lower amount of sediments compared to the bed geometry with upstream facing blunt edges and downstream horizontal edges.

The associating blunt edge small sediment concentration deposited in the corner of the blunt edge was also visible for $S3$. Shape $S5$ produced the maximum sediment concentration for all its aspect ratios. The concentration contours behave similarly to shape $S2$ at $c/h = 8$ with no major flow separation. Shields parameter θ was observed to be greater than its critical value on the entire surface of the geometry.

The inclined face opposing the flow produced a higher amount of $\overline{\tau_w}$ than the trailing face.

The contour lines for $S6$ and $S7$ clearly indicate that the spacing w has a significant influence on the sediment suspension. The associated contour lines appear to be distributed in a more parallel orientation for cases with horizontal spacing ($S1 - S4$) compared to cases without horizontal spacing ($S5 - S7$). Also, similar to cases with spacing, the contour lines appear to be less disturbed (more parallel) with the increase in ratio c/h. Moreover, the particle mass fraction contour lines in the outer region of the flow are more disturbed for $S6$ with the blunt edge compared to $S7$ with the inclined edge in the direction of the flow. In $S6$, $\overline{\tau_w}$ decreased down the inclined bed leading to a lower rate of erosion down the inclined bed before the secondary vortex.

In $S7$ the vortex intensity is increased with the increase in c/h and slight decrease in reattachment length. The particle mass fraction contours for $\phi = 200\ \mu m$ at $c/h = 7$ show that more sediment concentration are deposited in the recirculating streamlines by the increase in the vortex intensity. Thus this section concluded that finer sediment are more likely to be kept in suspension by turbulence. Also, the increase in c/h resulted in enhancement of sediment mass fraction for all tested cases.

7.5.2 Deposition and erosion

Figure 7.9 shows the net deposition and erosion $\dot{\eta}$, curves on the bedforms lower boundary surfaces for $\phi = 100$ and $200\ \mu m$. For all bed geometries, the flow separated due to the discontinuity in the roughness element at sharp points. Such regions are often associated with peak value in τ_w particularly when angled to the direction of the flow as also noted by Cuba (2009), Leonardi (2003) and Ashrafian (2004). These points have been excluded from the curves in figure 7.9 for better observation of the erosional and depositional process in other regions in the vicinity of the roughness elements.

The $\dot{\eta}$ curves for $S1$ show a high rate of erosion occur on the top of the roughness element. The erosion rate appears to decrease downstream of the top. The entire cavity is associated with deposition. Moreover, a decrease in the deposition rate can be seen which corresponds to high erosion rate on the cavity bed perpendicular to the focal region of the recirculating streamlines.

The anomaly clearly moves downwards with the increase in turbulence intensity. it is noted that the anomaly is much more apparent for $\phi = 100$ microns than 200 by the increase in intensity of the vortex from coarser to finer sediment. Here, both the erosion and deposition rate increased for higher c/h. As expected for $S2$, most erosion occurs on the tip of the geometry. Two anomalies are observable for $S2$. The primary anomaly is controlled by the vortex intensity on the focal region and the secondary anomaly corresponds to erosion produced by the inward flow downstream of the recirculating region. The amount of shear stress produced by the inward flow is related to the strength and size of the primary separation zone.

The level of erosion is detected to increase with the relative intensity of the primary vortex. Vortex intensity is observed to be lower in shape $S3$ than $S2$, as there is barely an anomaly in the regions of rotational flow at $c/h = 1$ and 2. In $S3$, the flow is depositional in the cavity width w at $c/h = 1$ and 2 and becomes erosional with the absence of the rotational streamlines at $c/h = 4$ and 8. Further, the corner of the downstream edge produced a high deposition rate as a result of the erosional effect upstream which can be better visualised for $c/h = 4$ and 8. For $S4$ cases, the flow is also mostly erosional on the crest of the geometries. The level of flow intensity by rotational flow is found to be of highest in contrast to other bed topographies.

One conclusion which can be derived from the comparison between $c/h = 1$ and $c/h = 8$, is that the recirculating vortices do not have significant effect on the overall erosion of the system. In $S5$, the flow in lee side is erosional and on the stoss side is depositional. The rate of deposition increases in stoss side with the increase in c/h. For $S6$ geometry, the flow is erosional on the lee side, however the flow becomes depositional towards the blunt edge of the geometry. The anomaly for shape $S7$ represent the erosional effect of the centre region of the vortex. The flow is depositional in the recirculation region and becomes erosional up the stoss side of the geometry. In conclusion, all bed topographies showed an increase in deposition and erosion process with the decrease in ϕ. Also, lowering the slope angle of the stoss and lee side resulted in higher flow erosion and particle deposition rate.
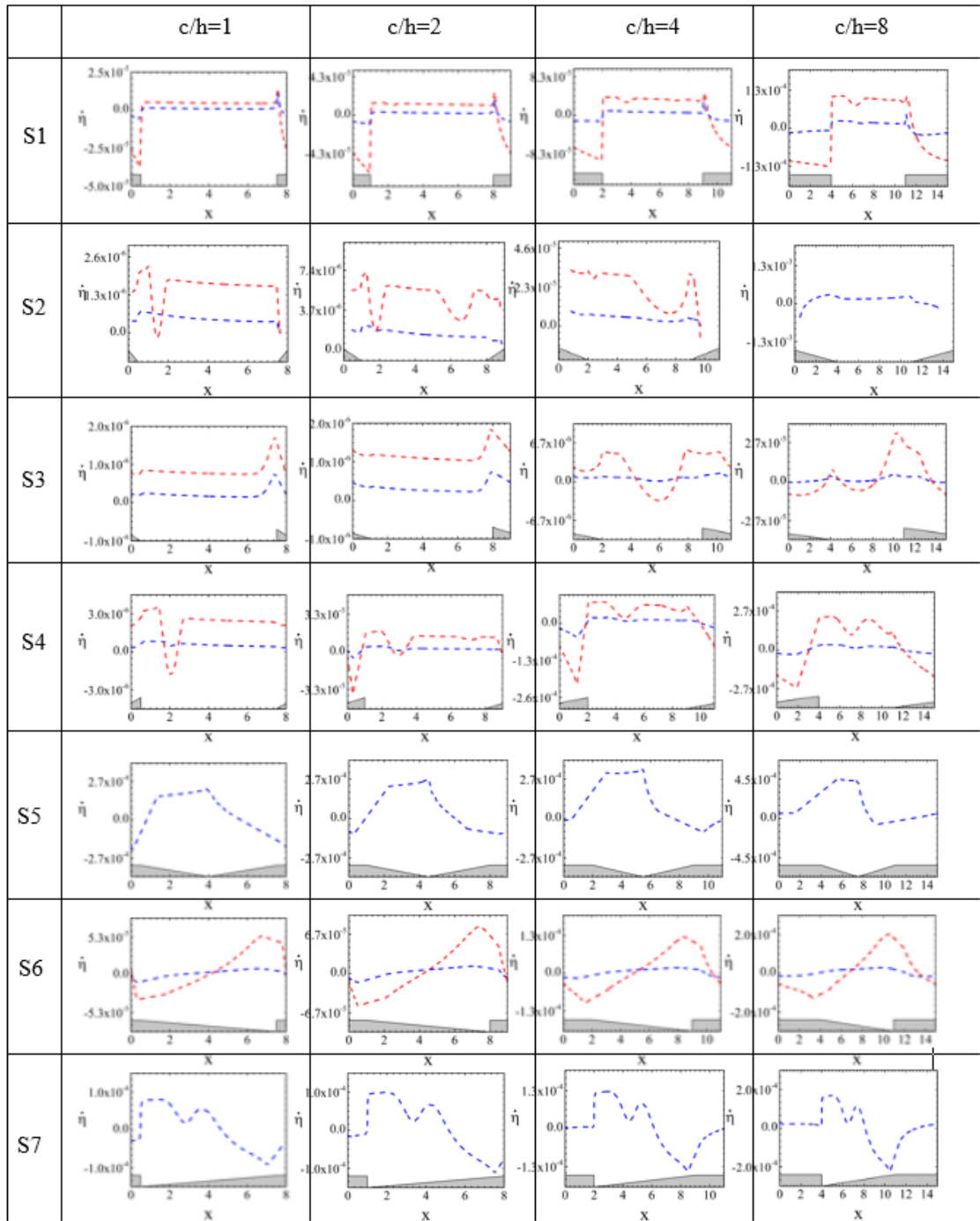
Figure 7. 9: Comparison of net deposition erosion results of flow over various bedforms with different aspect ratio for $\phi = 100\,\mu m$ (red dashed line) and $\phi = 200\,\mu m$ (blue dashed line).

7.6 Quantitative Data Analysis

In turbidity flows, the suspended sediments provide the excess density to keep the flow moving. Suspended sediment can also severely stratify the flow and can completely damp turbulence in turbidity flows (Shringarpure et al., 2012, Talling et al., 2007, Cantero et al., 2012a, Cantero et al., 2012b, Cantero et al., 2009). The energy to suspend the sediments is retained by the turbulence energy counteracting by settling tendency of sediments.

7.6.1 Flow capacity

The maximum amount of sediment which can be carried in suspension by the flow is quantified by computing the total particle volume fraction α_{Ave} , over the entire depth as follows,

$$\alpha_{Ave} = \frac{1}{\Omega} \int_{\Omega} \alpha_d \, d\Omega$$

(7.45)

Where α_d is the sediments volume fraction and Ω is the overall volume of the computational domain. The capacity of flow over bedforms is thus compared and normalized to that over a flat bed.

7.6.1.1 Potential Energy

The potential energy for each phase is defined as the energy expended to retain the sediments in suspension against the gravitational forces. To correlate the potential energy for all bed topographies the computational domain in each case has been truncated using a relative step function to integrate the PE over a fixed height. This is done such that given a uniform concentration at the inlet, the potential energy of the flow should is the same as the flat bed case. This takes into account the geometrical bias driven by variations in (mean) bed elevation. Figure 7.10 shows how this is determined for case $S2$:
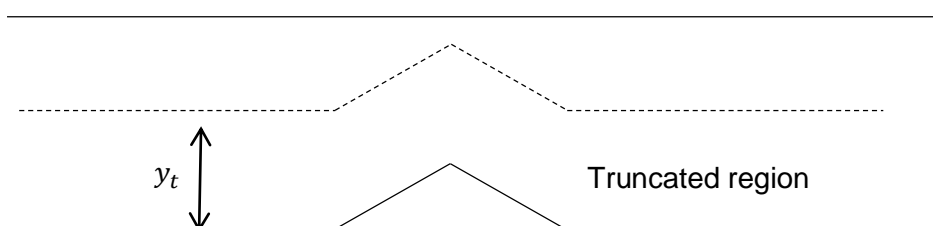
Figure 7. 10: Truncated region for the calculation of the PE over a fixed height for shape $S2$.

In a fluid-sediment mixture, the potential energy of the flow for the dispersed phase Π_d is obtained by the vertical component of the work done against gravity on the suspended sediments as follows:

$$\Pi_d = \frac{g\rho_s}{\Omega} \int_\Omega y_t \Phi_d \, d\Omega \tag{7.46}$$

where Φ_d is the volume-weighted average sediments mass concentration of fluid sea-water and y_t is the truncated flow depth. The PE for the continuous phase Π_c is defined as

$$\Pi_c = \frac{g\rho}{\Omega} \int_\Omega y_t \Phi_c \, d\Omega \tag{7.47}$$

where Φ_c is the volume-weighted average saline water mass concentration, y_t is the truncated flow depth and note the subscript c denotes the variable for the continuous phase and d for the dispersed phase.

7.6.1.2 Kinetic Energy

The average kinetic energy of dispersed phase Θ_d can be expressed as,

$$\Theta_d = \frac{\rho}{2\Omega} \int_\Omega \Phi_d (u_d^2 + v_d^2) \, d\Omega \tag{7.48}$$

$$u_d = u_c + u_p \tag{7.49}$$

$$v_d = v_c + v_p \tag{7.50}$$

where u_p and v_p are, respectively, the sediments slip velocity in $x-$ and $y-$direction. Likewise here we have considered the truncated region to compute KE to investigate its relation to PE for various bedforms. Accordingly, the kinetic energy of the continuous phase is calculates as follows:

$$\Theta_c = \frac{\rho}{2\Omega} \int_\Omega \Phi_c (u_c^2 + v_c^2) \, d\Omega \tag{7.51}$$

7.6.2 Richardson number

For the purpose of this study a densimetric Richardson R_{id} is formulated which can be expressed via the following relation,

$$R_{id} = \frac{\Pi_d}{\Theta_d} \tag{7.52}$$

The densimetric Richardson number R_{id} measures the ratio between the potential energy and kinetic energy of the dispersed phase. The motion of turbidity currents is derived by the conversion of potential energy into kinetic energy. For flows over bedforms with high values of R_{id} the turbidity current is expected to attain a longer run-out via having greater potential energy to support sediments in suspension. On the contrary, for cases with lower value of R_{id} the current is expected to experience a shorter run-out length via a larger kinetic energy sink by flow resistance.

7.6.3 Stratification

It has been suggested that the combination of stratification and confinement of gravity currents between levees may have a significant influence on enhancing the run-out length (Blazek, 2005). A large number of flow models in the literature make the Shallow Water approximation, closed by the assumption of insignificant stratification (Launder and Spalding, 1972). The analysis presented here critically evaluates this assumption, and nullifies some of the assumptions in the Launder and Spalding (1972) paper. The volume-weighted average PE of a stratified fluid subscripted by s, with varying sediments concentration Φ_s can be expressed as,

$$\Pi_s = \frac{g\rho}{A} \int_\Omega y \Phi_s \ d\Omega \tag{7.53}$$

For an unstratified fluid subscripted by u, the PE reads,

$$\Pi_u = \frac{g\rho}{\Omega} \Phi_u \int_\Omega y d\Omega \tag{7.54}$$

Where the sediments concentration is constant and equal to volume weighted average Φ_u everywhere in the system as follows,

$$\Phi_{\mathrm{u}} = \frac{1}{\Omega} \int_{\Omega} \Phi_{\mathrm{s}} \; d\Omega \tag{7.55}$$

Therefore, the amount of stratification in the system is described as,

$$\frac{\Pi_{\mathrm{s}}}{\Pi_{\mathrm{u}}} = \frac{\int_{\Omega} y \Phi_{\mathrm{s}} \; d\Omega}{\Phi_{\mathrm{u}} \int_{\Omega} y d\Omega} \tag{7.56}$$

In a similar manner, the stratification is quantified in terms of KE as,

$$\Theta_{\mathrm{s}} = \frac{\rho}{2} \int_{\Omega} \Phi_{\mathrm{s}} \, U^2 \mathrm{d}\Omega \tag{7.57}$$

$$\bar{u} = \frac{1}{\Omega} \int_{\Omega} U \, \mathrm{d}\Omega \tag{7.58}$$

$$\Theta_{u} = \frac{\rho}{2} \; \Phi_{\mathrm{u}} \overline{u^2} \tag{7.59}$$

$$\frac{\Theta_{s}}{\Theta_{u}} = \frac{\dfrac{\int_{\Omega} \Phi_{\mathrm{s}} \, U^2 \mathrm{d}\Omega}{\Omega}}{\Phi_{\mathrm{u}} \bar{u}^2} \tag{7.60}$$

for the momentum the equation is,

$$\frac{M_{S}}{M_{u}} = \frac{\dfrac{\int_{A} U^2 \, \mathrm{d}A}{A}}{\left(\dfrac{\int_{A} U \, \mathrm{d}A}{A}\right)^2} \tag{7.61}$$

and for the mass flux it is,

$$\frac{J_{s}}{J_{u}} = \frac{\dfrac{\int_{\Omega} \Phi_{\mathrm{s}} U \; \mathrm{d}\Omega}{\Omega}}{\Phi_{\mathrm{u}} \bar{u}} \tag{7.62}$$
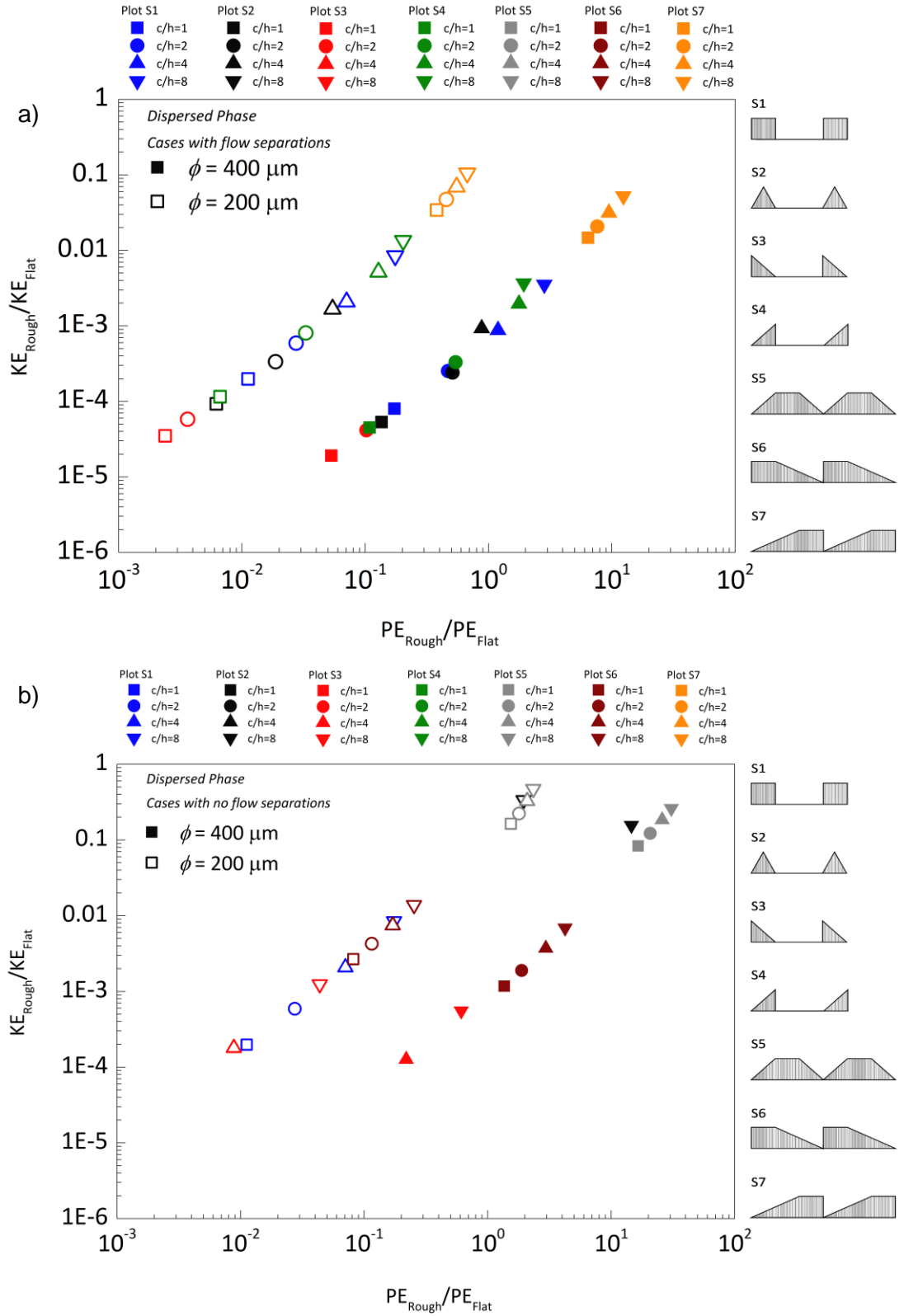
Figure 7. 11: Comparison of the energy budget for bedforms (a) with flow separation, and (b) without flow separation.

7.7 Energy budget

Initially, attention is restricted to the energy budget of the flat-bed case for which the production and dissipation of turbulence kinetic energy takes place in the bottom boundary layer rather than in the shear layers associated with recirculation zones. Under the periodic boundary condition implemented in this work, extending the length of the channel in the streamwise direction will have no effect on the total energy per unit length of the system. Here, the total energy of the system ϵ_T is given by:

$$\epsilon_T = \Theta_d + \Theta_c + \Pi_d + \Pi_c$$

(7.63)

To check the dependence of ϵ_T to ϕ for particle laden flow over a flat plate, two particle diameter sizes, $\phi = 200\ \mu m$ and $\phi = 400$, were examined. Both Θ_c and Π_c were recorded to be lower for the continuous phase at $\phi = 400\ \mu m$ than $\phi = 200\ \mu m$. However the Θ_d and Π_d were detected to be higher for $\phi = 200\ \mu m$ than $\phi = 400\ \mu m$. This can be explained by the conversion of energy from the continuous phase to the dispersed phase, as small particles are more easily carried by the flow.

The tests also showed that ϵ_T for $\phi = 400\ \mu m$ is greater than ϵ_T for $\phi = 200\ \mu m$. This is due to the larger energy dissipation via the viscous drag as more sediments are entrained from the bed for finer particles. Figure 7.11 displays the plots for the mean distribution of kinetic energy versus potential energy of the dispersed phase for bedform cases with (a) flow separation and (b) without flow separation. Here, only the data for particle diameter size ϕ= 200 and 400 μm are shown as for smaller sediment diameter than this range, the simulations of flat bed attained a physically unrealistic converged solution, whereby the domain becomes filled with the particulate phase occupying mass fraction almost equal to unity. To plot the energy budget variables, here only the solution of cases which produce a particle mass fraction solution lower than 10% is considered. Both the mean kinetic energy of the rough bed Θ_d and Π_d are normalised by the solution of the flat bed to evaluate the energy loss/gain for kinetic and potential energy of sediment-laden flow over each bed topography relative to that of the flat bed case.

Let us first consider the energy budget analysis for the bed roughness, namely $S1$ at ratio $c/h = 1$ for size ϕ= 200 and 400 μm. The value Θ_c is found higher and the value Π_c lower for flow with coarser sediment. For the dispersed phase both Π_d and Θ_d showed a greater value for coarser sediment flow. This suggested that more energy has been converted from the continuous to dispersed phase for PE than KE.

Consequently this leads to a slight reduction of the PE for flow comprising finer sediment. Unlike the flat bed case, for the rough bed the value of ϵ_T increased with the decrease in sediment diameter. This discrepancy is due to the generation of eddies by the bedform which resulted in the dissipation of the flow energy by turbulent eddies.

Overall for all rough bed cases sediment-laden flow only encountered loss and no gain in kinetic energy for the dispersed phase as all the data were below unity for the kinetic energy ratio $\Theta_{d(\text{rough})}/\Theta_{d(\text{flat})}$. This is to be expected, as the work in the previous chapter indicates that bed roughness always increases drag, and hence decreases kinetic energy. If this were the only significant effect, it would tend to decrease runout length. For all cases, the loss in Θ_d decreased with the increase in ratio c/h. Similar behaviour is observed for friction factor f which decreased for higher aspect ratio c/h (see Chapter 6). Further for all rough bed cases the loss in Θ_d appears to be slightly greater at $\phi = 400\ \mu\text{m}$ than $\phi = 200\ \mu\text{m}$. Thus, sediment size does not play an important role in the kinetic energy of the dispersed phase Θ_d.

In contrast, for the potential energy of the dispersed phase Π_d, some bed roughness achieved a value above unity for the ratio $\Pi_{d(\text{rough})}/\Pi_{d(\text{flat})}$. Such bed roughnesses have the potential to increase flow capacity, and hence increase run out length relative to the flat bed case. Also, the increase in c/h value produced higher Π_d for all cases. The influence of sediment size on the PE is found to be more pronounced for PE than its counterpart KE. As the particle diameter increased, the computed $\Pi_{d(\text{rough})}/\Pi_{d(\text{flat})}$ shifted towards gaining more potential energy.

As can be observed in Figure 7.11, the horizontal spacing w plays an important role in the flow energy budget. The total energy ϵ_T is found to be lower for bedforms with spacing w than the surfaces with closed gap between the rougheness elements. The potential and kinetic energy of both dispersed and continuous phases were computed as being lower for cases with spacing. For the flat plate the energy dissipation is controlled by the amount of particles entrained, providing more particle drag. For the rough case the energy dissipation is more dominated by turbulence energy and diffusion. It should be mentioned that the flow separation has no significant effect on the flow energy budget: the main control is rather the density and shape of the roughness elements.

a)

b)

c)

d)
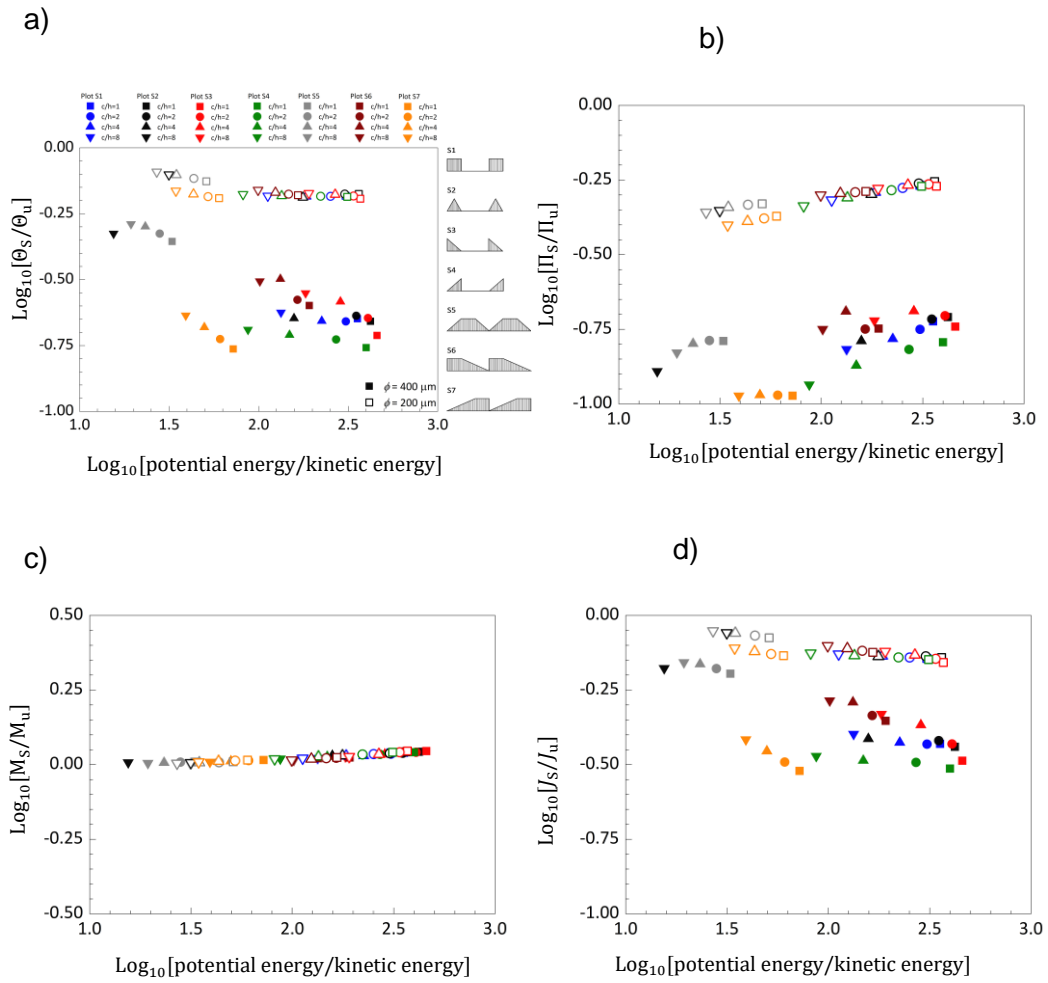
Figure 7. 12: Dependence of the stratification effect for (a) kinetic energy (b) potential energy, (c)momentum, and (d) mass flux on flow Richardson number in different bedforms.

In order to make a summary of this subsection, the average energy budget over the entire phase (continuous phase + dispersed phase) of the computational domain was also computed. The kinetic energy of the total phase (continuous phase + dispersed phase) is more effected with the change in bedform shape and particle diameter size than the potential energy. Also in the case of the total phase, the flow resulted in an overall loss of kinetic energy and an overall gain of potential energy. For all bed geometries, the ratio KE_{rough}/KE_{flat} for the total phase resulted in a slightly higher value for the smaller particle size as more sediments were entrained by the flow. However, for the potential energy no significant change occurred between the two

particle sizes. Further, a linear gain in potential energy was observed with respect to that of the kinetic energy of the dispersed phase with increasing sediment diameter ϕ.

7.8 Stratification effect

This section studies the influence of stratification on the flow energy budget, momentum and mass flux. Figure 7.12 reports the change in kinetic energy, potential energy, momentum and mass flux as a result of flow stratification in various bedforms for $\phi = 200$ and $400\,\mu$m. In figure 7.12 (a), (b) and (d), the results appear to be grouped into four clusters. The particle diameter ϕ further splits the data into two upper and lower clusters.

The upper cluster, which is closer to unity, corresponds to the finer particle ($\phi = 200\,\mu$m) with a weak flow stratification. This is because the flow is able to pick up more particles from the bed and thus reducing stratification. The lower cluster corresponds to coarser sediments which are more difficult to be entrained by the flow and hence produce a more stratified flow. In other words, the higher the sediment concentration is the weaker the flow stratification.

The computed Θ_s/Θ_u ratio as a function of R_{id} for different bed roughness is shown in figure 7.12 (a). It should be noted that the kinetic energy of the stratified flow with a varying concentration $\int_V \phi\, y dV$ is lower than that of the unstratified flow with a fixed concentration for all bedforms. The kinetic energy for both the unstratified and stratified flow increases with the ratio c/h, hence, as expected, there is a decrease in drag with the ratio c/h for both the unstratified and stratified flow. Also, the ratio Θ_s/Θ_u is increased for higher aspect ratio c/h as a result of flow stratification.

The flow is less stratified in cases with recirculating zones than the cases without. The trend appears to be opposite to that of the Π_s/Π_u ratio when comparing separated and unseparated cases in figure 7.12(b). This is because as the near-bed velocity is small, the ratio Θ_s/Θ_u is less affected by the flow stratification than the ratio Π_s/Π_u

The ratio of the momentum between a stratified flow and the unstratified flow is found to be negligible and slightly above unity for all cases (see figure 7.12 (c)). The ratio M_s/M_u showed a slight increase with the ratio c/h similar to the ratio Π_s/Π_u. The stratification of the mass flux, presented in figure 7.12 (d), demonstrates the same trend as Θ_s/Θ_u and this means the mass flux is not much affected by the flow

stratification. Finally, the values of Richardson number behaves differently for each bedform. R_{id} is found to show a similar behaviour for all plotted ratios in figure 7.12, that is an increase in R_{id} with the increase in eddy viscosity and overall flow losses by the bedforms (Darcy friction factor). The value of the ratio R_{id} is increased with the decrease in aspect ratio c/h. R_{id} exhibits a large value for blunt edge facing flow bedforms and a lower value for sloped edged facing bedforms; in particular R_{id} is lower for surfaces with a closed spacing between the roughness elements.

7.9 Flow capacity

The results of the normalised flow capacity for various bedforms are shown in figure 7.13. The flow capacity predicted over α_r is normalised by the transport sediment concentration of the flat bed α_f of the same sediment diameter ϕ. This allows a focus on the gain and loss in transported volume fraction of the sediments over bedforms.

A novel finding of this work is that the trend between the change in flow capacity and the division of flow energy consists of two zones. The dashed green zone in figure 7.13 corresponds to bed geometries with blunt edges (round symbols) in opposite to the x-direction of the fluid generating high flow capacity, high skin friction, decreased flow resistance, decreased turbulent mixing and no flow separation. In contrast, the orange zone in figure 7.13 is attributed to the cases (square symbols) with shallow slopes which produce large flow resistance, high turbulent mixing, low skin friction and flow separation. Further this study finds that for more roughened surfaces, the turbulent diffusivity is increased with the enhancement in flow turbulence, thus reducing the concentration of sediments in suspension compared to the flat bed. A polynomial curve is fitted to all the data, which shows a slowly changing slope connecting the cases with blunt edges and those with angled sloped bedforms. The curves rarely goes above zero, and when it does, only slightly. Hence, in almost all cases, the overall capacity of the flow over bedforms is reduced relative to the flat bed case. Therefore, as we also concluded in the previous chapter, there is little or no evidence that the presence of bedforms will increase the runout length of turbidity currents.

Comparing the data between the two different particle sizes, it is clear that $\phi = 400\,\mu\text{m}$ result in a higher flow capacity than particle size than $\phi = 200\,\mu\text{m}$ for all bedform types, with the expeption of all aspect ratios for S5 and at c/h=8 for case $S2$. Only for the stated exceptional bedform the ratio α_r/α_f goes slightly above unity and for other bedforms it remains well below unity. This suggests that flow capacity is

reduced in almost all bed geometries. Also, the loss in flow capacity increases as ratio c/h decreases. It can also be seen that the bedforms with low flow capacity experience a significantly higher loss in dispersed phase potential and kinetic energies compared to cases with high flow capacity. The best case for enhanced capacity and runout appears to be that of shallow dunes (Shape $S2$ at $c/h = 8$) spread far apart. It may be that important real world scenarios lie outside the ranges considered here (Wynn and Stow, 2002). If so, this would be the subject of further work.
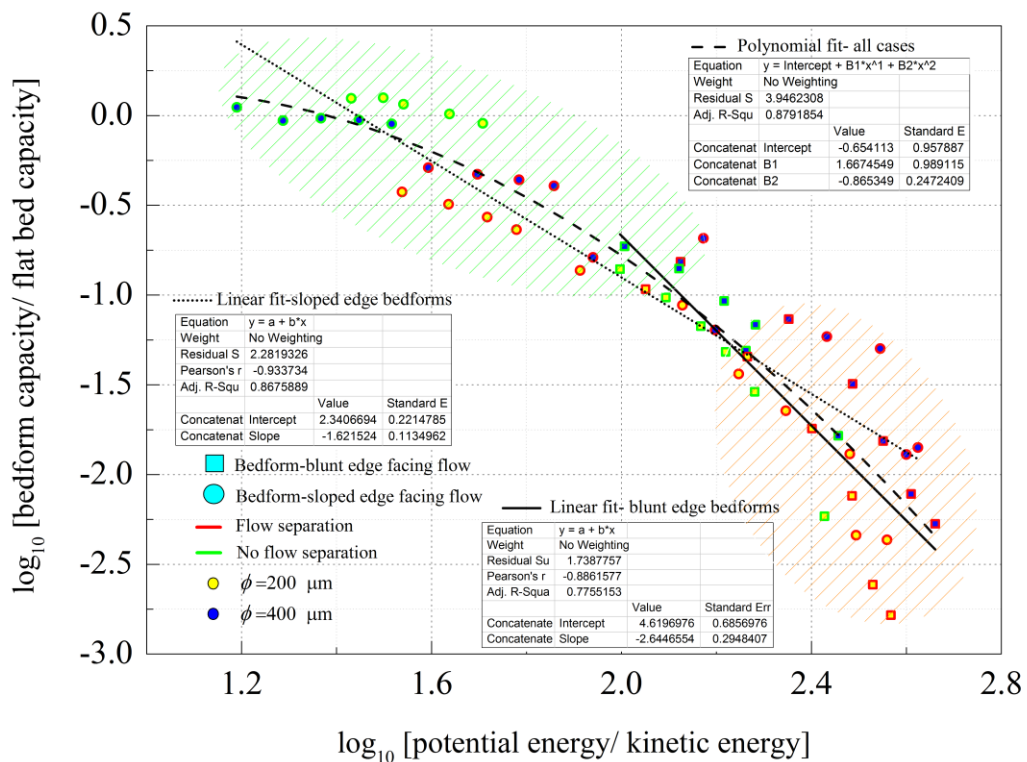
Figure 7. 13: The sediment suspension flow capacity of various idealised bedform as a function of flow Richardson number. Implications for turbidity currents

7.10 Implications for turbidity currents

A significant result of the present study is that that flow capacity is decreased with the increase in turbulent mixing and flow resistance resulting in a lower flow stratification. That the ratio α_r/α_f lies below unity for the majority of the bedform implies that such bedforms reduce the run-out length. This is contrary to the original hypothesis based on the work by (Eggenhuisen and McCaffrey, 2012) for turbidity current flow over a single fixed roughness element. Thus this work suggests that

other factors must come into play to explain long run-out lengths of turbidity currents. These factors are as follows:

i.   Channel sinuosity may increase turbulence, thus increasing flow capacity.
ii. The combined effect of confinement between channel levees may increase runout length.
iii. It is possible that three-dimensional bedforms may behave significantly differently to two-dimensional bedforms (Best, 2005).

Further, the greatest reduction in flow capacity correspond to blunt edge facing cases. Thus, turbidity current propagating over such features will experience a large flow resistance and a large energy sink leading to reduction in run-out length as predicted by the simplified model.

7.11 Conclusions

Numerical simulations were conducted to determine the relation between sediment vertical mixing, flow drag and flow capacity over a range of idealized bedforms. The main results are as follows:

(i)   Large flow resistance and turbulent mixing result in large kinetic energy sink and shorter predicted run-out lengths.
(ii) Large skin friction result in greater capacity to keep particles in suspension leading to a long run-out lengths under significant flow stratification.
(iii) In almost all cases, bedforms are inferred to reduce run-out lengths suggesting other factor must come into play.

Chapter 8
Bedform evolution and stability due to suspended load sediment transport

8.1 Motivation

In the previous chapter, we studied flow and sediment transport over fixed dunes. In reality, there is a 2-way interaction between the fluid flow and the dunes which causes the dunes to move slowly. However, the velocity of the dune motion is very small compared to the fluid flow velocity, and this justifies the use of the quasi-steady state calculations that were performed in the previous chapter. The main motivation for the work detailed in this chapter is to build upon the fixed–dune studies to consider the evolution of non-fixed dunes from a given starting point, and to assess the long term stability of such dunes.

8.2 Introduction

The nature of a bed form depends upon the flow strength and depth, and upon sediment grain size (Leeder, 2009b). For fine to medium sand, the typical sequence of bed forms produced under conditions of constant depth and increasing strength of the unidirectional flow is: no movement; ripples; sand waves; dunes and upper flow-regime plane bed. In coarse sand, a lower flow-regime plane bed develops first, then ripples, followed by sand waves, then dunes, and an upper flow-regime plane bed. At higher-strength flows, the upper flow regime plane bed is replaced by antidunes. The antidunes form beneath sand waves of water that periodically steepen, migrate, and then break upstream. The antidunes bed form is characterized by shallow foresets which dip upstream at relatively low angles (approximately 10°). Their preservation potential is low, but they can be identified by low-angle (less than 10°) foresets, and dipping up-currents (Fourriere et al., 2010). Antidunes tend to show a close association with upper-flow regime plane beds. Thus "little ripples at one's feet at the seashore, or on a dry river bed, or in the desert; gigantic dunes and (even more common, but not apparent to the casual observer) in large rivers, deep sea and shallow oceans are all common examples of bed forms (Jain and Kennedy, 1974). These examples are best illustrated in graphic from in a bedform phase diagram, which can show the presence of one or more stable bed states. This stability is

defined when the bedform is in equilibrium, and shows no sign of change with time, at the same flow condition.

Apart from their intrinsic interest, bed forms are important in both geology and engineering. Large subaqueous bed forms many meters high can be obstacles to navigation, and their movement can be a threat to submarine structures in deep sea and shallow oceans. The rugged topography of bed forms in rivers and tidal channels causes flow separation at the crests and therefore large values of form drag. Thus, bed forms are the most important determinant of resistance to channel flow, and hydraulic engineers have expended much effort on the development of depth-discharge predictors based on the hydraulic relationships of the bed states (Vanoni, 2006). The bed state is also closely bound up with the sediment transport rate and stability in unidirectional flows, in that the down-current movement of the bed forms largely involves recycling of bed load within bed forms. Sedimentologists have given attention to bed forms mostly because of their role in generating stratification in sedimentary deposits - one of the most useful tools available for interpreting ancient sedimentary environments (Lowe, 1982, Middleton, 1993).

At higher flow strength, dunes are commonly stable. These larger shaped bedforms are very much similar to current ripples, but present a dynamically distinctive behaviour (Allen, 1976). This can be typically shown graphically by the lack of intersection between ripples and dunes in a plot of height as a function of wavelength. In general terms, dunes do not manifest from sediment of coarse silt grade and fines. As to the interpretation of the bedform phase diagram, lower plane beds arise at low rates of sediment transport, whereas dunes transition via washed out dunes to upper plane beds formed by under high flow rates of sediment transport.

Two final bedform types can occur. The first of these bedforms are of sinusoidal types which are typically accompanied by in-phase water waves. They can be confused, and thus misleadingly termed antidunes. Antidunes are most commonly observed in very fast, shallow flows, which are roughly characteristic of a rapid (supercritical) flow. Regularly, referred to as antidunes and stationary waves, they are frequently observed in natural alluvial streams and rivers. In conventional terms, they are found in steep streams and carry a heavy load of sediments with heights of several meters (Leeder, 2012).

Antidunes commonly manifest in long trains, in which the wave form may be motionless or may periodically steepen, travel upstream and breakdown in a great rush of turbulence. One may call this a cyclic process. This is also known as antidune

breaking waves (Ferraro and Dey, 2015, Leclair et al., 2015, Winsemann et al., 2015).
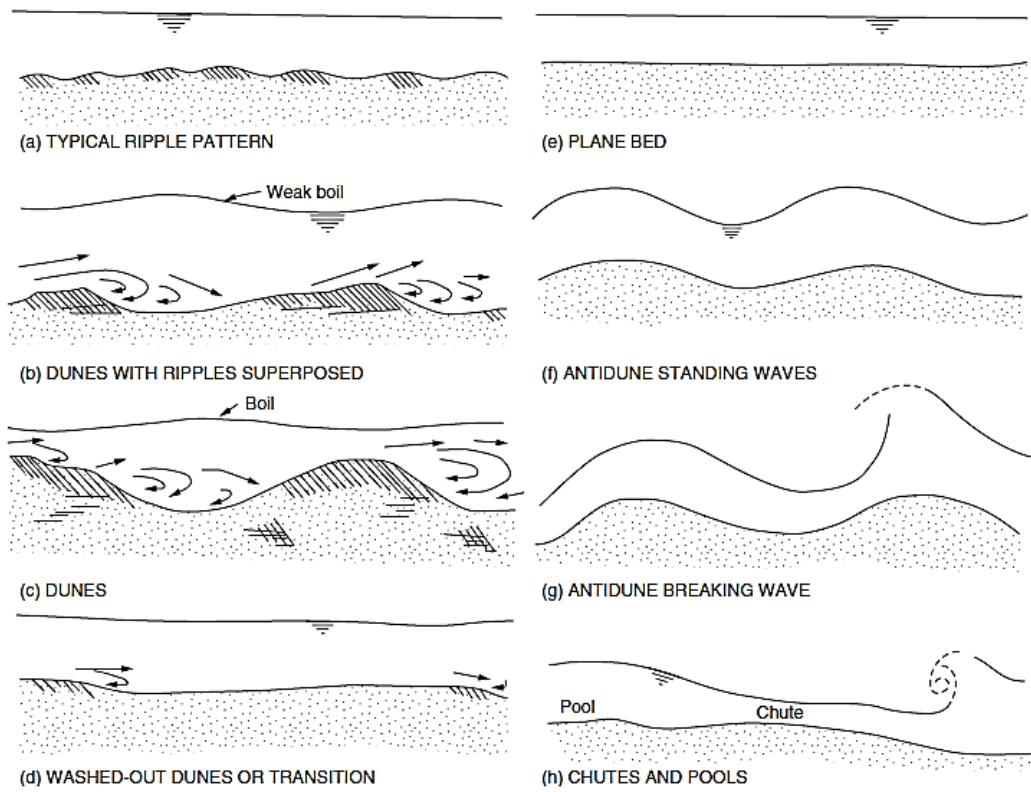
Figure 8. 1: A schematic of water morphology, including surface and river bedforms in an alluvial channel (Huddart and Stott, 2013).

As previously mentioned, when antidunes are formed under the influence of higher flow velocity, chute-and-pool structures develop. Chutes are best described as shallow, rapid, supercritical flow with high slopes which breakdown abruptly in deep water pools, commonly referred to as a natural formation of still water (at subcritical flow conditions). The rapid water flow into a pool, whose upstream boundary is marked by a region of highly violent and turbulent breaking, is a form of a hydraulic jump. Evidently, this is shown as a decrease in the kinetic energy of the fluid flow, which is also referred to by geophysicists as a zone of flow deceleration (Klingeman, 1998).

Figure 8.1 demonstrates (by the sequences of bed phases from part (a) to (h)), the characteristic evolution of bedforms as the flow strength increases. Ripples, lower phase plane beds and dunes all occur in a lower flow regime, in which flow resistance is quite high. Also water waves and blasts of large eddies at the water surface are not in phase with the bed undulations. By way of contrast, upper plane beds,

antidunes, chutes and pool structures form under higher flow regimes, in which all surface waves are in phase with any bed undulations.
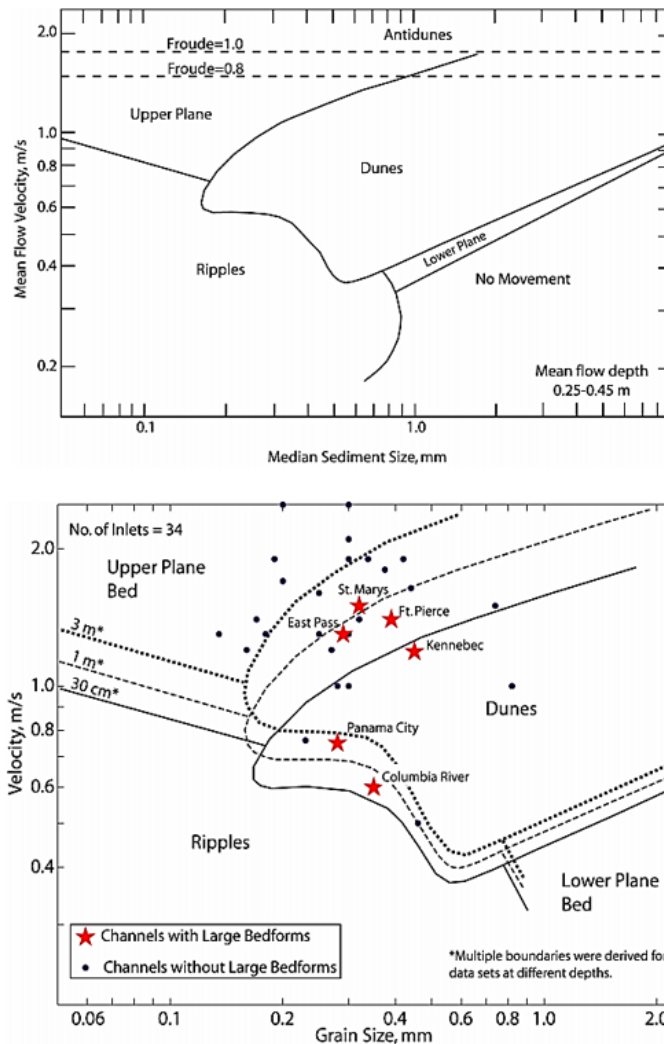
Figure 8. 2: (Top figure): Velocity-grain size plot for predicting sea bed configuration (Ashley, 1990). (Bottom figure): shows the bed form stability based on the work of Southard and Boguchwal (1990).

In accordance with the work of Best (2005), ripples and dunes both exhibit flow separation and reattachment characteristics. The turbulence energy generated from this process illustrates an increase in the frictional resistance enforced by the bed on the flows. For lower flow regimes bedforms the friction coefficients are on average three times those calculated for upper flow regimes bedforms . It is worth remarking that in the case of lower phase flat beds the resistance to flow arises solely from grain drag and has nothing to do with bedform drag (Allen and Leeder, 1980). This has a

direct influence in the mean flow velocity, as can be seen from the bed phase stability diagram illustration in Figure 8.2.

Figure 8.2 shows (via the top graph) how the mean-flow velocity and median sediment size varies as a function of flow depth and velocity and grain size, within the dune stability field. The effect of mean-flow velocity on median sediment size is clearly evident from the fact that as flow velocity increases dunes become both longer and higher. The velocity grain size diagram (at the bottom of Figure 8.1) shows that the dune length increases with flow velocity but is also affected by decreasing grain size (Bridge, 1981). This is primarily the case since the longest dunes tend to develop on beds of the finest sand. In contrast, dune height is only partially resolved by grain size, since fine sand has a greater probability of forming higher dunes. In the case of all sand sizes, with increasing flow velocity, dune height is first increased and then decreases rapidly towards the upper velocity limit of dune stability (Tilston et al., 2015). This is solely the reason for the development of washed out dunes, which can also be seen in part (d) of Figure 8.1.

8.3 Methodology

In general, the interaction between the bedform and saline water is a two-way interaction problem. The motion of the bed form influences the surrounding flow field, while the shear stress distribution on the bedform surface boundary generated by the flow determines bed form evolution. Thus, because of the coupling between fluid and bed motion, it is important to take the hydrodynamic equations into consideration when solving the motion of the bed and vice versa (Celik and Rodi, 1988, Huang et al., 2005, Huang et al., 2008, Huang et al., 2007) . The hydrodynamic model used is the same as in the previous chapter, with erosion and deposition modelled using mass source and sink boundary conditions as described in chapter 7, section 7.4.3. As in previous chapters, the standard $k - \varepsilon$ model was adapted for turbulence closure. This model is supplemented by a model for the bed motion which uses the moving-mesh facilities implemented in ANSYS CFX. A standard Exner equation (Exner, 1927; Dorrell et al, 2013) expression is used to control the motion of the nodes on the lower wall boundary:

$$\frac{\partial \eta}{\partial t} = E_v - D_v$$

<div align="right">(8.1)</div>

where η is the bed height, and E_v and D_v are the volumetric erosion and deposition rates. These are modelled as described in Section 7.4.3; equations (7.30) – (7.40).

The motion of the interior mesh nodes is determined using a method whereby neighbouring mesh nodes are imagined to be connected by springs of variable degrees of stiffness (ANSYS, 2015). Thus, interior mesh displacements are determined by a displacement diffusion equation as follows:

$$\nabla.\left(\Gamma_{disp}\nabla\delta\right) = 0$$

(8.2)

where δ is the node displacement corresponding to the position of the previous cell and Γ_{disp} is the mesh stiffness. This equation is solved at the start of each outer iteration or time step for the coupled flow field and scalar transport equations. In the simplest form of this algorithm, the initial mesh connectivity is preserved as the mesh motion takes place. Under extreme mesh displacement, this can generate highly distorted cells and/or negative cell volumes. In such circumstances, it may be necessary to remesh the problem. However, this was not done in the work reported here.

As mentioned above, the parameter Γ_{disp} can be adjusted by the user to control the amount of mesh displacement in different parts of the mesh. This is beneficial to our application, as it is important that the displaced mesh preserve certain beneficial characteristics of the initial mesh, namely, dense mesh resolution along the bottom boundary layer, and in the vicinity of sharp corners. This is achieved using the following formula for mesh stiffness:

$$\Gamma_{disp} = 1/\mathrm{Max}(y, y_b)^2,.$$

(8.3)

where $y_b = 0.2\ (m)$. Hence, the mesh is rigid from the wall to the vertical distance $y_b = 0.2\ (m)$ above the bed. At a distance greater than $y_b > 0.2\ (m)$ the grids exponentially loses stiffness and becomes more flexible.

In this preliminary study, attention is focused only on shape S2, which represents subaqueous symmetric dunes, as we are primarily interested in modelling the evolution of symmetric dunes to see whether they become stable asymmetric dunes. As mentioned in Kostaschuk and Villard (1996), large subaqueous symmetric dunes found in the Fraser River Canada have stoss and lee slope angles of less than 8°. Accordingly, in this study, the aspect ratio for shape $S2$ is increased to $c/h = 16$ to produce a stoss and slope angle approximately equal to $7.12°$.
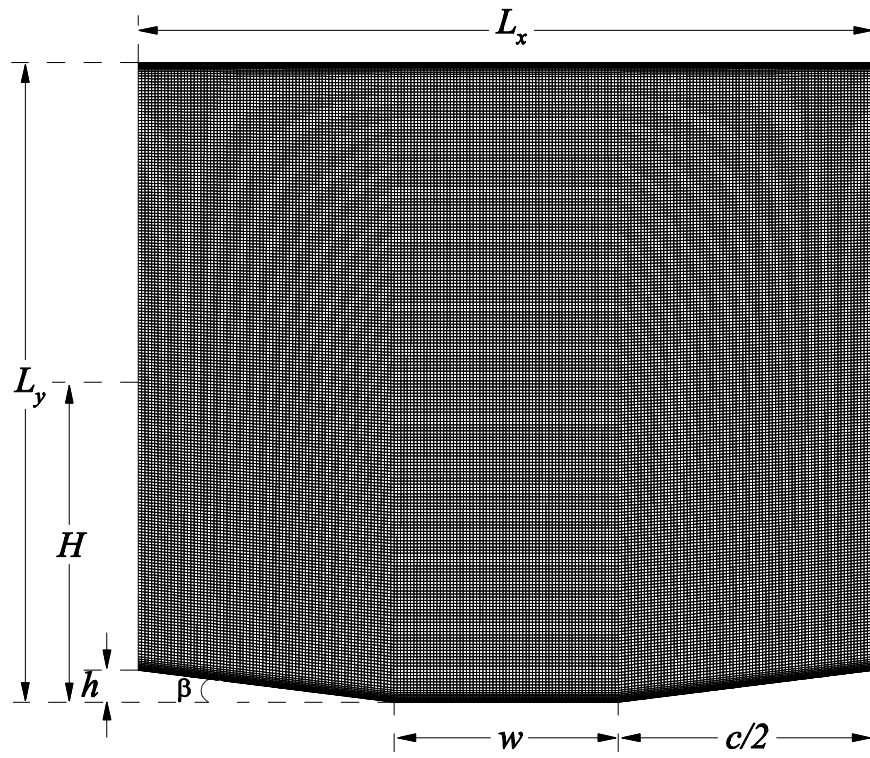
Figure 8. 3: Computational domain and grid system for low-angled symmetric dune.

A two-dimensional computational domain describing the initial condition of the low-angled symmetric dune was generated using a BiGeometric mesh law. This is illustrated in figure 8.3. High mesh resolution near the wall boundaries (Ratio 1.2 and initial spacing 0.004 m) and uniform meshing (no stretching) was applied in the x −direction. The grid dimensions were $N_x \times N_y = 225 \times 230$. The periodic boundary applied uses the same boundary condition as in the previous chapter with a mean pressure gradient via introducing only a streamwise Cartesian component of the momentum source for the external energy input to the flow $(dp/dx = 0.5 \ \mathrm{kg} \, \mathrm{m}^2 \mathrm{s}^{-2})$.

The CFD model is fully transient with constant time interval equal to 1 (s) and the total analysis time 400,000 (s). It uses a first-order backward Euler scheme for the transient discretisation with a high resolution second-order advection scheme for spatial discretisation. The model is simulated for three sediment diameters: $\phi = 400$, 500 and 600 μm. In order to test the model, the simulation was initially run for particle diameter $\phi = 500$ μm. Note that the larger two grain sizes are larger than those studied in Chapter 7. Larger grain sizes are preferred because firstly the dune stability

field on the phase stability diagrams is larger for larger grains and secondly because initial experiments indicated that the simulations did not converge for smaller grain sizes due to mesh distortion (the value of net deposition-erosion rate is higher for smaller particle diameter resulting in greater bed deformation).

8.4 Results

This section discusses the computed results for the interaction between the saline water flow and periodic symmetric dune geometry placed in the lower wall boundary in a channel. The stability of the bed form will be discussed as well as model prediction of the variation of flow resistance with changing bed morphology. The symmetric dunes undergo the process of deposition and erosion. The interaction of the turbulent flow with sediments on the bed of the symmetric dunes leads to the formation of migrating asymmetric dunes and at later stages results in development of sand waves with straightened crest. The developed bedforms migrate downstream over long time scales.

8.4.1 Mean velocity

Figure 8.4 shows the contours of velocity magnitude for a channelized flow with a fixed Reynolds number based on shear velocity $\mathrm{Re}_\tau \approx 4.5 \times 10^5$ over an array of two-dimensional low-angled symmetric dunes consisting of sharp crests at various instants in time. In this figure the contours display the velocity magnitude for particle diameter $\phi = 500 \ \mu\mathrm{m}$. For the contours in figure 8.4, lines were inserted on the crest region of the bedform for each phase. The curve highlights the geometrical variation of the bedforms at each time t. Therefore when the curve show an increase in downstream a bedform take a shape of an asymmetric dune, as the curve head upstream the morphology of the bedform become similar to anti-dune. Finally, when there is no upstream and downstream variation of the curve, the bedform takes shape of a symmetric dune. For all the evolved bedforms at different time steps, the value of velocity magnitude is highest over the crests of the bedforms and lowest above the troughs regions. Further no region of flow recirculation is visible over the evolving bedforms. It is worth noting that the x-velocity component u contributes mostly to the velocity magnitude and has a higher value than the y-velocity component v for over these bedforms.

In the case of the symmetric dunes with eroded crests at $t = 10$ s, the velocity component v was observed to be positive over flow facing stoss slope and near the crests regions and negative above the slope of the lee-side downstream. These zones of positive and negative value in velocity components were further extended in the outer region of the flow away from the bedforms towards the centre of the channel. The pattern in velocities over symmetric dunes are similar to pattern reported in previous field (Kostaschuk, 2000, Best et al., 2001, Lobo et al., 2000) and flume studies (Shugar et al., 2010, Kostaschuk et al., 2004, Parsons et al., 2007, Kostaschuk et al., 2005, Best and Kostaschuk, 2002, Parsons et al., 2005, Wren et al., 2007, Maddux et al., 2003b, Maddux et al., 2003a, Venditti, 2007).

The model predicts a rapid transition from symmetric dunes to asymmetric dunes. At $t = 2 \times 10^4$ s, asymmetric dunes are formed, and the magnitude of average flow velocity show a slight increase compared to the symmetric dunes at $t = 0$ s. This increase is due to acceleration of the flow due to decreased resistance to the flow under the action of a fixed pressure gradient. The area of the positive v over the stoss side of the asymmetric dunes increases with the increase in length of the stoss side and the negative velocity v decreases over the lee side with the decrease in the length of the lee-side.

The magnitude of the average velocity is further increased as the bedforms transform from asymmetric dunes into anti-dunes at $t = 1.1 \times 10^5$ s. Figure 8.4 follows the path of the maximum location of the bed, hence indicating the change in position of the dunes crest as a function of time. Further observation of the velocity components contour $t = 1.1 \times 10^5$ showed a similarity with the behaviour of anti-dunes observed in previous experiments (Kostaschuk and Villard, 1996, Best and Kostaschuk, 2002, Villard and Kostaschuk, 1998). The bedform at $t = 1.1 \times 10^5$ s shows similar characteristics to that of anti-dunes. In other words, it has a large region of negative vertical velocity over the downstream facing lee-side, and a smaller region of positive velocity v over the upstream facing stoss side.

The relation between the flow velocity and bedform morphology, as a function of time, is shown in figure 8.5. This figure indicate that various bedform shapes occur under specific average velocity. At $t = 10$ s, the erosion of the crest of the symmetric dunes results in an increase in flow velocity. In this figure, two general flow regimes can be distinguished: a lower flow regime where symmetric and asymmetric dunes are formed under low velocity condition from $t = 0 - 50,000 \, s$ and an upper flow regime where anti-dunes are being formed under low flow velocity condition from $t =$

$50,000 - 130,000\,s$. Moreover, the bedforms in low flow regimes are associated with low mean flow velocity and hence large flow resistance, and bed-forms in upper flow regimes have relatively high mean velocity, and hence low flow resistance.

 The symmetric dunes are transformed into fully developed asymmetric dunes from $t = 0 - 20,000\,s$. Here fully developed refers to the phase when the bed roughness is developed into an ideal bedform shape. After the fully developed phase, the bedform transitions into a different shape. At $t = 20,000\,s$ the asymmetric dune reaches its fully developed phase. After this phase the asymmetric dune are being washed out and transition into approximately a plane bed at $t = 50,000\,s$. This phase is referred to as approximately plane bed because the bed elevation reaches its lowest value and does not vary significantly on the top surface of the bed geometry compared to other phases.

The morphology of the bed in transition from the dunes in lower flow regimes to an almost moving plane bed in the upper flow regime appears to be intermittent. Subsequently, from approximately $t = 60,000\,s$ the bedform change shape into anti-dunes at $t = 110,000\,s$. Clearly, the figure 8.5 demonstrates how the velocity is significantly higher for anti-dunes compared to symmetric and asymmetric dunes. This difference in velocity was observed in previous experimental studies (Kostaschuk and Church, 1993, Kostaschuk, 2000, Kostaschuk et al., 1989, Kostaschuk and Ilersich, 1995, Best et al., 2001, Kostaschuk and Villard, 1999, Kostaschuk et al., 2009).

From $t = 110,000 - 130,000\,s$ the anti-dunes lose the ideal morphology of an anti-dune. Later, from $t = 130,000 - 150,000\,s$ the bedform transform into asymmetric dunes again. In contrast to asymmetric dunes observed at $t = 20,000\,s$, here the asymmetric dunes have result in lower mean flow velocity and therefore higher flow resistance. This is thought to occur due to the lee side being more inclined towards the incoming flow. At final time steps ($t = 150,000 - 200,000\,s$) bed forms are produced which result in lower flow velocity due to increase in their lee slope angle compared to initial symmetric dune shapes.
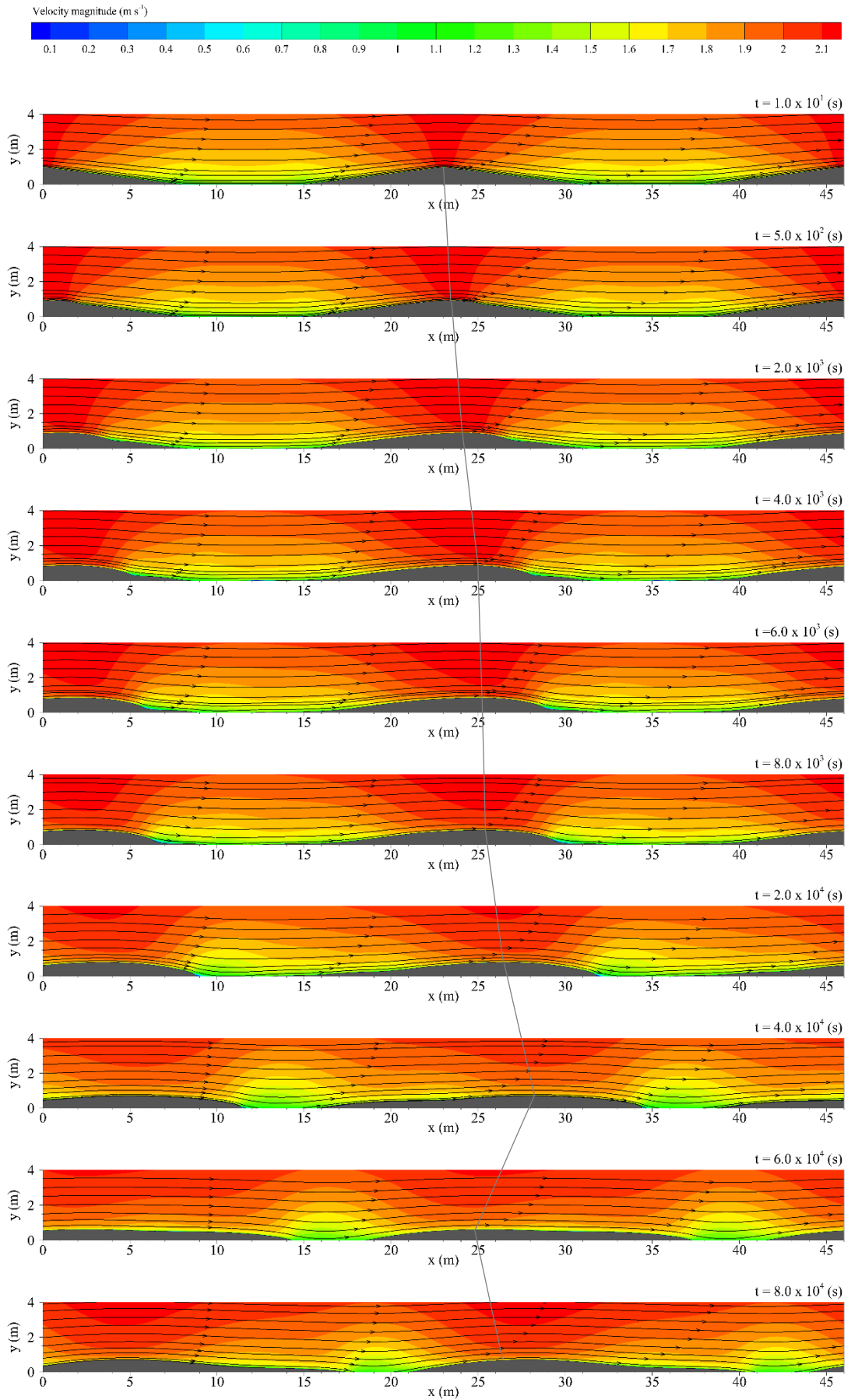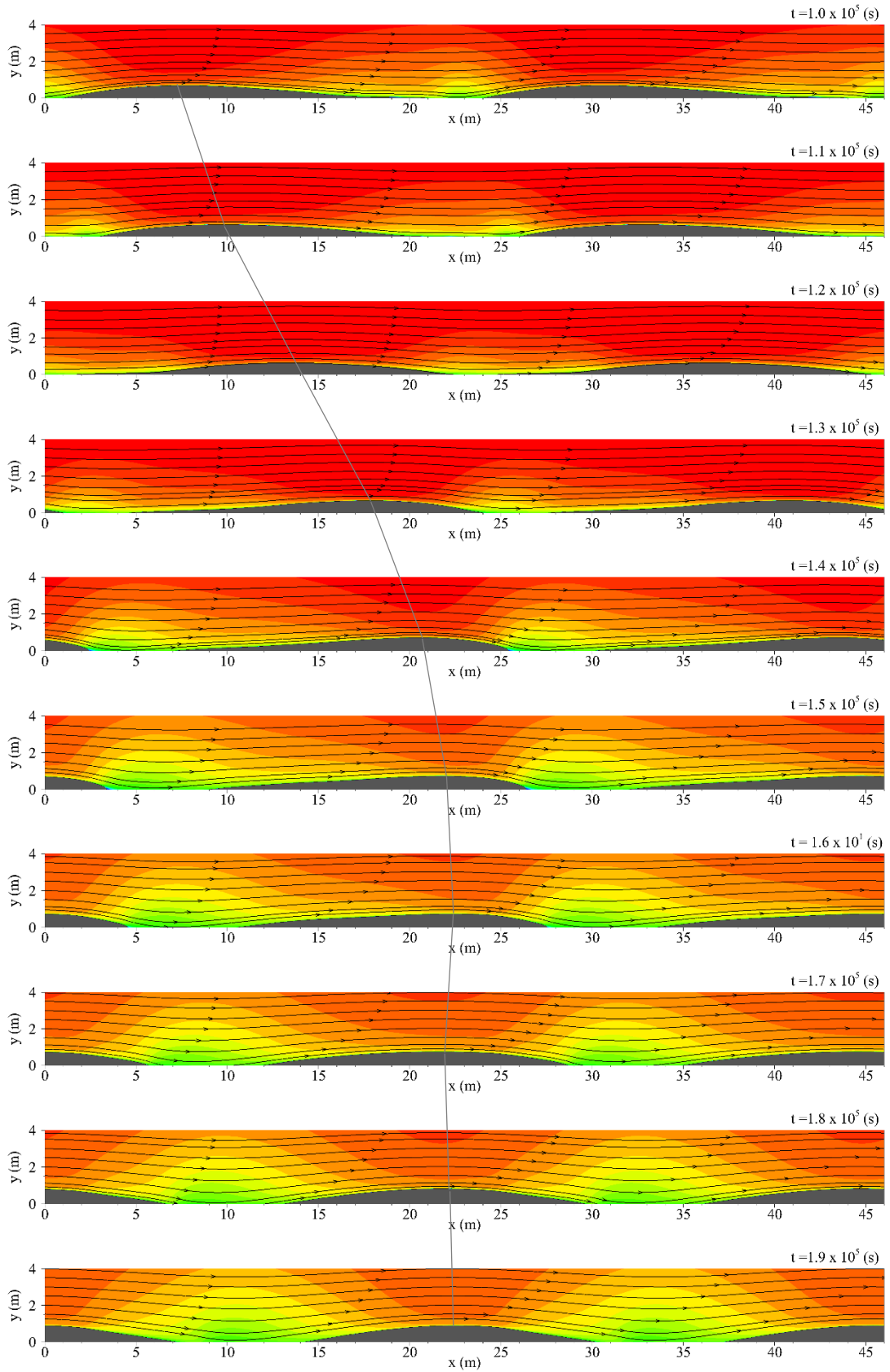
Figure 8. 4: Time dependent velocity magnitude plots from the hydro-morphodynamic model.
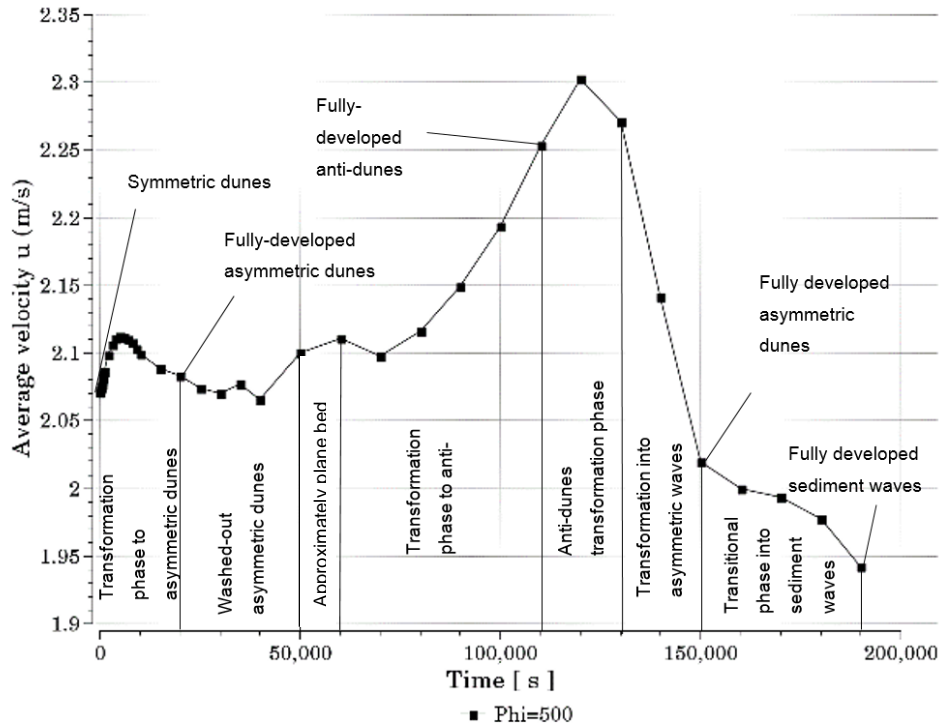
Figure 8. 5: The bedform stability plot which highlights how the bedform develop with both velocity and time.

8.4.2 Sediments concentration field

In figure 8.6, the particle mass fraction contours are shown with bedform evolution as a function of time for $\phi = 500$ μm. No apparent difference is observed between the produced contours. Thus, to look more closely to the rate at which the particles are suspended, in figure 8.7 the normalised flow capacity is plotted in log scale as a function of time; the flow capacity plotted is defined as the total particle volume fraction in fluid c_t (at specific bed evolution time t) divided by the initial total particle volume fraction c_0. The model predicts a relatively small sediment transport rate for the bedforms in the lower flow regime and a large sediment transport rate for the cases in higher flow regime. Note that c_t/c_0 for the straight-crested sediment waves is larger than sharp symmetric dunes at initial time in figure 8.7. The results clearly show that the bed configuration has not yet reached an equilibrium bed configuration since the flow characteristic and sediment transport are not constant.
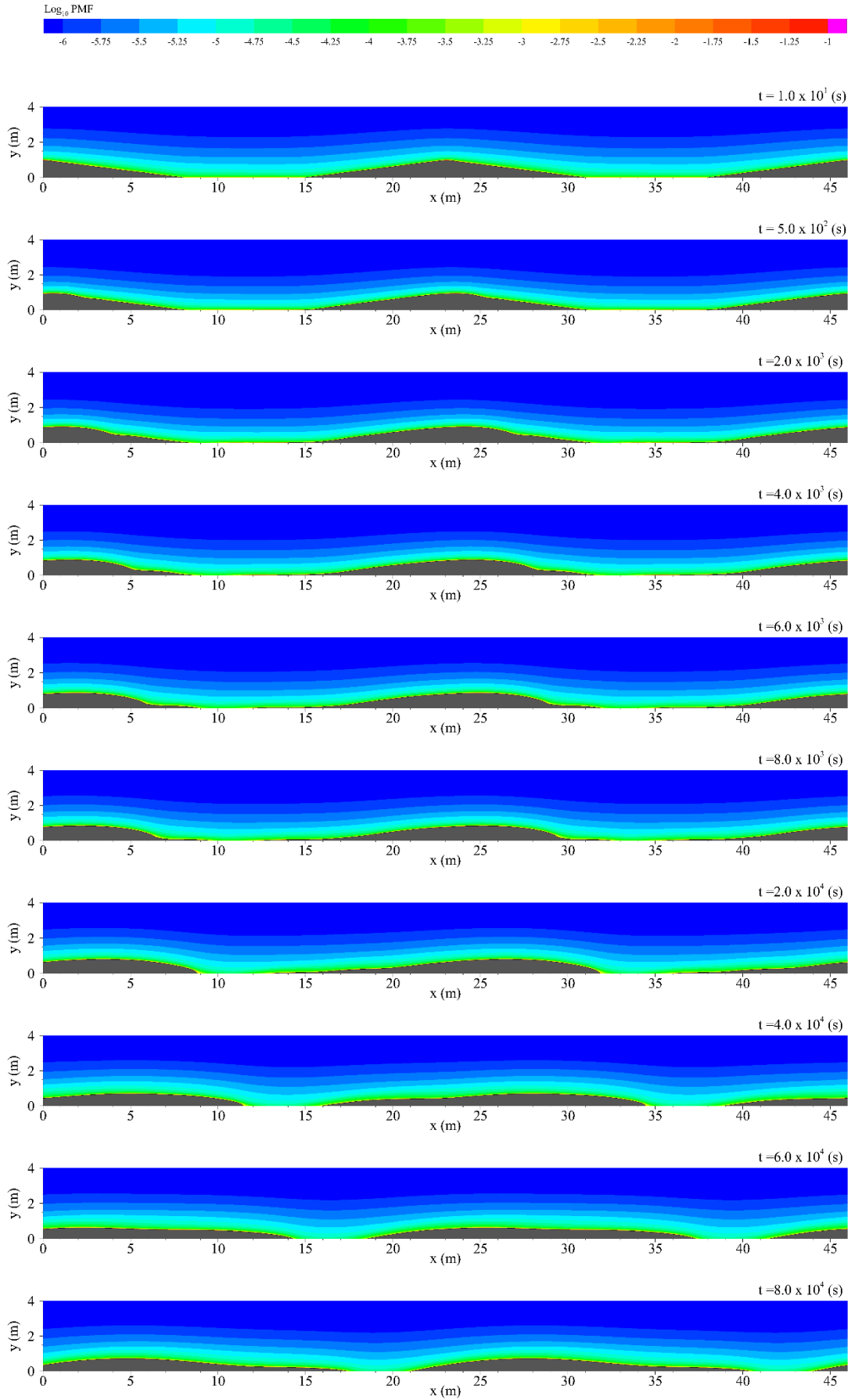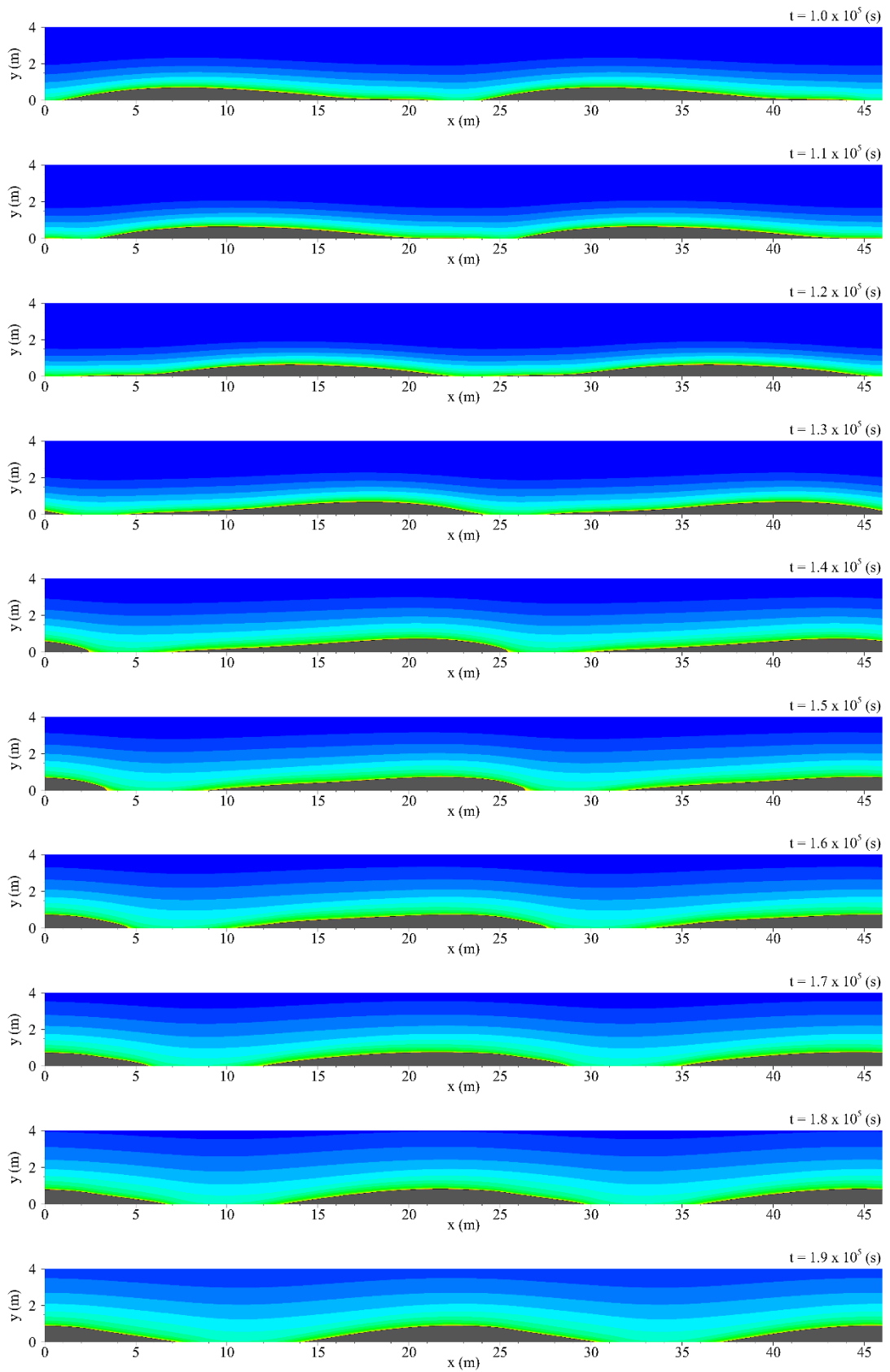
Figure 8. 6: Time dependent concentration iso-surface from the hydro-
morphodynamic model.
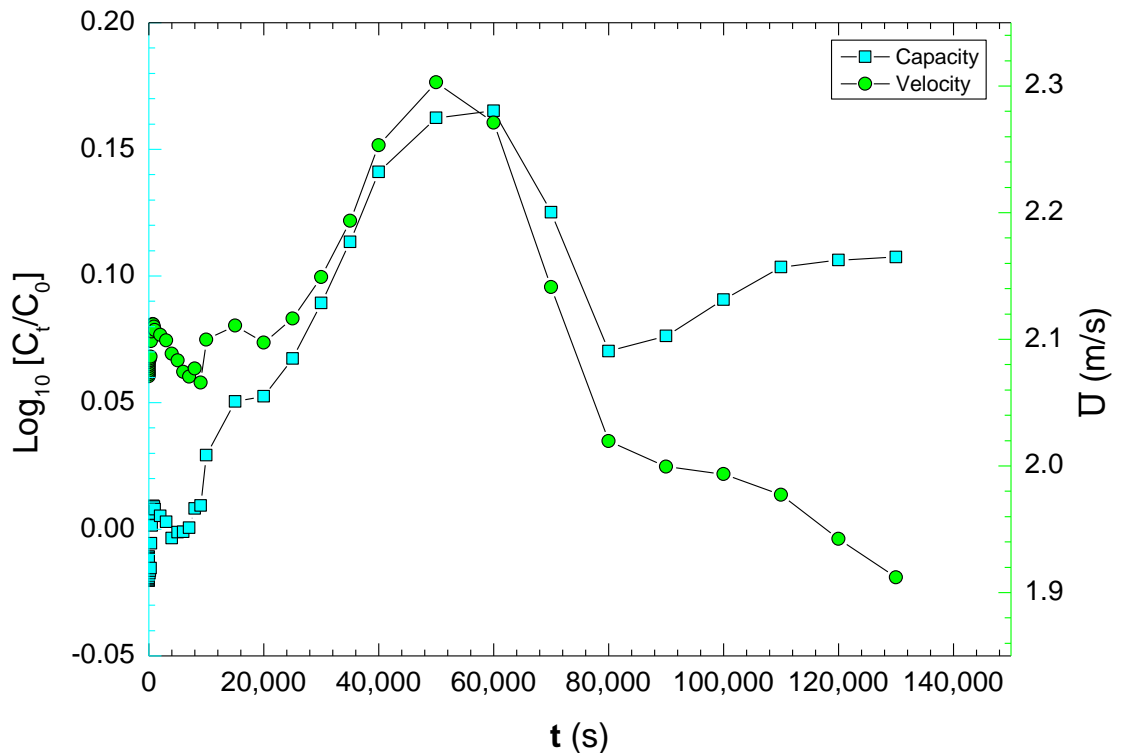
Figure 8. 7: Total particles volume fraction in fluid water c_t normalised to that of initial time c_0 at various instant in time.

8.4.3 Net erosion-deposition

Figure 8.8 demonstrates the net deposition-erosion profiles for the moving bed configuration with flow streamlines as a function of downstream distance x and time t. At initial time (see $t = 1 \times 10^1$ s), the dunes crests are affected by the high rate of flow erosion on the upstream-facing stoss side. Consequently, there is an associated high rate of sediment deposition downstream of the crest line on the lee-side slope. As can be noted for symmetric dunes in figure 8.8 at $t = 1 \times 10^1$ s, the net deposition-erosion rate $\dot{\eta}$ of the stoss side is equal to the lee-side except in the crest region of the symmetric dunes.

As figure 8.8 shows there is almost no variation in the net deposition-erosion rate $\dot{\eta}$, along the width w between the neighbouring dunes in all time steps. At $t = 5 \times 10^2$ s, the sharp crests of the symmetric dunes are deformed into smoothly rounded profiles. The values of deposition and erosion rate on the dunes surfaces are much more reduced than for bed condition at $t = 1 \times 10^1$ s. This is because now the flow

produces a lower wall shear stress τ_w on the rounded tip resulting in a lower rate of erosion and hence lower sediment deposition. Further, there is now a larger region of the stoss side length which is affected by the flow erosion. The rate of sediment deposition shows a shift to the right from the initial time to $t = 5 \times 10^2$ s covering a greater length by the incoming flow as the upper surface of the bedform becomes more eroded. As the time proceeds, flow begins to erode on the lee-side of the dune with slightly a higher value than the erosion rate on the dune crests.

In the transformation phase from symmetric to asymmetric dunes (from $t = 1 \times 10^1$ s to $t = 2 \times 10^4$ s, the flow erosion clearly becomes extended further downstream of the lee-side, thus shortening its length. During this period, the rate of sediment deposition increases upstream of the stoss side and slightly decreases on the crest region of the lee-side. It is of interest to note how the lee-side is eroded and deformed while the stoss side forms into a more curved profile as a result of the net deposition-erosion rate.

As the bedforms transform into a fully developed asymmetric dunes, both the erosion and deposition rates appear to reach steady values at $t = 2 \times 10^4$ s. At later times, as the asymmetric dunes become washed out, the net deposition-erosion profile becomes zero almost on the entire surface of the bedform, and turns it into a roughly plane bed (see $t = 6 \times 10^4$ s). In the transition phase to anti-dunes, the erosion rate begins to only slightly decrease on the stoss side and gradually increase on the lee-side.

At final time-steps shown on the plots, the net deposition-erosion rate only weakly varies along the surface of the bed features. The odd irregularities downstream of the lee side are found to occur whenever the slope angle becomes greater than the angle of repose in figure 8.8. At these points, there is a rapid increase in net deposition-erosion rate, followed by a rapid decrease.
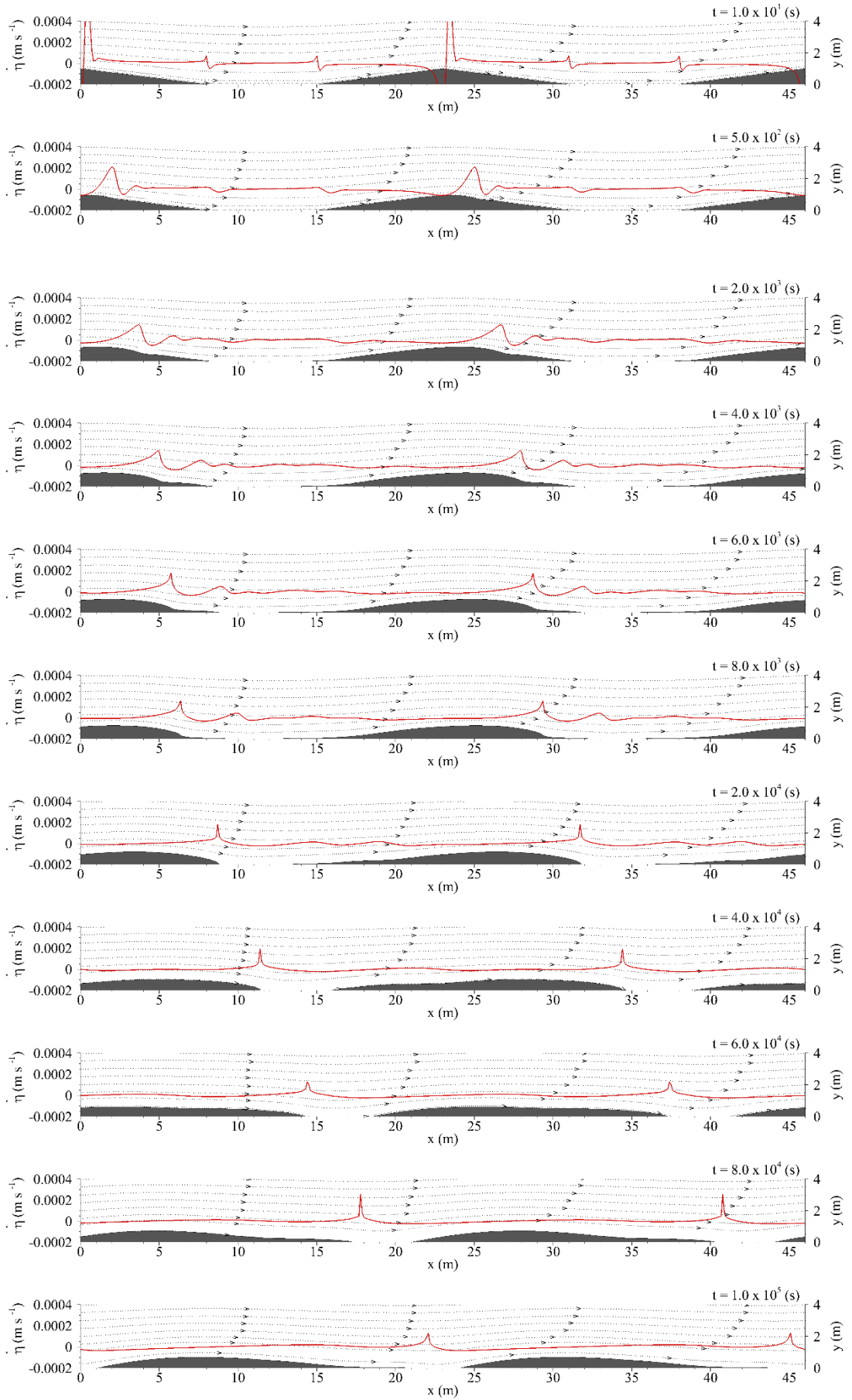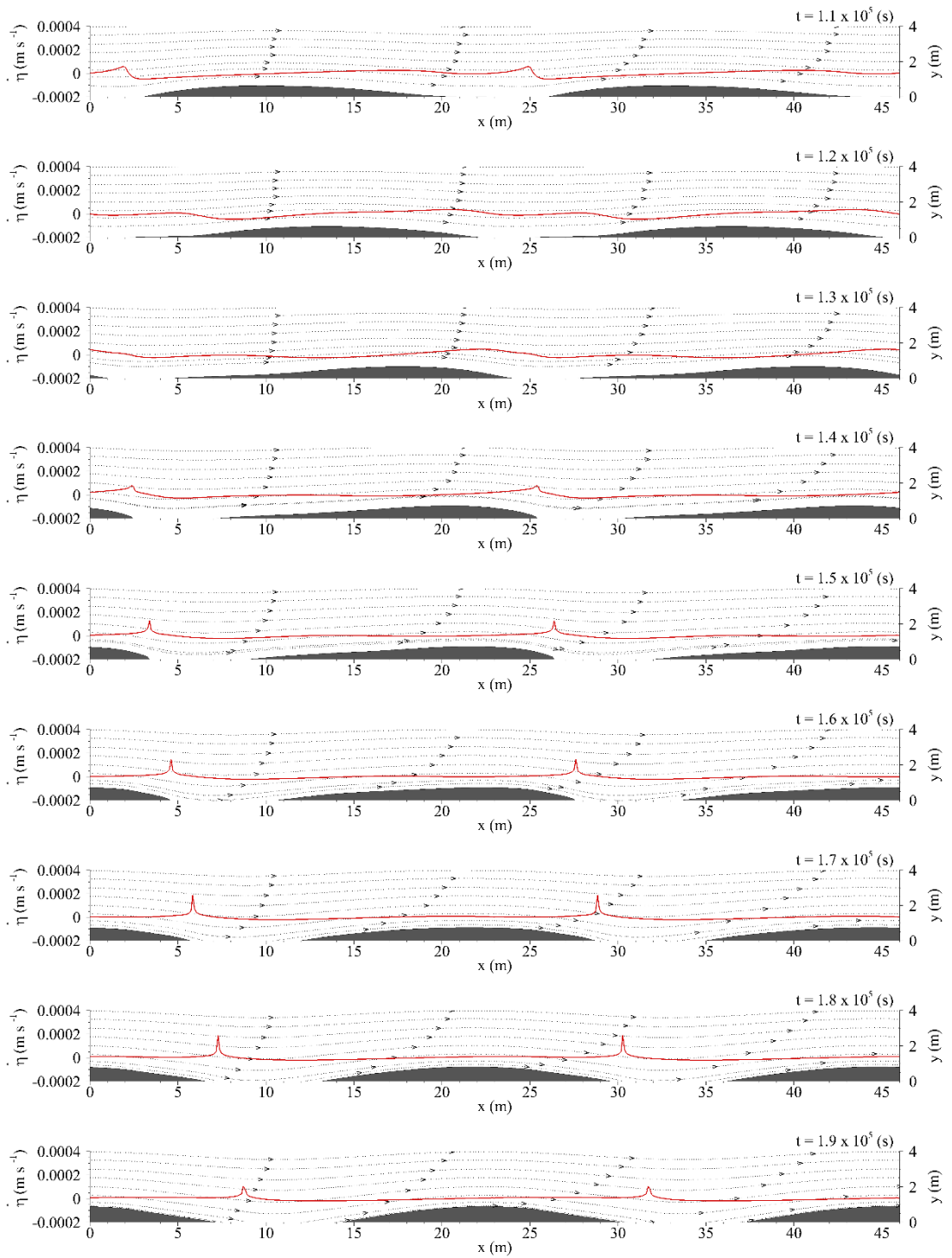
Figure 8. 8: Time dependent net deposition-erosion profiles with flow streamlines the hydro-morphodynamic model.

8.4.4 Effect of particle diameter

The effect of the sediment diameter ϕ is examined in this section. A comparison for the net deposition-erosion rates for various particle sizes with lower evolved bed boundaries is shown in figure 8.9. The results clearly indicate that the evolution of the bed is dependent on the particle size. The highest deposition rate is seen on the down-stream lee-side of the symmetric dunes for $\phi = 400\,\mu m$ in both time steps. Conversely, the higher erosion rate can be seen for $\phi = 600\,\mu m$. These results indicate that symmetric dunes may evolve more slowly for flows carrying particles of smaller sediment diameter. Longer elongated dunes evolve for small grain size in which they eventually get washed out. For larger grain sizes the bedforms have more pronounced rounded crests and have shorter wave lengths.

In figure 8.10 the average mean flow velocity is compared for various particle diameters as a function of time. Considering the bed evolutions for all sediment sizes before $t = 50,000s$, the figure shows that the average flow velocity is higher for smaller particle sizes. As can be seen in figure 8.10, the flow is faster for small particle sizes due to greater dune elongation and lower resistance for all phases except for the bedform transition phases into similar shape to anti-dune.

Furthermore, the comparison of the flow capacity for different particle diameters is shown in figure 8.11. No significant variation in flow capacity can be observed before $t = 60,000s$. However, after this time step the transported sediment load is seen much higher for $\phi = 500\,\mu m$.
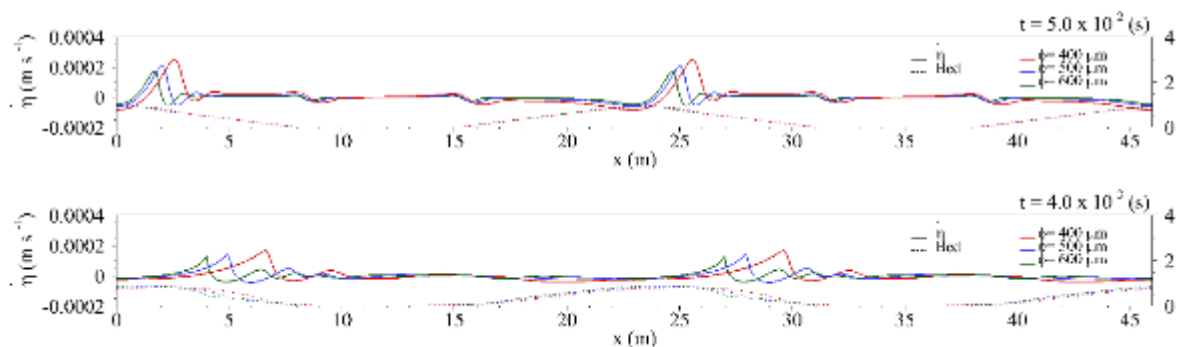
Figure 8. 9: The net-deposition erosion and bed level change for different particle diameters.
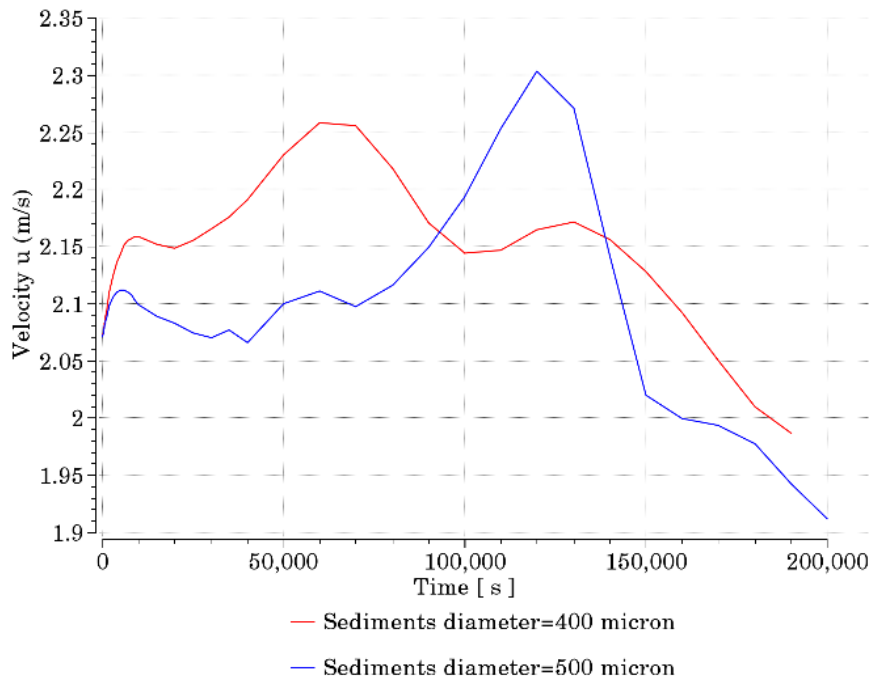
Figure 8. 10: Comparisons of the area-weighted average velocity for various particle diameters
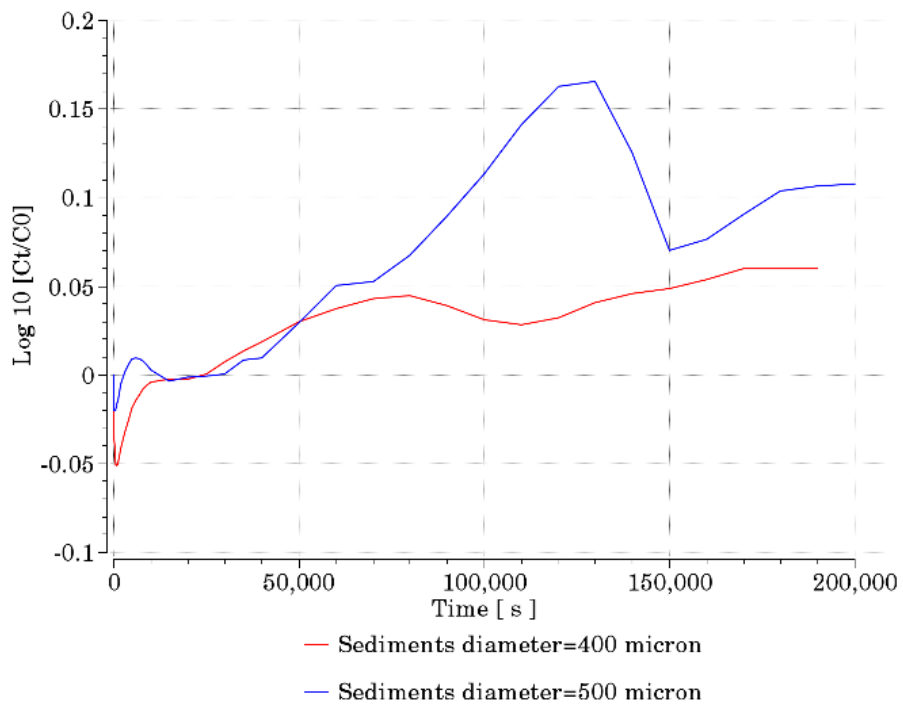
Figure 8. 11: The dimensionless flow capacity for various particles diameter.

8.4.5 Bed elevation

Figure 8.12 shows the variation of the slope angle for various time-steps as a function of downstream distance x for sediment diameter size 500 microns. The first observation that can be derived from this figure is that the highest angle occurs for the crest and head of the dune. The value of angle β which is the slope angle increases with time t up to the plane bed phase at $= 1.1 \times 10^5$, eventually exceeding the angle of repose at $20°$. Eventually, the angle β is found to decrease for the transition phase from plane bed to anti-dunes. At $t = 1.1 \times 10^5$ s, the highest angle appears to occur at the head of the anti-dunes. As the anti-dune morphology becomes deformed, the angle β begins to increase again on the lee-side of the newly developed asymmetric dunes. Further, it can be noted that the horizontal width w disappears eventually with the stoss side of the dunes with the continuing time. The velocity at the crest and trough is plotted as a function of time in figure 8.13 for $\phi = 500$ μm. In figure 8.13 The first thing to note is that both the profiles highlight an exponential decrease in velocity, reaching a value close to zero at final time steps. Secondly, the velocity of the crest is slightly higher for the trough than the crest up to $t \approx 1 \times 10^5$ s. Figure 8.14 demonstrates the distance moved by the crest and trough of the bedform in the streamwise direction with continuing time t. As the results for displacement of the crest and trough as a function of time indicate the migration of the bedform is in the stream-wise direction. The position of the bedform crests is significantly changed downstream from $t = 0$ (s) to $t = 50,000$ s. Although, the bedform crests is significantly changed downstream from $t = 0$ (s) to $t = 50,000$ s. Although, the bedform troughs only move gradually in the direction of the increasing x. From $t = 60,000$ s up to $t = 140,000$ s the bedform crests move further downstream. In addition, the crest show no movement after $t = 150,000$ s and the trough only show a slight increase in their position downstream after this time step .

Figure 8.15 compares the morphological details of the subaqueous asymmetric dunes found in Fraser river Canada (Kostaschuk and Villard, 1996) with the bed configuration of the asymmetric dunes obtained by the model in the present study. It should be noted that these bedforms have been developed under different flow conditions and flow density. The stoss slope of the asymmetric dunes in the present study is not straight and is superimposed by low-amplitude bed waves similar to asymmetric dunes found in Fraser river Canada and in other studies (Livesey et al., 1998, Venditti et al., 2005c, Bennett, 1995) .
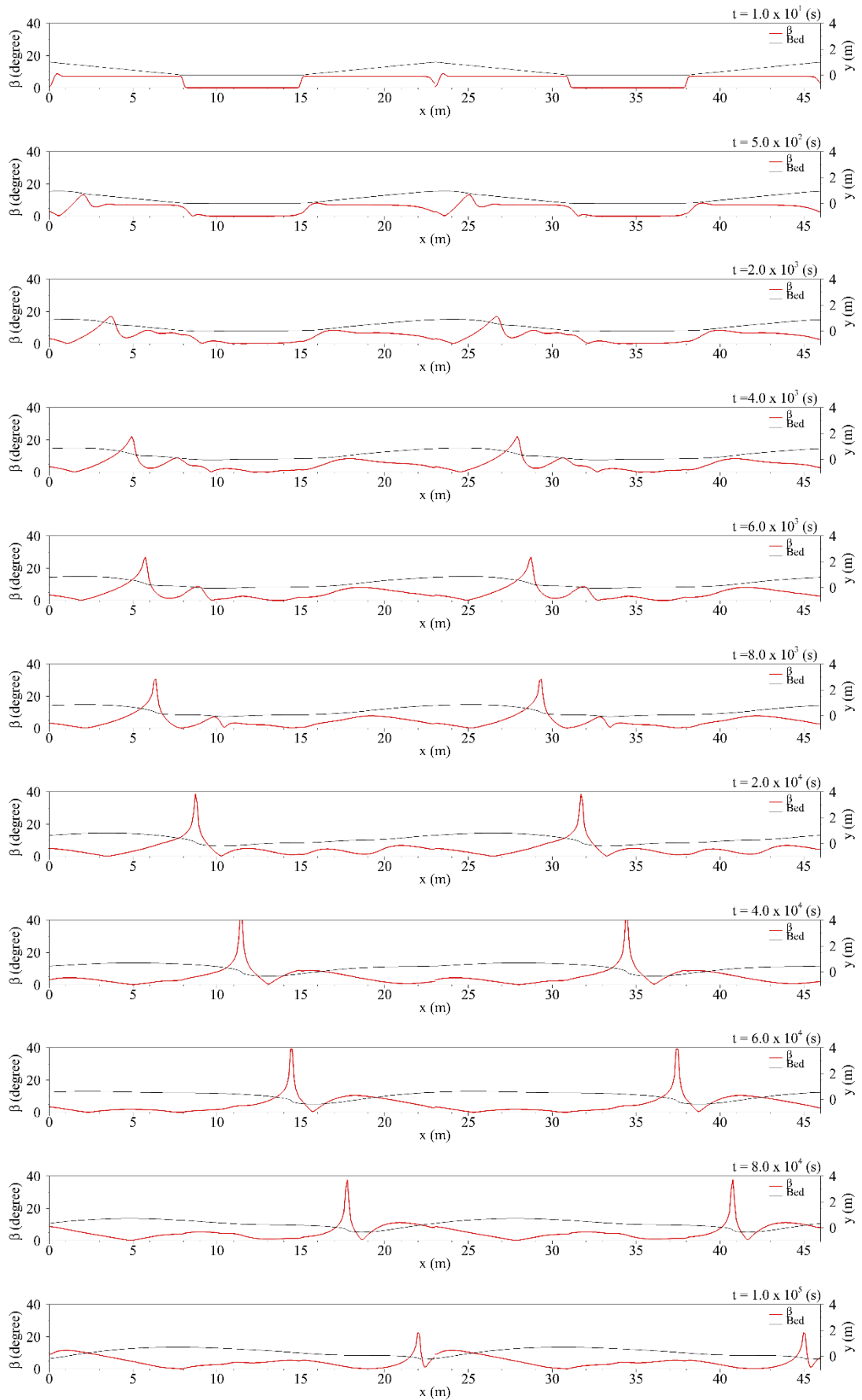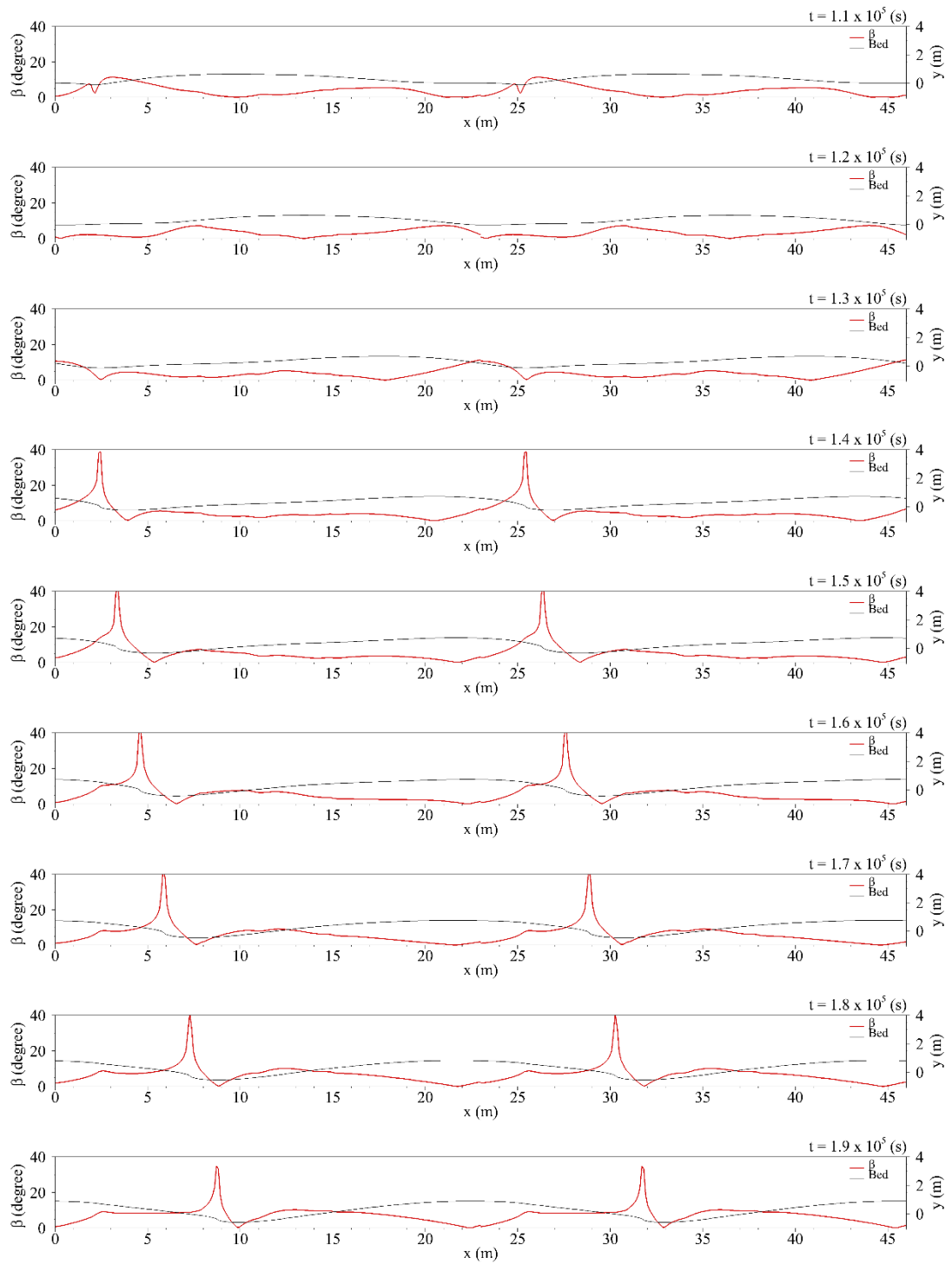
Figure 8. 12: Time dependent angle β plots from the hydro-morphodynamic model.
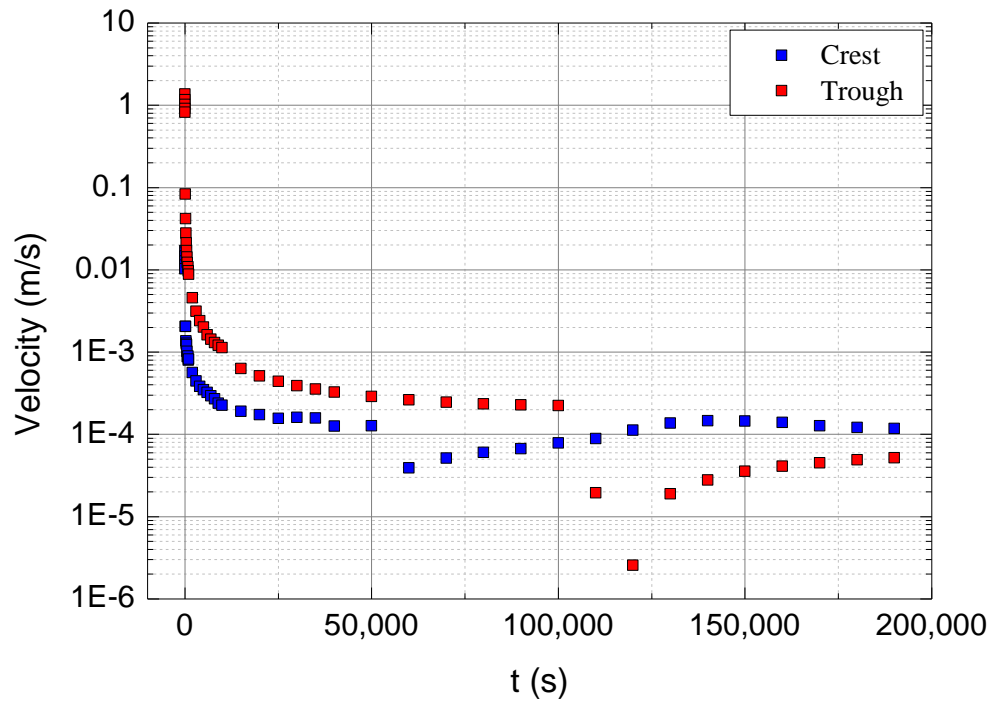
Figure 8. 13: The velocity of crest and trough as a function of time for $\phi = 500$ μm.
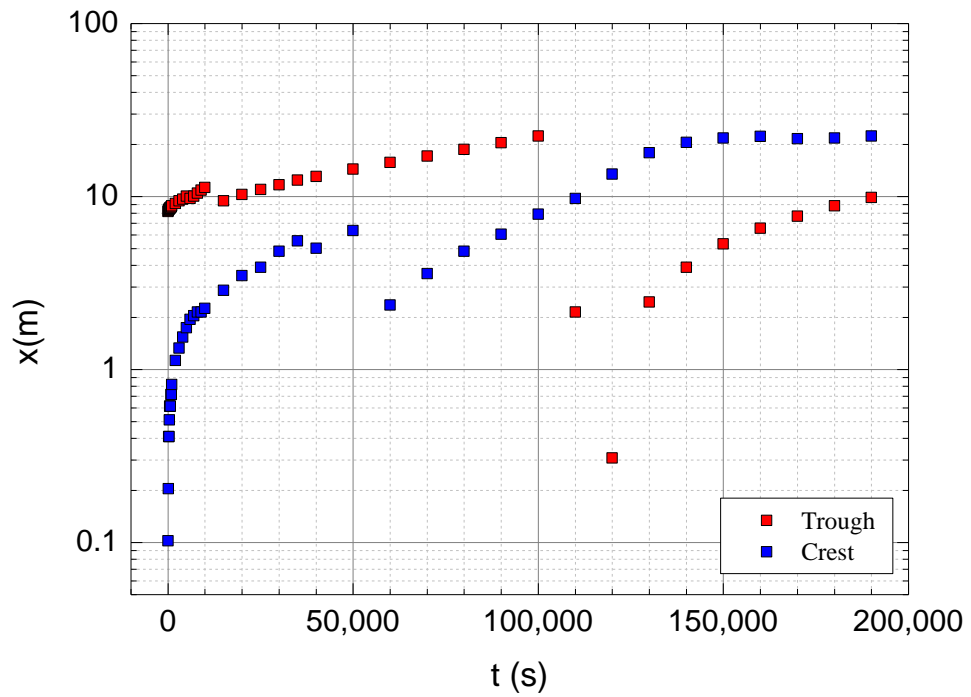
Figure 8. 14: The distanced moved by the crest in the x-direction as a function of time and trough as a function of time for $\phi = 500$ μm.
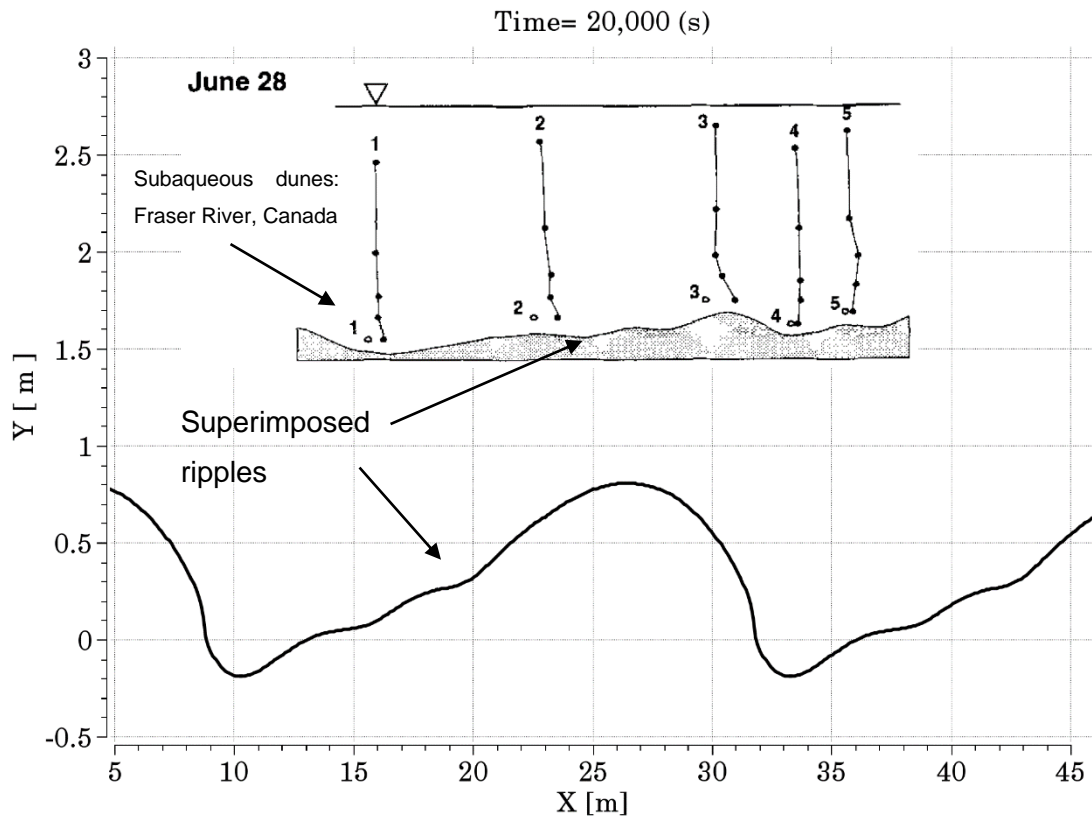
Figure 8. 15: Comparison of the subaqueous asymmetric dunes observed in Fraser river Canada (Kostaschuk and Villard, 1996) and in the present study. Similar to dunes in the Fraser river, the dunes in present result show superimposed ripples on their stoss sides.

8.5 Slip-velocity model

At early time steps in the simulation, the slope angle exceeded the angle of repose which led to mesh skewness, the development of negative cell volumes, and convergence failures at final time-steps. This artefact is discussed in more detail in the results section. As a consequence, a modified model was formulated which replaced the no-slip wall boundary condition with a specified slip boundary condition at locations where the angle of repose was exceeded. This is motivated by the observation that particles will slide down the boundary wall whenever the angle of repose is exceeded. The wall slip boundary conditions are given by:

$$u_x = u_s \cos(\beta)$$ (8.4)

$$u_y = -u_s \sin(\beta)$$ (8.5)

where u_s is the particle slip velocity. This was modelled on dimensional grounds as follows:

$$u_s = \tau g'$$

(8.6)

where g' is the reduced gravity, and the particle slip time scale τ is a modifiable constant that was set equal to 0.01 (s). Figure 8.16 shows the new results for the implemented slip velocity model. The attempted slip velocity model appears to not make a significant change to the angle β_{max}. Consequently, all work presented here has used the original model, without the slip boundary condition, and the evolution of bedforms considered only up to the point where the critical angle is reached.
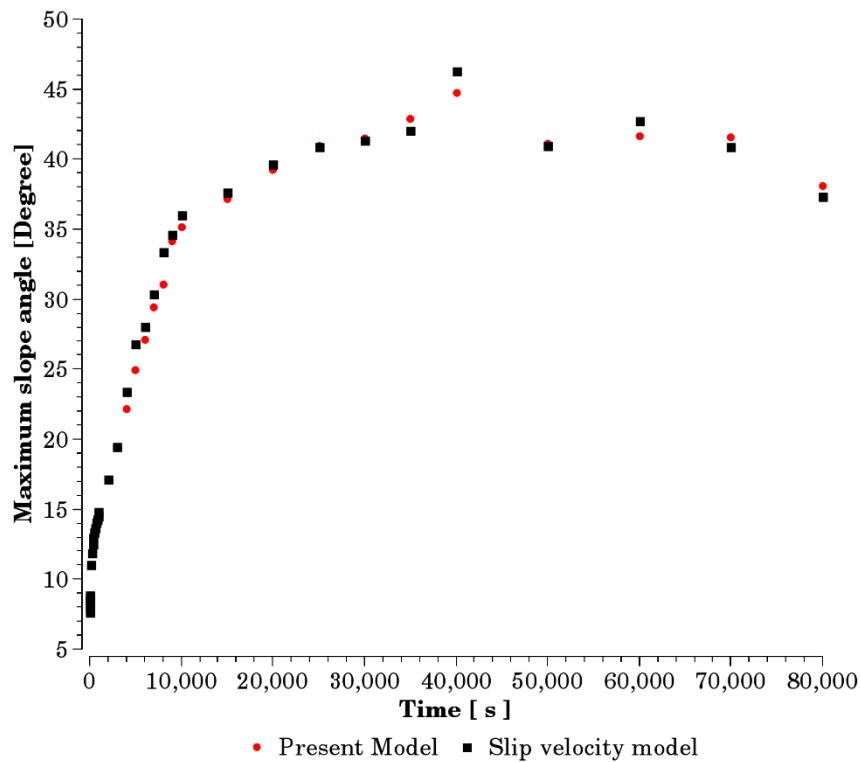
Figure 8. 16: Comparison of the maximum slope angle $\boldsymbol{\beta}$ between the original model and the original model with implemented slip velocity model as a function of time.

8.6 Conclusions

Despite the preliminary nature of this model, it predicts some interesting behaviour that is worthy of further. study. First of all, we found that for sufficiently large particle sizes, the system evolves away from the inherited flow conditions without developing a flat bed. This suggests that there is a grain size threshhold below which washout

occurs, and above which an inherited rugosity due to the bedforms is maintained, albeit in a way which may evolve in time. Also, there is an implication for natural systems such as turbidite systems, that when the flows inherit a certain roughness condition, they evolve the sea floor so as to make a characteristic roughness condition that is not a flat bed, and that will affect the efficiency of overpassing flows. However, the question as to whether flows will be more or less efficient is still open.

Also, the form to which our modelled bedforms evolve corresponds, broadly, to the class in which a sloped edge faces the flow. It is interesting at this point to refer back to the work in Chapter 7, in which we noted a first order conclusion that lower boundary rugosity was more likely than not to reduce turbidity current runout, depending on the type of bedform. However, it was also concluded that the best case for enhanced capacity and runout appears to be that of shallow dunes spread far apart. This coincides with the evolved state of our initially symmetric dune. Thus, it provides some support for the hypothesis that natural systems involving turbidity currents evolve in such a way as to promote run out length.

Finally, in the model, we appear to have a cyclic alternation between different bedforms. This is interesting, but it is not clear whether this behaviour represents what is seen in real world systems, or whether it's a modelling artefact. It is quite likely to be a modelling artefact due to the fact that our simulations are performed at a fixed mean pressure gradient driving the flow. Thus, a decrease in flow resistance will provide a corresponding increase in mean flow velocity, and vice versa. Hence, the behaviour that we observe is only likely to occur in systems which are driven by a fixed driving force, for example, turbidity current flows on sloping beds. This would be an interesting topic for further work.

Chapter 9
Conclusions

9.1 Conclusions

In this thesis, we have studied the effect of bedform roughness on turbulent sedimentary flows in the natural environment. The work was originally motivated by the conjecture of Eggenhuissen and McCaffrey that bed form roughness may be one factor in explaining the unexpectedly high runout lengths of turbidity currents. For that reason, we have paid particular attention to studying when enhanced turbulence mixing occurs, as that is considered to be responsible for keeping particles in suspension, and increasing the capacity of the flow over long distances. In addition, we have focused attention on the competing physical effect of resistive drag to the flow, as that tends to act as a drain on kinetic energy, and hence reduce the runout lengths of gravity currents.

In Chapter 5, we performed numerical simulations of periodic turbulent shear flow over a wide range of rectangular roughness elements, and a wide range of Reynolds numbers. This was motivated by the observation that such flows are a reasonable approximation to flow below the velocity maximum in the main body for overpassing flow of a gravity current. Because of the large number of cases that we needed to study, we chose to use 2D RANS turbulence modelling for the computations. We performed a validation exercise comparing the results of range of RANS-based turbulence models against experimental results and previous LES calculations. This exercise indicated that the standard $K - \varepsilon$ model was the most suitable for our application. The results of the study showed that enhanced mixing and turbulence production did indeed occur at a critical width-to-height ratio of $w/h \approx 7$. A linear rate of turbulence enhancement is seen up to $w/h = 7$, followed by an exponential rate of perturbation decay beyond this critical ratio, with no significant dependence on flow Reynolds number.

It was also observed that the same critical width-to-height ratio gave rise to a peak in resistance to the flow. Hence, the two competing processes that promote and diminish long runout lengths appear to peak at the same width-to-height ratio. Consequently, we were unable to conclude whether or not runout lengths would be increased or diminished by the presence of roughness elements. Flow over erosional roughness is a source of turbulence generation for turbidity currents, but further work

is required to constrain the interplay between drag enhancement and particle diffusion is required to clarify the implications for flow propagation.

The results also have implications for the optimised engineering designs to enable maximum enhancement of heat transfer. In this application, it is worthy to note that the design that optimises heat transfer by turbulent convection also requires the largest pressure drop.

In Chapter 6, we extended the work of chapter 5 by considering high Reynolds number periodic shear flow over a series of idealised lower boundary roughness elements comprising a range of idealized bedform shapes, of varying crestal length to height ratio c/h at a fixed width to height ratio (w/h). These were chosen to approximate the shape of naturally occurring bedforms, such as symmetric and asymmetric dunes and anti-dunes. In order to reduce the number of cases considered, the width-to-height ratio was kept fixed at the value equal to 7, found to be optimal for flow over rectangular elements. The total basal shear stress is split into skin friction and form drag and to show how the respective magnitudes vary as a function of bedform shape and scale.

The results demonstrate how bedforms affect the balance of energy lost (through frictional) vs. potential energy gained (through turbulent mixing). The drag coefficient results demonstrate that the total flow resistance decreases with the increasing aspect ratio (c/h). This suggests that turbidity currents may expend less energy in overcoming the obstacles and hence promoting increased run-out distance. However, the dimensionless eddy viscosity, which represents turbulent mixing of the flow, also decreases with the increasing ratio c/h. As a consequence the potential energy of the turbidity current reduces, promoting shorter run-out. We found that the relation between the friction factor and non-dimensionalised eddy viscosity collapsed to a single straight line for all cases considered. This indicates that the combined optimisation of turbulent mixing and bed resistance is a somewhat universal phenomenon. To elucidate bed form roughness effects on the potential run-out distance of turbidity currents further work is needed to investigate change in kinetic and potential energy through increased drag and decreased mixing or decreased drag and increased mixing.

In Chapter 7, we extended the work of chapter 6 to study details of quasi-steady sediment transport in the suspended load over stationary bed forms. Numerical

simulations were conducted to determine the relation between sediment vertical mixing, flow drag and flow capacity over a range of idealized bedforms. The motivation for this was to study in more detail the distribution of sediment concentration, in order to understand how different bedform shapes affect flow capacity, stratification, and the potential energy vs kinetic energy budget.

The modelling approach adopted was to use the Algebraic Slip model to compute the combined motion of the fluid and the sediments, coupled with models for erosion and deposition on the bed, modelled using boundary mass sources and sinks. A significant finding is that in virtually all cases, the flow capacity is smaller than that which occurs on a flat bed. The only case that shows a very slight increase in flow capacity over that of a flat-bed is the case of shallow dunes, spread far apart.

It is found convenient to express the energy budget of the flow in terms of a densimetric Richardson number defined as the ratio of potential energy to kinetic energy of the particulate phase. A novel finding is that when flow capacity relative to that of a flat bed is plotted against this Richardson number, the results lie close to a curve consisting of two zones:

- An upper branch, for geometries with no flow separation, promoting high flow capacity, high skin friction, decreased flow resistance, and decreased turbulent mixing.
- A lower branch, for geometries with flow separation, promoting large flow resistance, high turbulent mixing and low skin friction and flow separation.

As almost all cases have reduced flow capacity relative to that of a flat bed, the results indicate that the presence of bedforms tends in general to reduce rather than promote runout lengths. However, bedforms close to the top of the upper branch of Figure 7.17 favour higher flow capacity and longer runout lengths relative to other bedforms.

In Chapter 8, we reported a preliminary study using the model developed in chapter 7 to study the two-way interaction between the flow and mobile bedforms, with a view to assessing the long term stability of inherited bedforms, and ultimately to predict and to be able to understand better the structure of empirically derived bed-form stability diagrams. Due to time limitations, we only considered the case of evolution of an initially symmetric inherited bedform. The results indicated that, for sufficiently large grain sizes, the system is not washed away to a flat bed, but rather evolves to a sequence of asymmetric dunes and anti-dunes. This suggests that there is a grain

size threshhold below which washout occurs, and above which an inherited rugosity due to the bedforms is maintained, albeit in a way which may evolve in time. Also, there is an implication for natural systems such as turbidite systems, that when the flows inherit a certain roughness condition, they evolve the sea floor so as to make a characteristic roughness condition that is not a flat bed, and that will affect the efficiency of overpassing flows. However, the question as to whether flows will be more or less efficient is still open.

The form to which our modelled bedform evolves appears to correspond broadly to the class in which a sloped edge faces the flow. This is likely to be in the class of bedform shapes that have low form drag and high skin friction, and hence maximise the capacity relative to that of a flat bed, as was found in Chapter 7. Thus, it provides some support for the hypothesis that natural systems involving turbidity currents evolve in such a way as to promote run out length. However, it would require further work to prove this hypothesis.

The model predicts an interesting evolution to a cyclic alternation between different bedforms. However, this is likely to be a modelling artefact, due to our restriction to shear flows over a fixed imposed pressure gradient. It would be an interesting topic for further work to determine whether or not this behaviour occurs in natural systems.

The model in Chapter 8 proved to be deficient in that it was not able to maintain slopes below the maximum angle of repose. Consequently, the results cannot be trusted to be entirely reliable. On the other hand, it is reasonable to expect that future work that removes this modelling deficiency will maintain many of the qualitative features of the results obtained here.

Overall Summary

On balance, most of the evidence that we have found negates the hypothesis of Eggenhuisen and McCaffrey that rough bedforms promote the runout lengths of turbidity currents. This appears to be due to the fact that increased production of turbulence is intimately linked to increased drag acting on the flow, and these are competing effects in promoting or diminishing runout length. On the other hand, we have produced evidence that those bedform shapes that tend to avoid flow separation, with low form drag, high skin friction, and low turbulence mixing promote greater flow capacity than other bed form shapes. We also have very tentative evidence that bedforms tend to evolve towards the class that promote greater flow capacity.

9.2 Further Work

Our work indicates that, contrary to initial expectation, boundary roughness is not a major contributory factor to the unexpectedly large runout lengths observed in natural gravity currents. So, other factors may also play a significant part in explaining the long run-out lengths of turbidity currents. Channel sinuosity produces a large amount of additional shear, due to the presence of significant secondary flows. This may provide an additional contribution to enhanced turbulence production that is worthy of future investigation, both experimentally and numerically. Another other factor may be confinement of stratified flows within levees, preventing overspill, and hence increasing runout length (Dorrell et al 2013a).

It is possible that our results are biased because of our restriction to 2D flows. (Best 2005) suggests that that the flow over truly 3D bedforms may behave significantly differently from that over 2D bedforms. For example, drag over 3D dunes maybe quite different to that over 2D dunes, as there are greater degrees of freedom for the flow to follow a path of least resistance. Hence, the role of three-dimensionality may be important in the formation of bedforms. Therefore, it would be interesting to extend our work to investigate the flow structure and sediment flow capacity of flows over 3D bedforms.

In our work, we have not performed full simulations of the time-dependent flow of turbidity currents over a rough bed. Such calculations would give direct predictions of runout length. However, they would be computationally much more expensive as we can no longer assume periodicity, so it would be necessary to generate meshes over a very large number of roughness elements. Some work has been done in this direction by Tokyay et al 2011a and 2011b, for both compositional gravity currents, and particulate gravity currents. The morphodynamic model developed on Chapter 8 is a simple geometrically based model, employing an Exner equation with erosion and deposition models based on local flow conditions. This proved to be too simple to prevent exceeding the maximum angle of repose. Future work should be done to remove this deficiency. It may prove necessary to replace the geometric Exner model with a dynamically coupled model linking the fluid flow to the dense particle flow on the bed. Also, our work in Chapter 8 was restricted to high Reynolds number cases where only the suspended load is significant. A truly general model should also consider bedload transport, incorporating models for particles saltating along the bed, and for flow in the dense porous medium provided by the bedload particles.

Bibliography

ABRAHAM, G. & VREUGDENHIL, C. B. 1971. Discontinuities in stratified flows. *Journal of Hydraulic Research,* 9**,** 293-308.

AKINLADE, O. G. 2005. *Effects of surface roughness on the flow characteristics in a turbulent boundary layer.* University of Saskatchewan Saskatoon.

ALLEN, J. 1976. Computational models for dune time-lag: general ideas, difficulties, and early results. *Sedimentary Geology,* 15**,** 1-53.

ALLEN, J. & LEEDER, M. 1980. Criteria for the instability of upper-stage plane beds. *Sedimentology,* 27**,** 209-217.

ALTINAKAR, M., GRAF, W. & HOPFINGER, E. 1996. Flow structure in turbidity currents. *Journal of Hydraulic Research,* 34**,** 713-718.

ALTWAY, A., SETYAWAN, H. & WINARDI, S. 2001. Effect of particle size on simulation of three-dimensional solid dispersion in stirred tank. *Chemical Engineering Research and Design,* 79**,** 1011-1016.

AMY, L., HOGG, A., PEAKALL, J. & TALLING, P. 2005. Abrupt transitions in gravity currents. *Journal of Geophysical Research: Earth Surface (2003–2012),* 110.

AN, R.-D. & JIA, L. 2010. Characteristic analysis of the plunging of turbidity currents. *Journal of Hydrodynamics, Ser. B,* 22**,** 274-282.

ANDERSON, W. & MENEVEAU, C. 2011. Dynamic roughness model for large-eddy simulation of turbulent flow over multiscale, fractal-like rough surfaces. *Journal of Fluid Mechanics,* 679**,** 288-314.

ANSYS, C. 2015. 11.0 help document. *Ansys Inc.*

ANSYS, I. 2009. CFX-Solver Theory Guide. R.

ANTONIA, R. & KROGSTAD, P. 2000. Effect of different surface roughnesses on a turbulent boundary layer. *Journal of the Brazilian Society of Mechanical Sciences,* 22**,** 1-15.

ANTONIA, R. & SMALLEY, R. 2000. Velocity and temperature scaling in a rough wall boundary layer. *Physical Review E,* 62**,** 640.

ANTONIA, R. A. & DJENIDI, L. On the outer layer controversy for a turbulent boundary layer over a rough wall. IUTAM symposium on the physics of wall-bounded turbulent flows on rough walls, 2010. Springer, 77-86.

ARFAIE, A., BURNS, A., DORRELL, R., EGGENHUISEN, J., INGHAM, D. & MCCAFFREY, W. 2014. Optimised mixing and flow resistance during shear flow over a rib roughened boundary. *International Communications in Heat and Mass Transfer,* 58**,** 54-62.

ARMI, L. 1986. The hydraulics of two flowing layers with different densities. *Journal of Fluid Mechanics,* 163**,** 27-58.

ASHLEY, G. M. 1990. Classification of large-scale subaqueous bedforms: a new look at an old problem-SEPM bedforms and bedding structures. *Journal of Sedimentary Research,* 60.

ASHRAFIAN, A. & ANDERSSON, H. I. 2006. The structure of turbulence in a rod-roughened channel. *International Journal of Heat and Fluid Flow,* 27**,** 65-79.

ASHRAFIAN, A., ANDERSSON, H. I. & MANHART, M. 2004. DNS of turbulent flow in a rod-roughened channel. *International Journal of Heat and Fluid Flow,* 25**,** 373-383.

AUPOIX, B. 2007. A general strategy to extend turbulence models to rough surfaces: Application to Smith's kl model. *Journal of Fluids Engineering,* 129**,** 1245-1254.

BAAS, J. H. & BEST, J. L. 2008. The dynamics of turbulent, transitional and laminar clay-laden flow over a fixed current ripple. *Sedimentology,* 55**,** 635-666.

BAAS, J. H., BEST, J. L. & PEAKALL, J. 2015. Predicting bedforms and primary current stratification in cohesive mixtures of mud and sand. *Journal of the Geological Society.*

BAGCHI, P. & BALACHANDAR, S. 2002. Effect of free rotation on the motion of a solid sphere in linear shear flow at moderate Re. *Physics of Fluids (1994-present),* 14**,** 2719-2737.

BALACHANDAR, S. & EATON, J. K. 2010. Turbulent dispersed multiphase flow. *Annual Review of Fluid Mechanics,* 42**,** 111-133.

BANDYOPADHYAY, P. R. 1987. Rough-wall turbulent boundary layers in the transition regime. *Journal of Fluid Mechanics,* 180**,** 231-266.

BASTIA, R. & RADHAKRISHNA, M. 2012. *Basin Evolution and Petroleum Prospectivity of the Continental Margins of India*, Elsevier Science.

BATT, R. L. 2008. *The influence of bed roughness on the dynamics of gravity currents.* University of Leeds.

BENJAMIN, T. B. 1968. Gravity currents and related phenomena. *Journal of Fluid Mechanics,* 31**,** 209-248.

BENNETT, J. P. 1995. Algorithm for resistance to flow and transport in sand-bed channels. *Journal of hydraulic engineering,* 121**,** 578-590.

BERTOLOTTO, D., MANERA, A., FREY, S., PRASSER, H.-M. & CHAWLA, R. 2009. Single-phase mixing studies by means of a directly coupled CFD/system-code tool. *Annals of Nuclear Energy,* 36**,** 310-316.

BEST, J. 1993. On the interactions between turbulent flow structure, sediment transport and bedform development: some considerations from recent experimental research. *Turbulence: Perspectives on Flow and sediment transport***,** 61-92.

BEST, J. 2005. The fluid dynamics of river dunes: A review and some future research directions. *Journal of Geophysical Research: Earth Surface (2003–2012),* 110.

BEST, J. & KOSTASCHUK, R. 2002. An experimental study of turbulent flow over a low-angle dune. *Journal of Geophysical Research: Oceans (1978–2012),* 107**,** 18-1-18-19.

BEST, J., KOSTASCHUK, R. & HARDY, R. 2004. The fluid dynamics of low-angle river dunes: results from integrated field monitoring, laboratory experimentation and numerical modelling. *Marine Sandwave and River Dune Dynamics II, University of Twente, Enschede, Netherlands***,** 17-23.

BEST, J., KOSTASCHUK, R. & VILLARD, P. 2001. Quantitative visualization of flow fields associated with alluvial sand dunes: results from the laboratory and field using ultrasonic and acoustic Doppler anemometry. *Journal of Visualization,* 4**,** 373-381.

BLAZEK, J. 2005. *Computational Fluid Dynamics: Principles and Applications:(Book with accompanying CD)*, Elsevier.

BONNECAZE, R. T., HALLWORTH, M. A., HUPPERT, H. E. & LISTER, J. R. 1995. Axisymmetric particle-driven gravity currents. *Journal of Fluid Mechanics,* 294**,** 93-121.

BONNECAZE, R. T., HUPPERT, H. E. & LISTER, J. R. 1993. Particle-driven gravity currents. *Journal of Fluid Mechanics,* 250**,** 339-369.

BONNECAZE, R. T., HUPPERT, H. E. & LISTER, J. R. Patterns of sedimentation from polydispersed turbidity currents. Proceedings of the Royal Society of London A: Mathematical, Physical and Engineering Sciences, 1996. The Royal Society, 2247-2261.

BONNECAZE, R. T. & LISTER, J. R. 1999. Particle-driven gravity currents down planar slopes. *Journal of Fluid Mechanics,* 390**,** 75-91.

BOU-ZEID, E., MENEVEAU, C. & PARLANGE, M. 2005. A scale-dependent Lagrangian dynamic model for large eddy simulation of complex turbulent flows. *Physics of Fluids (1994-present),* 17**,** 025105.

BRIDGE, J. S. 1981. Bed shear stress over subaqueous dunes, and the transition to upper-stage plane beds. *Sedimentology,* 28**,** 33-36.

BRITTER, R. & SIMPSON, J. 1978. Experiments on the dynamics of a gravity current head. *Journal of Fluid Mechanics,* 88**,** 223-240.

BROWNLIE, W. R. & BROOKS, N. H. 1982. *Prediction of flow depth and sediment discharge in open channels.* California Institute of Technology Pasadena, CA.

BUCKEE, C., KNELLER, B. & PEAKALL, J. 2009. Turbulence structure in steady, solute-driven gravity currents. *Particulate gravity currents*, 173-187.

BURATTINI, P., LEONARDI, S., ORLANDI, P. & ANTONIA, R. 2008. Comparison between experiments and direct numerical simulations in a channel flow with roughness on one wall. *Journal of Fluid Mechanics,* 600**,** 403-426.

BUSSE, A. & SANDHAM, N. D. 2012. Parametric forcing approach to rough-wall turbulent channel flow. *Journal of Fluid Mechanics,* 712**,** 169-202.

CACCHIONE, D. A., THORNE, P. D., AGRAWAL, Y. & NIDZIEKO, N. J. 2008. Time-averaged near-bed suspended sediment concentrations under waves and currents: Comparison of measured and model estimates. *Continental Shelf Research,* 28**,** 470-484.

CANTERO, M., GARCÍA, M., BUSCAGLIA, G., BOMBARDELLI, F. & DARI, E. Multidimensional CFD simulation of a discontinuous density current. Proceedings of the XXX IAHR International Congress, 2003. 24-29.

CANTERO, M. I., BALACHANDAR, S., CANTELLI, A., PIRMEZ, C. & PARKER, G. 2009. Turbidity current with a roof: Direct numerical simulation of self-stratified turbulent channel flow driven by suspended sediment. *Journal of Geophysical Research: Oceans (1978–2012),* 114.

CANTERO, M. I., CANTELLI, A., PIRMEZ, C., BALACHANDAR, S., MOHRIG, D., HICKSON, T. A., YEH, T.-H., NARUSE, H. & PARKER, G. 2012a. Emplacement of massive turbidites linked to extinction of turbulence in turbidity currents. *Nature Geoscience,* 5**,** 42-45.

CANTERO, M. I., LEE, J., BALACHANDAR, S. & GARCIA, M. H. 2007. On the front velocity of gravity currents. *Journal of Fluid Mechanics,* 586**,** 1-39.

CANTERO, M. I., SHRINGARPURE, M. & BALACHANDAR, S. 2012b. Towards a universal criteria for turbulence suppression in dilute turbidity currents with non-cohesive sediments. *Geophysical Research Letters,* 39.

CAO, Z. 1997. Turbulent bursting-based sediment entrainment function. *Journal of Hydraulic Engineering,* 123**,** 233-236.

CAO, Z., EGASHIRA, S. & CARLING, P. A. 2003. Role of suspended-sediment particle size in modifying velocity profiles in open channel flows. *Water resources research,* 39.

CAO, Z., PENDER, G. & CARLING, P. 2006. Shallow water hydrodynamic models for hyperconcentrated sediment-laden floods over erodible bed. *Advances in Water Resources,* 29**,** 546-557.

CARLING, P., GOLZ, E., ORR, H. & RADECKI-PAWLIK, A. 2000. The morphodynamics of fluvial sand dunes in the River Rhine, near Mainz, Germany. I. Sedimentology and morphology. *Sedimentology,* 47**,** 227-252.

CARRIER, G. 1958. Shock waves in a dusty gas. *Journal of Fluid Mechanics,* 4**,** 376-382.

CASTRO, I. P. 2007. Rough-wall boundary layers: mean flow universality. *Journal of Fluid Mechanics,* 585**,** 469-485.

CASTRO, I. P. 2009. Turbulent flow over rough walls. *Advances in Turbulence XII.* Springer.

CASTRO, I. P., SEGALINI, A. & ALFREDSSON, P. H. 2013. Outer-layer turbulence intensities in smooth-and rough-wall boundary layers. *Journal of Fluid Mechanics,* 727**,** 119-131.

CELIK, I. & RODI, W. 1985. Mathematical modelling of suspended sediment transport in open channels.

CELIK, I. & RODI, W. 1988. Modeling suspended sediment transport in nonequilibrium situations. *Journal of hydraulic engineering,* 114**,** 1157-1191.

CELIK, I. & RODI, W. 1991. Suspended sediment-transport capacity for open channel flow. *Journal of hydraulic engineering,* 117**,** 191-204.

CELLINO, M. & GRAF, W. 1999. Sediment-laden flow in open-channels under noncapacity and capacity conditions. *Journal of Hydraulic Engineering,* 125**,** 455-462.

CHOW, V. 1959. Open channel hydraulics.

CHU, D. C. & KARNIADAKIS, G. E. 1993. A direct numerical simulation of laminar and turbulent flow over riblet-mounted surfaces. *Journal of Fluid Mechanics,* 250**,** 1-42.

COLEMAN, N. L. 1981. Velocity profiles with suspended sediment. *Journal of Hydraulic Research,* 19**,** 211-229.

COLEMAN, S. E., FEDELE, J. J. & GARC ı´ A, M. H. 2003. Closed-conduit bed-form initiation and development. *Journal of hydraulic engineering,* 129**,** 956-965.

CORNEY, R. K., PEAKALL, J., PARSONS, D. R., ELLIOTT, L., AMOS, K. J., BEST, J. L., KEEVIL, G. M. & INGHAM, D. B. 2006. The orientation of helical flow in curved channels. *Sedimentology,* 53**,** 249-257.

CUI, J., PATEL, V. C. & LIN, C.-L. 2003. Large-eddy simulation of turbulent flow in a channel with rib roughness. *International Journal of Heat and Fluid Flow,* 24**,** 372-388.

CUI, J. P., VIRENDRA C LIN, CHING-LONG 2003. Large-eddy simulation of turbulent flow in a channel with rib roughness. *International Journal of Heat and Fluid Flow,* 24**,** 372-388.

D'ALESSIO, S., MOODIE, T., PASCAL, J. & SWATERS, G. 1997. Intrusive gravity currents. *Studies in Applied Mathematics,* 98**,** 19-46.

DADE, W. B. & HUPPERT, H. E. 1995a. A box model for non-entraining, suspension-driven gravity surges on horizontal surfaces. *Sedimentology,* 42**,** 453-470.

DADE, W. B. & HUPPERT, H. E. 1995b. Runout and fine-sediment deposits of axisymmetric turbidity currents. *Journal of Geophysical Research: Oceans (1978–2012),* 100**,** 18597-18609.

DALY, B. J. & PRACHT, W. E. 1968. Numerical Study of Density-Current Surges. *Physics of Fluids (1958-1988),* 11**,** 15-30.

DAVIES, T. R. 1982. Lower flow regime bedforms: rational classification. *Journal of the Hydraulics Division,* 108**,** 343-360.

DEARDORFF, J. W. 1970. A numerical study of three-dimensional turbulent channel flow at large Reynolds numbers. *Journal of Fluid Mechanics,* 41**,** 453-480.

DIDDEN, N. & MAXWORTHY, T. 1982. The viscous spreading of plane and axisymmetric gravity currents. *Journal of Fluid Mechanics,* 121**,** 27-42.

DJENIDI, L., ELAVARASAN, R. & ANTONIA, R. 1999. The turbulent boundary layer over transverse square cavities. *Journal of Fluid Mechanics,* 395**,** 271-294.

DJENIDI, L. E., R ANTONIA, RA 1999. The turbulent boundary layer over transverse square cavities. *Journal of Fluid Mechanics,* 395**,** 271-294.

DORRELL, R., DARBY, S., PEAKALL, J., SUMNER, E., PARSONS, D. & WYNN, R. 2013a. Superelevation and overspill control secondary flow dynamics in submarine channels. *Journal of Geophysical Research: Oceans,* 118**,** 3895-3915.

DORRELL, R., HOGG, A. & PRITCHARD, D. 2013b. Polydisperse suspensions: Erosion, deposition, and flow capacity. *Journal of Geophysical Research: Earth Surface,* 118**,** 1939-1955.

EGGENHUISEN, J. T. & MCCAFFREY, W. D. 2012. The vertical turbulence structure of experimental turbidity currents encountering basal obstructions: implications for vertical suspended sediment distribution in non-equilibrium currents. *Sedimentology,* 59**,** 1101-1120.

EGGENHUISEN, J. T., MCCAFFREY, W. D., HAUGHTON, P. D. & BUTLER, R. W. 2010. Small-scale spatial variability in turbidity-current flow controlled by roughness resulting from substrate erosion: field evidence for a feedback mechanism. *Journal of Sedimentary Research,* 80**,** 129-136.

EGGENHUISEN, J. T., MCCAFFREY, W. D., HAUGHTON, P. D. & BUTLER, R. W. 2011. Shallow erosion beneath turbidity currents and its impact on the

architectural development of turbidite sheet systems. *Sedimentology,* 58**,** 936-959.

EINSTEIN, H. & CHIEN, N. 1953. Transport of Sediment Mixtures with Large Ranges of Grain Sizes, MRD Sediment Series No. 2. *United States Army Engineer Division, Missouri River*.

EINSTEIN, H. A. 1950. *The bed-load function for sediment transportation in open channel flows*, US Department of Agriculture.

EL-BATSH, H. M., DOHEIM, M. A. & HASSAN, A. F. 2012. On the application of mixture model for two-phase flow induced corrosion in a complex pipeline configuration. *Applied Mathematical Modelling,* 36**,** 5686-5699.

ENGELUND, F. & HANSEN, E. 1967. A monograph on sediment transport in alluvial streams. TEKNISKFORLAG Skelbrekgade 4 Copenhagen V, Denmark.

ESCH, T. & MENTER, F. 2003. Heat transfer predictions based on two-equation turbulence models with advanced wall treatment. *Turbulence, heat and mass transfer,* 4**,** 633-640.

FARACI, C. & FOTI, E. 2002. Geometry, migration and evolution of small-scale bedforms generated by regular and irregular waves. *Coastal Engineering,* 47**,** 35-52.

FARIA, R., FERREIRA, A. D., SISMEIRO, J. L., MENDES, J. C. & SOUSA, A. C. 2011. Wind tunnel and computational study of the stoss slope effect on the aeolian erosion of transverse sand dunes. *Aeolian Research,* 3**,** 303-314.

FERNANDEZ, R., BEST, J. & LÓPEZ, F. 2006. Mean flow, turbulence structure, and bed form superimposition across the ripple-dune transition. *Water resources research,* 42.

FERRARO, D. & DEY, S. 2015. Principles of Mechanics of Bedforms. *Rivers– Physical, Fluvial and Environmental Processes.* Springer.

FERRY, J. & BALACHANDAR, S. 2001. A fast Eulerian method for disperse two-phase flow. *International Journal of Multiphase Flow,* 27**,** 1199-1226.

FERRY, J. & BALACHANDAR, S. 2002. Equilibrium expansion for the Eulerian velocity of small particles. *Powder Technology,* 125**,** 131-139.

FLUENT, A. 2009. Theory guide. *US: ANSYS Inc*.

FOURRIERE, A., CLAUDIN, P. & ANDREOTTI, B. 2010. Bedforms in a turbulent stream: formation of ripples by primary linear instability and of dunes by nonlinear pattern coarsening. *Journal of Fluid Mechanics,* 649**,** 287-328.

FRANK, E. & JØRGEN, F. 1976. A sediment transport model for straight alluvial channels. *Nordic Hydrology,* 7**,** 293-306.

FURUYA, Y., MIYATA, M. & FUJITA, H. 1976. Turbulent boundary layer and flow resistance on plates roughened by wires. *Journal of Fluids Engineering,* 98**,** 635-643.

GARCIA, M. & PARKER, G. 1991. Entrainment of bed sediment into suspension. *Journal of Hydraulic Engineering,* 117**,** 414-435.

GARCIA, M. & PARKER, G. 1993. Experiments on the entrainment of sediment into suspension by a dense bottom current. *Journal of Geophysical Research: Oceans (1978–2012),* 98**,** 4793-4807.

GARDINER, B. Airflow Over Forests and Forest Gaps. BWEA Tree Workshop Forestry Commission, 2004.

GIORGIO SERCHI, F. 2010. *CFD modelling of density currents and sinuous channels.* University of Leeds.

GIORGIO SERCHI, F., PEAKALL, J., INGHAM, D. & BURNS, A. 2011. A unifying computational fluid dynamics investigation on the river-like to river-reversed secondary circulation in submarine channel bends. *Journal of Geophysical Research: Oceans (1978–2012),* 116.

GLADSTONE, C. & WOODS, A. W. 2000. On the application of box models to particle-driven gravity currents. *Journal of Fluid Mechanics,* 416**,** 187-195.

GONZALEZ-JUEZ, E. & MEIBURG, E. 2009. Shallow-water analysis of gravity-current flows past isolated obstacles. *Journal of Fluid Mechanics,* 635**,** 415-438.

GONZALEZ-JUEZ, E., MEIBURG, E. & CONSTANTINESCU, G. 2009. Gravity currents impinging on bottom-mounted square cylinders: flow fields and associated forces. *Journal of Fluid Mechanics,* 631**,** 65-102.

GONZALEZ-JUEZ, E., MEIBURG, E., TOKYAY, T. & CONSTANTINESCU, G. 2010. Gravity current flow past a circular cylinder: forces, wall shear stresses and implications for scour. *Journal of Fluid Mechanics,* 649**,** 69-102.

GOVERS, G. & RAUWS, G. 1986. Transporting capacity of overland flow on plane and on irregular beds. *Earth surface processes and landforms,* 11**,** 515-524.

GRANT, W. D. & MADSEN, O. S. 1982. Movable bed roughness in unsteady oscillatory flow. *Journal of Geophysical Research: Oceans (1978–2012),* 87**,** 469-481.

GROENENBERG, R. M. 2007. *Process-based modelling of turbidity-current hydrodynamics and sedimentation*, TU Delft, Delft University of Technology.

GRUNDY, R. & ROTTMAN, J. W. 1985. The approach to self-similarity of the solutions of the shallow-water equations representing gravity-current releases. *Journal of fluid mechanics,* 156**,** 39-53.

GUST, G. 1976. Observations on turbulent-drag reduction in a dilute suspension of clay in sea-water. *Journal of Fluid Mechanics,* 75**,** 29-47.

GUST, G. 1988. Skin friction probes for field applications. *Journal of Geophysical Research: Oceans (1978–2012),* 93**,** 14121-14132.

GUST, G. & WALGER, E. 1976. The influence of suspended cohesive sediments on boundary-layer structure and erosive activity of turbulent seawater flow. *Marine Geology,* 22**,** 189-206.

HACKER, J., LINDEN, P. & DALZIEL, S. 1996. Mixing in lock-release gravity currents. *Dynamics of Atmospheres and Oceans,* 24**,** 183-195.

HALLWORTH, M. A., HUPPERT, H. E., PHILLIPS, J. C. & SPARKS, R. S. J. 1996. Entrainment into two-dimensional and axisymmetric turbulent gravity currents. *Journal of Fluid Mechanics,* 308**,** 289-311.

HAND, B. M. 1974. Supercritical flow in density currents. *Journal of Sedimentary Research,* 44.

HANJALIC, K. & LAUNDER, B. 1972. Fully developed asymmetric flow in a plane channel. *Journal of Fluid Mechanics,* 51**,** 301-335.

HANZEVACK, E. & DEMETRIOU, G. 1989. Effect of velocity and pipeline configuration on dispersion in turbulent hydrocarbon-water flow using laser image processing. *International Journal of Multiphase Flow,* 15**,** 985-996.

HARLOW, F. H. & WELCH, J. E. 1965. Numerical calculation of time-dependent viscous incompressible flow of fluid with free surface. *Physics of fluids,* 8**,** 2182.

HÄRTEL, C., MEIBURG, E. & NECKER, F. 2000. Analysis and direct numerical simulation of the flow at a gravity-current head. Part 1. Flow topology and front speed for slip and no-slip boundaries. *Journal of Fluid Mechanics,* 418**,** 189-212.

HEATHERSHAW, A. & THORNE, P. 1985. Sea-bed noises reveal role of turbulent bursting phenomenon in sediment transport by tidal currents.

HEEZEN, B. C. & HOLLISTER, C. 1964. Deep-sea current evidence from abyssal sediments. *Marine Geology,* 1**,** 141-174.

HESP, P. A., SMYTH, T. A., NIELSEN, P., WALKER, I. J., BAUER, B. O. & DAVIDSON-ARNOTT, R. 2015. Flow deflection over a foredune. *Geomorphology,* 230**,** 64-74.

HISCOTT, R. N. 1994. Loss of capacity, not competence, as the fundamental process governing deposition from turbidity currents. *Journal of Sedimentary Research,* 64.

HOGG, A. J., UNGARISH, M. & HUPPERT, H. E. 2000. Particle-driven gravity currents: asymptotic and box model solutions. *European Journal of Mechanics-B/Fluids,* 19**,** 139-165.

HOULT, D. P. 1972. Oil spreading on the sea. *Annual Review of Fluid Mechanics,* 4**,** 341-368.

HOYES, J. R. 2008. *Homogeneous and particle-driven gravity currents.* University of Leeds.

HUANG, H., IMRAN, J. & PIRMEZ, C. 2005. Numerical model of turbidity currents with a deforming bottom boundary. *Journal of hydraulic engineering,* 131**,** 283-293.

HUANG, H., IMRAN, J. & PIRMEZ, C. 2007. Numerical modeling of poorly sorted depositional turbidity currents. *Journal of Geophysical Research: Oceans (1978–2012),* 112.

HUANG, H., IMRAN, J. & PIRMEZ, C. 2008. Numerical study of turbidity currents with sudden-release and sustained-inflow mechanisms. *Journal of Hydraulic Engineering,* 134**,** 1199-1209.

HUDDART, D. & STOTT, T. 2013. *Earth Environments: Past, Present and Future*, Wiley.

HUPPERT, H. E. 1982. The propagation of two-dimensional and axisymmetric viscous gravity currents over a rigid horizontal surface. *Journal of Fluid Mechanics,* 121**,** 43-58.

HUPPERT, H. E. & SIMPSON, J. E. 1980. The slumping of gravity currents. *Journal of Fluid Mechanics,* 99**,** 785-799.

ICHIMIYA, K. 1987. Effects of several roughness elements on an insulated wall for heat transfer from the opposite smooth heated surface in a parallel plate duct. *Journal of heat transfer,* 109**,** 68-73.

IKEDA, T. & DURBIN, P. 2002. Direct simulations of a rough-wall channel flow. Report No. TF 81. Dep. of Mech. Engineering. Stanford University, Stanford, California.

IMRAN, J., KASSEM, A. & KHAN, S. 2004. Three-dimensional modeling of density current. I. Flow in straight confined and unconfined channels. *Journal of Hydraulic Research,* 42**,** 578-590.

ISHII, M. 1977. One-dimensional drift-flux model and constitutive equations for relative motion between phases in various two-phase flow regimes. Argonne National Lab., Ill.(USA).

ISSLER, D., DE BLASIO, F., ELVERHØI, A., ILSTAD, T., HAFLIDASON, H., BRYN, P. & LIEN, R. 2003. Issues in the assessment of gravity mass flow hazard in the Storegga area off the western Norwegian coast. *Submarine Mass Movements and Their Consequences.* Springer.

JACKSON, P. 1981. On the displacement height in the logarithmic velocity profile. *Journal of Fluid Mechanics,* 111**,** 15-25.

JAIN, S. C. & KENNEDY, J. F. 1974. The spectral evolution of sedimentary bed forms. *Journal of Fluid Mechanics,* 63**,** 301-314.

JAMES, C. & COTTINO, C. 1995. An experimental study of flow over artificial bed forms. *WATER SA-PRETORIA-,* 21**,** 299-306.

JIMENEZ, J. 2004. Turbulent flows over rough walls. *Annual Review of Fluid Mechanics,* 36**,** 173-196.

JIMÉNEZ, J. 2000. Intermittency and cascades. *Journal of Fluid Mechanics,* 409**,** 99-120.

JIMÉNEZ, J. 2004. TURBULENT FLOWS OVER ROUGH WALLS. *Annual Review of Fluid Mechanics,* 36**,** 173-196.

JOHN, V. 2012. *Large eddy simulation of turbulent incompressible flows: analytical and numerical results for a class of LES models*, Springer Science & Business Media.

JOHNSON, D. A. & KING, L. 1985. A mathematically simple turbulence closure model for attached and separated turbulent boundary layers. *AIAA journal,* 23**,** 1684-1692.

JUNGE, J. & WESTERHELLWEG, A. 2011. Estimation of Zero Plane Displacement Heights in The Vicinity of a Forest.

KARCZ, I. & KERSEY, D. 1980. Experimental study of free-surface flow instability and bedforms in shallow flows. *Sedimentary Geology,* 27**,** 263-300.

KASSEM, A. & IMRAN, J. 2004. Three-dimensional modeling of density current. II. Flow in sinuous confined and uncontined channels. *Journal of Hydraulic Research,* 42**,** 591-602.

KAYS, W. & CRAWFORD, M. 1993. Convection heat transfer. McGraw-Hill, New York.

KEEVIL, G. M., PEAKALL, J., BEST, J. L. & AMOS, K. J. 2006. Flow structure in sinuous submarine channels: velocity and turbulence structure of an experimental submarine channel. *Marine Geology,* 229**,** 241-257.

KEIRSBULCK, L., LABRAGA, L., MAZOUZ, A. & TOURNIER, C. 2002. Surface roughness effects on turbulent boundary layer structures. *Journal of fluids engineering,* 124**,** 127-135.

KENDALL, J. M. 1990. The effect of small-scale roughness on the mean flow profile of a laminar boundary layer. *Instability and transition.* Springer.

KEULEGAN, G. 1957. An experimental study of the motion of saline water from locks into fresh water channels. *Nat. Bur. Stand. Rept,* 5168.

KHOSRONEJAD, A. & SOTIROPOULOS, F. 2014. Numerical simulation of sand waves in a turbulent open channel flow. *Journal of Fluid Mechanics,* 753**,** 150-216.

KIM, J., MOIN, P. & MOSER, R. 1987. Turbulence statistics in fully developed channel flow at low Reynolds number. *Journal of fluid mechanics,* 177**,** 133-166.

KLEMP, J. B., ROTUNNO, R. & SKAMAROCK, W. C. 1994. On the dynamics of gravity currents in a channel. *Journal of Fluid Mechanics,* 269**,** 169-198.

KLINE, S. J., COLES, D. E., HIRST, E. A., RESEARCH, U. S. A. F. O. O. S. & DIVISION, S. U. T. 1969. *Computation of Turbulent Boundary Layers--1968 AFOSR-IFP-Stanford Conference: Compiled data. Editors: D. E. Coles and E. A. Hirst. Bibliography (p. 18-19)*, Thermosciences Division, Stanford University.

KLINGEMAN, P. C. 1998. *Gravel-bed Rivers in the Environment*, Water Resources Publications.

KNELLER, B. 2003. The influence of flow parameters on turbidite slope channel architecture. *Marine and Petroleum Geology,* 20**,** 901-910.

KNELLER, B. & BUCKEE, C. 2000. The structure and fluid mechanics of turbidity currents: a review of some recent studies and their geological implications. *Sedimentology,* 47**,** 62-94.

KNELLER, B. C., BENNETT, S. J. & MCCAFFREY, W. D. 1999. Velocity structure, turbulence and fluid stresses in experimental gravity currents. *Journal of Geophysical Research: Oceans (1978–2012),* 104**,** 5381-5391.

KNOPP, T., EISFELD, B. & CALVO, J. B. 2009. A new extension for k–ω turbulence models to account for wall roughness. *International Journal of Heat and Fluid Flow,* 30**,** 54-65.

KOLMOGOROV, A. 1942. Equations of motion of an incompressible turbulent fluid. *Izv Akad Nauk SSSR Ser Phys,* 6**,** 56-58.

KOSTASCHUK, R. 2000. A field study of turbulence and sediment dynamics over subaqueous dunes with flow separation. *Sedimentology,* 47**,** 519-531.

KOSTASCHUK, R., BEST, J., VILLARD, P., PEAKALL, J. & FRANKLIN, M. 2005. Measuring flow velocity and sediment transport with an acoustic Doppler current profiler. *Geomorphology,* 68**,** 25-37.

KOSTASCHUK, R. & CHURCH, M. 1993. Macroturbulence generated by dunes: Fraser River, Canada. *Sedimentary Geology,* 85**,** 25-37.

KOSTASCHUK, R., CHURCH, M. & LUTERNAUER, J. 1989. Bedforms, bed material, and bedload transport in a salt-wedge estuary: Fraser River, British Columbia. *Canadian Journal of Earth Sciences,* 26**,** 1440-1452.

KOSTASCHUK, R. & ILERSICH, S. 1995. dune geometry and sediment transport: Fraser River, British Columbia. *River geomorphology***,** 19-36.

KOSTASCHUK, R., SHUGAR, D., BEST, J., PARSONS, D., LANE, S., HARDY, R. & ORFEO, O. 2009. Suspended sediment transport and deposition over a dune: Río Paraná, Argentina. *Earth Surface Processes and Landforms,* 34**,** 1605.

KOSTASCHUK, R. & VILLARD, P. 1996. Flow and sediment transport over large subaqueous dunes: Fraser River, Canada. *Sedimentology,* 43**,** 849-863.

KOSTASCHUK, R. & VILLARD, P. Turbulent sand suspension over dunes. Proceedings of the 6th International Conference on Fluvial Sedimentology, edited by ND Smith, and J. Rogers, 1999. 3-14.

KOSTASCHUK, R., VILLARD, P. & BEST, J. 2004. Measuring velocity and shear stress over dunes with acoustic Doppler profiler. *Journal of hydraulic engineering,* 130**,** 932-936.

KROGSTAD, P.-A. 1991. Modification of the van Driest damping function to include the effects of surface roughness. *AIAA journal,* 29**,** 888-894.

KROGSTAD, P.-Å., ANDERSSON, H. I., BAKKEN, O. M. & ASHRAFIAN, A. 2005. An experimental and numerical study of channel flow with rough walls. *Journal of Fluid Mechanics,* 530**,** 327-352.

KROGSTAD, P.-Å., ANTONIA, R. & BROWNE, L. 1992. Comparison between rough- and smooth-wall turbulent boundary layers. *Journal of Fluid Mechanics,* 245**,** 599-617.

KUBO, Y. S. 2004. Experimental and numerical study of topographic effects on deposition from two-dimensional, particle-driven density currents. *Sedimentary Geology,* 164**,** 311-326.

LACY, J. R., RUBIN, D. M., IKEDA, H., MOKUDAI, K. & HANES, D. M. 2007. Bed forms created by simulated waves and currents in a large flume. *Journal of Geophysical Research: Oceans (1978–2012),* 112.

LASTRAS, G., ARZOLA, R., MASSON, D., WYNN, R., HUVENNE, V., HÜHNERBACH, V. & CANALS, M. 2009. Geomorphology and sedimentary features in the Central Portuguese submarine canyons, Western Iberian margin. *Geomorphology,* 103**,** 310-329.

LAUNDER, B., REECE, G. J. & RODI, W. 1975. Progress in the development of a Reynolds-stress turbulence closure. *Journal of fluid mechanics,* 68**,** 537-566.

LAUNDER, B. E. & SPALDING, D. B. 1972. Lectures in mathematical models of turbulence.

LAWSON, S. A., THRIFT, A. A., THOLE, K. A. & KOHLI, A. 2011. Heat transfer from multiple row arrays of low aspect ratio pin fins. *International Journal of Heat and Mass Transfer,* 54**,** 4099-4109.

LE BOUTEILLER, C. & VENDITTI, J. 2015. Sediment transport and shear stress partitioning in a vegetated flow. *Water resources research,* 51**,** 2901-2922.

LECLAIR, S., CARLING, P. & BREAKSPEAR, R. Preserved stratification from deposition/erosion sequences of progressive and breaking antidunes. EGU General Assembly Conference Abstracts, 2015. 14390.

LEE, J. H., SUNG, H. J. & KROGSTAD, P.-Å. 2011. Direct numerical simulation of the turbulent boundary layer over a cube-roughened wall. *Journal of Fluid Mechanics,* 669**,** 397-431.

LEEDER, M. 2009a. On the interactions between turbulent flow, sediment transport and bedform mechanics in channelized flows. *Modern and Ancient Fluvial Systems***,** 3-18.

LEEDER, M. R. 2009b. *Sedimentology and sedimentary basins: from turbulence to tectonics*, John Wiley & Sons.

LEEDER, M. R. 2011. *Sedimentology and Sedimentary Basins: From Turbulence to Tectonics*, Wiley.

LEEDER, M. R. 2012. *Sedimentology: Process and Product*, Springer Netherlands.

LEONARDI, S. & CASTRO, I. P. 2010. Channel flow over large cube roughness: a direct numerical simulation study. *Journal of Fluid Mechanics,* 651**,** 519-539.

LEONARDI, S., ORLANDI, P. & ANTONIA, R. 2007. Properties of d-and k-Type Roughness in a Turbulent Channel Flow. *Physics of Fluids (1994-present),* 19**,** 125101.

LEONARDI, S., ORLANDI, P., SMALLEY, R., DJENIDI, L. & ANTONIA, R. 2003. Direct numerical simulations of turbulent channel flow with transverse square bars on one wall. *Journal of Fluid Mechanics,* 491**,** 229-238.

LEONARDI, S., TESSICINI, F., ORLANDI, P. & ANTONIA, R. A. 2006. Direct numerical and large-eddy simulations of turbulent flows over rough surfaces. *AIAA journal,* 44**,** 2482-2487.

LEONARDI, S. C., IAN P 2010. Channel flow over large cube roughness: a direct numerical simulation study. *Journal of Fluid Mechanics,* 651**,** 519-539.

LEONARDI, S. O., P ANTONIA, RA 2007. Properties of d-and k-Type Roughness in a Turbulent Channel Flow. *Physics of Fluids (1994-present),* 19**,** 125101.

LEONARDI, S. O., P DJENIDI, L ANTONIA, RA 2004. Structure of turbulent channel flow with square bars on one wall. *International Journal of Heat and Fluid Flow,* 25**,** 384-392.

LI, L., SMYTH, W. & THORPE, S. 2015. Destabilization of a stratified shear layer by ambient turbulence. *Journal of Fluid Mechanics,* 771**,** 1-15.

LIEN, K., MONTY, J., CHONG, M. & OOI, A. The entrance length for fully developed turbulent channel flow. 15th Australian Fluid Mechanics Conference, 2004. 356-363.

LIN, C. & EBADIAN, M. 2008. A numerical study of developing slurry flow in the entrance region of a horizontal pipe. *Computers & Fluids,* 37**,** 965-974.

LIOU, T.-M., HWANG, J.-J. & CHEN, S.-H. 1993. Simulation and measurement of enhanced turbulent heat transfer in a channel with periodic ribs on one principal wall. *International Journal of Heat and Mass Transfer,* 36**,** 507-517.

LIU, S. & SAKR, M. 2013. A comprehensive review on passive heat transfer enhancements in pipe exchangers. *Renewable and Sustainable Energy Reviews,* 19**,** 64-81.

LIVESEY, J., ASHWORTH, P., BENNETT, S. & BEST, J. 1998. Flow structure, sediment transport and bedform dynamics for a bimodal sediment mixture.

LOBO, F., HERNANDEZ-MOLINA, F., SOMOZA, L., RODERO, J., MALDONADO, A. & BARNOLAS, A. 2000. Patterns of bottom current flow deduced from dune asymmetries over the Gulf of Cadiz shelf (southwest Spain). *Marine Geology,* 164**,** 91-117.

LOWE, D. R. 1982. Sediment gravity flows: II Depositional models with special reference to the deposits of high-density turbidity currents. *Journal of Sedimentary Research,* 52.

LYN, D. 1993. Turbulence measurements in open-channel flows over artificial bed forms. *Journal of hydraulic engineering,* 119**,** 306-326.

MACDONALD, H. A., WYNN, R. B., HUVENNE, V. A., PEAKALL, J., MASSON, D. G., WEAVER, P. P. & MCPHAIL, S. D. 2011. New insights into the morphology, fill, and remarkable longevity (> 0.2 my) of modern deep-water erosional scours along the northeast Atlantic margin. *Geosphere,* 7**,** 845-867.

MADDUX, T., MCLEAN, S. & NELSON, J. 2003a. Turbulent flow over three-dimensional dunes: 2. Fluid and bed stresses. *Journal of Geophysical Research: Earth Surface (2003–2012),* 108.

MADDUX, T., NELSON, J. & MCLEAN, S. 2003b. Turbulent flow over three-dimensional dunes: 1. Free surface and flow response. *Journal of Geophysical Research: Earth Surface (2003–2012),* 108.

MANNINEN, M., TAIVASSALO, V. & KALLIO, S. 1996. On the mixture model for multiphase flow. Technical Research Centre of Finland Finland.

MANVILLE, V. & WHITE, J. 2003. Incipient granular mass flows at the base of sediment-laden floods, and the roles of flow competence and flow capacity in the deposition of stratified bouldery sands. *Sedimentary Geology,* 155**,** 157-173.

MARBLE, F. E. 1970. Dynamics of dusty gases. *Annual Review of Fluid Mechanics,* 2**,** 397-446.

MARINO, B., THOMAS, L. & LINDEN, P. 2005. The front condition for gravity currents. *Journal of Fluid Mechanics,* 536**,** 49-78.

MCCAFFREY, W. D., KNELLER, B. C. & PEAKALL, J. 2001. *Particulate Gravity Currents: (Special Publication 31 of the IAS)*, John Wiley & Sons.

MCCAVE, I. 1984. Erosion, transport and deposition of fine-grained marine sediments. *Geological Society, London, Special Publications,* 15**,** 35-69.

MCCAVE, I. 2012. *The Benthic Boundary Layer*, Springer US.

MCLEAN, S., NELSON, J. & WOLFE, S. 1994. Turbulence structure over two-dimensional bed forms: Implications for sediment transport. *Journal of Geophysical Research: Oceans (1978–2012),* 99**,** 12729-12747.

MCLEAN, S. & NIKORA, V. 2006. Characteristics of turbulent unidirectional flow over rough beds: Double-averaging perspective with particular focus on sand dunes and gravel beds. *Water resources research,* 42.

MCLEAN, S. & SMITH, J. D. 1986. A model for flow over two-dimensional bed forms. *Journal of Hydraulic Engineering,* 112**,** 300-317.

MEIBURG, E. & KNELLER, B. 2010. Turbidity currents and their deposits. *Annual Review of Fluid Mechanics,* 42**,** 135-156.

MEIBURG, E., RADHAKRISHNAN, S. & NASR-AZADANI, M. 2015. Modeling Gravity and Turbidity Currents: Computational Approaches and Challenges. *Applied Mechanics Reviews,* 67**,** 040802.

MENTER, F., KUNTZ, M. & LANGTRY, R. 2003. Ten years of industrial experience with the SST turbulence model. *Turbulence, heat and mass transfer,* 4.

MENTER, F. R. 1992. Improved two-equation k-omega turbulence models for aerodynamic flows. *NASA STI/Recon Technical Report N,* 93**,** 22809.

MENTER, F. R. 1994. Two-equation eddy-viscosity turbulence models for engineering applications. *AIAA journal,* 32**,** 1598-1605.

MICHAELIDES, E. E. 1986. Heat transfer in particulate flows. *International Journal of Heat and Mass Transfer,* 29**,** 265-273.

MIDDLETON, G. V. 1993. Sediment deposition from turbidity currents. *Annual Review of Earth and Planetary Sciences,* 21**,** 89-114.

MIDDLETON, G. V. & SOUTHARD, J. B. 1984. Mechanics of sediment movement. SEPM.

MILLWARD-HOPKINS, J., TOMLIN, A., MA, L., INGHAM, D. & POURKASHANIAN, M. 2011. Estimating aerodynamic parameters of urban-like surfaces with heterogeneous building heights. *Boundary-Layer Meteorology,* 141**,** 443-465.

MILNES, J., BURNS, A. & DRIKAKIS, D. 2012. Computational modelling of the HyperVapotron cooling technique. *Fusion Engineering and Design,* 87**,** 1647-1661.

MOIN, P. & MAHESH, K. 1998. Direct numerical simulation: a tool in turbulence research. *Annual review of fluid mechanics,* 30**,** 539-578.

MOSER JR, R. 1984. Direct numerical simulation of curved turbulent channel flow.

MUSTE, M. & PATEL, V. 1997. Velocity profiles for particles and liquid in open-channel flow with suspended sediment. *Journal of hydraulic engineering,* 123**,** 742-751.

MUTTI, E. 1977. Distinctive thin-bedded turbidite facies and related depositional environments in the Eocene Hecho Group (south-central Pyrenees, Spain). *Sedimentology,* 24**,** 107-131.

MUTTI, E. & RICCI LUCCHI, F. 1978. Turbidites of the northern Apennines: introduction to facies analysis. *International geology review,* 20**,** 125-166.

NASR-AZADANI, M. & MEIBURG, E. 2014a. Turbidity currents interacting with three-dimensional seafloor topography. *Journal of Fluid Mechanics,* 745**,** 409-443.

NASR-AZADANI, M. M. & MEIBURG, E. 2014b. Influence of seafloor topography on the depositional behavior of bi-disperse turbidity currents: a three-dimensional, depth-resolved numerical investigation. *Environmental Fluid Mechanics,* 14**,** 319-342.

NECKER, F., HÄRTEL, C., KLEISER, L. & MEIBURG, E. 2005. Mixing and dissipation in particle-driven gravity currents. *Journal of Fluid Mechanics,* 545**,** 339-372.

NELSON, J. M., MCLEAN, S. R. & WOLFE, S. R. 1993. Mean flow and turbulence fields over two-dimensional bed forms. *Water Resour. Res,* 29**,** 3935-3953.

NEUFELD, J. 2002. *Lobe-cleft patterns in the leading edge of a gravity current.* Master Thesis, University of Toronto.

NEWITT, D., RICHARDSON, J., ABBOTT, M. & TURTLE, R. 1955. Hydraulic conveying of solids in horizontal pipes. *Trans. Inst. Chem. Eng,* 33**,** 93-113.

NICHOLSON, M. & FLYNN, M. R. 2015. Gravity current flow over sinusoidal topography in a two-layer ambient. *Physics of Fluids (1994-present),* 27**,** 096603.

NIELSEN, P. & TEAKLE, I. A. 2004. Turbulent diffusion of momentum and suspended particles: A finite-mixing-length theory. *Physics of fluids,* 16**,** 2342-2348.

NIKURADSE, J. 1933a. Str {ö} mungsgestze in rauhen Rohren.

NIKURADSE, J. 1933b. Stromungsgesetze in rauhen rohren. Forsch, Arb. Ing.-Wes., 361. *English translation as NACA-TM-1292*.

NIÑO, Y. & GARCÍA, M. 1998. Using Lagrangian particle saltation observations for bedload sediment transport modelling. *Hydrological Processes,* 12**,** 1197-1218.

NORMARK, W. R. 1970. Growth patterns of deep-sea fans. *AAPG bulletin,* 54**,** 2170-2195.

OKAMOTO, S., SEO, S., NAKASO, K. & KAWAI, I. 1993. Turbulent shear flow and heat transfer over the repeated two-dimensional square ribs on ground plane. *Journal of Fluids Engineering,* 115**,** 631-637.

OKE, T. R. 1988. Street design and urban canopy layer climate. *Energy and buildings,* 11**,** 103-113.

OKIISHI, M. Y., MUNSON, B. & YOUNG, D. 2006. Fundamentals of Fluid Mechanics. *John Wiley & Sons, Inc.*

ORLANDI, P. L., S ANTONIA, RA 2006. Turbulent channel flow with either transverse or longitudinal roughness elements on one wall. *Journal of Fluid Mechanics,* 561**,** 279-305.

ORSZAG, S. A. & PATTERSON JR, G. 1972. Numerical simulation of three-dimensional homogeneous isotropic turbulence. *Physical Review Letters,* 28**,** 76.

OZAN, A. Y., CONSTANTINESCU, G. & HOGG, A. J. 2015. Lock-exchange gravity currents propagating in a channel containing an array of obstacles. *Journal of Fluid Mechanics,* 765**,** 544-575.

ÖZGÖKMEN, T. M. & FISCHER, P. F. 2008. On the role of bottom roughness in overflows. *Ocean Modelling,* 20**,** 336-361.

PARKER, G., FUKUSHIMA, Y. & PANTIN, H. M. 1986. Self-accelerating turbidity currents. *Journal of Fluid Mechanics,* 171**,** 145-181.

PARKER, G. & GARCÍA, M. 2006. River, coastal and estuarine morphodynamics. *Proc., RCEM 2005*.

PARKER, G., GARCIA, M., FUKUSHIMA, Y. & YU, W. 1987. Experiments on turbidity currents over an erodible bed. *Journal of Hydraulic Research,* 25**,** 123-147.

PARSONS, D., BEST, J., ORFEO, O., HARDY, R., KOSTASCHUK, R. & LANE, S. 2005. Morphology and flow fields of three-dimensional dunes, Rio Paraná, Argentina: Results from simultaneous multibeam echo sounding and acoustic Doppler current profiling. *Journal of Geophysical Research: Earth Surface (2003–2012),* 110.

PARSONS, D. R., BEST, J. L., LANE, S. N., ORFEO, O., HARDY, R. J. & KOSTASCHUK, R. 2007. Form roughness and the absence of secondary flow in a large confluence-diffluence, Rio Parana, Argentina. *Earth Surface Processes and Landforms,* 32**,** 155-162.

PARSONS, D. R., WALKER, I. J. & WIGGS, G. F. 2004. Numerical modelling of flow structures over idealized transverse aeolian dunes of varying geometry. *Geomorphology,* 59**,** 149-164.

PARSONS, J. D. & GARCıA, M. H. 1998. Similarity of gravity current fronts. *Physics of Fluids (1994-present),* 10**,** 3209-3213.

PARTHENIADES, E. 1965. Erosion and deposition of cohesive soils. *Journal of the Hydraulics Division,* 91**,** 105-139.

PATEL, R. 1974. A note on fully developed turbulent flow down a circular pipe. *Aeronautical Journal,* 78**,** 93-97.

PATERA, A. T. 1984. A spectral element method for fluid dynamics: laminar flow in a channel expansion. *Journal of computational Physics,* 54**,** 468-488.

PERICLEOUS, K. 1987. Mathematical simulation of hydrocyclones. *Applied Mathematical Modelling,* 11**,** 242-255.

PERILLO, M., PROKOCKI, E., BEST, J. & GARCÍA, M. 2014. Bed form genesis from bed defects under unidirectional, oscillatory, and combined flows. *Journal of Geophysical Research: Earth Surface,* 119**,** 2635-2652.

PERRY, A. E., SCHOFIELD, W. H. & JOUBERT, P. N. 1969. Rough wall turbulent boundary layers. *Journal of Fluid Mechanics,* 37**,** 383-413.

PETERS, W. D. & VENART, J. 1999. *Rough-surface gravity current flows.* University of New Brunswick, Department of Mechanical Engineering.

PIZZUTO, J. E. 1987. Sediment diffusion during overbank flows. *Sedimentology,* 34**,** 301-317.

PLAPP, J. E. & MITCHELL, J. P. 1960. A hydrodynamic theory of turbidity currents. *Journal of Geophysical Research,* 65**,** 983-992.

PRANDTL, L. 1952. Essentials of Fluid Dynamics with Applications to Hydraulics. *Aeronautics, Meteorology and other Subjects: Bombay, Blackie & Son, Ltd*.

QIAN, G., DONG, Z., LUO, W. & WANG, H. 2009. Variations of horizontal and vertical velocities over two-dimensional transverse dunes: A wind tunnel simulation of the effect of windward slope. *Journal of arid environments,* 73**,** 1109-1116.

RAJAN, K., SRIVASTAVA, S., PITCHUMANI, B. & DHASANDHAN, K. 2008. Experimental study of thermal effectiveness in pneumatic conveying heat exchanger. *Applied Thermal Engineering,* 28**,** 1932-1941.

RAO, C. & PICOT, J. The effect of turbulence promoters on heat and momentum transfer for air flow in an annulus. Proceedings of 4th International Heat Transfer Conference, 1970. 1-12.

RAUDKIVI, A. 1966. Bed forms in alluvial channels. *Journal of Fluid Mechanics,* 26**,** 507-514.

RAUPACH, M. R. 1992. Drag and drag partition on rough surfaces. *Boundary-Layer Meteorology,* 60**,** 375-395.

REBESCO, M., CAMERLENGHI, A. & VAN LOON, A. 2008. Contourite research: a field in full development. *Contourites, Developments in Sedimentology,* 60**,** 3-10.

REBESCO, M., HERNÁNDEZ-MOLINA, F. J., VAN ROOIJ, D. & WÅHLIN, A. 2014. Contourites and associated sediments controlled by deep-water circulation

processes: state-of-the-art and future considerations. *Marine Geology,* 352**,** 111-154.

RIJN, L. C. V. 1984. Sediment transport, part II: suspended load transport. *Journal of hydraulic engineering,* 110**,** 1613-1641.

ROTTA, J. 1951. Statistische theorie nichthomogener turbulenz. *Zeitschrift für Physik,* 129**,** 547-572.

ROTTMAN, J. W. & SIMPSON, J. E. 1983. Gravity currents produced by instantaneous releases of a heavy fluid in a rectangular channel. *Journal of Fluid Mechanics,* 135**,** 95-110.

ROUSE, H. 1937. Modern conceptions of the mechanics or fluid turbulence. *Transactions of the American Society of Civil Engineers,* 102**,** 463-505.

ROUSSINOVA, V. & BALACHANDAR, R. 2011. Open channel flow past a train of rib roughness. *Journal of Turbulence***,** N28.

RYU, D., CHOI, D. & PATEL, V. 2007. Analysis of turbulent flow in channels roughened by two-dimensional ribs and three-dimensional blocks. Part I: Resistance. *International Journal of Heat and Fluid Flow,* 28**,** 1098-1111.

SAGAUT, P. 2013. *Large Eddy Simulation for Incompressible Flows: An Introduction*, Springer Berlin Heidelberg.

SAITO, N., PULLIN, D. I. & INOUE, M. 2012. Large eddy simulation of smooth-wall, transitional and fully rough-wall channel flow. *Physics of Fluids (1994-present),* 24**,** 075103.

SAMASIRI, P. & WOODS, A. W. 2015. Mixing in axisymmetric gravity currents. *Journal of Fluid Mechanics,* 782**,** R1.

SCHIJF, J. & SCHÖNFLED, J. Theoretical considerations on the motion of salt and fresh water. Proceedings Minnesota International Hydraulic Convention, 1953. IAHR.

SCHILLER, L. & NAUMANN, A. 1935. A drag coefficient correlation. *Vdi Zeitung,* 77**,** 51.

SCHLICHTING, H. 1936. Experimentelle untersuchungen zum rauhigkeitsproblem. *Archive of Applied Mechanics,* 7**,** 1-34.

SCHLICHTING, H. 1960. Boundary layer theory; Trans. J. Kestin.

SCHLICHTING, H., GERSTEN, K. & GERSTEN, K. 2000. *Boundary-layer theory*, Springer Science & Business Media.

SCHMIDT, W. 1911. Zur mechanik der boen. *Z. Meteorol,* 28**,** 355-362.

SEMINARA, G., COLOMBINI, M. & PARKER, G. 1996. Nearly pure sorting waves and formation of bedload sheets. *Journal of Fluid Mechanics,* 312**,** 253-278.

SEQUEIROS, O. E., SPINEWINE, B., BEAUBOUEF, R. T., SUN, T., GARCIA, M. H. & PARKER, G. 2010. Bedload transport and bed resistance associated with density and turbidity currents. *Sedimentology,* 57**,** 1463-1490.

SHANMUGAM, G. 2000. 50 years of the turbidite paradigm (1950s—1990s): deep-water processes and facies models—a critical perspective. *Marine and Petroleum Geology,* 17**,** 285-342.

SHIN, J., DALZIEL, S. & LINDEN, P. 2004. Gravity currents produced by lock exchange. *Journal of Fluid Mechanics,* 521**,** 1-34.

SHOTORBAN, B. & BALACHANDAR, S. 2006. Particle concentration in homogeneous shear turbulence simulated via Lagrangian and equilibrium Eulerian approaches. *Physics of Fluids (1994-present),* 18**,** 065105.

SHRINGARPURE, M., CANTERO, M. I. & BALACHANDAR, S. 2012. Dynamics of complete turbulence suppression in turbidity currents driven by monodisperse suspensions of sediment. *Journal of Fluid Mechanics,* 712**,** 384-417.

SHUGAR, D. H., KOSTASCHUK, R., BEST, J. L., PARSONS, D. R., LANE, S. N., ORFEO, O. & HARDY, R. J. 2010. On the relationship between flow and suspended sediment transport over the crest of a sand dune, Río Paraná, Argentina. *Sedimentology,* 57**,** 252-272.

SIMONIN, C. & VIOLLET, P. 1990. Predictions of an oxygen droplet pulverization in a compressible subsonic coflowing hydrogen flow. *Numerical Methods for Multiphase Flows, FED91***,** 65-82.

SIMONS, D. & RICHARDSON, E. 1963. Forms of bed roughness in alluvial channels. *Transactions of the American Society of Civil Engineers,* 128**,** 284-302.

SIMONS, D. B. & ŞENTÜRK, F. 1992. *Sediment Transport Technology: Water and Sediment Dynamics*, Water Resources Publications.

SIMPSON, J. 1969. A comparison between laboratory and atmospheric density currents. *Quarterly Journal of the Royal Meteorological Society,* 95**,** 758-765.

SIMPSON, J. & BRITTER, R. 1979. The dynamics of the head of a gravity current advancing over a horizontal surface. *Journal of Fluid Mechanics,* 94**,** 477-495.

SIMPSON, J., MANSFIELD, D. & MILFORD, J. 1977. Inland penetration of sea-breeze fronts. *Quarterly Journal of the Royal Meteorological Society,* 103**,** 47-76.

SIMPSON, J. E. 1972. Effects of the lower boundary on the head of a gravity current. *Journal of Fluid Mechanics,* 53**,** 759-768.

SIMPSON, J. E. 1987. Density Currents: In the environment and the laboratory. Cambridge University Press.

SIMPSON, J. E. 1999. *Gravity currents: In the environment and the laboratory*, Cambridge University Press.

SKUDARNOV, P., KANG, H., LIN, C., EBADIAN, M., GIBBONS, P., ERIAN, F. & RINKER, M. Experimental investigation of single-and double-species slurry transportation in a horizontal pipeline. Proc. ANS 9th International Topical Meeting on Robotics and Remote Systems, Seattle, WA, 2001.

SMAGORINSKY, J. 1963. General circulation experiments with the primitive equations: I. the basic experiment*. *Monthly weather review,* 91**,** 99-164.

SMITH, J. D. & MCLEAN, S. 1977. Spatially averaged flow over a wavy surface. *Journal of Geophysical research,* 82**,** 1735-1746.

SOFFIENTINO, B. & PILSON, M. 2005. The Bosphorus Strait. A Special Place in the History of Oceanography. *Oceanography,* 18**,** 16-23.

SOHN, Y. 2000. Coarse-grained debris-flow deposits in the Miocene fan deltas, SE Korea: a scaling analysis. *Sedimentary Geology,* 130**,** 45-64.

SOLOMOS, S., KALLOS, G., MAVROMATIDIS, E. & KUSHTA, J. 2012. Density currents as a desert dust mobilization mechanism. *Atmospheric Chemistry and Physics,* 12**,** 11199-11211.

SOULSBY, R. 1997. *Dynamics of marine sands: a manual for practical applications*, Thomas Telford.

SOULSBY, R. & WAINWRIGHT, B. 1987. A criterion for the effect of suspended sediment on near-bottom velocity profiles. *Journal of Hydraulic Research,* 25**,** 341-356.

SOUTHARD, J. B. & BOGUCHWAL, L. A. 1990. Bed configurations in steady unidirectional water flows. Part 2. Synthesis of flume data. *Journal of Sedimentary Research,* 60.

SPARKS, R. S. J., BONNECAZE, R. T., HUPPERT, H. E., LISTER, J. R., HALLWORTH, M. A., MADER, H. & PHILLIPS, J. 1993. Sediment-laden gravity currents with reversing buoyancy. *Earth and Planetary Science Letters,* 114**,** 243-257.

SPEZIALE, C. G., SARKAR, S. & GATSKI, T. B. 1991. Modelling the pressure–strain correlation of turbulence: an invariant dynamical systems approach. *Journal of Fluid Mechanics,* 227**,** 245-272.

STACEY, M. W. & BOWEN, A. J. 1988a. The vertical structure of density and turbidity currents: theory and observations. *Journal of Geophysical Research: Oceans (1978–2012),* 93**,** 3528-3542.

STACEY, M. W. & BOWEN, A. J. 1988b. The vertical structure of turbidity currents and a necessary condition for self-maintenance. *Journal of Geophysical Research: Oceans (1978–2012),* 93**,** 3543-3553.

STEELE, J. H., THORPE, S. A. & TUREKIAN, K. K. 2009. *Ocean Currents: A derivative of the encyclopedia of Ocean Sciences*, Academic Press.

STOW, D. A., HERNÁNDEZ-MOLINA, F. J., LLAVE, E., SAYAGO-GIL, M., DEL RÍO, V. D. & BRANSON, A. 2009. Bedform-velocity matrix: the estimation of bottom current velocity from bedform observations. *Geology,* 37**,** 327-330.

STRAUB, K. M., MOHRIG, D., BUTTLES, J., MCELROY, B. & PIRMEZ, C. 2011. Quantifying the influence of channel sinuosity on the depositional mechanics of channelized turbidity currents: A laboratory study. *Marine and Petroleum Geology,* 28**,** 744-760.

SUN, H. & FAGHRI, M. 2003. Effect of surface roughness on nitrogen flow in a microchannel using the direct simulation Monte Carlo method. *Numerical Heat Transfer: Part A: Applications,* 43**,** 1-8.

TACHIE, M., BERGSTROM, D. & BALACHANDAR, R. 2000. Rough wall turbulent boundary layers in shallow open channel flow. *Journal of Fluids Engineering,* 122**,** 533-541.

TALLING, P., WYNN, R., MASSON, D., FRENZ, M., CRONIN, B., SCHIEBEL, R., AKHMETZHANOV, A., DALLMEIER-TIESSEN, S., BENETTI, S. & WEAVER, P. 2007. Onset of submarine debris flow deposition far from original giant landslide. *Nature,* 450**,** 541-544.

TALLING, P. J., ALLIN, J., ARMITAGE, D. A., ARNOTT, R. W., CARTIGNY, M. J., CLARE, M. A., FELLETTI, F., COVAULT, J. A., GIRARDCLOS, S. & HANSEN, E. 2015. Key future directions for research on turbidity currents and their deposits. *Journal of Sedimentary Research,* 85**,** 153-169.

TANI, I. 1987. Turbulent boundary layer development over rough surfaces. *Perspectives in turbulence studies.* Springer.

THOM, A. 1971. Momentum absorption by vegetation. *Quarterly Journal of the Royal Meteorological Society,* 97**,** 414-428.

THORPE, S. 1973. Experiments on instability and turbulence in a stratified shear flow. *Journal of Fluid Mechanics,* 61**,** 731-751.

TILSTON, M., ARNOTT, R., RENNIE, C. & LONG, B. 2015. The influence of grain size on the velocity and sediment concentration profiles and depositional record of turbidity currents. *Geology,* 43**,** 839-842.

TOKYAY, T. & CONSTANTINESCU, G. 2015. The effects of a submerged non-erodible triangular obstacle on bottom propagating gravity currents. *Physics of Fluids (1994-present),* 27**,** 056601.

TOKYAY, T., CONSTANTINESCU, G., GONZALEZ-JUEZ, E. & MEIBURG, E. 2011a. Gravity currents propagating over periodic arrays of blunt obstacles: Effect of the obstacle size. *Journal of Fluids and Structures,* 27**,** 798-806.

TOKYAY, T., CONSTANTINESCU, G. & MEIBURG, E. 2011b. Lock-exchange gravity currents with a high volume of release propagating over a periodic array of obstacles. *Journal of Fluid Mechanics,* 672**,** 570-605.

TOWNSEND, A. A. 1980. *The structure of turbulent shear flow*, Cambridge university press.

TSIKATA, J. & TACHIE, M. 2013. Adverse pressure gradient turbulent flows over rough walls. *International Journal of Heat and Fluid Flow,* 39**,** 127-145.

TUBAU, X., PAULL, C. K., LASTRAS, G., CARESS, D. W., CANALS, M., LUNDSTEN, E., ANDERSON, K., GWIAZDA, R. & AMBLAS, D. 2015. Submarine canyons of Santa Monica Bay, Southern California: Variability in morphology and sedimentary processes. *Marine Geology,* 365**,** 61-79.

TUCHOLKE, B. E. 1982. Origin of longitudinal triangular ripples on the Nova Scotian continental rise.

VAN DEN BERG, J. 1987. Bedform migration and bed-load transport in some rivers and tidal environments. *Sedimentology,* 34**,** 681-698.

VAN RIJN, L. C. 1984. Sediment transport, part III: bed forms and alluvial roughness. *Journal of Hydraulic Engineering,* 110**,** 1733-1754.

VAN RIJN, L. C. 1985. *Mathematical models for sediment concentration profiles in steady flow*, Waterloopkundig Laboratorium.

VAN RIJN, L. C., VAN RIJN, L. C. & VAN RIJN, L. C. 1990. *Principles of fluid flow and surface waves in rivers, estuaries, seas and oceans*, Aqua Publications Amsterdam, The Netherlands.

VANDRIEST, E. R. 1956. On turbulent

fow near a wall. *J Aerospace Sci,* 23**,** 1007-1011.

VANONI, V. A. Sedimentation engineering. 2006. ASCE.

VENDITTI, J. G. 2007. Turbulent flow and drag over fixed two-and three-dimensional dunes. *Journal of Geophysical Research: Earth Surface (2003–2012),* 112.

VENDITTI, J. G. & BAUER, B. O. 2005. Turbulent flow over a dune: Green River, Colorado. *Earth Surface Processes and Landforms,* 30**,** 289-304.

VENDITTI, J. G. & BENNETT, S. J. 2000. Spectral analysis of turbulent flow and suspended sediment transport over fixed dunes. *Journal of Geophysical Research: Oceans (1978–2012),* 105**,** 22035-22047.

VENDITTI, J. G., CHURCH, M. & BENNETT, S. J. 2005a. Morphodynamics of small-scale superimposed sand waves over migrating dune bed forms. *Water resources research,* 41.

VENDITTI, J. G., CHURCH, M. & BENNETT, S. J. 2005b. On the transition between 2D and 3D dunes. *Sedimentology,* 52**,** 1343-1359.

VENDITTI, J. G., CHURCH, M. A. & BENNETT, S. J. 2005c. Bed form initiation from a flat sand bed. *Journal of Geophysical Research: Earth Surface (2003–2012),* 110.

VERSTEEG, H. K. & MALALASEKERA, W. 2007. *An introduction to computational fluid dynamics: the finite volume method*, Pearson Education.

VILLARD, P. & KOSTASCHUK, R. 1998. The relation between shear velocity and suspended sediment concentration over dunes: Fraser Estuary, Canada. *Marine Geology,* 148**,** 71-81.

VILLARET, C. & TROWBRIDGE, J. 1991. Effects of stratification by suspended sediments on turbulent shear flows. *Journal of Geophysical Research: Oceans (1978–2012),* 96**,** 10659-10680.

VON KARMAN, T. 1940. The engineer grapples with nonlinear problems. *Bulletin of the American Mathematical Society,* 46**,** 615-683.

WALLIS, G. B. 1969. *One-dimensional two-phase flow*, McGraw-Hill New York.

WEBB, R. & ECKERT, E. 1972. Application of rough surfaces to heat exchanger design. *International Journal of Heat and Mass Transfer,* 15**,** 1647-1658.

WEBB, R., ECKERT, E. & GOLDSTEIN, R. 1971. Heat transfer and friction in tubes with repeated-rib roughness. *International Journal of Heat and Mass Transfer,* 14**,** 601-617.

WEIMER, P., SLATT, R. M. & BOUROULLEC, R. 2007. *Introduction to the petroleum geology of deepwater settings*, AAPG/Datapages.

WIBERG, P. L. & NELSON, J. M. 1992a. Unidirectional flow over asymmetric and symmetric ripples. *Journal of Geophysical Research: Oceans,* 97**,** 12745-12761.

WIBERG, P. L. & NELSON, J. M. 1992b. Unidirectional flow over asymmetric and symmetric ripples. *Journal of Geophysical Research: Oceans (1978–2012),* 97**,** 12745-12761.

WILCOX, D. C. 1988. Reassessment of the scale-determining equation for advanced turbulence models. *AIAA journal,* 26**,** 1299-1310.

WILCOX, D. C. 1993. Comparison of two-equation turbulence models for boundary layers with pressure gradient. *AIAA journal,* 31**,** 1414-1421.

WILCOX, D. C. 1998. *Turbulence modeling for CFD*, DCW industries La Canada, CA.

WILCOX, D. C. 2006. *Turbulence Modeling for CFD: CD-ROM*, DCW Industries.

WINSEMANN, J., LANG, J. & VAN DEN BERG, J. H. From cyclic steps to humpback dunes: bedforms created by glacial lake-outburst floods. EGU General Assembly Conference Abstracts, 2015. 1750.

WREN, D., KUHNLE, R. & WILSON, C. 2007. Measurements of the relationship between turbulence and sediment in suspension over mobile sand dunes in a laboratory flume. *Journal of Geophysical Research: Earth Surface (2003–2012),* 112.

WYNN, R. & MASSON, D. 2008. Sediment waves and bedforms. *Developments in sedimentology,* 60**,** 289-300.

WYNN, R. B., KENYON, N. H., MASSON, D. G., STOW, D. A. & WEAVER, P. P. 2002. Characterization and recognition of deep-water channel-lobe transition zones. *AAPG bulletin,* 86.

WYNN, R. B. & STOW, D. A. 2002. Classification and characterisation of deep-water sediment waves. *Marine Geology,* 192**,** 7-22.

WYNN, R. B., WEAVER, P. P., ERCILLA, G., STOW, D. A. & MASSON, D. G. 2000. Sedimentary processes in the Selvage sediment-wave field, NE Atlantic: new insights into the formation of sediment waves by turbidity currents. *Sedimentology,* 47**,** 1181-1197.

YAM, K., MCCAFFREY, W. D., INGHAM, D. B. & BURNS, A. D. 2011. CFD modelling of selected laboratory turbidity currents. *Journal of Hydraulic Research,* 49**,** 657-666.

YAMADA, Y., KAWAMURA, K., IKEHARA, K., OGAWA, Y., URGELES, R., MOSHER, D., CHAYTOR, J. & STRASSER, M. 2012. *Submarine mass movements and their consequences*, Springer.

YOUNG, B. & VAN VLIET, B. 1988. The effect of surface roughness on fluid-to-particle mass transfer in a packed adsorber bed. *International Journal of Heat and Mass Transfer,* 31**,** 27-34.

ZANOUN, E.-S., DURST, F. & NAGIB, H. 2003. Evaluating the law of the wall in two-dimensional fully developed turbulent channel flows. *Physics of Fluids (1994-present),* 15**,** 3079-3089.

ZHU, J., LEE, C., CHEN, G. & LEE, J. 2006. PIV observation of instantaneous velocity structure of lock release gravity currents in the slumping phase. *Communications in Nonlinear Science and Numerical Simulation,* 11**,** 262-270.

ZYSERMAN, J. A. & FREDSØE, J. 1994. Data analysis of bed concentration of suspended sediment. *Journal of hydraulic engineering,* 120**,** 1021-1042.